INVESTIGATION OF BLOWN TUBERCLES WITH APPLICATION TO TILT-WING AIRCRAFT

INVESTIGATION DES TUBERCULES SOUFFLÉS AVEC APPLICATION AUX AÉRONEFS À VOILURE BASCULANTE

A Thesis Submitted to the Division of Graduate Studies
of the Royal Military College of Canada
by

Felix Junho Sim, BEng
Second Lieutenant

In Partial Fulfillment of the Requirements for the Degree of
Master of Applied Science in Aeronautical Engineering

May, 2023

To my parents, for their endless support of my endeavours.

Acknowledgements

I would like to express my gratitude to my supervisor, Dr. Ruben E. Perez for always motivating me to raise the bar. His expert advice and guidance was invaluable for my education. I would like to extend my thanks to Dr. Peter Jansen, who I could always rely on for a sound, second opinion, Dr. Asad Asghar, for his advice regarding experimental testing, and Dr. Billy Allan, who was instrumental in developing my technical writing and presentation skills.

Abstract

Sim, Felix Junho. MASc. Royal Military College of Canada, May 2023. *Investigation of Blown Tubercles with Application to Tilt-Wing Aircraft.* Supervised by Ruben E. Perez, BEng, MASc, PhD, PEng, Associate Professor.

Tilt-wing aircraft combine the vertical takeoff and landing (VTOL) capability of rotorcraft with the forward flight performance of fixed wing aircraft, simultaneously providing low speed manoeuvrability, extended range, longer endurance, and operational versatility. This combination of capabilities makes tilt-wing aircraft a key enabler of advanced air mobility. As part of an advanced air mobility network, operation in highly populated urban areas is a requirement, where safety is paramount. A critical flight phase for a tilt-wing aircraft is the transition between forward flight and vertical flight modes, where the wing must operate at post-stall angles of attack. Tubercles are bio-inspired, passive flow control devices that have been shown to drastically improve post stall aerodynamic performance of lifting surfaces. This study explores the application of tubercles to the propeller blown wing of a tilt-wing aircraft. Six different tubercle geometries were applied to the leading edge of a propeller blown wing and tested in a wind tunnel to characterize the behaviour of tubercles in the presence of a propeller slipstream. An empirical model was developed using the experimental results, and applied to an analytical simulation of transition. Finally, a preliminary flight test of a surrogate research vehicle with a similar aerodynamic environment to a tilt-wing aircraft was conducted. The experimental wind tunnel campaign showed that tubercles can increase the post-stall lift coefficient of a blown wing by up to 27%. This increased lift performance was shown to reduce the minimum required forward flight speed during transition by up to 9.6%, expanding the transition corridor. The flight test of the surrogate vehicle demonstrated that tubercles significantly reduce power requirements for a blown system that operates at high angles of attack. The reduction in power required translates to increased range, endurance, or payload capacity. This study shows that tubercles are an effective method for improving the safety of tilt-wing transition, with added utility of reducing the power required in transition.

Keywords: VTOL, tilt-wing, transition, applied aerodynamics, tubercles, bio-inspired, blown wing, propeller-wing interactions, wind tunnel, experimental, UAV, urban air mobility

Résumé

Sim, Felix Junho. MASc. Collège militaire royale du Canada, mai 2023. *Investigation des Tubercules Soufflés avec Application aux Aéronefs à Voilure Basculante*. Thèse dirigée par Ruben E. Perez, BEng, MASc, PhD, PEng, Professeur adjoint.

Les aéronefs à voilure basculante combinent la capacité d'aéronef à décollage et atterrissage vertical (ADAV) des giravions avec les performances de vol en palier des aéronefs à voilure fixe, offrant simultanément une manœuvrabilité à faible vitesse, une distance franchissable étendue, une plus grande autonomie et une flexibilité opérationnelle. Cette combinaison fait des aéronefs à voilure basculante un élément clé pour la mobilité aérienne avancée. Les réseaux de mobilité aérienne avancée nécessitent des opérations dans des zones urbaines très peuplées, où la sécurité est primordiale. Une phase de vol critique pour un avion à voilure basculante est la transition entre les modes de vol en palier et de vol vertical, où l'aile fonctionne à des angles d'attaque post-décrochage. Les tubercules sont un dispositif de commande d'écoulement d'air passif et bio-inspiré qui ont démontré une amélioration considérable des performances aérodynamiques post-décrochage des surfaces portantes. Cette étude explore l'application des tubercules à l'aile soufflée d'un aéronef à voilure basculante. Six ailes munies de géométries différentes de tubercules sur leurs bords d'attaque furent testées dans une soufflerie pour caractériser leur comportement dans le souffle de l'hélice. Un modèle empirique fut développé à partir des résultats expérimentaux et appliqué à une simulation analytique de la transition. Enfin, un vol d'essai préliminaire d'un véhicule de recherche de substitution dans un environnement aérodynamique similaire à celui d'un aéronef à voilure basculante a été réalisé. Les essais en soufflerie ont montré que les tubercules peuvent augmenter le coefficient de portance post-décrochage d'une aile soufflée de 27 %. Il a été démontré que cette augmentation de la portance permet de réduire la vitesse minimale de vol en palier requise pendant la transition par 9,6 %, élargissant ainsi le domaine de transition. Le vol d'essai du véhicule de substitution a démontré que les tubercules réduisent considérablement les besoins en puissance d'un système soufflé fonctionnant à des grands angles d'attaque. La réduction de la puissance requise se traduit par une augmentation de la distance franchissable, du temps de vol ou de la charge utile. Cette étude montre que les tubercules sont une méthode efficace d'améliorer la sécurité de la transition des ailes basculantes, et qu'ils permettent en outre de réduire la puissance nécessaire à la transition.

Mots-clés: ADAV, avions à voilure basculante, aérodynamique appliquée, tubercules, bio-inspiré, aile soufflée, interaction hélice-aile, expérimental, véhicule aérien sans pilote, soufflerie, mobilité aérienne urbaine

Contents

List of Tables

List of Figures

Nomenclature

Roman Symbols

A	Tubercle amplitude	[%c]
a	Acceleration	[g's]
B	Magnetic field strength	[G]
c	Chord length	[m]
$C_{n,\beta}$	Yaw stability derivative	[rad^{-1}]
D	Drag	[N]
d	Diameter	[m]
F	Force	[N]
f	Frequency	[Hz]
h	Height	[m]
I	Current	[A]
i	Arbitrary index variable	[-]
L	Lift	[N]
l	Length	[m]
M	Moment	[Nm]
m	Mass	[g]
P	Power	[W]
p	Pressure	[Pa]
Q	Torque	[Nm]
R	Radius	[m]
S	Reference area	[m^2]
T	Thrust or Temperature	[N or K]

t	Time	[s]
U	Freestream velocity	[m/s]
V	Voltage	[V]
v	Velocity	[m/s]
W	Weight	[N]
w	Velocity in a fully developed propeller slipstream	[m/s]
x	Chordwise position	[m]
y	Spanwise position	[m]
z	Vertical position	[m]

Greek Symbols

α	Angle of attack	[°]
β	Coning angle	[°]
Δ	Change in value	[-]
δ	Uncertainty	[-]
ϵ	Downwash or sidewash angle	[°]
η	Efficiency	[-]
κ	Dynamic pressure ratio	[-]
Λ	Leading edge sweep	[°]
λ	Tubercle wavelength, or rotor inflow	[%c, -]
Ω	Rotational speed	[RPM]
ω	Rotational speed	[rad/s]
ρ	Density	[kg/m^3]
σ	Rotor solidity	[-]
θ	Angle	[°]

Dimensionless Groups

$\Delta C_{L_{\mathrm{p},\%}}$	Relative lift augmentation
$\Delta C_{L_{\mathrm{p}}}$	Lift augmentation
C_D	Drag coefficient
C_L	Lift coefficient

C_N	Propeller normal force coefficient
C_P	Power coefficient
C_p	Pressure coefficient
C_Q	Torque coefficient
C_T	Thrust coefficient
$C_{L_{\text{off}}}$	Power off lift coefficient
$C_{L_{\text{tot}}}$	Total lift coefficient
$C_{M_{c/4}}$	Moment coefficient about the quarter chord
dC_P	Incremental power coefficient
dC_T	Incremental thrust coefficient
E	Aerodynamic efficiency
F	Prandtl's tip loss factor
$f(x)$	Fitness function
J	Advance ratio
K	Empirical fit constants
k_w	Slipstream velocity correction factor
r	Non-dimensional radial position
Re	Reynolds number
W	Weighting factor
X_{p}	Chordwise propeller position normalized by propeller diameter
Z_{p}	Vertical propeller position normalized by propeller diameter

Subscripts

0	Installation
∞	Freestream conditions
air	Property of air
b	Blade
c	Cable losses
$c/2$	About the half chord
$c/4$	About the quarter chord

emp	Empirical value
exp	Experimental value
f	Fuselage
i	Indexing variable
i	Induced component
j	Blown segment
L, α	Change in lift with respect to angle of attack
m	Motor
max	Maximum value
min	Minimum value
N	Normal component
off	Power off condition
on	Power on condition
p	Propeller
s	Value at stall
SLE	Straight leading edge
T	Tangential component, or thrust component
t	Telemetry pad
tbr	Tubercle
tot	Total value
tw	Twist
u	Unblown segment
v	Vertical tail
w	Wing
x	In the x-direction
y	In the y-direction
z	In the z-direction

Abbreviations

2D	Two-dimensional

3D	Three-dimensional
AAM	Advanced air mobility
AC	Aerodynamic centre
ASA	Acrylic styrene acrylonitrile
BEMT	Blade element momentum theory
BFGS	Broyden-Fletcher-Goldfarb-Shanno algorithm
BPF	Blade passing frequency
CA	Contraction area
CAD	Computer aided design
CFD	Computational fluid dynamics
CG	Centre of gravity
DAQ	Data acquisition system
ESC	Electronic speed controller
FDM	Fused deposition modelling
FOM	Figure of merit
IMU	Inertial measurement unit
LAS	Lift augmentation score
LES	Large eddy simulation
LiPo	Lithium polymer
LW-PLA	Light weight polylactic acid
OGE	Out of ground effect
PIV	Particle image velocimetry
PLA	Polylactic acid
PSD	Power spectral density ..... [W/Hz]
RANS	Reynolds-averaged Navier-Stokes
RMC	Royal Military College of Canada
RMSE	Root mean square error
RPM	Rotations per minute
SCRV	Streamwise counter-rotating vortices
SLE	Straight leading edge

TRV	Transition Research Vehicle
UAM	Urban air mobility
UAV	Unmanned aerial vehicle
VLM	Vortex lattice method
VTOL	Vertical takeoff and landing

1 Introduction

1.1 Motivation for the Research

Since their inception, rotary wing vehicles, or rotorcraft, have seen widespread application in military and civil aviation. Their appeal lies in their vertical takeoff and landing (VTOL) capabilities, excellent low speed manoeuvrability, and ability to hover in place. These characteristics allow for rotorcraft to operate in locations without runways, such as urban settings and remote locations where fixed wing aircraft cannot. However, these desirable characteristics come at the cost of significantly reduced range, forward flight speed, and endurance when compared to fixed wing aircraft. In an attempt to combine the VTOL capabilities of rotorcraft while retaining the forward flight performance of fixed wing aircraft, a new class of hybrid aircraft, which will be referred to here as transitional aircraft, have been of major interest for the aviation industry [1, 2].

The numerous transitional aircraft configurations that have emerged can be organized into five broad categories: tilt-rotor, tilt-wing, thrust vectoring, tail sitter, and dual-system [3, 4]. Tilt-rotors consist of rotors that can be tilted between a forward and vertical position to be used for both forward and vertical flight. An example of a tilt-rotor aircraft is the *Bell Boeing V-22 Osprey* [5] or the *Bell Eagle Eye* [6]. Tilt-wings consist of wing mounted propellers that are tilted from horizontal to vertical along with the entire wing for forward and vertical flight. Examples of tilt-wing aircraft include the *Canadair CL-84* [7], the *NASA GL-10 Greased Lightning* [8], and the *Airbus* A^3 *Vahana* [9]. A thrust vectoring configuration, such as the *McDonnell Douglas AV-8B Harrier II* [10], uses ducts to redirect jets for forward and vertical flight. Tail sitters are similar to tilt-wing configurations but the entire aircraft is tilted rather than just the wing. An example of such an aircraft is the *Convair XFY-1* [11], or the *AeroVironment SkyTote* [12]. Finally, the dual-system configuration uses separate propulsion systems for vertical flight and forward flight. The *Dassault Mirage III V* [13] and the *AeroVironment JUMP® 20* [14] are examples of this configuration.

In recent years, interest in transitional aircraft have increased significantly alongside the rising popularity of advanced air mobility (AAM) and urban air mobility (UAM). AAM is a transportation system that allows for safe and accessible air transportation of passengers, goods, and services between urban, suburban, and rural areas [15,16]. UAM is a subset of AAM that constrains the transportation system to urban and suburban operations. Transitional aircraft that are VTOL capable and also possess efficient high speed cruise capabilities are a key enabler of AAM and UAM [17]. Of the five categories of transitional aircraft, the tilt-wing configuration has potential to become this key enabler by virtue of its inherent design benefits that make it an attractive configuration

option for high speed VTOL aircraft [18–20]. Since the entire wing along with the wing mounted propellers are rotated through the transition between horizontal and vertical flight, the aerodynamic environment of the wing of a tilt-wing aircraft departs drastically from the typical environment of a conventional fixed wing. The aerodynamics of a tilt-wing aircraft are dominated by two major factors: a wide range of angles of attack as it transitions from horizontal to vertical and vice versa, and the effect of the propeller slipstream on the wing throughout those angles.

A critical flight phase for any VTOL aircraft is the transition between forward and vertical flight, and vice versa. The performance of a VTOL aircraft through this transition can be characterized by a transition corridor. The transition corridor shows the allowable forward flight speeds for each tilt angle between forward flight and vertical flight. Figure 1.1 shows an example of a transition corridor for the *Bell XV-15* [21]. The transition corridor is bound on the right hand side by the maximum speed of the aircraft. On the left hand side the corridor is bound by the lowest allowable flight speed before the aircraft no longer produces sufficient lift to remain in flight. The left bound is highly dependant on the stall behaviour of the wing, especially for tilt-wing configurations where the entire wing is tilted through a wide range of angles of attack, including angles in the post-stall regime. The handling qualities of the aircraft during transition have also been shown to suffer from the stalling of the wing [7, 22]. If the stall behaviour of the wing can be improved, the left bound of the transition corridor can be moved further left and the controllability of the aircraft can be improved, ultimately allowing for safer operation at lower speeds which is imperative in urban settings.

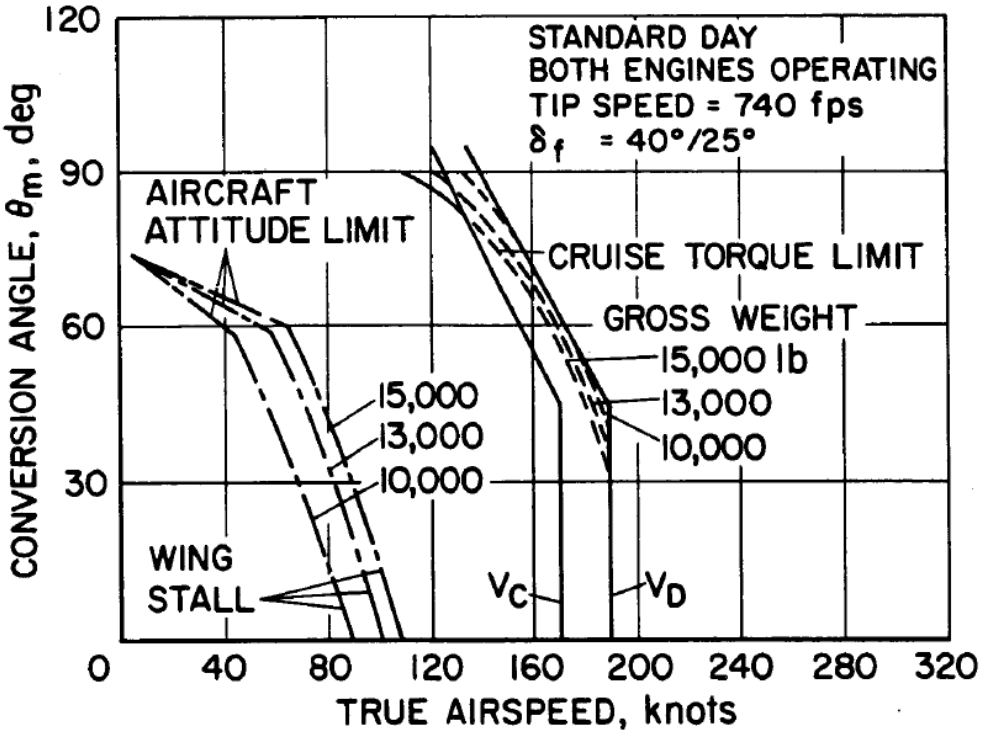

Figure 1.1: Transition corridor of the *Bell XV-15* at sea level [21].

Leading edge tubercles are a bio-inspired, passive flow control device that has been shown to drastically improve the stall characteristics and post stall performance of lifting surfaces. Although the impact of tubercles on the aerodynamic performance of blown wings, like those found on tilt-wing aircraft, have not yet been investigated, applying tubercles to a tilt-wing aircraft has the potential to improve significantly the stall behaviour during transition. This could translate to an expanded lower bound of the transition corridor and improved handling qualities during transition. The scope of this thesis includes this application of leading edge tubercles on the blown lifting surfaces of tilt-wing aircraft.

1.2 Research Objectives

The aim of this research is to investigate the application of leading edge tubercles on the transition of tilt-wing aircraft. An experimental approach is used to explore the effect of tubercles on a blown lifting surface angles of attack, involving a wind tunnel campaign as well as a low-order numerical simulation of transition. This study also includes a flight test campaign of a surrogate test vehicle. Specifically, the objectives of this research are:

i. Experimentally characterize the effect of propeller position on the aerodynamic performance of a blown lifting surface at high angles of attack,
ii. Develop a method of assessing the effectiveness of a propeller position in the context of transition and use this method to determine the optimal propeller position for transition,
iii. Experimentally characterize the aerodynamic performance of a blown and unblown lifting surface with leading edge tubercles at the optimal propeller position for transition,
iv. Develop a method to simulate the transition of a tilt-wing aircraft using low-order numerical methods,
v. Determine the impact of tubercles on the transition corridor of a representative transitional vehicle using a simulation, and
vi. Demonstrate the effectiveness of tubercles on a blown system that experiences high angles of attack through the flight testing of a monocopter.

1.3 Thesis Layout

The remainder of this thesis is organized as follows. Chapter 2 presents a literature review of the existing body of knowledge regarding the application and aerodynamic performance of tubercles to lifting surfaces. Existing research on propeller blown wings will also be presented. Chapter 3 presents the experimental wind tunnel campaign conducted to characterize the effect of propeller position on the aerodynamic performance of a lifting surface at high angles of attack. Chapter 4 presents an extension of the experimental wind tunnel campaign conducted to characterize the effect of different tubercle geometries on the aerodynamic performance of a blown and unblown lifting surface at high angles of attack. Chapter 5 presents the design of a representative tilt-wing UAV and the prediction of its transition corridor using low order numerical methods. That chapter will also discuss the effect of the addition of tubercles to the transition corridor of this representative tilt-wing UAV. Chapter 6 presents an application of the

results of the experimental wind tunnel campaign in a practical setting through the flight testing of a surrogate vehicle that possesses a blown system that operates at high angles of attack. Finally Chapter 7 concludes the thesis with concluding remarks and recommendations for future research regarding this topic.

1.4 Contributions

The contributions of this study include:

i. The characterization of the effect of propeller position on the aerodynamic performance of a blown lifting surface at high angles of attack.
ii. The first study to investigate experimentally the aerodynamic performance of tubercles on blown lifting surfaces at high angles of attack.
iii. The first study to investigate the effect of leading edge tubercles on the transition of tilt-wing aircraft.
iv. A flight test campaign of a monocopter to demonstrate the potential performance benefits of applying tubercles to a blown system that experiences high angles of attack.
v. A method to increase the safety of VTOL vehicles during transition between vertical and horizontal flight.

2 Literature Review

Many different applications for tubercles have been explored, including but not limited to planar lifting surfaces [23,24], rotor blades [25], gas turbine blades [26] and propellers [27]. This chapter will only touch on the current body of knowledge concerning the application of tubercles to planar lifting surfaces. In addition, this chapter includes a review of existing literature concerning propeller blown wing systems.

2.1 Background on Tubercles

Tubercles are passive flow control devices that are bio inspired by the flippers of humpback whales [28–30]. Humpback whales have been known to possess a unique flipper design that features protuberances along the leading edge as shown in Figure 2.1. These protuberances are called tubercles. Tubercles create a wavy leading edge geometry that was hypothesized to allow for humpback whales to employ feeding strategies that involve tight turning manoeuvres to herd prey for easy consumption [29, 31]. Fish and Battle were the first to study the humpback whale flipper and the effects of tubercles in the context of hydrodynamic design, which was subsequently applied to aerodynamic design [29]. They speculated that the tubercles generate streamwise vortices that help to postpone stall and maintain lift at higher angles of attack. Numerous experimental and computational studies to elucidate the mechanisms by which tubercles operate and to better understand the effects of the tubercles followed. These will be summarized in the following section.

Figure 2.1: Right pectoral flipper of a humpback whale clearly exhibiting the tubercles along the leading edge [32].

The most studied tubercle geometry is a sinusoidal leading edge shape. The sinusoidal form allows for a simple and effective way to parameterize the tubercle shape. It is defined by two parameters known as the tubercle amplitude and wavelength. The exact conventions used for describing the tubercle amplitude and wavelength are not widely agreed upon, but both parameters are generally defined as a percentage of the chord. The sinusoidal shape creates peaks and valleys along the leading edge of the flipper that interacts with the freestream and creates the secondary flows responsible for the changes in the performance of lifting surfaces. While other tubercle geometries have been studied, they will not be included in this review [33, 34].

2.2 Tubercle Mechanisms

The early work conducted by Fish and Battle suggested the presence of streamwise vortices generated by the tubercles, but concluded that more investigation was required to draw a definitive conclusion [29]. The generation of streamwise vortices was confirmed by Pedro and Kobayashi through a computational fluid dynamics (CFD) simulation of a representative whale flipper with and without tubercles [35]. The whale flipper modelled had a span of 0.5625 m and a mean chord of 0.127 m, at an angle of attack of 15°. The simulation used a large eddy simulation (LES) turbulence model in conjunction with a Reynolds-averaged Navier-Stokes (RANS) solver, and was conducted at a Reynolds number (Re) of approximately 5.0×10^5. The results of the simulation clearly showed regions of high vorticity on the flipper with tubercles that did not exist on the flipper without tubercles. Another computational investigation by Skillen *et al.*, using an LES turbulence model with a RANS solver on a rectangular wing section at $\mathrm{Re} = 1.2 \times 10^5$, supported the findings of Pedro and Kobayashi [36]. Skillen *et al.* concluded that the tubercle peaks deflected the freestream flow into the tubercle valleys where it is then accelerated. This enhances the suction peak of the wing section within the tubercle valleys resulting in the creation of a spanwise flow. This spanwise flow is responsible for the generation of streamwise vortices [36]. The acceleration of the flow within the tubercle valleys was also predicted earlier by Fish and Battle by their observation of the lack of barnacles attached to the humpback whale flipper between the tubercles, and later confirmed by Hansen *et al.* through particle image velocimetry (PIV) [29, 37]. Furthermore, the simulation by Skillen *et al.* identified that the vortices were generated in pairs that are counter-rotating [36].

Several experimental investigations behind the generation of the streamwise counter-rotating vortices (SCRV) by the tubercles have also been conducted. Stanway experimentally investigated the vortices generated by tubercles using PIV on a whale flipper model in a water tunnel, at $\mathrm{Re} = 9.0 \times 10^4$ [38]. Stanway's measurements clearly showed the development of the SCRV that increased in strength with increasing angle of attack. Similar PIV measurements were conducted by Custodio on a rectangular wing section in a water tunnel at $\mathrm{Re} = 1.2 \times 10^4$, which showed the same development of the SCRV [39]. Hydrogen bubble flow visualization by Hansen *et al.* also revealed the SCRV [40, 41].

2.2.1 Vortex Generator Theory

As demonstrated above, the existence of the SCRV generated by the tubercles is a generally accepted conclusion that is well supported by multiple independent sources. However, the exact mechanism by which these SCRV augment the performance of lifting surfaces is not widely agreed upon. The earliest theory is that tubercles behave like vortex generators [29, 40, 42]. Vortex generators function by creating a vortex that induces the mixing of high momentum fluid that exists outside of the boundary layer into the lower momentum fluid within the boundary layer [42–44]. This re-energizes the boundary layer which delays flow separation. This hypothesis was rejected by van Nierop *et al.* who noted that the size of the tubercles, in both amplitude and wavelength, are much larger than the boundary layer thickness suggesting that tubercles operate through a different mechanism at a larger scale. They proposed that the SCRV impart a downwash that decreases the effective angle of attack, consequently delaying stall [45]. Another key proposal by van Nierop *et al.* is that the changing chord length due to the tubercles results in regions where the airfoil thickness to chord is increased (valleys) and the local stall angle is decreased, or the airfoil thickness to chord is decreased (peaks) and the local stall angle is increased. This gives rise to an overall gradual stall behaviour as different sections stall at different angles of attack. Skillen *et al.* combined the vortex generator theory with the conclusions of van Nierop *et al.* by suggesting that the effects of the SCRV are two fold. They serve to re-energize the boundary layer in a similar fashion to vortex generators via momentum transport, while also producing strong secondary flows that alter the spanwise pressure distribution [36].

2.2.2 Vortex Lift Theory

Another popular theory is that the vortices generated by tubercles are analogous to the vortices generated by delta wings, augmenting lift by means of vortex lift [37–39, 46]. In delta wings, a leading edge vortex is generated on the suction surface due to the geometry of the wing planform, which creates a region of decreased pressure resulting in an increased suction peak on the suction surface. This increases the lift generated, and is known as vortex lift [47]. Delta wings generate leading edge vortices even at high angles of attack, which is similar to the behaviour of the SCRV created by tubercles. Custodio goes as far as stating that tubercles are analogous to a spanwise row of delta wings along the leading edge [39]. While convincing arguments for both the vortex generator theory as well as the vortex lift theory exist, the currently most accepted theory is that tubercles behave like vortex generators. However, the exact source of the performance improvements seen with tubercles are likely a result of a combination of these mechanisms rather than one or the other in isolation [48].

2.2.3 Flow Compartmentalization

A secondary effect of the SCRV generated by the tubercles is the compartmentalization of spanwise flow. This effect was first hypothesized by Watts and Fish as an explanation for a reduction in induced drag observed through a three-dimensional (3D) panel method simulation conducted on a finite wing [30]. They concluded that the reduction in induced drag was due to the perturbation of the spanwise lift distribution, reducing the strength of the tip vortex. This was later confirmed through PIV imagery of the wing tip vortex of a finite wing in a water tunnel conducted by Custodio, which showed a reduced wing

tip vortex strength at angles of attack between 6° and 18° [39]. Pedro and Kobayashi also observed the same phenomenon in their CFD study of a humpback whale flipper and likened them to wing fences. The existence of the SCRV disrupted the propagation of tip stall towards the root of the flipper allowing for more of the flipper to maintain attached flow [35]. This theory is further supported by separate investigation conducted by Miklosovic *et al.* and Johari *et al.* who determined that the reduction in drag was only observable for finite wings as opposed to infinite wings where spanwise flow is no longer a factor [49, 50].

2.3 Effect of Tubercles on Performance

By the mechanism introduced in the previous section, the generation of the SCRV has been shown to modify significantly the stall characteristics, stall performance, and post-stall performance of lifting surfaces. The main performance parameters that were examined consisted of the lift coefficient, drag coefficient, and aerodynamic efficiency. Watts and Fish were the first to obtain quantifiable results through a 3D panel method simulation of a finite rectangular wing with an aspect ratio of 2.04, at an angle of attack of 10° [30]. Two simulations were conducted at Re = 12 000: the first simulation as a baseline with a straight leading edge (SLE) and a second simulation with the addition of tubercles to the leading edge. Details on the exact geometry of the tubercles are not disclosed. They reported a 4.8% increase in lift and a 10.9% decrease in drag, resulting in an overall 17.6% increase in aerodynamic efficiency. Due to the limitations of a 3D panel method, their simulation did not account for the development of the boundary layer, or boundary layer separation. In addition, only a single angle of attack before stall was investigated, contrary to one of their conclusions that even greater performance gains could be expected at higher angles of attack in the post-stall regime.

An experimental wind tunnel campaign undertaken by Miklosovic *et al.* presented a more complete set of data on the effect of tubercles over a wider range of angles. Their tests were conducted on a humpback whale flipper model using a NACA 0020 airfoil with a span of 0.5652 m, through an angle of attack range of −2° to 20° [42]. The Reynolds number was on the order of 500 000. The exact tubercle geometry is not described in detail beyond that they were modelled based on the left pectoral flipper of a 9.02 m humpback whale. Their testing showed that for angles of attack below 8.5°, tubercles did not alter the lift coefficient or drag coefficient. As stall was approached (between 9.3° and 12°) a decrease in lift coefficient of up to 9% was observed. Accompanying this decrease in lift, the drag coefficient was reported to increase by up to 34% in a similar range of angles just before stall (between 10.3° to 11.8°). For angles of attack larger than 12° the flipper with tubercles was shown to greatly outperform the baseline flipper by delaying stall from 12° to 16.3°, and increasing the maximum lift coefficient by 6%. The drag coefficient was also decreased compared to the baseline by up to 32% in post-stall angles of attack. This study confirmed the hypothesis suggested by Watts and Fish that the largest gains in performance can be expected to occur at post-stall angles of attack. These results were used to validate CFD simulations conducted by Weber *et al.* who used two different commercially available RANS solvers (STAR-CCM+ and SFS) to simulate the same flipper geometry at similar Reynolds numbers [51]. While good agreement with the experimental results was obtained for angles of attack before

stall, the complex flow structure of the tubercles at post-stall angles of attack that include detached vortices was difficult to model accurately using a RANS solver. It was acknowledged that better results for post-stall angles of attack were obtained by Pedro and Kobayashi through the use of detached eddy simulations at the cost of being more computationally expensive [35]. None of these studies shed any light on the effect of varying the tubercle geometry on the performance of lifting surfaces, as only one geometry was tested. In addition, the geometry tested was the unique planform of a whale flipper, which is a complex organic shape that incorporates varying local chord length and sweep that introduces other factors that could obscure the effect of tubercles.

Several studies investigated the effect of changing the tubercle geometry, namely the tubercle amplitude and wavelength. Johari *et al.* conducted water tunnel testing on two-dimensional (2D) airfoils with varying tubercle amplitudes and wavelengths [49]. Their main objective was to characterize the effect of varying the tubercle geometry on the performance of a NACA 63_4-021 airfoil. Six different tubercle geometries were tested with amplitudes of 2.5%, 5% or 12% of the chord, at two different wavelengths of 25% or 50%. Angles of attack between $-6°$ and $30°$ were tested at $\mathrm{Re} = 1.83 \times 10^5$. Their results showed agreement with the general trends observed by Miklosovic *et al.* although a much more significant decrease in lift and increase in drag just before stall was reported. The drag was also reported to remain largely unchanged compared to the SLE at post-stall angles of attack. This discrepancy was explained by the absence of 3D effects in the results of Johari *et al.* which was later shown to be crucial to the reduction of induced drag via flow compartmentalization as discussed in Section 2.2. The tubercle amplitude was found to have a much greater effect on the performance of the airfoils compared to the wavelength. In general, Johari *et al.* observed that increasing the tubercle amplitude led to a more gradual stall behaviour. For the largest amplitude tested, a near-constant lift coefficient between angles of attack of $10°$ to $26°$ was observed, whereas the baseline airfoil exhibited a more typical abrupt stall, characterized by a 50% loss of lift at an angle of attack of $21°$. The smaller amplitude tubercle exhibited stall behaviour closer to the baseline airfoil, but only experienced a 16% decrease in lift at an angle of attack of $16.5°$. All airfoils with tubercles showed a decrease in maximum lift coefficient and a decrease in stall angle, proportional to the tubercle amplitude, suggesting that gradual stall behaviour comes at the cost of reduced maximum lift coefficient.

Custodio, as well as Hansen *et al.*, also investigated the effects of varying the tubercle amplitude and wavelength on performance [39, 40]. The study by Custodio was an extension of the water tunnel investigation conducted by Johari *et al.*, thus it examined the same six tubercle geometries introduced above. Custodio's major contribution was the elucidation of the effect of the tubercle amplitude and wavelength on the vortices generated by the tubercles. Through PIV imaging, he concluded that larger amplitudes generated larger pressure gradients between the tubercle peaks and valleys resulting in stronger SCRV. The wavelength dictated the spanwise proximity of each vortex to their neighbours, which determined the extent of their interaction with one another [39]. The study by Hansen *et al.* consisted of wind tunnel testing of a 2D NACA 0021 airfoil with varying tubercle geometries that include amplitudes ranging from 3% to 11% of the chord, and wavelengths ranging from 11% to 86% [40]. Tests were conducted at $\mathrm{Re} = 120\,000$. Larger amplitudes resulted in a more gradual onset of stall with the

lowest maximum lift coefficients, while smaller amplitudes showed a more favourable maximum lift coefficient and higher stall angle while still outperforming the baseline at post-stall angles of attack. These trends were also reported by Custodio, who reported the lowest amplitude tubercles to be the best performers when considering stall angle, maximum lift coefficient, and post-stall performance [39]. Among the conclusions of Hansen *et al.* was the importance of the ratio of the tubercle amplitude and wavelength. They observed that reducing the wavelength increased the maximum lift coefficient and stall angle until an inflection point before a reduction in both parameters were reported. This suggested the existence of an optimum wavelength for a given amplitude for maximum performance benefits.

The majority of the current literature regarding tubercles suggests that tubercles have the potential to improve the performance of aerodynamic systems that experience high angles of attack. Current applications that have been explored include ship rudders [52], horizontal and vertical axis wind turbines [53, 54], helicopter rotor blades [25], propellers [26], gas turbine blades [27], and UAVs [23]. An application that is yet to be explored is the use of tubercles in propeller blown systems. The behaviour of tubercles when placed in a propeller slipstream, such as those found on tilt-wing aircraft, have not been investigated at the time of writing. Tilt wing aircraft must operate at high angles of attack during transition, an environment well-suited for tubercles. Filling this knowledge gap by quantifying the effect of tubercles on the performance of tilt-wing aircraft is an objective of this thesis.

2.4 Blown Wing Systems

When a lifting surface is placed downstream of a propeller, the propeller slipstream greatly affects the aerodynamic performance of the lifting surface. In certain configurations, the presence of the propeller slipstream has been shown to increase the stall angle, and increase the maximum lift coefficient to values close to four times the value achieved without a propeller [55]. The source of this significant augmentation of lifting capabilities is a well studied field. Jameson identified three principal effects of the propeller slipstream on the wing: an increase in the dynamic pressure, the alteration of the local angle of attack, and the interference of the propeller slipstream with the flow over the wing [56]. The increased dynamic pressure is simply due to the increase in velocity in the propeller slipstream. The change in local angle of attack is caused by a tangential velocity component produced by the propeller. Finally the interference of the slipstream alters the flow over the wing surface, leading to significant changes in wing aerodynamic performance. These three effects are generally agreed upon in the current body of knowledge [57–62]. Due to the intuitive nature of the first effect, only studies regarding the last two of these effects will be summarized in this section.

2.4.1 Change in Local Angle of Attack

As the propeller rotates, the rotating motion of the propeller itself imparts a tangential velocity component to the flow. This tangential velocity acts to either increase or decrease the local angle of attack of the wing segments immediately behind the propeller depending on the direction of rotation. Witkowski *et al.* labelled this phenomenon an effective twist [58]. For clarity of explanation, consider a simple configuration of

a wing with one propeller where the inboard propeller tip is rotating in the upward direction (clockwise when viewed from upstream, as seen in Figure 2.2). The wing can be divided into four regions as labelled in Figure 2.2. They proposed that in Region II, the tangential component of the propeller swirl causes an upwash that acts to increase the apparent angle of attack of the wing and in Region III the propeller swirl causes a downwash that decreases the apparent angle of attack.

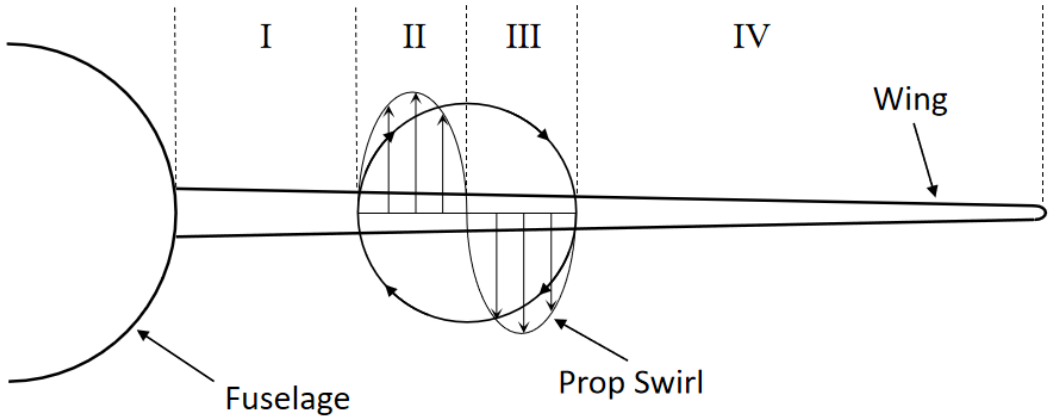

Figure 2.2: Four different regions behind a simple propeller-wing configuration viewed from upstream (adapted from [58]).

Witkowski *et al.* concluded that the primary effect of this upwash and downwash is the augmentation of the section lift coefficient for Region II and a diminishment in section lift coefficient for Region III that is caused directly by the change in local angle of attack [63]. They also identified a secondary effect of the upwash and downwash. The change in apparent freestream direction due to the upwash and downwash results in the forwards rotation of the lift vector in Region II (decomposing into a lift component and thrust component) and a backwards rotation of the lift vector in Region III (decomposing into a lift component and drag component). This effect was also observed by van den Borne and van Hengst in their in-flight wing pressure measurements of a *Fokker 50* aircraft [64]. The wings of the test aircraft were instrumented with 10 rows of static pressure orifices to measure the chordwise pressure distribution at various spanwise locations. Eight of the pressure belts were placed in the propeller slipstream: two on either side of each propeller. The pressure readings were used to calculate the section lift coefficients at each of the spanwise locations, which showed an increased section lift coefficient where the propeller tip was travelling upwards (as in Region II of Figure 2.2), and a decreased section lift coefficient where the propeller tip was travelling downwards (as in Region III of Figure 2.2). Duivenvoorden *et al.* reported the same effect through pressure readings of a propeller, wing and flap configuration tested in a wind tunnel [61].

2.4.2 Slipstream-Wing Interaction

The interaction of the slipstream with the flow over the wing is greatly affected by the position of the propeller. There are two general configurations: the tractor configuration, where the propeller is placed upstream from the leading edge, and the pusher configuration, where the propeller is placed downstream of the trailing edge. The loca-

tion of the propeller can be further specified relative to the position of the wing in the vertical, spanwise, and streamwise directions. With the application to tilt-wing aircraft in mind, this section will focus on the tractor configuration. Veldhuis conducted a study on the effect of varying the vertical, spanwise and streamwise position of a propeller for a tractor configuration [59]. The test model consisted of a half-span rectangular wing with a NACA 64_2-015 airfoil, aspect ratio of 5.33, half-span of 0.64 m, and a chord length of 0.24 m. A 0.236 m diameter propeller was mounted on a 3-axis traverse, separate from the wing that could be moved to various propeller positions. Three angles of attack were tested: 4°, 8°, and 12°. The results showed that the vertical propeller position had the most significant influence on wing performance. In general, propeller positions above the chord line resulted in higher lift coefficients. This effect was attributed to the contraction of the slipstream augmenting the local angle of attack, as well as presenting the wing with higher dynamic pressures associated with the higher velocity flow closer to the propeller tip. Ananda *et al.* reported the same trend concerning the vertical position of the propeller [65]. While this study by Veldhuis provided an overview on the general effect of propeller positioning, only three angles of attack were investigated, none of which included post-stall angles of attack. Conversely, a collection of earlier studies undertaken by Fink *et al.* investigated the aerodynamic performance of a blown wing over a much larger range of angle of attack, but only included 3 different vertical propeller positions [66–68]. In addition, Fink *et al.* focused on the performance of various flow control devices, such as leading edge slats, wing fences, and flaps in the presence of the propeller slipstream, thus they did not come to any significant conclusions regarding the effects of propeller position.

A recent study by Hawkswell *et al.* presented an investigation of the effects of vertical positioning of a propeller in tractor configuration that included a wider range of angles through 2D CFD simulations [62]. They used an *ANSYS Fluent* RANS solver along with a Spalart-Allmaras turbulence model for viscous calculations. Three vertical positions were simulated: one with the propeller 5% of the wing chord above the wing chord line, another in line with the wing chord, and a final position with the propeller 5% of the wing chord below the wing chord line. When examining their results for angles of attack before stall, they are in agreement with the conclusions of Veldhuis and Ananda *et al.* However, the larger lift associated with higher propeller positions was shown to come at the cost of a decreased stall angle. Hawkswell *et al.* explained this behaviour by noting that the higher propeller position resulted in the wing exiting the propeller slipstream at a lower angle of attack, at which point the wing stalled. This is in agreement with the earlier conclusions of Hassell and Kirby [69]. Hawkswell *et al.* included a wider range of angles of attack but had a limited variety of propeller positions. In addition, they did not investigate post-stall angles of attack, likely due to limitations in the CFD modelling and computational costs associated with higher fidelity models, which are of interest when discussing tilt-wing aircraft.

The effect of streamwise propeller position, while not as influential as the vertical propeller position, is not insignificant. A different study by Veldhuis simulated the effect of streamwise propeller position using a vortex lattice method (VLM) to model a fixed wing, twin engine turboprop aircraft similar to the *Fokker 50* [70]. 8 different streamwise positions were simulated ranging from 0.5 to 4 times the propeller radius measured upstream from the leading edge. A streamwise propeller position of 2 times the propeller

radius was taken as a baseline. It was found that moving the propeller farther upstream resulted in greater lift and less drag. However, the change in lift and drag coefficients for the different streamwise positions only varied from -4% to 1%, and -2% to 1% respectively when compared to the baseline position. The change in wing performance with streamwise position is attributed to the development of the slipstream with distance in the streamwise direction. The positions farther upstream allowed for the propeller slipstream to develop higher velocities before interacting with the wing, increasing the dynamic pressure. Veldhuis highlighted the impracticality of mounting propellers significant distances away from the leading edge, since they would require longer nacelles that are likely to cancel any performance gain. Results obtained by Chinwicharnam *et al.* appeared to contradict those of Veldhuis by stating that a streamwise propeller position closer to the leading edge was more beneficial [60]. Although Veldhuis does not state the angles of attack used for the VLM simulations, it can be inferred that a lower angle of attack, more representative of a cruise condition, was investigated. The conclusion drawn by Chinwicharnam *et al.* is concerned with stall behaviour, which is very dependant on keeping the wing immersed in the propeller slipstream [62, 69], in which case, reducing the chordwise distance between the leading edge and the propeller is desirable.

2.4.3 Impact of Blown Wings on Transition

Wing stall has been identified as a major problem for tilt-wing vehicles during transition [7, 22, 69]. The interaction between the propeller slipstream and the wing serves to alleviate this problem to a certain degree by delaying stall and augmenting lift, as discussed in Section 2.4. The wing is more likely to stall during landing, or inbound transition (transition from forward to vertical flight), which requires a low throttle setting to decelerate the aircraft, than during takeoff, or outbound transition (transition from vertical to forward flight), where a higher throttle setting is used. The lower throttle setting results in decreased velocities in the propeller slipstream and a reduction in lift augmentation and stall delay effects [22, 69, 71]. This leads to a higher likelihood of stall, which is accompanied by buffeting and general loss of stability and control [22, 69, 71]. Schade *et al.* reproduced this phenomenon through the flight testing of a $1/4$ scale, remote control, tilt-wing aircraft inside a large wind tunnel [71]. Figure 2.3 shows a three-view drawing of the remote control vehicle used in testing. To avoid stall during transition and the accompanying undesirable consequences, Hawkswell *et al.* and Chinwicharnam *et al.* proposed that positioning the propeller such that the wing remains within the propeller slipstream for as many angles of attack as possible can help to avoid wing stall [60, 62].

In addition to confirming the dangers of wing stall to tilt-wing transition, Schade *et al.* demonstrated the effectiveness of two high-lift devices to delay wing stalling by increasing the lifting capability of the wing: a full-span slotted flap at the trailing edge, and a Krueger type flap at the leading edge [71]. In the presence of a propeller slipstream, the effectiveness of the high lift devices were augmented. While tubercles cannot be classified as high lift devices, they have the potential to provide the same effect of increasing the lifting capability of a wing, with the added benefits of providing a more gradual stall characteristic (as opposed to the abrupt stalling of straight leading edge wings), as well as being less mechanically complex. Their lift enhancing effects

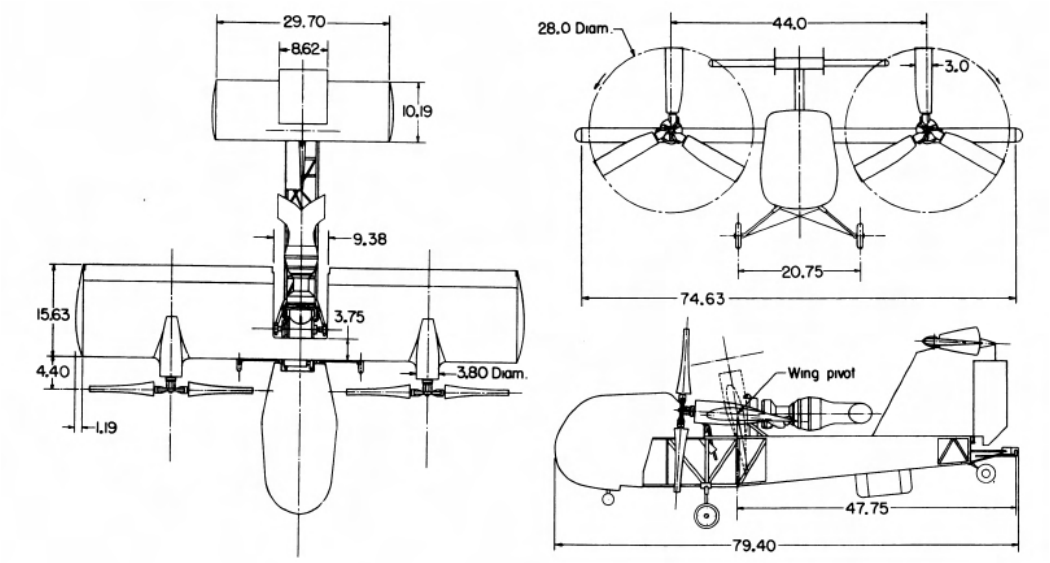

Figure 2.3: Three-view drawing of the 1/4 scale flight test vehicle tested by Schade *et al.* [71]. All dimensions are in inches.

while in a propeller slipstream may also be further improved in a similar fashion to high lift devices.

2.5 Knowledge Gaps

Current research on tubercles has shifted from understanding the mechanisms responsible for performance benefits seen when applied to lifting surfaces, to exploring various applications of tubercles. As mentioned in Section 2.3, one application that has not yet been explored is the application of tubercles to tilt-wing aircraft. An inherent aerodynamic feature of tilt-wing aircraft is the effect of the propeller slipstream on the wing, often referred to as a blown wing system. Blown wing systems well-researched, and efforts are being directed towards wind tunnel testing of novel blown wing configurations and new modelling methods to allow for the accurate estimation of the performance of a blown wing at the conceptual design level. Although the existing body of knowledge includes studies that characterize the effect of propeller position on wing performance, it lacks a comprehensive investigation encompassing a more extensive set of propeller positions at a wider range of angles of attack including the post-stall region. Furthermore, there is a gap in knowledge regarding the behaviour of tubercles in the presence of a propeller slipstream. The interaction between the propeller slipstream and the SCRV generated by tubercles is yet to be investigated. Ultimately, this thesis aims to fill these identified knowledge gaps and to demonstrate the applicability of tubercles to tilt-wing vehicles.

3 Effect of Propeller Position on Wing Aerodynamics

This chapter presents the methodology, results and discussion of the experimental wind tunnel campaign conducted to characterize the effect of propeller position on the aerodynamics of a lifting surface at high angles of attack. To quantitatively assess the effect of tubercles on a blown lifting surface, baseline measurement is required. This experimental campaign is only concerned with an unmodified, straight leading edge geometry in order to serve as this baseline. The effect of tubercles will be explored in the following chapter (Chapter 4). This investigation consisted of force/torque transducer measurements to obtain the lift coefficient, C_L, drag coefficient, C_D, and aerodynamic efficiency, E, for various propeller positions relative to the wing leading edge. The power-off case (no propeller) is used as a baseline to assess the influence of the propeller slipstream on the aerodynamic performance of a lifting surface at each relative propeller position. These results are complemented by surface pressure readings for select propeller positions of particular interest to provide further insight into the flow behaviour.

3.1 Methodology

This section presents the experimental objectives, a description of the experimental setup, wind tunnel, instrumentation and data acquisition system, experimental procedures, and data post processing methods. Throughout this thesis, the position of the propeller is described by two parameters: the chordwise and the propeller vertical position. The distance between the propeller and the leading edge of the wing, x_p, normalized by the propeller diameter, d_p, will be referred to as the propeller chordwise position, X_p. The distance of the propeller above or below the wing chord line, z_p, normalized by the propeller diameter, d_p, will be referred to as the propeller vertical position, Z_p, with positive values indicating positions above the wing chord line and negative values indicating positions below. This convention is defined in Equation 3.1 and shown in Figure 3.1.

$$\begin{aligned} X_\mathrm{p} &= \frac{\text{distance from propeller plane to leading edge of the wing}}{d_\mathrm{p}} = \frac{x_\mathrm{p}}{d_\mathrm{p}} \\ Z_\mathrm{p} &= \frac{\text{distance of propeller axis above wing chord line}}{d_\mathrm{p}} = \frac{z_\mathrm{p}}{d_\mathrm{p}} \end{aligned} \tag{3.1}$$

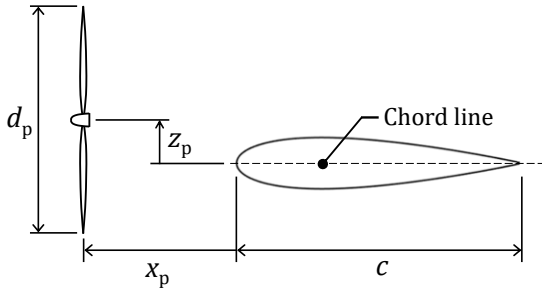

Figure 3.1: Propeller position convention.

3.1.1 Experimental Objectives

A characteristic feature of tilt-wing aircraft is the presence of a propeller slipstream over a large portion, or the entirety, of the wing. This propeller blown wing must operate at high angles of attack in the post-stall regime during the transition between vertical and forward flight modes. It has been previously demonstrated that the propeller slipstream augments wing performance, with the position of the propeller being a significant factor in dictating the extent of this augmentation [59, 65]. This experimental campaign aims to expand on the existing body of knowledge about the effect of propeller position on wing aerodynamics by accomplishing three objectives. The first objective is to investigate experimentally the aerodynamic performance of a blown lifting surface over a comprehensive set of propeller positions and wide range of angles of attack including post-stall. The second objective is to characterize the flow around the wing for different propeller positions through surface pressure readings. The third and final objective is to obtain a set of data for an unmodified, straight leading edge, propeller-blown wing that can be used as a baseline for comparison with an equivalent propeller-wing configuration with tubercles.

3.1.2 Experimental Setup

A new experimental setup was developed for this wind tunnel campaign. It borrowed elements from a propeller test setup used by Asghar *et al.*, and a quasi-two-dimensional wing test setup used by Peristy *et al* [26, 46]. The experimental setup consisted of two main components: a wing setup and a propeller setup. Figure 3.2 illustrates the complete experimental setup. Both wing and propeller setups were mounted to a central disc attached to the floor of the wind tunnel test section. This allowed for the same relative position of the propeller with respect to the wing to be maintained at every angle of attack, which would be the case for a propeller-wing configuration found on an aircraft. The central disc was rotated manually to set the angle of attack of the wing and propeller. The propeller assembly was separate from the wing to allow for easy adjustment of the propeller position. The wing setup could be translated in the chordwise direction to adjust X_p, while the propeller setup could be translated towards either wall of the test section to control Z_p. This design decision sacrificed the ability to capture interference effects between a nacelle and the wing, which was deemed an acceptable trade-off since relative changes in aerodynamic performance were of more interest than absolute values. Nevertheless, this limitation was taken into account when analyzing the results.

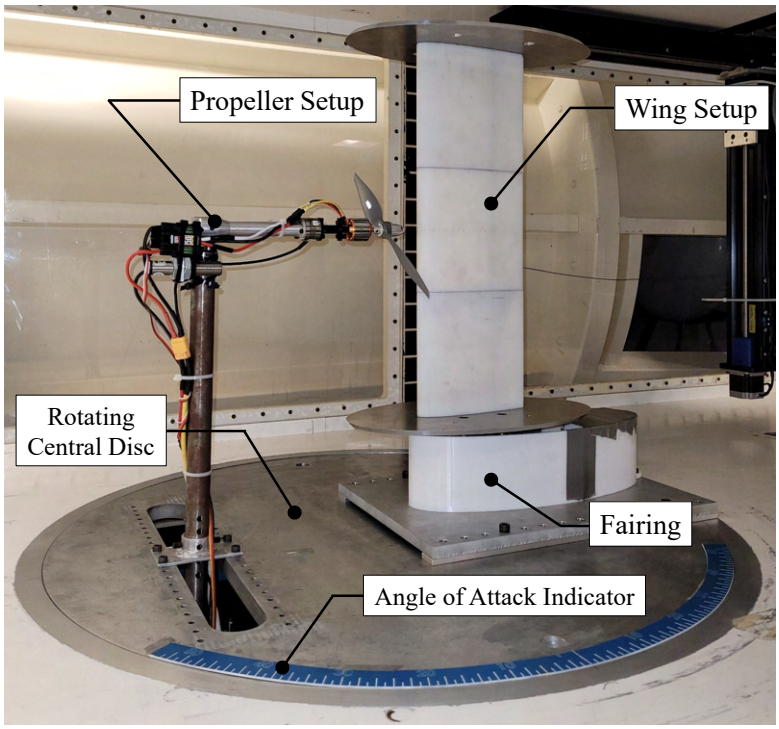

Figure 3.2: Complete experimental setup with wing rig and propeller rig.

Wing Setup

This experimental campaign investigated the performance of a NACA 0018 airfoil, selected for its wide use in unmanned aerial vehicles, with additional applicability to wind turbines [46,53,72]. As shown in Figure 3.3, an existing wing model, with a chord length of 0.1524 m (6 in) and a span of 0.4572 m (18 in) was used, as described by Peristy *et al.* [46]. The wing model was 3D printed from *VeroWhitePlus*™ plastic using a *Stratasys Objet30 Pro*™ high-definition rapid prototyping system, which has a minimum buildup layer of 28 μm. The surface of the wing was manually polished until a roughness height of Ra $= 0.8 \pm 0.2\mu$m was achieved. The surface roughness was measured using a *Mitutoyo Surftest SJ-400* portable surface roughness tester. The wing was manufactured in three segments with one set of pressure taps integrated at the centre of the wing. *Tygon*® tubes connected the centre segment via stainless steel tube inserts and were routed through the inside of the remaining wing segments to the pressure transducer. Figure 3.3 also shows the layout of the pressure taps, as well as the stainless steel tube inserts and routing of the *Tygon*® tubes.

The wing segments were assembled with two 0.4953 m by 1/4 inch threaded rods that fastened elliptical end plates to either side of the wing, as shown in Figure 3.4. Putty was used to fill any gaps between the segments. The wing with end plates was then mounted to a six-axis force/torque transducer with 0.0572 m spacers to lift the wing out of the boundary layer of the test section floor. The force/torque transducer and spacers were placed inside a plastic fairing to shield the spacers from the flow in order to prevent the force/torque transducer from reading the aerodynamic forces generated by the spacers. The pressure transducer was also placed inside this plastic fairing. The entire wing,

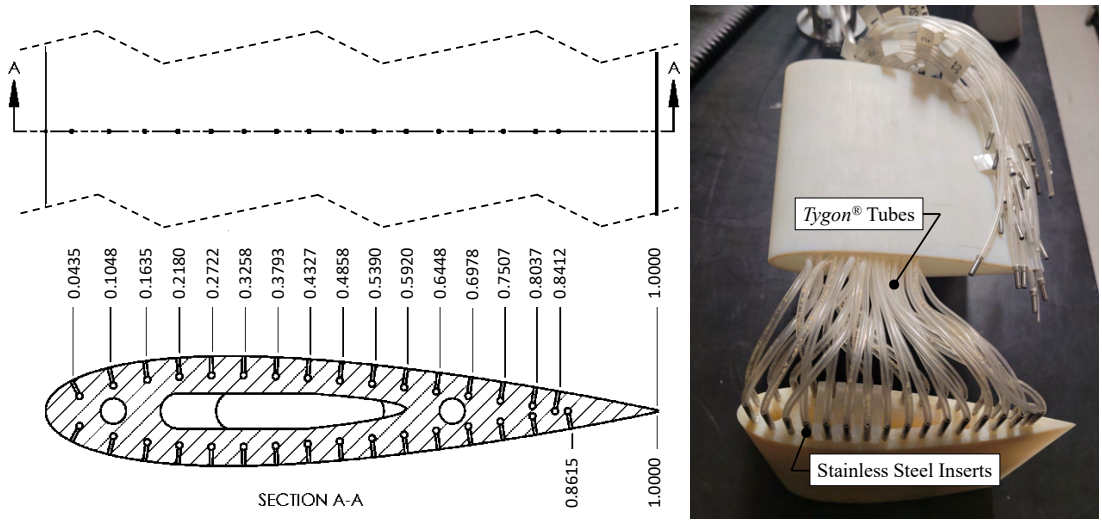

(a) Location of pressure taps. (b) Stainless steel inserts.

Figure 3.3: Surface pressure tap configuration.

end plate, and force/torque transducer assembly was mounted to an aluminum plate that was firmly fixed to the central disc on the test section floor (see Figure 3.2). The aluminum plate could be mounted to the central disc at different positions to allow for the propeller chordwise position to be modified. Figure 3.4 shows the complete wing setup with the fairing removed to expose the force/torque transducer.

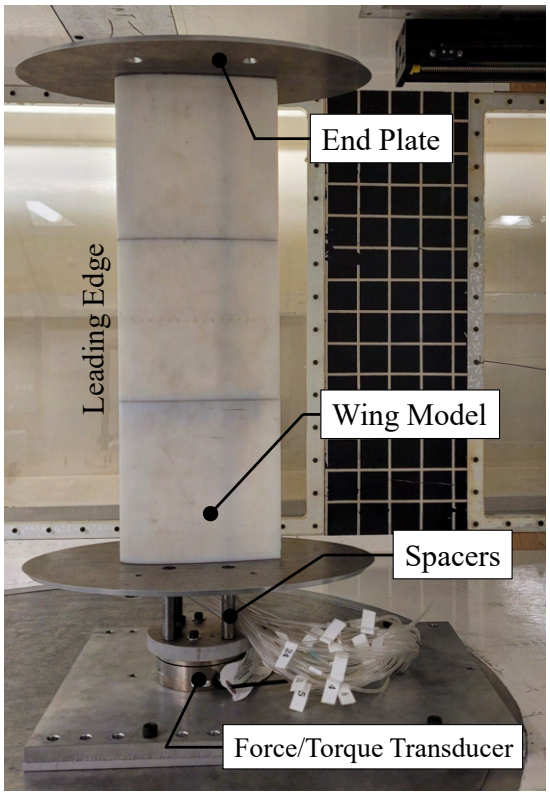

Figure 3.4: The wing assembly and aluminum plate.

Propeller Setup

The propeller setup, as shown in Figure 3.1, was an adaptation of that used by Asghar *et al* [26]. The rig consisted of a horizontal sting mounted on top of a vertical member with a swivel mechanism that allows for the angle of attack to be modified. For this investigation, the angle of attack of the propeller sting was maintained at zero degrees to keep the propeller blades parallel with the leading edge of the wing (rotational axis of the propeller perpendicular to the leading edge). The vertical member was secured directly to the central disc on the test section floor. The propeller vertical position was dictated by the mounting point of this vertical member to the central disc. A six-axis force/torque transducer was mounted at the end of the horizontal sting to measure the propeller forces. A *Cheetah A2217-7* electric motor was mounted to the force/torque transducer with a nylon coupler to thermally insulate the temperature sensitive force/-torque transducer. The electric motor powered an *APC Thin Electric* 10×5E propeller, which had a diameter of 0.254 m (10 in). Figure 3.5 shows the complete propeller setup.

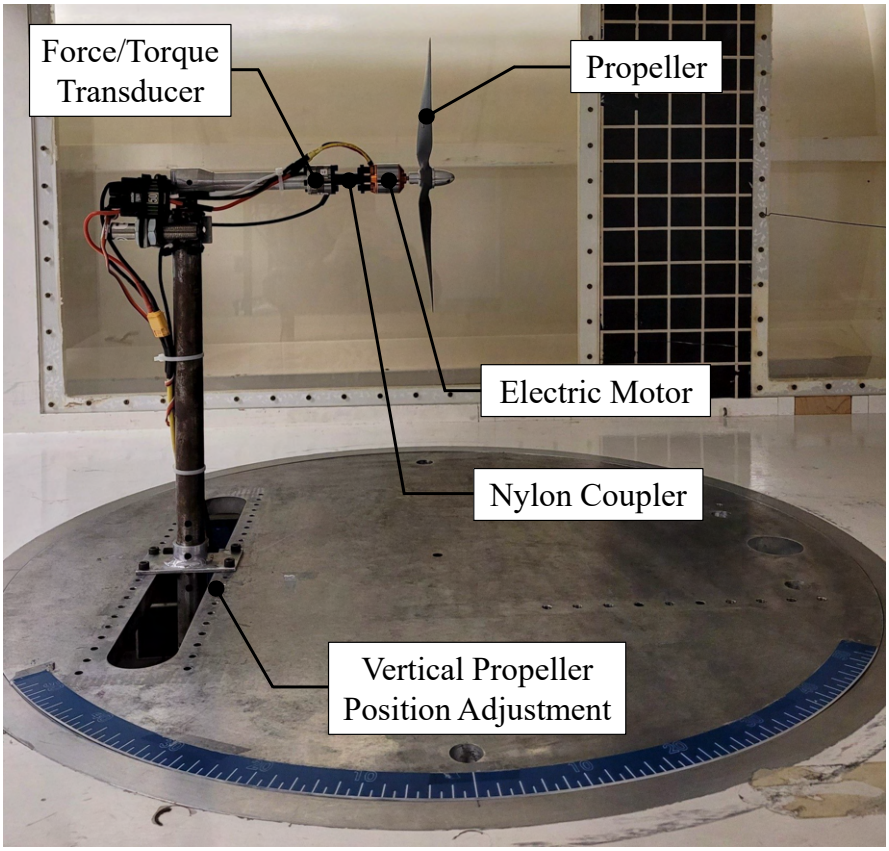

Figure 3.5: Propeller setup.

3.1.3 Wind Tunnel

The experiments were carried out in the Royal Military College of Canada (RMC) wind tunnel. It is a large, closed-circuit, sub-sonic wind tunnel, capable of producing freestream speeds up to 60 m/s. It is powered by a 75 kW three-phase electric motor.

The turbulence intensity of this wind tunnel has been measured to be 0.2% in previous experiments [73]. The test section measures 0.76 m in height and 1.08 m in width. Figure 3.6 shows a schematic diagram of the wind tunnel.

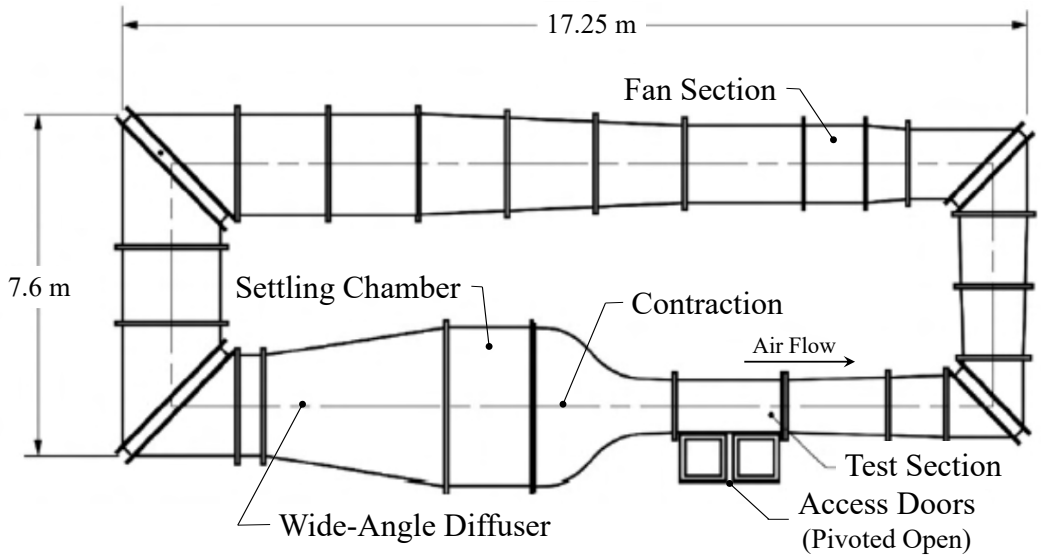

Figure 3.6: Schematic diagram of the RMC large wind tunnel (adapted from [73]).

3.1.4 Instrumentation and Data Acquisition

The schematic layout of the instrumentation used for this experimental campaign is shown in Figure 3.7. The six-axis force/torque transducer used to measure the wing forces was an *ATI Industrial Mini85*, while the propeller forces were measured using an *ATI Industrial Mini27 Titanium* force/torque transducer. The propeller RPM was controlled using a *Phoenix Edge 50* electronic speed controller (ESC), and measured with a *Monarch Instruments ROS-W Remote Optical LED Sensor* tachometer. The frequency input from the laser tachometer was converted to an output voltage by a *Monarch F2A3X Signal Converter*. The surface pressures on the wing were measured using a *Scanivalve MPS4264 Miniature Pressure Scanner*. The wind tunnel freestream velocity was measured 2.5 propeller diameters upstream from the propeller using a pitot-static tube with an *OMEGA PX164* pressure transducer. Sensor data from the *ATI Industrial Mini85* force/torque transducer were recorded at 125 kHz using an *ATI Industrial Wireless F/T* data acquisition (DAQ) system. The remaining sensors were connected to a *National Instruments USB-6210* DAQ system at a sampling rate of 100 kHz. The temperature and pressure of the air was recorded at the start of each test using an *OAKTON WD-03316-80* barometer and digital thermometer.

The measurement uncertainty for each value recorded from the sensors are summarized in Table 3.1. These values, obtained from their respective manufacturers, were used to determine the uncertainty in the calculated lift coefficient, drag coefficient and aerodynamic efficiency, using the Kline and McClintock uncertainty propagation method in order to ensure the validity of the results [74]. Further details on the uncertainty calculations can be found in Appendix A.

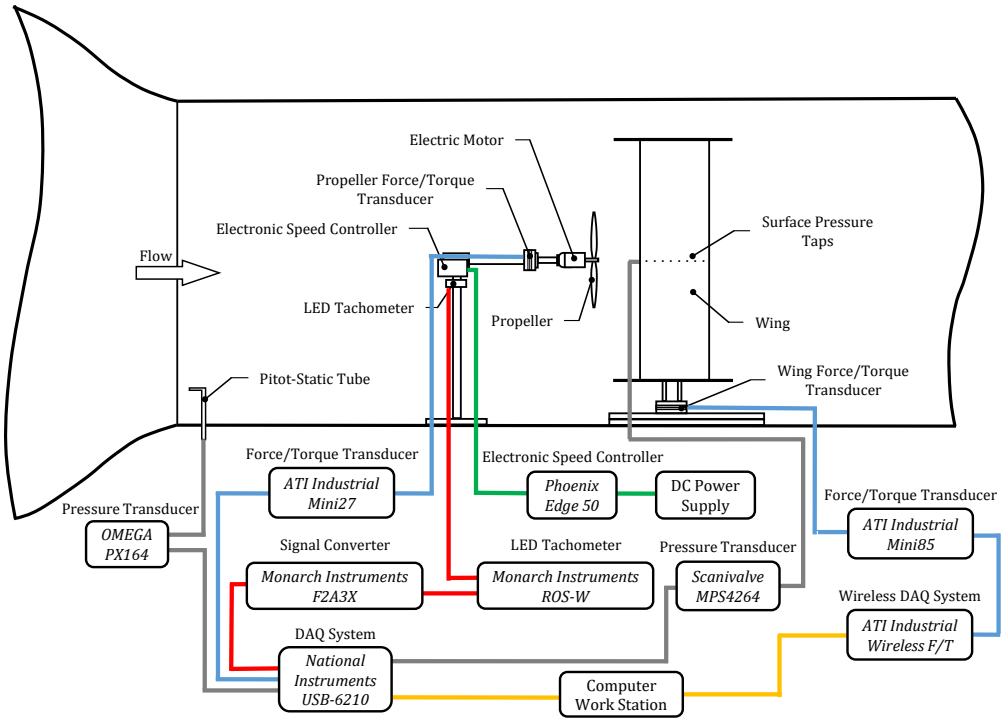

Figure 3.7: Schematic diagram of the instrumentation and data acquisition system.

Table 3.1: Measurement uncertainty for each sensor used in the experimental wind tunnel campaign.

Component	Parameter	Symbol	Uncertainty	Units
Propeller	Thrust	T_p	0.03	N
	Side forces		0.015	N
	Torque	Q_p	0.00025	Nm
	Rotational speed	Ω	12.5	RPM
Wing	Normal force	F_N	0.16	N
	Tangential force	F_T	0.16	N
	Moment	M	0.005	Nm
	Surface pressure	P	2.39	Pa
	Angle of attack	α	0.13	°
Air	Temperature	T	0.05	K
	Pressure	P	0.5	mbar

3.1.5 Data Post Processing

The distribution of data points collected was assumed to follow a normal distribution, allowing the average to be used as an acceptable representative value for the data set. This assumption was validated by creating a histogram of a sample data set. This was done for the *Scanivalve MPS4264 Miniature Pressure Scanner*, *ATI Industrial Mini85* force/torque transducer used for the wing, and the *ATI Industrial Mini27 Titanium*

force/torque transducer used for the propeller. Figure 3.8 shows that this is a valid assumption since all of the distributions were approximately normal.

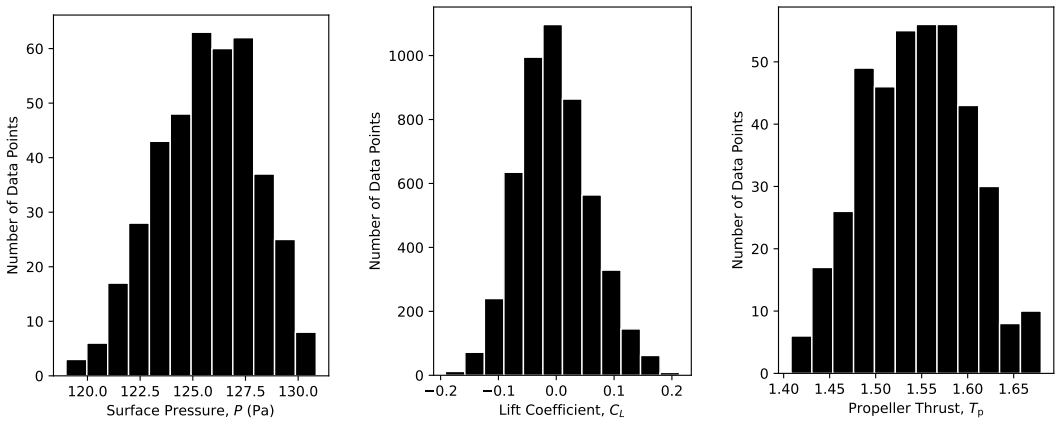

(a) *Scanivalve MPS4264.* (b) *ATI Mini85.* (c) *ATI Mini27 Ti.*

Figure 3.8: Histograms of three sample data sets.

The *ATI Industrial Mini85* force/torque transducer used to measure the wing forces was oriented such that the positive x direction was upstream along the wing chord line (towards the leading edge of the wing), the positive y direction was towards the pressure surface of the wing perpendicular to the wing chord line, and the positive z direction was upwards parallel with the span of the wing (from the floor to ceiling of the test section). This coordinate system rotated with the wing as the central disc was rotated to set the angle of attack. With this orientation in mind, the wing normal and tangential forces are defined as:

$$\begin{aligned} F_{\mathrm{N}} &= -F_{y,\mathrm{w}} \\ F_{\mathrm{T}} &= -F_{x,\mathrm{w}} \end{aligned} \tag{3.2}$$

where F_{N} is the normal force, F_{T} is the tangential force, and the subscripts x, w and y, w indicated the force components in the respective directions measured from the wing. Here, the tangential force refers to the force component parallel with the wing chord line. The normal and tangential forces were then transformed into lift and drag forces using the following equation [47]:

$$\begin{aligned} L &= F_{\mathrm{N}} \cos\alpha - F_{\mathrm{T}} \sin\alpha \\ D &= F_{\mathrm{N}} \sin\alpha + F_{\mathrm{T}} \cos\alpha \end{aligned} \tag{3.3}$$

where L and D are the lift and drag forces respectively, and α is the angle of attack. The lift and drag forces were normalized by the freestream dynamic pressure and wing planform area to obtain the lift coefficient, C_L, and the drag coefficient, C_D:

$$C_L = \frac{L}{\frac{1}{2}\rho U^2 S} \qquad C_D = \frac{D}{\frac{1}{2}\rho U^2 S} \tag{3.4}$$

where ρ is the density of the air, U is the freestream velocity, and S is the planform area of the wing. The force/torque transducer was located at $0.5c$, therefore the moment about the z-axis provided the moment about the half chord. This moment was translated to the quarter chord using the following relationship [47]:

$$-\frac{c}{4}F_{\mathrm{N}} + M_{c/4} = -\frac{c}{2}F_{\mathrm{N}} + M_{c/2} \tag{3.5}$$

where $M_{c/4}$ is the moment about the quarter chord, $M_{c/2}$ is the moment about the half chord (measured value), and c is the wing chord. The moment was normalized by the freestream dynamic pressure, wing planform area, and wing chord, to obtain the moment coefficient about the quarter chord:

$$C_{M_{c/4}} = \frac{M_{c/4}}{\frac{1}{2}\rho U^2 Sc} \tag{3.6}$$

The surface pressure data recorded by the *Scanivalve MPS4264* pressure transducer were used to calculate the pressure coefficient, C_P along the pressure and suction surfaces of the wing, using the following equation:

$$C_p = \frac{p - p_\infty}{\frac{1}{2}\rho U^2} = \frac{\Delta p}{\frac{1}{2}\rho U^2} \tag{3.7}$$

where p is the static pressure at the surface of the airfoil, and p_∞ is the atmospheric pressure. The *Scanivalve MPS4264* was calibrated to the atmospheric pressure before use, so it measured Δp directly.

The *ATI Industrial Mini27 Titanium* force/torque transducer was aligned such that the positive z direction aligned with the thrust vector, allowing the force in the z direction measured from the propeller, $F_{z,p}$, to be taken directly as the thrust force, T_{p}. The thrust force was then normalized by the propeller tip speed to calculate the thrust coefficient, C_T, using the following equation:

$$C_T = \frac{T_{\mathrm{p}}}{\rho \left(\frac{\Omega}{60}\right)^2 d_{\mathrm{p}}^4} \tag{3.8}$$

where Ω is the rotational speed of the propeller in RPM converted to rotations per second, and d_{p} is the propeller diameter. The moment about the z-axis provided the propeller torque, Q_{p}, which was normalized by the propeller tip speed, and propeller diameter, to obtain the torque coefficient, C_Q. The symbol ω in the numerator is the rotational speed in radians per second, while Ω in the denominator is the rotational speed in RPM converted to rotations per second.

$$C_Q = \frac{\omega Q_{\mathrm{p}}}{\rho \left(\frac{\Omega}{60}\right)^3 d_{\mathrm{p}}^5} \tag{3.9}$$

3.1.6 Experimental Procedure

Preliminary tests investigated the aerodynamic performance of the wing without a propeller, referred to, henceforth, as the *power-off* condition. Following the power-off tests, the experimental test campaign was conducted in three stages. Stage 1 investigated the effect of the propeller chordwise position. It also included a preliminary survey of a limited set of propeller vertical positions. Stage 2 investigated the effect of propeller vertical position. Finally, Stage 3 examined the flow behaviour at propeller positions of particular interest using surface pressure readings.

The propeller positions (X_p and Z_p) tested for Stage 1 are illustrated in Figure 3.9, and will be referred to as Grid 1. Normalized propeller chordwise positions between 0.15 and 1.05 were investigated at three different propeller vertical positions: $Z_p = -0.15$, 0, and 0.15. Based on previous work by Veldhuis and Ananda *et al.*, the propeller chordwise position is not as significant to the aerodynamic performance of a blown wing as the vertical position [65, 70]. For this reason, this phase of testing only investigated angles of attack between 0° and 20° at one freestream velocity of $U = 20$ m/s, corresponding to $\mathrm{Re} = 2.0 \times 10^5$, in order to reduce the number of hours required for testing.

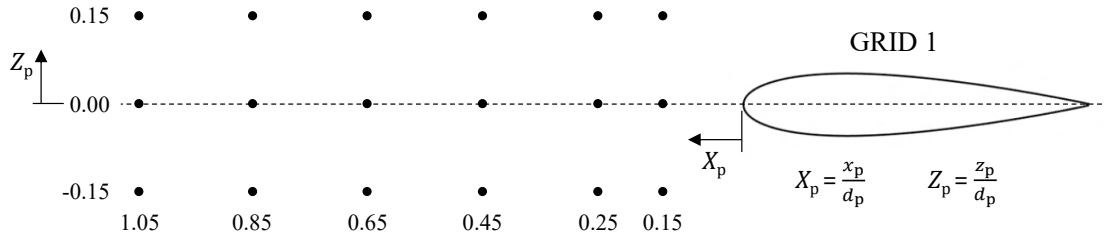

Figure 3.9: Grid 1 of propeller positions tested during Stage 1.

The matrix of propeller positions tested for Stage 2 is illustrated in Figure 3.10, and will be referred to as Grid 2. As the focus of this stage was to investigate the propeller vertical position, Grid 2 encompasses a wider range of propeller vertical positions ranging from -0.45 to 0.3, with a limited selection of propeller chordwise positions at $X_p = 0.25$, 0.45, and 0.65. Angles of attack from 0° to 45° were tested at freestream velocities of $10 \text{ m/s} \leq U \leq 25$ m/s in 5 m/s increments, corresponding to $\mathrm{Re} = 1.0 \times 10^5$, 1.5×10^5, 2.0×10^5, and 2.5×10^5 respectively.

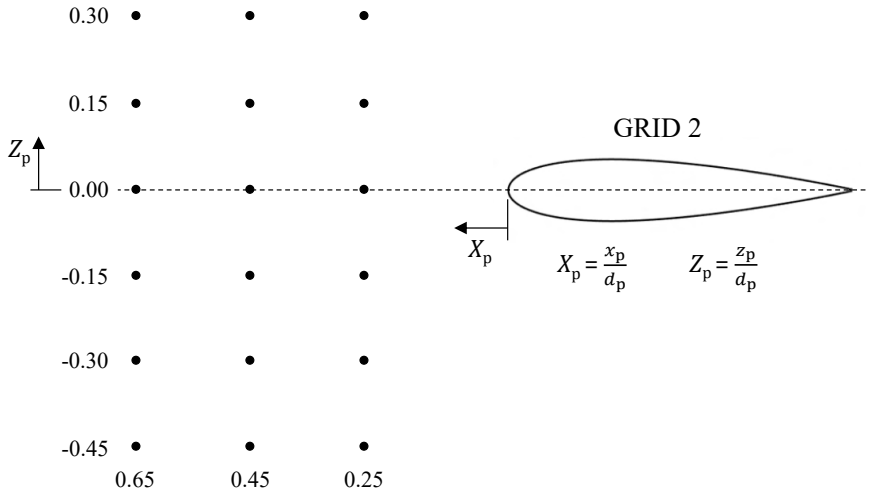

Figure 3.10: Grid 2 of propeller positions tested during Stage 2.

The surface pressure readings in Stage 3 were obtained for a much smaller set of propeller positions. Figure 3.11 shows the matrix of propeller positions for which surface pressure readings were obtained, referred to, henceforth, as Grid 3. This grid was selected to include one position each above, below, and in line with the chord, all at two different chordwise positions. A final position further below the wing chord was also

included. The range of angles of attack tested were the same as those investigated in Stage 1, with freestream velocities ranging from 10 m/s $\leq U \leq$ 20 m/s.

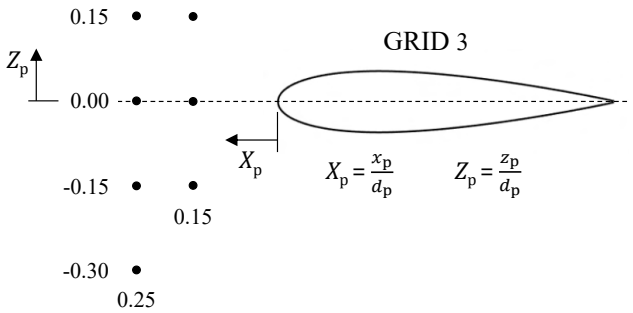

Figure 3.11: Grid 3 of propeller positions tested during Stage 3.

During Stages 1 and 2, the propeller rotational speed was maintained at 8000 RPM at all angles of attack and freestream speeds, which is representative of a high thrust setting that would be used during outbound transition (takeoff). For Stage 3, the propeller rotational speed was reduced to 6600 RPM, a lower throttle setting that would be more representative of an inbound transition (landing). Table 3.2 summarizes the test conditions that have been described for each stage of the experimental campaign.

Table 3.2: Summary of test conditions for each stage of the experimental campaign.

Stage	Positions	Angles of Attack (°)	Re ($\times 10^5$)	Propeller RPM
1	Grid 1	0, 8, 10, 13, 16, 20	2.0	8000
2	Grid 2	0, 8, 10, 12, 13, 14, 15, 17, 20, 25, 30, 35, 40, 45	1.0, 1.5, 2.0, 2.5	8000
3	Grid 3	0, 5, 8, 10, 13, 16, 20	1.0, 1.5, 2.0	6600

3.2 Results and Discussion

First among results, power-off data will be presented. Next, the effects of the propeller chordwise position obtained from Stage 1, followed by the effects of propeller vertical position from Stage 2 will be presented. The surface pressure readings from Stage 3 will be discussed throughout to supplement observations made during Stages 1 and 2. These results are focused on the lift coefficient of the wing, since the lift performance is of particular interest for tilt-wing aircraft during transition. Extended data showing moments, drag, and aerodynamic efficiency can be found in Appendix B.

3.2.1 Power-Off Analysis

The total lift generated by a propeller blown wing can be decomposed into two components: power-off lift and the lift augmentation provided by the slipstream. This is described by:

$$C_{L_{\text{tot}}} = C_{L_{\text{off}}} + \Delta C_{L_{\text{p}}} \quad \longrightarrow \quad \Delta C_{L_{\text{p}}} = C_{L_{\text{tot}}} - C_{L_{\text{off}}} \tag{3.10}$$

where $C_{L_{\text{tot}}}$ is the total lift generated by the wing in the propeller slipstream, $C_{L_{\text{off}}}$ is the lift generated by the wing in the power-off condition, and $\Delta C_{L_{\text{p}}}$ is the lift augmentation provided by the slipstream. It is important to distinguish the fact that the total lift, $C_{L_{\text{tot}}}$, does not include any forces generated by the propeller, such as side forces or the lift component of the thrust vector.

The effectiveness of each propeller position tested was evaluated based on the lift augmentation, $\Delta C_{L_{\text{p}}}$, that it provided. To determine the extent of the lift augmentation, a baseline measurement of the power-off lift was required. In addition, the power-off measurements functioned as a validation of the experimental setup. A set of data was recorded for Stage 1 and Stage 2, but only the results from Stage 2 will be presented since they cover a wider range of angles of attack and includ multiple Reynolds numbers. Figure 3.12 shows the lift coefficient for the power-off condition from Stage 2 of testing.

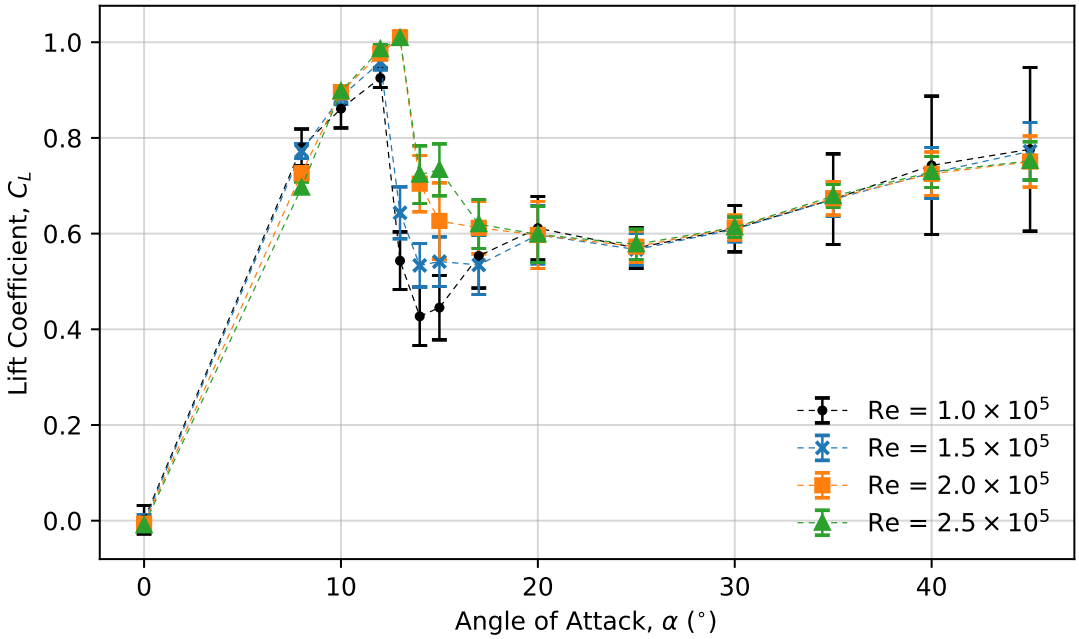

Figure 3.12: Lift coefficient of an unmodified, straight leading edge, NACA 0018 wing at the power-off condition.

At zero angle of attack a lift coefficient of $C_L = 0 \pm 0.01$ is observed regardless of Reynolds number. The lift curve slope, calculated with lift coefficient values at $\alpha = 0°$ and $\alpha = 8°$, is $C_{L,\alpha} = 5.58$ rad^{-1}, 5.55 rad^{-1}, 5.25 rad^{-1}, and 5.06 rad^{-1} for Reynolds numbers of 1.0×10^5, 1.5×10^5, 2.0×10^5, and 2.5×10^5 respectively. Since the Reynolds number increases, the maximum lift coefficient also increases from $C_{L_{\text{max}}} = 0.93$ to $C_{L_{\text{max}}} = 1.01$. For angles of attack greater than 20°, the lift coefficient appears to be independent of Reynolds number since the wing behaves more like a flat plate. All of these observations are expected results for a symmetric NACA 0018 profile, which provides confidence in the validity of the experimental setup and DAQ system. The

experimental uncertainty is shown to be significantly larger at lower Reynolds number, an effect caused by increased unsteadiness at low Reynolds numbers, especially at angles of attack greater than 30° where the vast majority of the flow is separated.

As an example for how these data were used to assess each propeller position, the power-off condition will be compared to a power-on configuration where the propeller is $0.25d_\mathrm{p}$ upstream of the leading edge, in line with the wing chord line ($X_\mathrm{p} = 0.25$, $Z_\mathrm{p} = 0$), at a Reynolds number of 2.0×10^5.

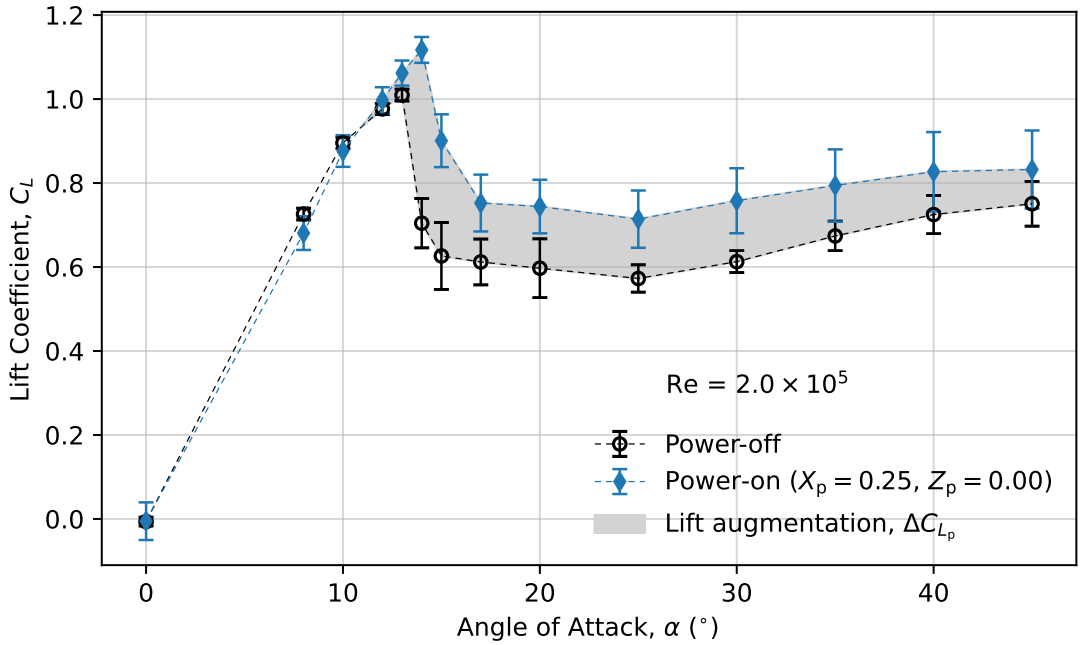

Figure 3.13: power-off and power-on lift coefficients showing the lift augmentation from the propeller slipstream.

Depending on the chordwise and vertical position of the propeller, the lift curve for the power-on case changes. This changes the measured lift augmentation at each angle of attack, modifying the shape and size of the grey region that represents the lift augmentation, ΔC_{L_p}, from the propeller slipstream. This allows for a quantitative comparison between the lift performance of each propeller position tested, through the angles of attack for each stage of testing summarized in Table 3.2.

3.2.2 Effect of Propeller Chordwise Position

Figure 3.13 clearly illustrates the lift augmentation for a single propeller position over the entire range of angles of attack tested. Another approach to presenting the results is in the form of a contour plot where the x-axis indicates the propeller chordwise position, the y-axis indicates the propeller vertical position, and the lift augmentation, ΔC_{L_p}, is represented with a colour bar. Presenting the results in the form of a contour plot allows for the simultaneous comparison of all propeller positions tested, but can only show one angle of attack at a time. In other words, the contour plot sacrifices showing trends with respect to angle of attack in favour of a clearer representation of trends with

respect to the position of the propeller. When concerned with elucidating the effects of the propeller position, this is an acceptable trade-off.

Figure 3.14 shows the lift augmentation for each propeller position in Grid 1 at $\alpha = 0°$. As introduced in the previous paragraph, the x-axis shows the propeller chordwise position, X_p, and the y-axis shows the propeller vertical position, Z_p. The brighter regions indicate propeller positions where the lift augmentation is the greatest, while the darker regions indicate propeller positions where the lift augmentation is the least. The power-off lift coefficient is provided in the figure caption to provide context to the extent of the lift augmentation.

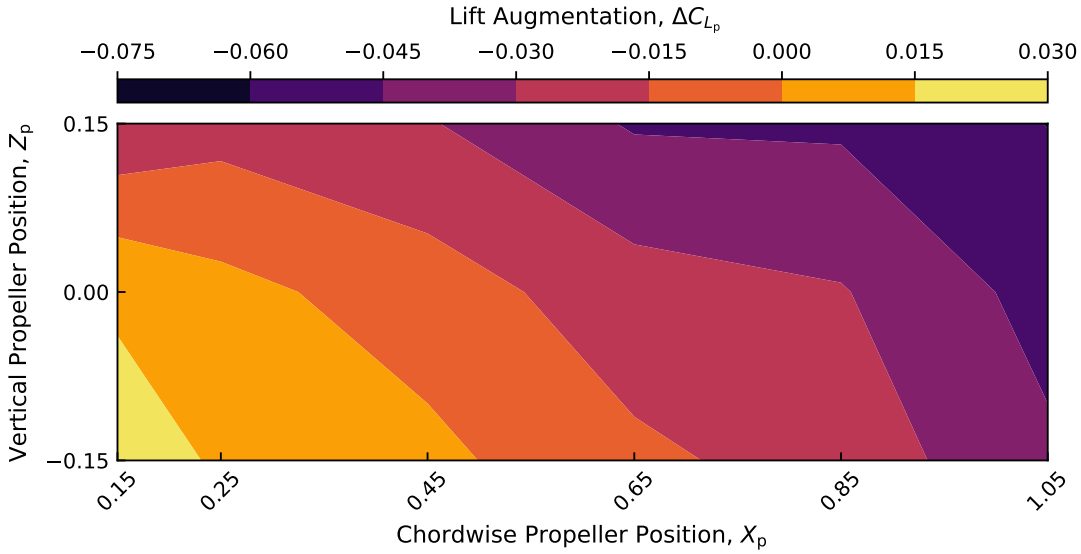

Figure 3.14: Lift augmentation at $\alpha = 0°$ for propeller positions in Grid 1 ($C_{L_{\mathrm{off}}} = 0.00$).

Despite the fact that a symmetrical NACA 0018 airfoil profile was used, non-zero lift coefficients were expected at $\alpha = 0°$ as a result of the propeller slipstream, especially for $z_\mathrm{p} = \pm 0.15$ where the propeller is not aligned with the wing chord. However, the lift coefficients were still expected to be close to zero. Since at $\alpha = 0°$ the power-off lift coefficient is zero, the values shown in Figure 3.14 can be interpreted as total lift coefficients as well ($C_{L_{\mathrm{tot}}} = \Delta C_{L_p}$). Although there appears to be a large gradient in lift coefficient with longitudinal propeller position, the scale of the colour bar should be noted. For example, at a propeller vertical position of $Z_\mathrm{p} = 0$, the lift coefficient only varies between $C_L = 0.01$ and $C_L = -0.06$ with increasing propeller chordwise position. As expected, all the lift coefficients are very close to zero, which makes any attempt to discern the exact effects of propeller chordwise position difficult.

When an angle of attack is introduced, the magnitude of the lift coefficient increase allows better insight into the effect of the propeller chordwise position. Figure 3.15 shows the lift augmentation for each propeller position in Grid 1 at $\alpha = 8°$. Here, the contour lines remain relatively horizontal, with the exception of the contour lines at $Z_\mathrm{p} = 0.15$ for higher X_p (top right quadrant). This can be interpreted as an insensitivity of lift augmentation to propeller chordwise position. For example at $Z_\mathrm{p} = -0.15$,

the lift augmentation increases from $\Delta C_{L_\mathrm{p}} = -0.01$ (-1.8%) to $\Delta C_{L_\mathrm{p}} = 0.02$ (+3.5%) as the propeller chordwise position increases to $X_\mathrm{p} = 1.05$, resulting in a total change in lift augmentation of only 0.03 (5.2%) with propeller chordwise position. The percentages given in parenthesis indicate a percent change from the power-off condition. This remains consistent for the $\alpha = 10°$ results shown in Figure 3.16.

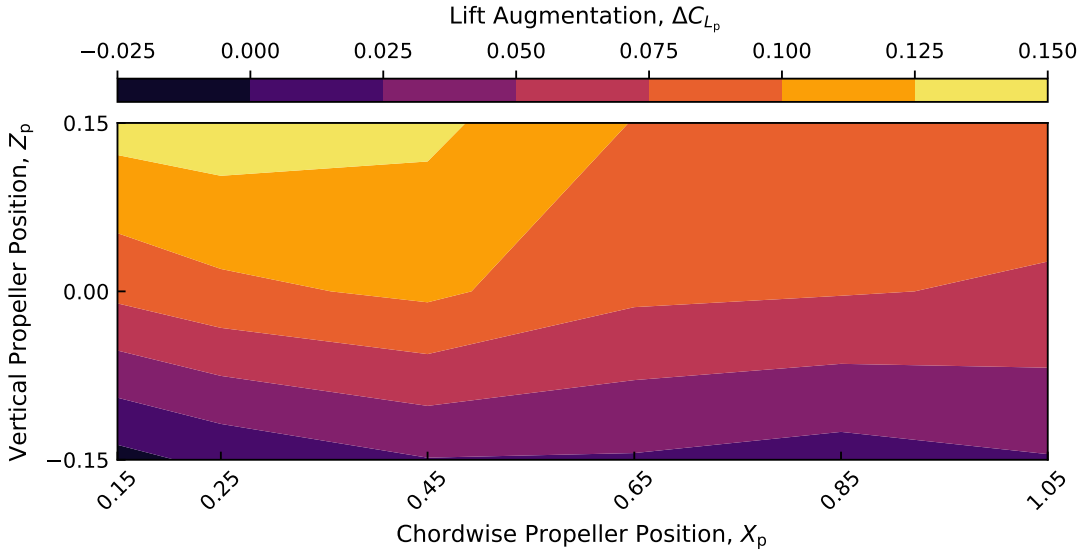

Figure 3.15: Lift augmentation at $\alpha = 8°$ for propeller positions in Grid 1 ($C_{L_\mathrm{off}} = 0.57$).

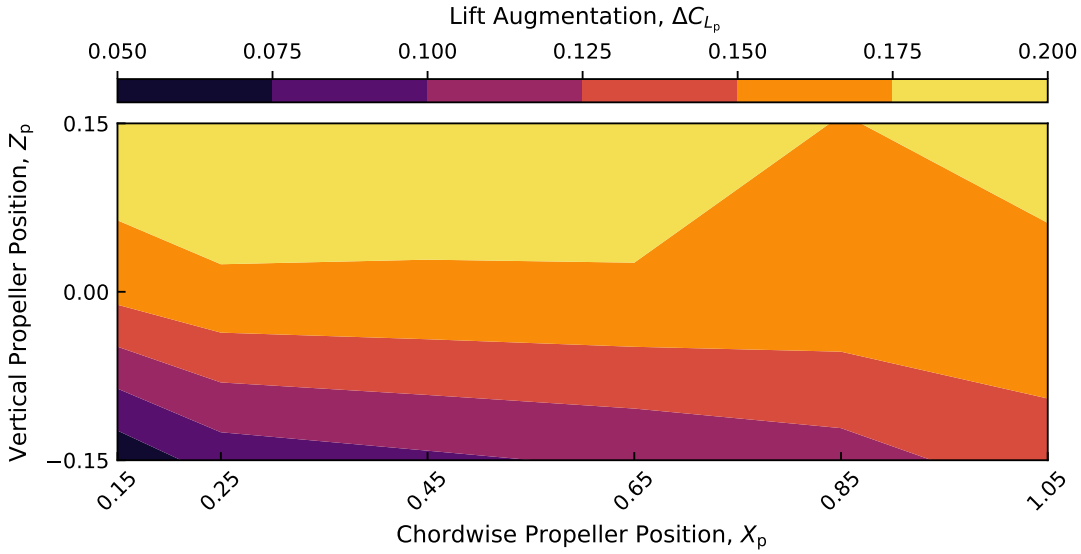

Figure 3.16: Lift augmentation at $\alpha = 10°$ for propeller positions in Grid 1 ($C_{L_\mathrm{off}} = 0.69$).

Figure 3.17 shows the lift augmentation for each propeller position in Grid 1 at $\alpha = 13°$. When the angle of attack is increased further, the horizontal contour lines begin to rotate in the clockwise direction resulting in a larger gradient in lift augmentation with propeller chordwise position. This is especially true for $Z_\mathrm{p} = -0.15$, where the lift

augmentation increases from $\Delta C_{L_p} = 0.16$ (+19.3%) to $\Delta C_{L_p} = 0.22$ (+26.5%) as X_p increases from $X_p = 0.15$ to 1.05. This is a maximum change in lift augmentation of 0.06 (7.2%), compared to 0.03 (5.2%) that was observed at $\alpha = 8°$ in Figure 3.15.

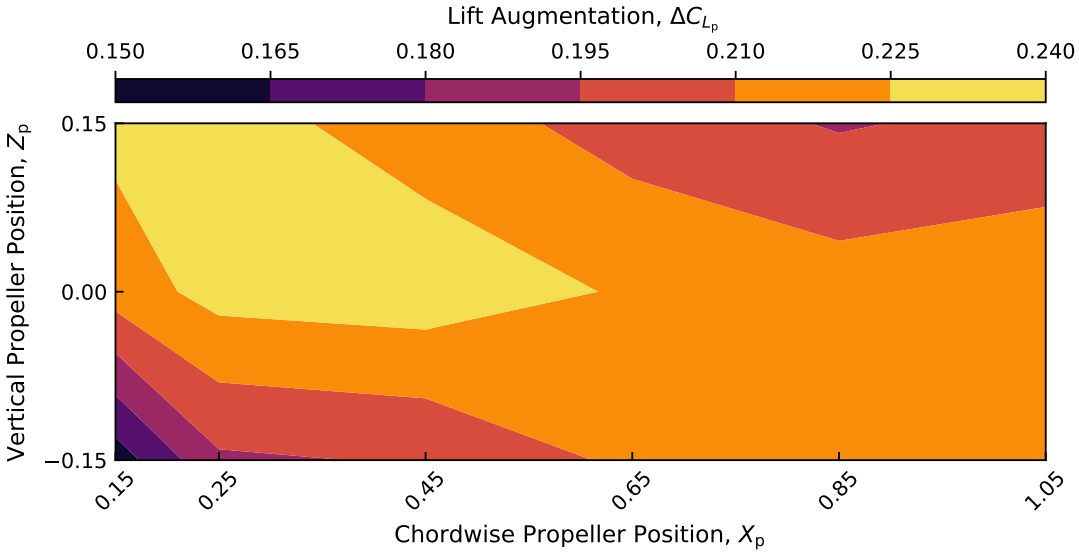

Figure 3.17: Lift augmentation at $\alpha = 13°$ for propeller positions in Grid 1 ($C_{L_{off}} = 0.83$).

The observed increase in lift augmentation with increasing propeller chordwise position for $Z_p = -0.15$ is in agreement with a previous study by Veldhuis [70], who simulated a *Fokker 50* (a turboprop aircraft with a low propeller position) using VLM. While no details are provided regarding the simulation flight conditions (angle of attack and freestream velocity), a chordwise position of $X_p = 1.00$ was reported to produce 4% more lift than $X_p = 0.25$, using the lift produced at $X_p = 1.00$ as the baseline. If an equivalent calculation is made using the results from Figures 3.15, 3.16, and 3.17, a chordwise position of $X_p = 1.05 \approx 1.00$ is shown to produce 3.3% more lift than $X_p = 0.25$ at $\alpha = 8°$, 6.0% more lift at $\alpha = 10°$, and 2.9% more lift at $\alpha = 13°$, all of which are on the same order of magnitude as the results presented by Veldhuis.

The increase in lift augmentation for increasing propeller chordwise position at negative propeller vertical positions (below the wing chord line) is explained by the development of the propeller slipstream, which has already been identified Veldhuis [70]. The velocity that the wing within the slipstream encounters is dependent on the extent to which the slipstream is developed. According to simple momentum theory, which simplifies a propeller as an actuator disc, the velocity in a fully developed slipstream, w, is two times the velocity induced at the disc, v_i [75]:

$$w = 2v_i = 2\sqrt{\frac{T_p}{2\rho S_p}} \tag{3.11}$$

where T_p is the propeller thrust, ρ is the air density, and S_p is the area of a disc with a diameter of d_p. Until the slipstream becomes fully developed achieving a velocity of $V_\infty + w$, the velocity within the slipstream approaches $V_\infty + w$ with increasing propeller chordwise position. The greater propeller chordwise positions gives the slipstream more

distance to develop before interacting with the wing, resulting in a general increase in velocities over the wing for larger propeller chordwise positions.

This hypothesis is supported by surface pressure readings obtained from Stage 3 of testing. Although the propeller was run at a slower RPM, the general trends remain the same and can still be applied here. Figure 3.18 shows the surface pressure coefficients for a propeller vertical position of $Z_\mathrm{p} = -0.15$ at two different longitudinal positions, $X_\mathrm{p} = 0.15$ and $X_\mathrm{p} = 0.25$, at $\alpha = 13°$. The most notable feature when examining Figure 3.18 are the pressure coefficients close to the leading edge on the pressure surface of the wing. The pressure coefficients were calculated using Equation 3.7.

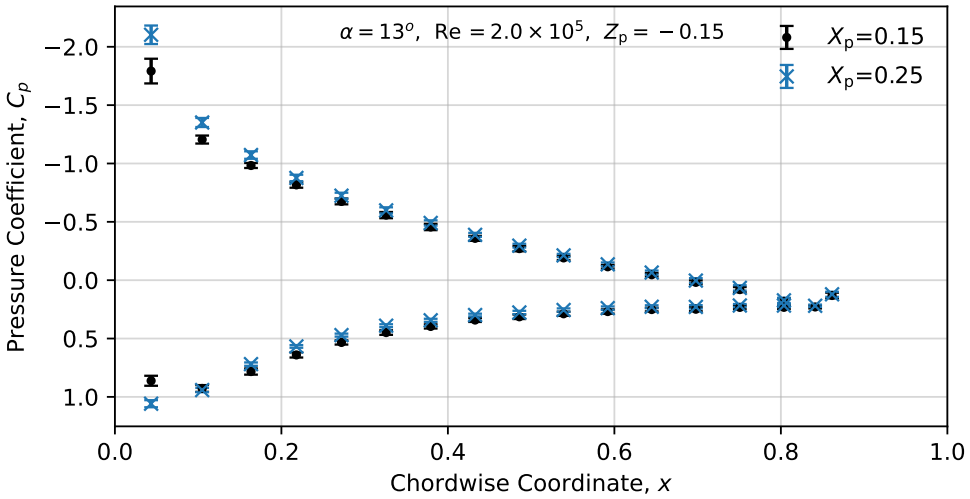

Figure 3.18: Surface pressure coefficients for two different propeller chordwise positions at $\alpha = 13°$.

For the power-off condition, a value of $C_p = 1$ is expected at the stagnation point since the static pressure would be equivalent to the total pressure in the freestream. For power-on conditions, the pressure coefficient at the stagnation point can increase beyond a value of one since the propeller slipstream velocity is greater than the freestream, effectively adding total pressure to the flow. This is what is occurring at the leading edge of the pressure surface in Figure 3.18. If the velocity within the slipstream were to increase, the pressure coefficient at the stagnation point would also increase as a result of an increased total pressure. Therefore the lower pressure coefficient at the leading edge of the pressure surface for $X_\mathrm{p} = 0.15$ suggests that the velocity in the slipstream is lower than that of $X_\mathrm{p} = 0.25$. The larger suction peak at the leading edge of the suction surface, as well as the slightly more negative pressure coefficients along the entire suction surface for $X_\mathrm{p} = 0.25$ when compared to $X_\mathrm{p} = 0.15$ are further indicators of higher velocities. A survey of the flow field at the surface of the wing for different longitudinal propeller positions using an anemometer would provide definitive data to validate these conclusions.

The development of the propeller slipstream does not explain the behaviour of lift augmentation at positive propeller vertical positions (above the wing chord line), where the lift augmentation is observed to generally decrease with increasing propeller chordwise

position. This behaviour is explained by the relative position of the propeller slipstream to the wing. Higher velocities associated with the faster moving propeller tips are experienced at the edges of the slipstream, while relatively slower air exists in the core of the slipstream. Changing the chordwise location of the wing within the slipstream will change the local velocities over the pressure and suction surface of the wing. At non-zero angles of attack, the propeller slipstream is shifted proportional to the angle of attack in the direction of the freestream. This shifting of the slipstream will be described, henceforth, as slipstream skew. This changes the location of the slipstream relative to the wing, and the amount that the slipstream is skewed before interacting with the wing is dependant on the propeller chordwise position. This effect is illustrated in Figure 3.19.

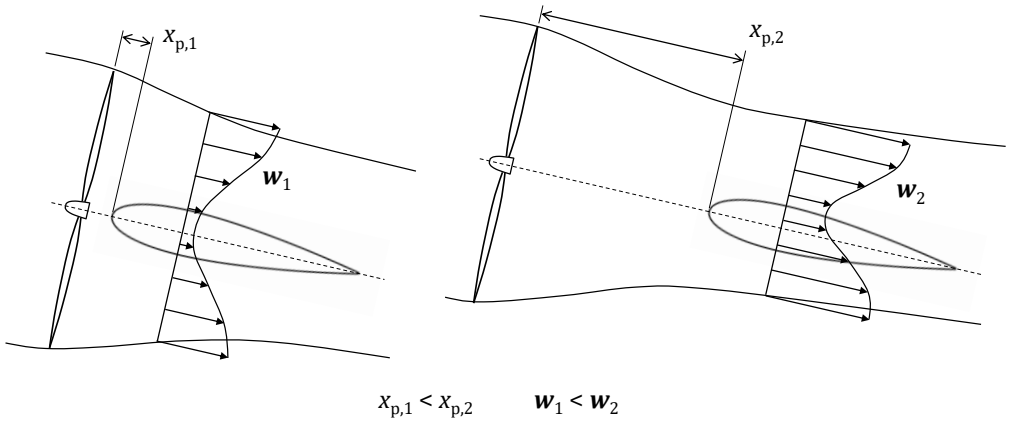

Figure 3.19: Approximate shape and velocities of the slipstream over the wing at different propeller chordwise positions at $\alpha > 0$.

At $\alpha = 8°$, the region of greater lift augmentation at lower propeller chordwise positions above the wing chord line as shown in Figure 3.15 (top left quadrant), is due to the suction surface being exposed to higher velocities within the propeller slipstream than the pressure surface. As the propeller chordwise position is increased the propeller slipstream is given an opportunity to skew, resulting in a change in the relative position of the propeller slipstream to the wing such that the suction surface no longer experiences a velocity increase as large as was experienced at smaller propeller chordwise positions. This applies to the contour plot at $\alpha = 10°$ and $\alpha = 13°$ shown in Figures 3.16 and 3.17 respectively.

At post-stall angles of attack, the effect illustrated by Figure 3.19 becomes amplified with the propeller slipstream skewing to a greater degree due to the larger angles of attack. In addition, flow separation that is characteristic in the post-stall regime can be delayed to varying degrees depending on the relative position of the propeller slipstream to the wing. This results in a larger range in lift augmentation for different propeller positions as shown by Figures 3.20 and 3.21, which presents the lift augmentation for each propeller position in Grid 1 at $\alpha = 16°$ and $\alpha = 20°$, respectively.

At $\alpha = 16°$, the lift augmentation varied between $\Delta C_{L_p} = -0.04$ (-6.3%) to $\Delta C_{L_p} = 0.31$ ($+48.4\%$) and at $\alpha = 20°$ the lift augmentation varied between $\Delta C_{L_p} = -0.16$

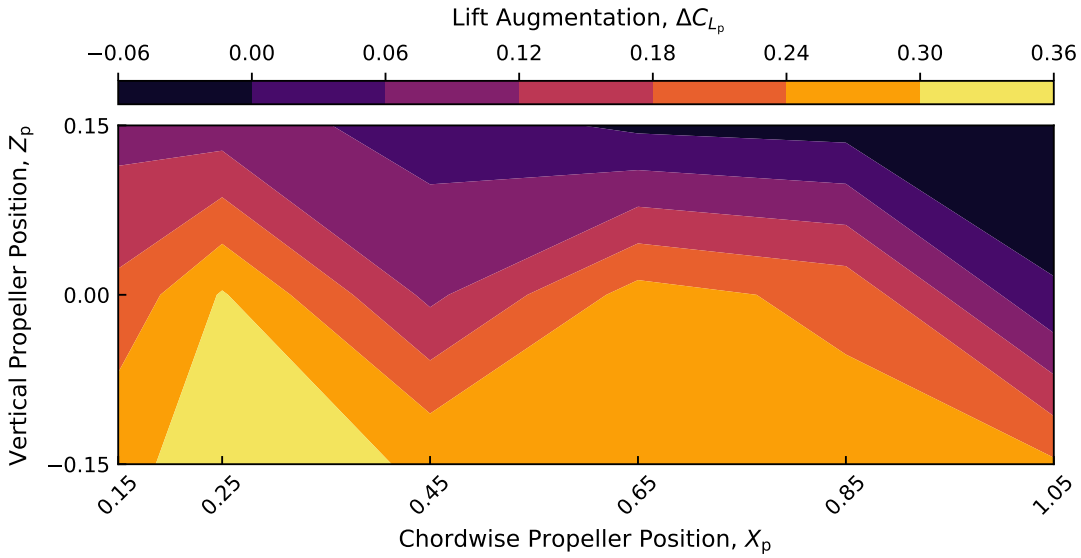

Figure 3.20: Lift augmentation at $\alpha = 16°$ for propeller positions in Grid 1 ($C_{L_{\text{off}}} = 0.64$).

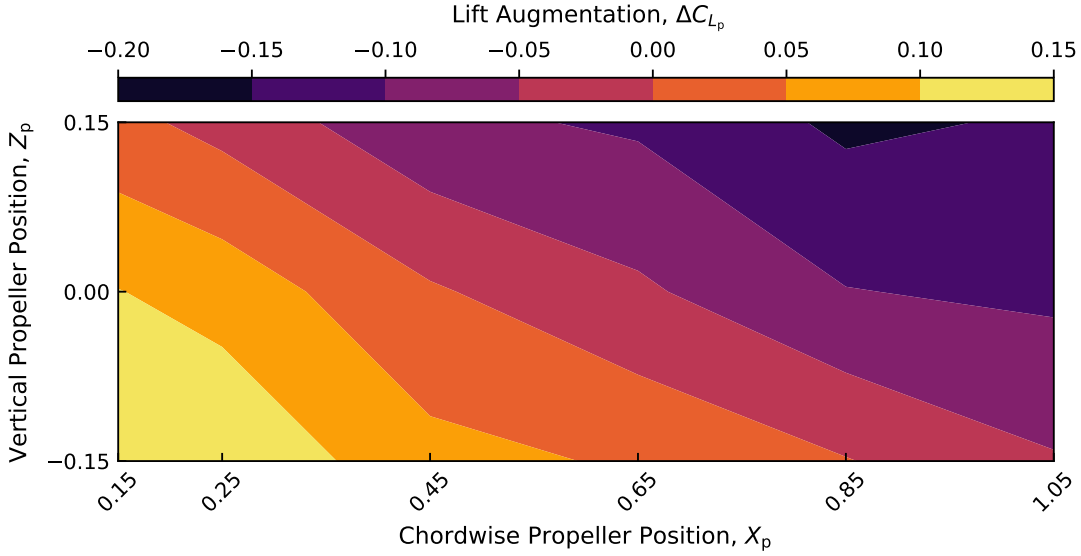

Figure 3.21: Lift augmentation at $\alpha = 20°$ for propeller positions in Grid 1 ($C_{L_{\text{off}}} = 0.72$).

(−22.2%) to $\Delta C_{L_p} = 0.23$ (+31.9%), or a maximum variation in lift augmentation of 0.35 (54.7%) and 0.39 (54.2%), respectively. As a result of the skewing of the propeller slipstream, the propeller slipstream misses the wing at certain propeller positions, namely large propeller chordwise positions above the wing chord line (top right quadrant). When the slipstream no longer interacts with the wing, all of the lift augmenting effects of the slipstream disappear.

3.2.3 Effect of propeller vertical position

In addition to examining the effect of propeller chordwise position, Stage 1 of testing included three propeller vertical positions. Even with this limited set of positions, it is clear that the propeller vertical position is much more influential to the lift augmentation of the wing, as indicated by the more significant gradient in lift augmentation with propeller vertical position seen in Figures 3.14 to 3.21. This was investigated further by testing the propeller positions in Grid 2 (Figure 3.10). Multiple Reynolds numbers were tested, but only the results at $\mathrm{Re} = 2.0 \times 10^5$ will be presented here to remain consistent with the results obtained from Stage 1.

Similar to the propeller chordwise position, changing the propeller vertical position modifies the relative position of the slipstream to the wing, but to a greater extent. Figure 3.22 shows the lift coefficient for each propeller position in Grid 2 at angles of attack of $\alpha = 0°$ and $\alpha = 8°$. The axes for these contour plots are the same as those found in Section 3.2.2, but they follow Grid 2 of propeller positions shown in Figure 3.10. Once again, the brighter regions indicate propeller positions where the lift augmentation was the largest, while the darker regions indicate positions where the lift augmentation was the smallest. At $\alpha = 0°$, $C_{L_{\mathrm{off}}} = 0$ and Figure 3.22a can be interpreted as the total lift coefficient as well as the lift augmentation ($C_{L_{\mathrm{tot}}} = \Delta C_{L_{\mathrm{p}}}$).

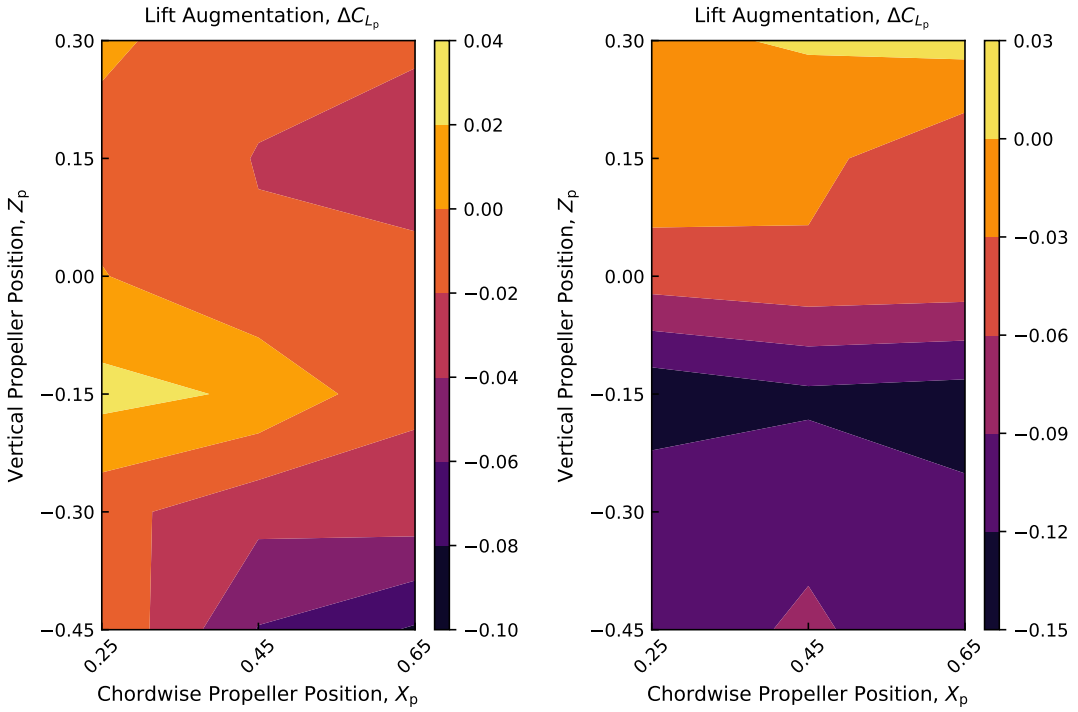

(a) $\alpha = 0°$ ($C_{L_{\mathrm{off}}} = 0.00$)

(b) $\alpha = 8°$ ($C_{L_{\mathrm{off}}} = 0.73$)

Figure 3.22: Lift augmentation for propeller positions in Grid 2 at $\mathrm{Re} = 2.0 \times 10^5$.

Comparing the region of the contour plots at $\alpha = 0°$ and $\alpha = 8°$ (Figures 3.22a and 3.22b) to the earlier results at $\alpha = 0°$ and $\alpha = 8°$ (Figures 3.14 and 3.15), the same trends are observed. As expected, at $\alpha = 0°$ non-zero lift coefficients were measured,

ranging from, $C_L = -0.09$ to $C_L = 0.02$, which is a larger range than was observed for the effect of the propeller chordwise positions. This is a result of the propeller slipstream modifying the velocities over the pressure and suction surfaces of the wing to varying degrees. The way the propeller slipstream interacts with the wing for varying propeller vertical positions at $\alpha = 0°$ can be generalized into four cases, which are illustrated in Figure 3.23.

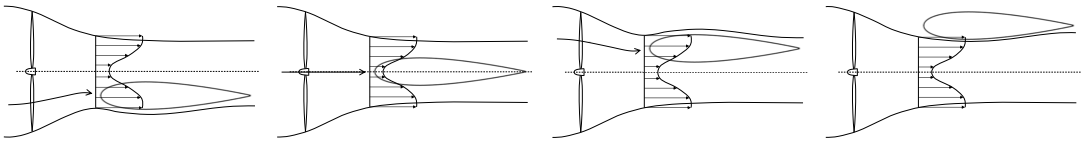

(a) Case IA (b) Case IIA (c) Case IIIA (d) Case IVA

Figure 3.23: Approximate propeller slipstream and wing interaction for different propeller vertical positions at $\alpha = 0°$.

The propeller slipstream has two effects on the wing. The primary effect is a change in the velocities over the pressure and suction surfaces and a secondary effect is a change in the effective angle of attack as a result of the slipstream encountering the wing. It is important to mention that the change in effective angle of attack described here is a generalization based on the idealization of the propeller slipstream. In reality, the swirl of the propeller slipstream will induce both positive and negative effective angles of attack on either side of the propeller depending on the direction of rotation [63, 64, 70]. However, the deformation of the slipstream around the wing causes a net change in the effective angle of attack over the segment of the wing within the propeller slipstream.

When $Z_\mathrm{p} = 0.15$ and 0.30, the propeller slipstream behaves as shown by Case IA (Figure 3.23a). The pressure surface of the wing experiences higher velocities that exist at the edge of the slipstream while the suction surface experiences a relatively lower velocity. This decreases the pressure differential between the two surfaces resulting in less lift. A slight downwash is also induced further reducing lift. This is shown by the regions of negative lift augmentation in the top third of the contour plot in Figure 3.22a.

When $Z_\mathrm{p} = 0$ the slipstream is aligned with the wing and behaves as shown in Case IIA (Figure 3.23b). Both the suction and pressure surfaces experience a similar increase in velocity resulting in little to no change in the lift coefficient. Since the wing is centred within the slipstream, the effective angle of attack remains unchanged. This is shown by near zero lift augmentation found for all propeller chordwise positions at $Z_\mathrm{p} = 0$ in Figure 3.22a.

When $Z_\mathrm{p} = -0.15$, the slipstream is partially below the wing as shown by Case IIIA (Figure 3.23c). The suction surface experiences a larger increase in velocity compared to the pressure surface. This increases the pressure differential between the two surfaces resulting in an increase in lift. An upwash is also induced further augmenting the lift. This effect is shown in Figure 3.22a by the brightest region at $Z_\mathrm{p} = -0.15$, indicating that those propeller positions produced the largest lift augmentation.

At more negative propeller vertical positions of $Z_p = -0.30$ and -0.45, the majority of the slipstream passes below the pressure surface of the wing, as shown by Case IVA (Figure 3.23d). This reduces the pressure on the pressure surface leading to a decrease in the pressure differential between the two surfaces, causing a decrease in lift. The displacement of the slipstream underneath the wing also induces a downwash that reduces the effective angle of attack. This results in the decreasing lift augmentation when the propeller is moved to more negative propeller vertical positions shown by the lower third of the contour plot in Figure 3.22a.

Although not observed in the set of propeller vertical positions tested, for more positive Z_p a situation analogous to Case IV (Figure 3.23d) where the majority of the slipstream passes over the suction surface instead of under the pressure surface is expected. This would serve to increase the velocity over the suction surface, augmenting the lift. While not directly shown in Figure 3.22a, the contour lines do appear to be trending towards greater lift augmentation at $Z_p > 0.30$.

These hypotheses regarding the slipstream-wing interaction depending on the propeller vertical position are supported by the surface pressure readings obtained in Stage 3. Figure 3.24 and 3.25 show the surface pressure coefficients on the suction and pressure surfaces for a propeller chordwise position of $X_p = 0.25$ at four different propeller vertical positions: $Z_p = 0.15$, 0, -0.15, and -0.30, at $\alpha = 0°$. At $Z_p = 0$, the pressure coefficients on the pressure and suction surfaces are similar, suggesting a similar increase in velocity over both of the surfaces as a result of the propeller slipstream. $Z_p = 0$ will be taken as a reference when comparing the pressure coefficients of the other propeller vertical positions presented in Figures 3.24 and 3.25.

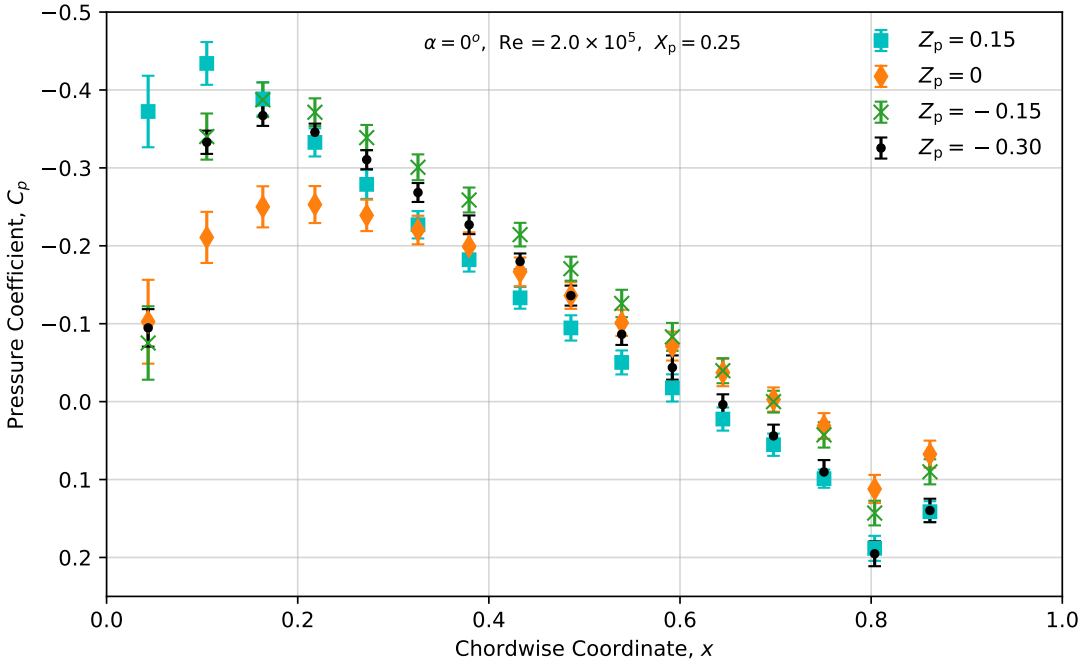

Figure 3.24: Suction surface pressure coefficients at $\alpha = 0°$ for four different propeller vertical positions.

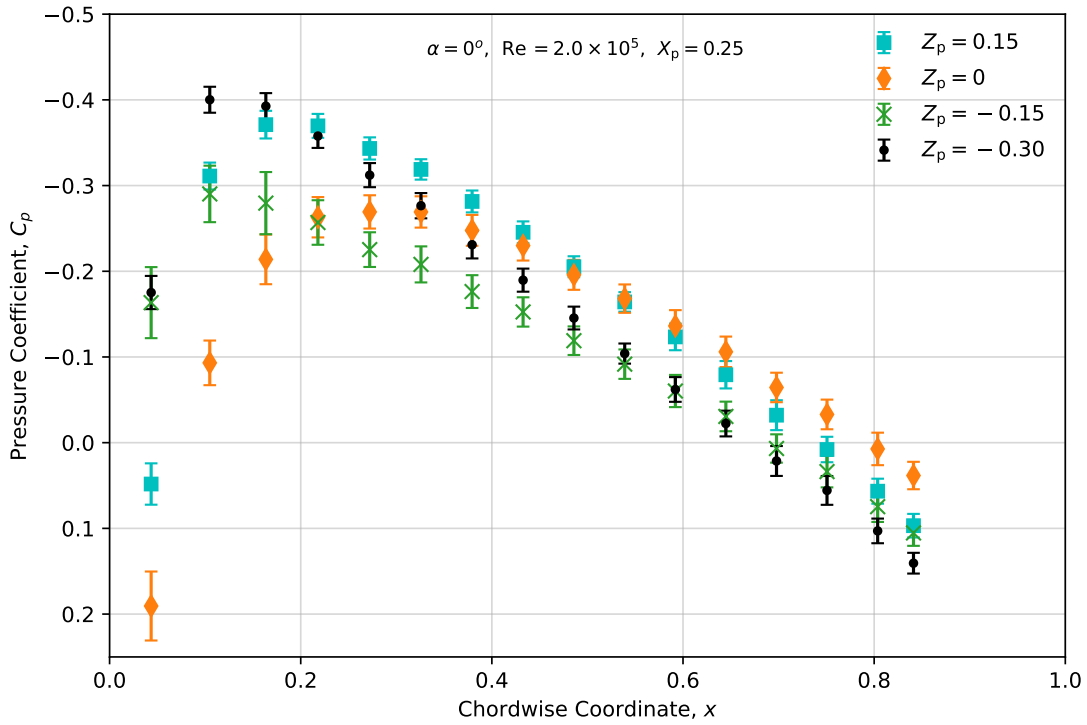

Figure 3.25: Pressure surface pressure coefficients at $\alpha = 0°$ for four different propeller vertical positions.

At $Z_p = 0.15$, suction surface pressure coefficients are shown to be less negative aft of the quarter chord than at $Z_p = 0$. This supports the claim that the slipstream behaves as shown in Case IA, leading to lower velocities over the suction surface when compared to other propeller positions. In addition, the pressure surface pressure coefficients in Figure 3.25 suggest an increase in velocity, indicated by the more negative pressure coefficients when compared to $Z_p = 0$. The overall result of these two observations is the generally negative lift augmentation at $Z_p \geq 0.15$ that is seen the contour plot of Figure 3.22a. In contrast, at $Z_p = -0.15$, the suction surface pressure coefficient is shown to be more negative aft of the quarter chord than at $Z_p = 0$, suggesting higher velocities. On the pressure surface the opposite is shown, resulting in a positive lift augmentation at $Z_p = -0.15$ as shown in Figure 3.22a. For $Z_p = -0.30$ the suction surface pressure coefficients are less negative than $Z_p = -0.15$, indicating slower velocities over the suction surface. The opposite is true for the pressure surface, indicating higher velocities which suggest that the majority of slipstream is passing underneath the pressure surface.

These observations regarding the pressure coefficients are less consistent between 0% and 20% of the chord. This is a result of the experimental setup. The propeller was positioned in the centre of the wing, in line with the pressure taps. The velocities near the centre of the slipstream possess the lowest velocities as a result of losses associated with the propeller hub, which likely influenced the results close to the leading edge. This effect is most apparent for $Z_p = 0$ when the pressure taps are immediately downstream of the propeller hub. This is shown in Figures 3.24 and 3.25, where the pressure coefficients on both pressure and suction surfaces are less negative for $Z_p = 0$.

Introducing the angle of attack results in two significant changes to the interaction between the propeller slipstream and the wing. First, it skews the slipstream proportional to the angle of attack in the direction of the freestream velocity. Second, the wing is rotated to a lower position relative to the propeller slipstream. These factors result in the slipstream interacting with the wing as if the propeller were located at more positive Z_p than it actually is. This effect is illustrated in Figure 3.26.

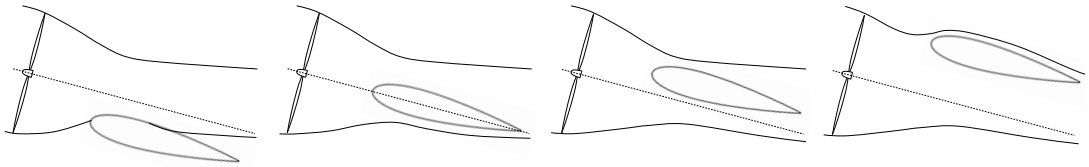

(a) Case IB (b) Case IIB (c) Case IIIB (d) Case IVB

Figure 3.26: Approximate propeller slipstream and wing interaction for different propeller vertical positions for $\alpha > 0°$.

As an example, when $\alpha = 0°$ at $Z_p = 0.30$, it was identified that the slipstream behaves as shown by Case IA in Figure 3.23a resulting in lift reduction. The equivalent slipstream-wing interaction with a positive angle of attack would be Case IIB in Figure 3.26b, which occurs when the propeller is roughly aligned with the wing chord. In other words, to obtain the same type of slipstream-wing interaction with an angle of attack greater than zero, the propeller must be placed at a lower position. This is shown in Figure 3.22b by the thin band of highest lift augmentation at $Z_p = 0.30$. At this position and angle of attack, the slipstream interacts with the wing as shown by Case IB in Figure 3.26a. This is a situation analogous to Case IVA (Figure 3.23d), where the majority of the slipstream passes over the suction surface of the wing, as mentioned when discussing Figure 3.23, leading to enhanced lift augmentation. If $Z_p > 0.30$ were included in Grid 2 at $\alpha = 0°$, a corresponding region of greater lift augmentation would be expected.

As the angle of attack is increased further, the effect becomes amplified. Figure 3.27 shows the lift augmentation for each propeller position in Grid 2 at angles of attack of $\alpha = 10°$ and $\alpha = 13°$. The thin band of highest lift augmentation at $Z_p = 0.30$ for $\alpha = 8°$ observed in Figure 3.22b is expanded towards $Z_p = 0.15$ when the angle of attack is increased to $\alpha = 10°$, shown in Figure 3.27a. Increasing the angle of attack further to $\alpha = 13°$ shifts this region of highest lift augmentation to even lower propeller vertical positions, shown by the brightest region of the contour plot in Figure 3.27b now including $Z_p = 0$.

This trend of the brightest region of the contour plots shifting towards lower propeller vertical positions continues into post-stall angles. Figure 3.28 shows the lift augmentation for each propeller position in Grid 2 at an angle of attack of $\alpha = 17°$ and $\alpha = 20°$. At $\alpha = 17°$, the brightest region is now between $Z_p = -0.15$ and $Z_p = -0.30$, and at $\alpha = 20°$ it has migrated to the bottom left quadrant of the contour plot between $Z_p = -0.30$ and $Z_p = -0.45$.

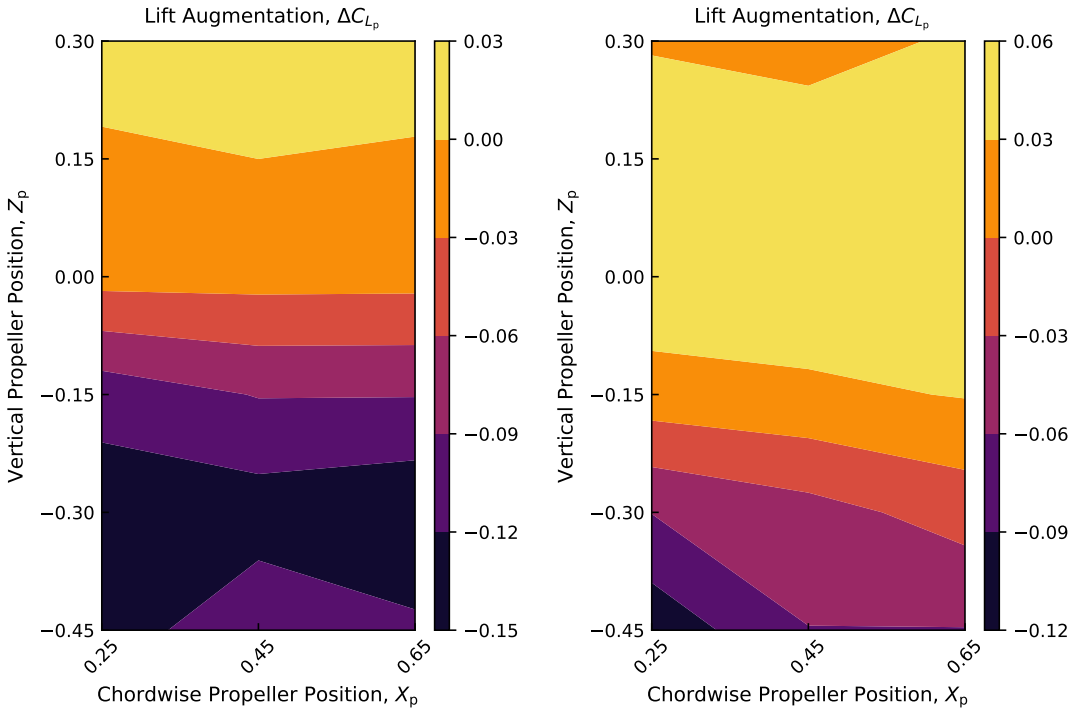

(a) $\alpha = 10°$ ($C_{L_{\text{off}}} = 0.90$) (b) $\alpha = 13°$ ($C_{L_{\text{off}}} = 1.01$)

Figure 3.27: Lift augmentation for propeller positions in Grid 2 at $\text{Re} = 2.0 \times 10^5$.

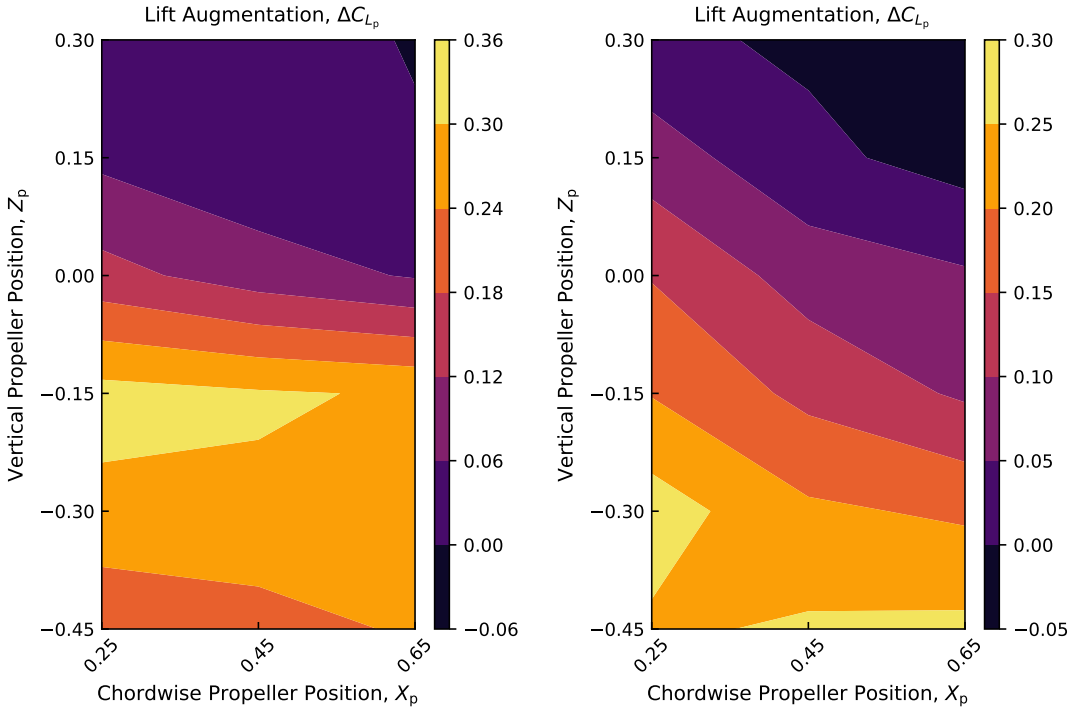

(a) $\alpha = 17°$ ($C_{L_{\text{off}}} = 0.61$) (b) $\alpha = 20°$ ($C_{L_{\text{off}}} = 0.60$)

Figure 3.28: Lift augmentation for propeller positions in Grid 2 at $\text{Re} = 2.0 \times 10^5$.

In addition to the vertical shift of the brightest region, the contour lines are shown to rotate clockwise, from the point of view of the analyst considering Figure 3.28, with increasing angle of attack, which is consistent with the results obtained with Grid 1. Figure 3.29 shows the lift augmentation for each propeller position in Grid 2 at $\alpha = 30°$ and 45°. The angle of the contour lines provides insight into the sensitivity of the lift augmentation of the wing to the chordwise and propeller vertical positions. Up to $\alpha = 13°$ the contour lines are relatively horizontal, as can be observed in Figures 3.22 and 3.27. This means that the propeller vertical position has a much larger impact on the extent of the lift augmentation of the wing than the propeller chordwise position. When the angle of attack increases past 20° the contour lines assume an angle and become oriented at a diagonal, as seen in Figure 3.28b. By $\alpha = 45°$, the contour lines are closer to a vertical orientation. This suggests that as the angle of attack increases, the lift augmentation becomes more sensitive to the propeller chordwise position than it is to propeller vertical position.

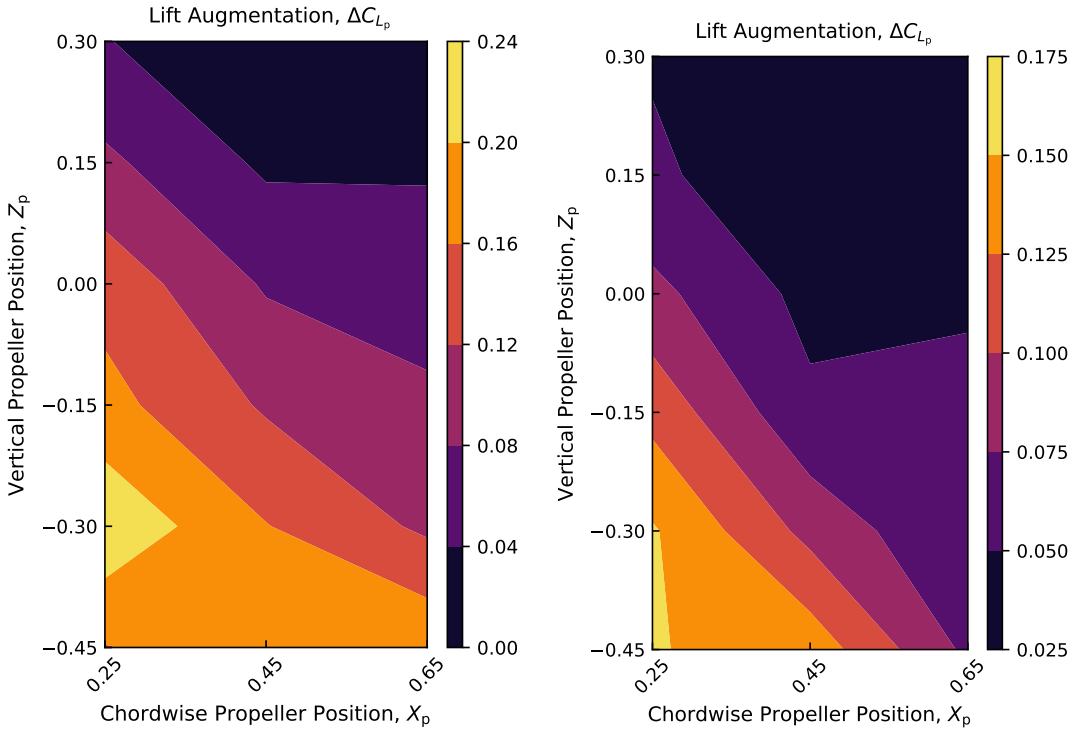

(a) $\alpha = 30°$ ($C_{L_{\text{off}}} = 0.61$)

(b) $\alpha = 45°$ ($C_{L_{\text{off}}} = 0.75$)

Figure 3.29: Lift augmentation for propeller positions in Grid 2 at $\text{Re} = 2.0 \times 10^5$.

When examining the contour plots for $\alpha = 0°$ to $\alpha = 45°$ as a whole, the lift augmentation from the propeller slipstream is observed to be most influential at post-stall angles of attack. This was also suggested by the shape of the grey region in Figure 3.13. At lower angles of attack the magnitude of the lift augmentation is smaller, with certain propeller vertical positions even reducing the lift performance of the wing. This is seen at low propeller vertical positions at $\alpha = 8°$ (Figure 3.22b), where the best performing propeller position only provides a $\Delta C_{L_p} = 0.01$ (+1.4%) while propeller vertical posi-

tions less than $Z_\mathrm{p} = 0$ produce a negative lift augmentation of up to $\Delta C_{L_\mathrm{p}} = -0.14$ (-19.2%). A similar result is shown at $\alpha = 10°$ (Figure 3.27a) with the best performing propeller position providing $\Delta C_{L_\mathrm{p}} = 0.03$ (+3.3%) and the propeller vertical positions less than $Z_\mathrm{p} = -0.15$ producing a lift reduction of up to $\Delta C_{L_\mathrm{p}} = -0.14$ (-15.6%).

At $\alpha = 13°$ the power-off condition is shown to stall, indicated by the sharp drop in lift coefficient shown in Figure 3.12 for $\mathrm{Re} = 2.0 \times 10^5$, at which point the propeller slipstream begins to provide more significant lift augmentation. Figure 3.27b shows a maximum lift augmentation of $\Delta C_{L_\mathrm{p}} = 0.05$ (+4.9%) for the best propeller position, which increases to $\Delta C_{L_\mathrm{p}} = 0.32$ (+52.4%) by $\alpha = 17°$. As was the case with the propeller chordwise positions, at high angles of attack the propeller slipstream can miss the wing completely for large propeller chordwise positions in conjunction with large propeller vertical positions. This is observed at $\alpha = 30°$ and $\alpha = 45°$ (Figure 3.29) in the top right quadrants of the contour plots, where the lift augmentation diminishes to zero.

For conventional propeller-driven, fixed-wing aircraft, operation at post-stall angles is rare and the conclusions of current literature stating that the propeller chordwise position has little effect on the performance of the wing remains valid [65, 70]. As for the propeller vertical position, the location of the highest lift augmentation remains above the wing chord line for angles of attack before stall. This means that a propeller position above the wing chord line is desirable. In the case of tilt-wing aircraft that must transition through post-stall angles of attack, these results demonstrate that the effect of the propeller chordwise position becomes increasingly significant as the angle of attack increases. At $\alpha \approx 45°$, the propeller chordwise position is shown to be as important as the propeller vertical position. Selecting a propeller vertical position is not as straightforward for tilt-wing aircraft as it is for conventional fixed-wing aircraft. The location of highest lift augmentation gradually shifts to lower propeller positions as the angle of attack increases past stall, presenting a trade-off between lift augmentation at lower angles of attack or lift augmentation at higher angles of attack. Selecting a propeller position above the wing chord line sacrifices lift augmentation at post-stall angles of attack for increased lift performance during cruise conditions. Selecting a propeller position below the wing chord line allows the wing to remain in the propeller slipstream at higher angles of attack at the cost of decreased lift performance at angles of attack before stall. This trade off is investigated in further detail in the next chapter.

The results presented in this chapter represent a subset of an extended set of results that best represented the arguments and conclusions made. The extended set of results are given in Appendix B. It includes contour plots showing the lift augmentation at all angles of attack specified for Stage 2 in Table 3.2, a discussion on the effect of Reynolds number on the lift augmentation, and the effect of propeller position on other aerodynamic parameters besides the lift coefficient (moment and drag coefficients, and aerodynamic efficiency).

4 Aerodynamic Performance of Blown Tubercles

This chapter presents the methodology, results and discussion of an extension of the experimental wind tunnel campaign introduced in Chapter 3. The results of Chapter 3 quantified the aerodynamic performance of a blown wing with an unmodified, straight leading edge. The extended wind tunnel campaign presented in this chapter uses those results as a baseline for comparison in order to characterize the performance of a blown wing with sinusoidal leading edge tubercles at high angles of attack. This investigation consists of force/torque transducer measurements to obtain the lift coefficient, drag coefficient, and aerodynamic efficiency, for six different tubercle geometries. No surface pressure measurements were collected. The results presented in this chapter serve as an aerodynamic database that will be used in the subsequent chapter to assess the effect of tubercles on the transition of a tilt-wing vehicle through a numerical simulation.

4.1 Methodology

This section presents the experimental objectives, a description of the experimental setup, and experimental procedures. The wind tunnel, instrumentation and DAQ system, and data post-processing methods are identical to those described in Chapter 3, details for which can be found in Sections 3.1.3 and Section 3.1.4 respectively.

4.1.1 Experimental Objectives

Tubercles have been shown to modify greatly the stall behaviour of lifting surfaces, delay stall, and to improve post-stall lift [39, 41, 42, 49, 50]. Their potential to improve the performance of various systems that operate at high angles of attack have been recognized, leading to various studies exploring possible applications. One application that is yet to be explored is the application of tubercles to a propeller blown lifting surface such as those found on the wings of tilt-wing aircraft. This extended wind tunnel campaign aims to fill this gap in knowledge by being the first study in the current body of knowledge to investigate experimentally the aerodynamic performance of tubercles on a blown lifting surface at high angles of attack. There are three main experimental objectives. The first objective is to determine the optimal propeller position for an unmodified, straight leading edge wing in the context of transition. The second objective is to compare the aerodynamic performance of a blown lifting surface with six different tubercle geometries to a straight leading edge with the propeller positioned at that optimal position. Finally, the third objective is to determine if the lift enhancement of tubercles can be further enhanced when placed in a propeller slipstream.

4.1.2 Experimental Setup

The experimental setup was the same as introduced in Chapter 3, Section 3.1.2 with the exception of the wing models, which will be described in this section. The leading edges for the wing models with tubercles were a sinusoidal profile defined by the following equation:

$$x(y) = Ac \sin\left(\frac{2\pi y}{\lambda c}\right) \tag{4.1}$$

where $x(y)$ is the modified chordwise coordinate of the leading edge as a function of the spanwise location, y, and A and λ are the tubercle amplitude and wavelength as a percentage of the chord length, c. A labelled sinusoidal leading edge profile is shown in Figure 4.1.

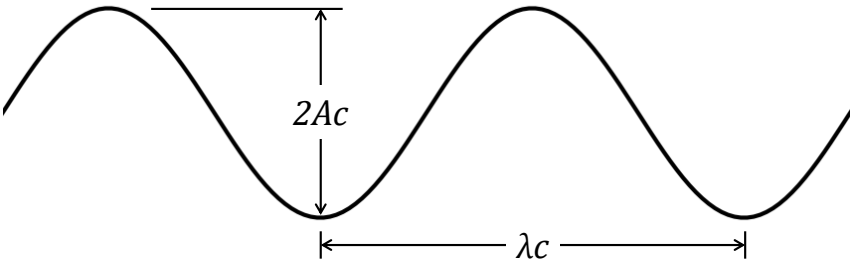

Figure 4.1: Sinusoidal leading edge tubercle parameters.

Different tubercle wings were identified and named based on their respective amplitude and wavelength. For example, a tubercle wing with a tubercle amplitude of 3% of the chord ($A = 0.03$) and a wavelength of 11% ($\lambda = 0.11$) was named A03λ11. The six tubercle geometries tested are summarized in Table 4.1, with Figure 4.2 showing a schematic drawing of the suction surface of each tubercle geometry. An amplitude and wavelength of zero indicates an unmodified geometry with a straight leading edge (SLE) that was used as a baseline for comparison.

Table 4.1: Summary of the tubercle geometries tested.

Name	Amplitude (% chord)	Wavelength (% chord)
SLE (baseline)	0.00	0.00
A02λ07	0.02	0.07
A02λ09	0.02	0.09
A03λ11	0.03	0.11
A04λ18	0.04	0.18
A05λ13	0.05	0.13
A06λ21	0.06	0.21

The tubercle wing models were designed such that their average chord lengths were equal to the chord length of an unmodified, straight leading edge to ensure that the total planform areas of the different wing models were consistent with one another. The airfoil profile aft of the location of maximum thickness was unmodified for all wing

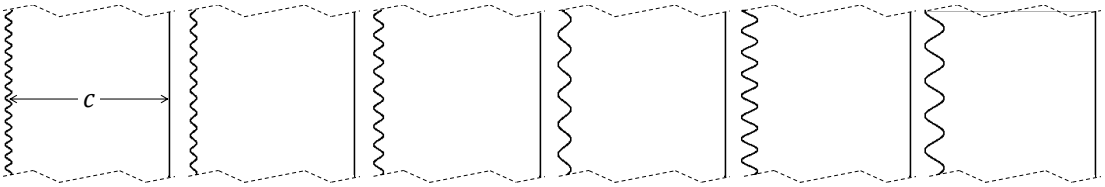

(a) A02λ07. (b) A02λ09. (c) A03λ11. (d) A04λ18. (e) A05λ13. (f) A06λ21.

Figure 4.2: Suction surface view of a wing segment for each tubercle geometry tested.

models. For the NACA 0018 the location of maximum thickness is located at 0.3c. The airfoil profile forward of the location of maximum thickness was generated by a loft operation using the unmodified airfoil geometry along the sinusoidal shape defined by Equation 4.1. Figure 4.3 shows the tubercle wing models.

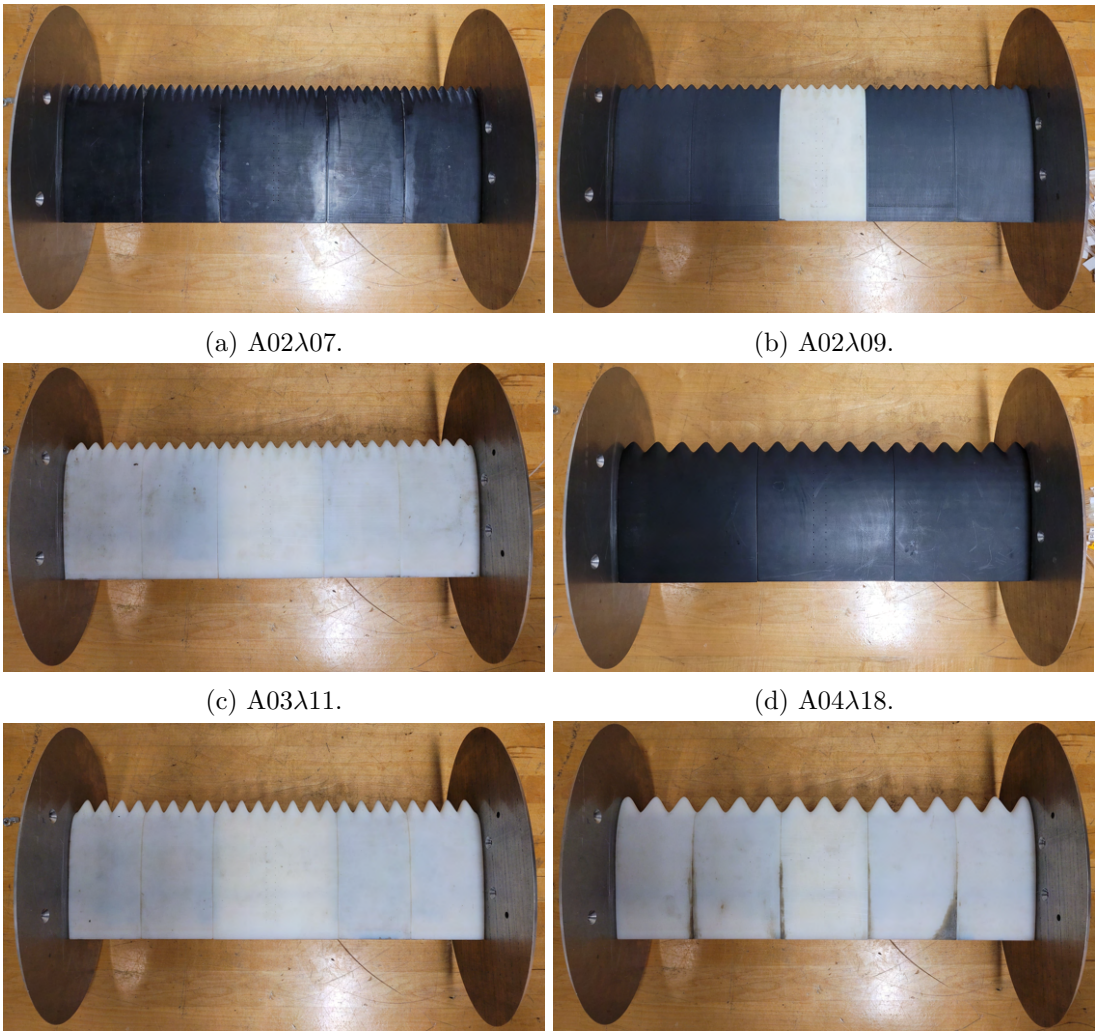

(a) A02λ07. (b) A02λ09.

(c) A03λ11. (d) A04λ18.

(e) A05λ13. (f) A06λ21.

Figure 4.3: Fully assembled tubercle wing models with end plates.

The tubercle wing models were manufactured from *VeroWhitePlus*™ or *VeroBlackPlus*™ plastic using a *Stratasys Objet30 Pro*™ high-definition rapid prototyping system, which

has a minimum buildup layer of 28 μm. The same surface finish as the SLE wing model with a roughness height of Ra $= 0.8 \pm 0.2\mu$m, measured with a *Mitutoyo Surftest SJ-400* portable surface roughness tester, was achieved with hand polishing.

The leading edge was designed such that a tubercle peak was located at the mid-span of the fully assembled wing model regardless of tubercle geometry. The completed wing consisted of three to five segments, with spackling putty used to fill any gaps between the assembled wing segments. Although not used, the wing models had two sets of surface pressure taps integrated into the centre segment. One set of pressure taps were placed at the tubercle peak at the mid-span, with the second set placed in an adjacent valley. During testing, since no surface pressure measurements were recorded the *Tygon*® tubes connected to the pressure taps were plugged with metal dowel pins. The SLE wing model from Chapter 3 was replaced with the tubercle wings. All other aspects of the experimental setup, which is described in detail in Section 3.1.2, were not modified. Figure 4.4 shows the complete experimental setup with the A03λ11 wing mounted. Note the similarity with Figure 3.2 with the exception of the different wing model.

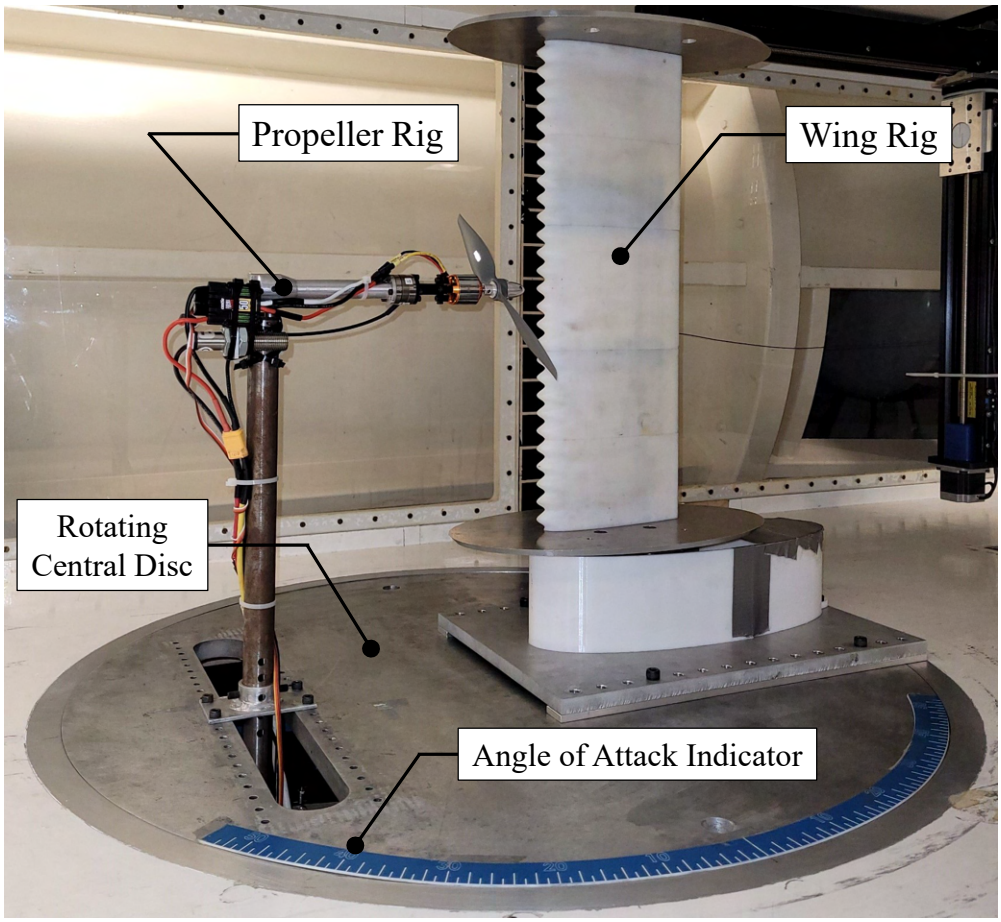

Figure 4.4: Complete experimental setup with the A03λ11 wing mounted.

4.1.3 Experimental Procedure

A total of 14 angles of attack between 0° and 45° were investigated at four freestream velocities of $U = 10$ m/s, 15 m/s, 20 m/s, and 25 m/s, corresponding to Re = 1.0×10^5, 1.5×10^5, 2.0×10^5, and 2.5×10^5 respectively. For power-on tests, the propeller rotational speed was maintained at 8000 RPM. The exact angles of attack and a summary of the test conditions are provided in Table 4.2. Note that these are the same test conditions as Stage 2 of testing in Chapter 3 to facilitate the comparison to the unmodified, straight leading edge results.

Table 4.2: Test condition matrix for the aerodynamic performance of tubercles.

Angles of Attack (°)	Re ($\times 10^5$)	Propeller RPM
0, 8, 10, 12, 13, 14, 15, 17, 20, 25, 30, 35, 40, 45	1.0, 1.5, 2.0, 2.5	8000

A practical approach to the design of this extended experimental campaign was taken in order to manage the number of hours required for testing. If a matrix of propeller positions, similar to the two matrices tested for the unmodified, straight leading edge wing was investigated for each of the six tubercle wings, the predicted number of hours required for testing exceeded 300 hours and was not practical. For test efficiency, the aerodynamic performance of each tubercle wing was investigated as a retrofit. Each of the propeller positions for the unmodified, straight leading edge wing tested in Grid 2 from Chapter 3 were assessed and an optimal propeller position, in the context of tilt-wing transition, was selected. Details for the selection criteria and selection method for the optimal propeller position are provided in Section 4.1.4. Next, with the propeller fixed at the optimal propeller position, the power-on aerodynamic performance of each of the six tubercle wings was measured. The results for the unmodified, straight leading edge wing at the same propeller position, collected in Chapter 3, was used as a baseline for comparison. In addition, power-off tests (no propeller) for each of the six tubercle wings were also conducted. These results were used to determine the lift augmentation of each tubercle wing in the same manner as described in Chapter 3.

4.1.4 Selection of the Optimal Propeller Position

One of the conclusions of Chapter 3 was that the propeller vertical position had a more significant effect than the propeller chordwise position on the aerodynamic performance of a blown wing until an angle of attack of 45°. The tests conducted with Grid 2 included a larger range of propeller vertical positions than Grid 1 did, as well as a larger range of angles of attack and Reynolds numbers. For these reasons, only the propeller positions in Grid 2, as was shown in Figure 3.10, were assessed when determining the optimal propeller position.

In order to determine the optimal propeller position for each wing, a selection criteria in the context of tilt-wing aircraft must be defined. The concept of a transition corridor was briefly introduced in Chapter 1 and will be reiterated here. As a tilt-wing aircraft transitions between forward flight and vertical flight, the angle of the wing relative to the freestream varies from 0° (forward flight) to 90° (vertical flight). For each wing angle, the aircraft has a minimum forward flight speed, dictated by the speed at which

the wing no longer generates enough lift to support the weight of the aircraft, and a maximum forward flight speed, dictated by the thrust capabilities of the propulsion system. This information can be represented in a figure with the forward flight speed on the horizontal axis and the wing angle on the vertical axis. The lines created by the minimum and maximum forward flight speeds defines a flight envelope known as the transition corridor. An example of a transition corridor is shown in Figure 1.1. The bound created by the minimum forward flight speeds will be referred to as the *left bound* and the bound created by the maximum forward flight speed will be referred to as the *right bound*.

In Chapter 3, the magnitude of the lift augmentation was shown to vary with propeller position, which in turn affected the total wing lift. The lift performance of the wing is directly linked to the left bound of the transition corridor. A wing that can generate more lift allows for lower minimum forward flight speeds. This makes the magnitude of the lift augmentation a prime candidate to be used as a quantitative measure of the effectiveness of each propeller position. The lift augmentation varies with angle of attack, which must be accounted for when determining the optimal position. The simplest method of accounting for variations with angle of attack is to integrate the lift augmentation with respect to angle of attack to obtain one representative number to quantify the effectiveness of each propeller position. This number will be referred to as the lift augmentation score (LAS). In practice, a numerical integration using a trapezoidal approximation of the discrete experimental data was used to obtain the LAS for each Reynolds number. Furthermore, a weighting was assigned to each angle of attack to control their relative importance. This is described in Equation 4.2:

$$\text{LAS} = \sum_{i=1}^{13} W_i \frac{\left[\Delta C_{L_\text{p}}\right]_{i+1} + \left[\Delta C_{L_\text{p}}\right]_i}{2} \left(\alpha_{i+1} - \alpha_i\right) \tag{4.2}$$

where ΔC_{L_p} is the lift augmentation (difference between the power-off lift and total lift with power-on, see Equation 3.10), α is the angle of attack, and the index i denotes which angle of attack, corresponding to each angle of attack tested in ascending order. The corresponding angle of attack to each index value is provided in Table 4.3. W_i is the weighting factor that is used to control the relative importance of each angle of attack.

The weighting factor for each angle of attack was selected with a typical mission profile for an urban air mobility (UAM) VTOL aircraft in mind. An example of such a mission profile can be found in Appendix C, as defined by Patterson *et al.* [76]. As tilt-wing aircraft must still be able to retain favourable forward flight performance, angles of attack before stall were given mid-value weighting factors. Wing stall has been identified as an important factor during transition, so the angles of attack near the stall angle were given the highest weighting factors [7,22,69,71]. As the wing tilts past 30°, the lift required by the wing decreases as the propeller thrust vector unloads the wing, which reduces the importance of the wing lift. For this reason, angles of attack greater than 30° were given the lowest weighting factors. The selected weighting factors for each angle of attack are summarized in Table 4.3.

Table 4.3: Weighting factors for evaluating the effectiveness of propeller positions and indexing for each angle of attack.

Index i	Angle of Attack α_i (°)	Weighting W_i
1	0	0.45
2	8	0.75
3	10	0.90
4	12	1.00
5	13	1.00
6	14	0.95
7	15	0.80
8	17	0.55
9	20	0.35
10	25	0.25
11	30	0.20
12	35	0.15
13	40	0.12
14	45	0.10

Equation 4.2 was applied to each Reynolds number and finally totalled across each Reynolds number to obtain an overall LAS that was representative of the effectiveness of the lift augmentation of each propeller position across all angles of attack and Reynolds numbers tested. The position with the greatest LAS was defined as the optimal propeller position.

4.2 Results and Discussion

This section presents the experimental results. First, the selection of the optimal propeller position will be presented, followed by power-off measurements for each of the six tubercle wings. Finally, the effect of the tubercles on the power-on lift performance of the wing will be presented. Moment, drag, and aerodynamic efficiency results can be found in Appendix C.

4.2.1 Optimal Propeller Position

Using Equation 4.2 along with the weightings summarized in Table 4.3 the LAS of each propeller position in the Grid 2 were calculated. This was completed for each Reynolds number, and finally totalled to obtain the overall LAS. The LAS of each propeller position can be represented with a contour plot, with the horizontal axis indicating the propeller chordwise position, vertical axis indicating the propeller vertical position, and the LAS indicated with a colour bar. Figure 4.5 shows the contour plot of the overall LAS of each propeller position. The marker indicates the position with the greatest LAS, $X_\mathrm{p} = 0.25$ and $Z_\mathrm{p} = 0$, with the value indicated with an equivalent marker on the colour bar.

The results of Chapter 3 revealed that a propeller position above the wing chord line provides the most lift augmentation for angles of attack before stall. However, those

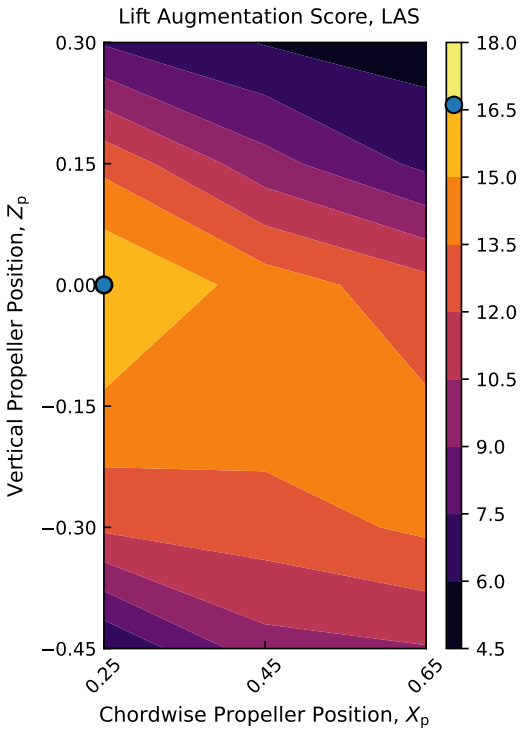

Figure 4.5: Lift augmentation scores (LAS) for each propeller position.

positions produced significantly less lift augmentation at post-stall angles of attack as the wing exited the propeller slipstream. The opposite was true for propeller positions below the wing chord line, with those positions providing the least lift augmentation at angles of attack before stall and the most lift augmentation at post-stall angles of attack. When the lift performance of the blown wing across all angles of attack are considered, a propeller position in line with the chord strikes a compromise. Up to $\alpha = 14°$, propeller positions in line with the wing chord were still comparable to the best performing positions in terms of lift augmentation. For $14° \leq \alpha \leq 45°$, they provided moderate lift augmentation that was neither the best nor the worst performing position. For these reasons, an optimal propeller position of $X_p = 0.25$ and $Z_p = 0$ was accepted as a reasonable result and used in subsequent testing of the different tubercle wings. If the weightings in Table 4.3 were modified to place more importance to lower angles of attack, the optimum propeller position would move to larger X_p values. The opposite would occur if higher angles of attack were given more important weightings.

4.2.2 Power-Off Analysis

In order to determine the lift augmentation of each tubercle wing, power-off measurements were required. Characteristic lift parameters for each tubercle wing, such as the maximum lift coefficient and stall angle, are are summarized in Table 4.4. Figures 4.6 through 4.9 shows the power-off lift coefficients for each tubercle wing at the four Reynolds numbers tested. The results for the unmodified, SLE wing are provided for comparison. The measurement uncertainty is only shown for $\mathrm{Re} = 2.5 \times 10^5$ to improve the readability of the figures.

Table 4.4: Characteristic lift curve parameters for each tubercle wing.

	Wing	Maximum Lift Coefficient $C_{L_{\max}}$	Stall Angle α_s (°)	Lift Curve Slope $C_{L,\alpha}$ (rad^{-1})
$Re = 1.0 \times 10^5$	SLE	0.92	12	5.58
	A02λ07	0.80	13	5.10
	A02λ09	0.88	12	5.40
	A03λ11	0.84	12	5.18
	A04λ18	0.83	10	5.28
	A05λ13	0.78	10	5.03
	A06λ21	0.82	10	5.06
$Re = 1.5 \times 10^5$	SLE	0.96	12	5.55
	A02λ07	0.85	14	5.16
	A02λ09	0.94	13	5.48
	A03λ11	0.90	13	5.35
	A04λ18	0.93	12	5.32
	A05λ13	0.82	10	5.16
	A06λ21	0.84	10	5.31
$Re = 2.0 \times 10^5$	SLE	1.01	13	5.24
	A02λ07	0.90	14	5.18
	A02λ09	1.01	14	5.50
	A03λ11	0.95	13	5.44
	A04λ18	0.95	12	5.14
	A05λ13	0.87	12	5.14
	A06λ21	0.86	10	5.29
$Re = 2.5 \times 10^5$	SLE	1.01	13	5.06
	A02λ07	0.93	15	5.02
	A02λ09	1.05	14	5.44
	A03λ11	0.98	14	5.23
	A04λ18	0.96	12	4.90
	A05λ13	0.91	13	4.98
	A06λ21	0.87	10	5.04

The lift coefficients for all tubercle wings at all four Reynolds numbers tested were expected to be zero. Figures 4.6 through 4.9 shows that the tubercle wings deviate from this expectation to varying degrees. However, the deviation is consistent for each tubercle wing across all four Reynolds numbers, suggesting that this error was likely due to asymmetry in the model. The alignment of the wing segments during the assembly of the wing models, as well as the putty that was used to fill gaps between the models are potential sources of asymmetry. The A06λ21 shows the most significant deviation, with lift coefficients of approximately 0.04 at $\alpha = 0°$ for all angles of attack. This source of error was acknowledged and accounted for when interpreting the results.

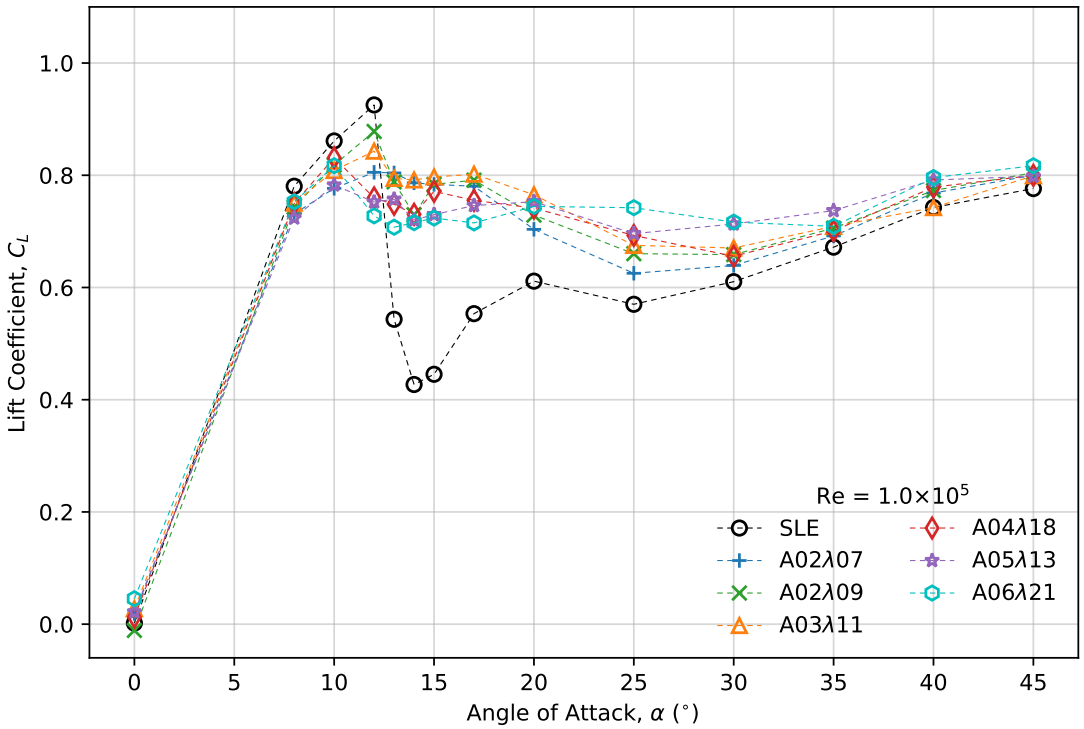

Figure 4.6: power-off lift coefficients for six tubercle wings at Re = 1.0×10^5.

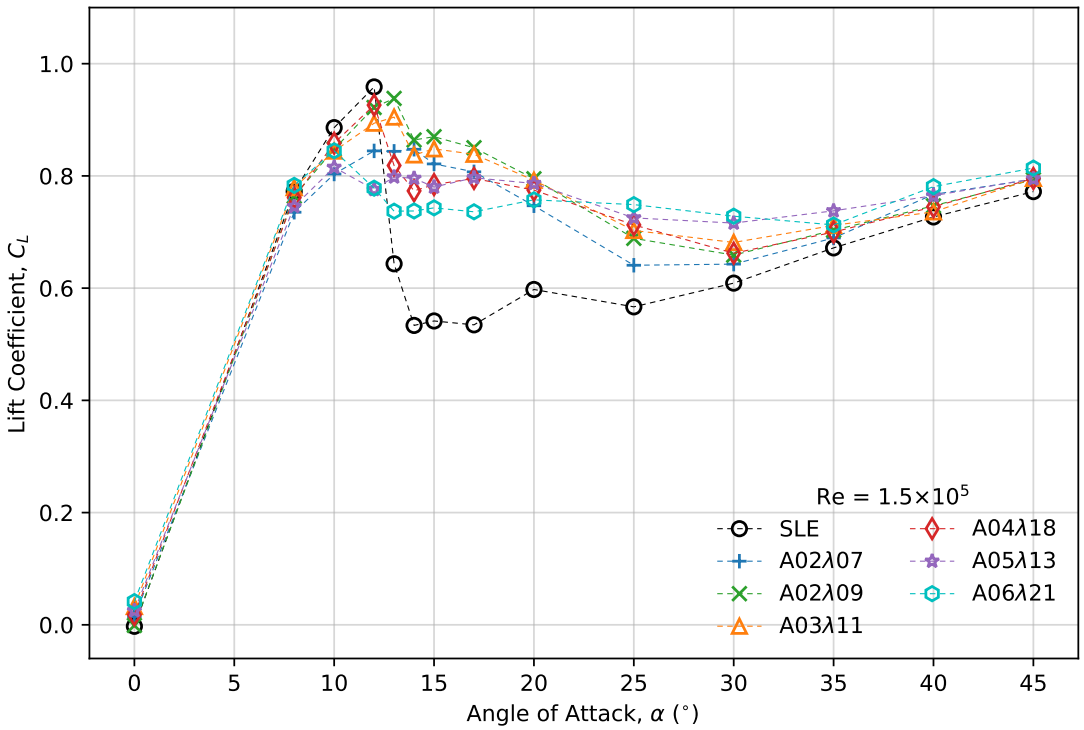

Figure 4.7: power-off lift coefficients for six tubercle wings at Re = 1.5×10^5.

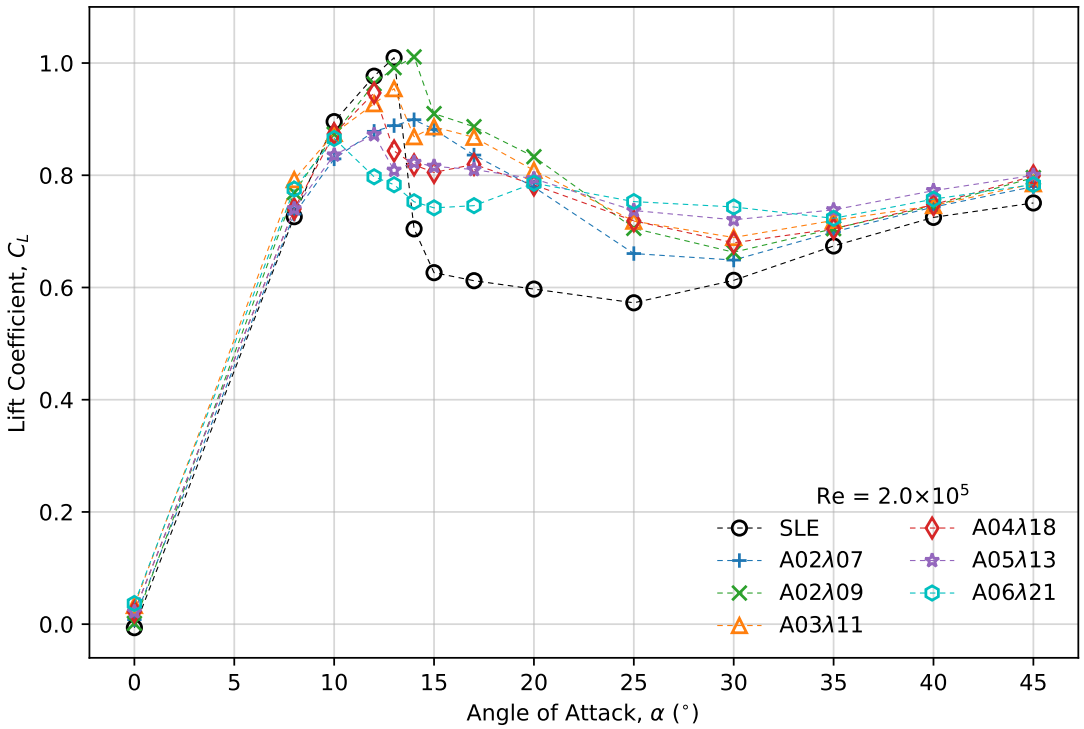

Figure 4.8: power-off lift coefficients for six tubercle wings at Re = 2.0×10^5.

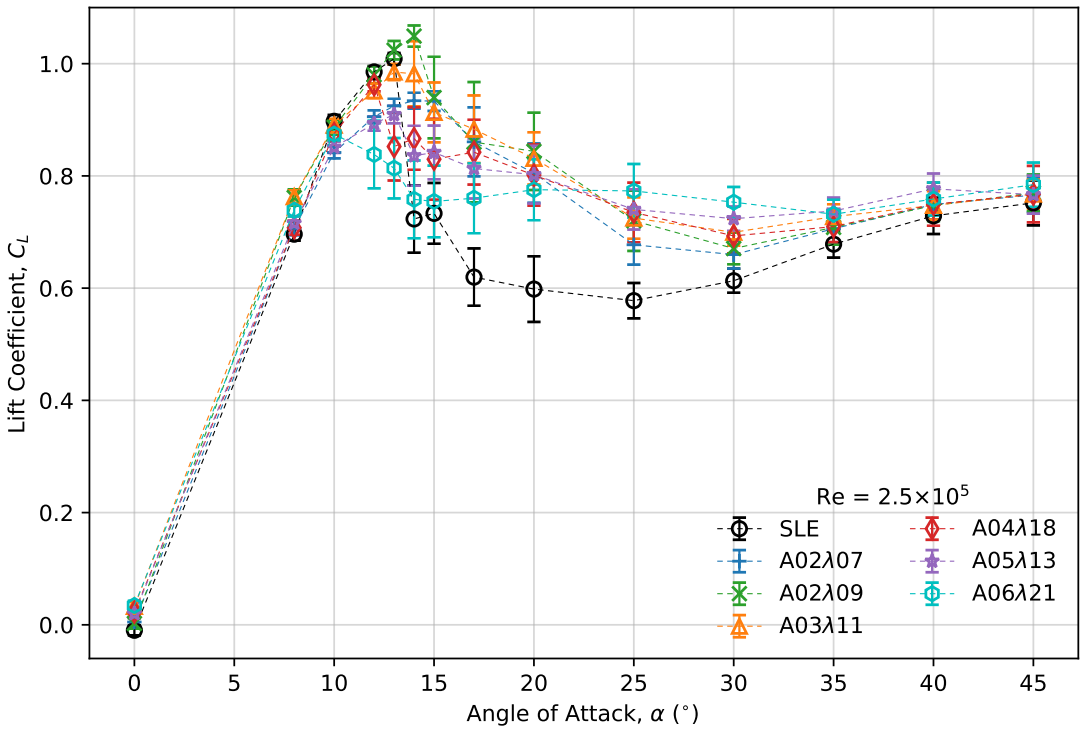

Figure 4.9: power-off lift coefficients for six tubercle wings at Re = 2.5×10^5.

For clarity, the angle of attack at which the maximum lift coefficient is observed will be referred to as the stall angle. This ranged from 10° to 15° depending on the Reynolds number and tubercle geometry, as summarized in Table 4.4. Angles of attack before stall will be referred to as pre-stall angles of attack. Angles of attack between stall and 25° will be referred to as post-stall angles of attack. Angles of attack greater than 25° will be referred to as high angles of attack. When discussing the effect of the tubercles, the relative magnitude of the sharp decrease in lift coefficient usually observed immediately after stall will be referred to as the stall characteristic of the wing. An abrupt stall characteristic describes a significant decrease in lift coefficient following stall, while a smoother stall characteristic refers to the attenuation of this decrease in lift coefficient. For example, the SLE wing has an abrupt stall characteristic, while the A06λ21 has a smoother stall characteristic (see Figures 4.6 to 4.9).

The maximum lift coefficients increased and the stall angles increased by 1° to 2° with increasing Reynolds number, regardless of wing geometry, which is not surprising. When compared to the lift performance of the SLE wing, the addition of tubercles increased the post-stall lift coefficients at the cost of a decreased maximum lift coefficient, which is in agreement with the current body of knowledge [29, 35, 37–42, 49, 50]. The lift performance of the A02λ09 wing at $\mathrm{Re} = 2.0 \times 10^5$ is an exception to this observation, as it generated a larger maximum lift coefficient than the SLE wing along with increased lift coefficients at post-stall angles of attack. The magnitude of the decrease in maximum lift coefficient and the extent of the post-stall lift enhancement varied with the tubercle geometry. These trends were generally consistent across all Reynolds numbers. For example in Figures 4.6 through 4.9, the position of each line relative to one another is fairly consistent, which represents consistency in the lift performance of each tubercle wing relative to one another. Certain exceptions can be found when examining values provided in Table 4.4 in detail, but these exceptions did not deviate significantly from the overall trends. This allows the observations concerning the trends in the lift performance with varying tubercle geometry made at one Reynolds number to be representative of the other Reynolds numbers. The results at $\mathrm{Re} = 2.0 \times 10^5$ will be used as a representative Reynolds number and examined in further detail as indicative of Reynolds-independent results.

The stall characteristic of the wing was shown to vary with tubercle geometry in Figure 4.8. In general, increasing tubercle amplitude resulted in a smoother stall characteristic at the cost of a reduced maximum lift coefficient and reduced stall angle. This trend is consistent with Hansen *et al.* and Custodio [39, 40]. An exception to this observation was the A02λ07 wing, which showed a smoother stall characteristic than the greater amplitude A04λ18 wing and A03λ11 wing, along with a lower maximum lift coefficient. This suggests that the tubercle wavelength also plays a role in dictating the lift performance of a tubercle wing. The tubercle amplitude-to-wavelength ratio, A/λ, a parameter proposed by Hansen, can be used to describe both aspects of the tubercle geometry [40]. A study by Peristy *et al.* concluded that increasing A/λ results in a general decrease in lift coefficient [46]. The results presented here support this conclusion, as illustrated by the lower lift coefficients generated by the A02λ07 wing ($A/\lambda = 0.28$) in the pre-stall and post-stall angles of attack compared to the A02λ09 wing ($A/\lambda = 0.22$), which both have the same tubercle amplitude with different A/λ. The previous obser-

vation regarding the trends with increasing tubercle amplitude still remain valid, as demonstrated by comparing the A02λ09 wing with the A04λ18 wing, which both have $A/\lambda = 0.22$. Despite the equivalent A/λ, the greater amplitude A04λ18 wing had a reduced maximum lift coefficient and a relatively smoother stall characteristic.

To illustrate better the effect of the different tubercle geometries, the relative change in lift coefficient can be examined. Figure 4.10 shows the relative change in lift coefficient for each tubercle wing using the SLE wing as a baseline, at a Reynolds number of 2.0×10^5. The relative change in lift coefficient at $\alpha = 0°$ is omitted due to the negligible magnitudes. For all tubercle wings at angles of attack between 10° and 13° (just before stall), the lift coefficient was reduced from the SLE wing by up to 22.4%. At all other angles of attack, the tubercle wings generated up to 45.2% more lift, with the largest increase in lift observed at post-stall angles of attack. This is in agreement with Miklosovic *et al.* who observed a similar reduction in lift before stall and increase in lift at all other angles [42].

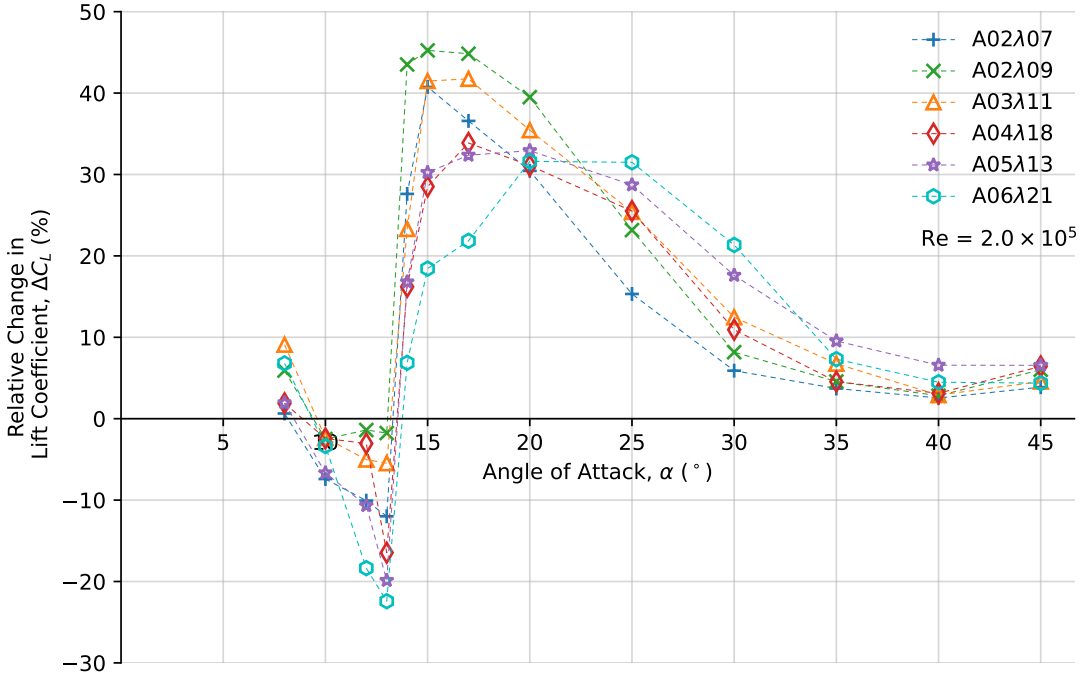

Figure 4.10: Relative change in lift coefficients for each tubercle geometry at $\mathrm{Re} = 2.0 \times 10^5$.

Figure 4.10 confirms the observations made from Figure 4.8. The larger tubercle amplitudes showed a greater reduction in lift coefficient at pre-stall angles of attack and a lower increase in lift coefficient at early post-stall angles of attack ($\alpha \lesssim 23°$) when compared to the smaller tubercle amplitudes. This resulted in a smoother stall characteristic for larger tubercle amplitudes. Further inspection of Figure 4.8 shows that the smoother stall characteristic exhibited by larger tubercle amplitudes extends into high angles of attack. While the smaller amplitude tubercles show a continual decrease in lift coefficient following stall, the larger amplitude tubercles show an almost constant lift coefficient, resulting in the larger tubercle amplitudes outperforming the smaller tu-

bercle amplitudes. This is also shown in Figure 4.10 by the A06λ21 wing producing the largest increase in lift coefficient at $\alpha = 25°$, followed by the A05λ13, A04λ18, A03λ11, A02λ09 and finally the A02λ07 wing. Johari *et al.* reported a similar result [49].

At high angles of attack ($\alpha \geq 25°$), the lift coefficients of all tubercle wings converged to an approximate 5% increase in lift coefficient regardless of tubercle geometry. This suggests that even at high angles of attack where most of the flow is expected to be separated, the tubercles continue to generate SCRV that provide a small lift enhancing effect. By $\alpha = 45°$, this minimal lift enhancement is virtually non existent as all wings begin to behave like flat plates. The agreement of these results with multiple different sources served as a validation of the experimental test rig and the tubercle wing models. A short discussion on the effect of tubercles on drag, moment, and aerodynamic efficiency of the wing for the power-off condition can be found in Appendix C.

4.2.3 Characterization of the Lift Performance of Blown Tubercles

This section presents the power-on results. All power-on measurements were taken with the propeller positioned at $X_\mathrm{p} = 0.25$ and $Z_\mathrm{p} = 0$, the optimal propeller position determined in Section 4.2.1. The lift performance of the tubercle wings were assessed based on two different parameters. The first parameter was the total lift coefficient, C_{L_tot}. Comparisons were made with the results of the SLE wing from Chapter 3. This allowed for the general characterization of the lift performance of each tubercle wing in the presence of a propeller slipstream, accomplishing the second experimental objective introduced in Section 4.1.1. The second parameter was the lift augmentation, ΔC_{L_p}. This parameter was compared to the lift augmentation of the SLE wing in order to determine if the aerodynamic performance of tubercles are enhanced by a propeller slipstream in a similar way that high lift devices, such as trailing edge flaps, are enhanced. This accomplishes the third experimental objective introduced in Section 4.1.1.

Total Lift Coefficient

Figures 4.11 through 4.14 show the total lift coefficient for each tubercle wing with the propeller at the optimal propeller position ($X_\mathrm{p} = 0.25$, $Z_\mathrm{p} = 0$), at $\mathrm{Re} = 1.0 \times 10^5$, 1.5×10^5, 2.0×10^5, and 2.5×10^5, respectively. The results for the SLE wing are provided for comparison. The measurement uncertainty is only shown for $\mathrm{Re} = 2.5 \times 10^5$ to improve the readability of the figures. The scale of the vertical axis is maintained for all figures to allow for comparison across the four Reynolds numbers.

As the Reynolds number increased, the magnitudes of the lift coefficients decreased overall. This was a a result of the change in the propeller thrust with increasing Reynolds number. This phenomenon is discussed in more detail in Appendix B.2. At the lowest Reynolds number of 1.0×10^5, the lift performance of all the tubercles were similar to one another despite their different amplitudes and wavelengths. They all eliminated the sharp decrease in lift coefficient that is expected after stall, creating a lift curve that smoothly transitions from pre-stall to post-stall angles of attack. This is different from the power-off condition shown in Figure 4.6, where the tubercle wings exhibited different stall characteristics, maximum lift coefficients, and stall angles depending on

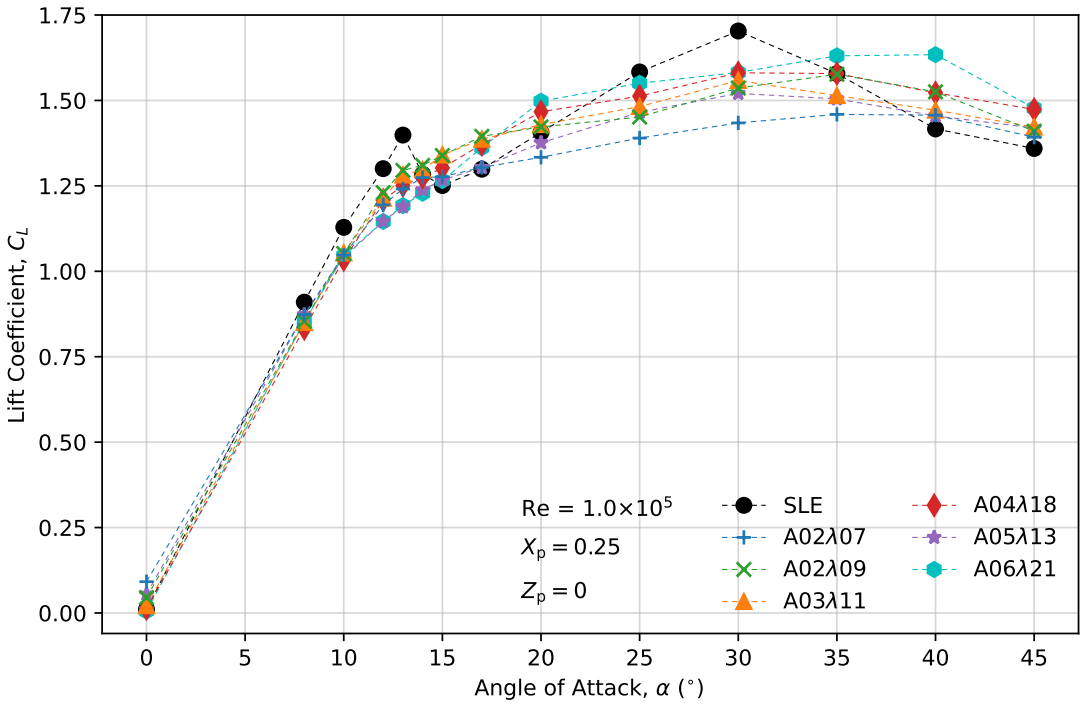

Figure 4.11: Power-on lift coefficients for six tubercle wings with the optimal propeller position at $\mathrm{Re} = 1.0 \times 10^5$.

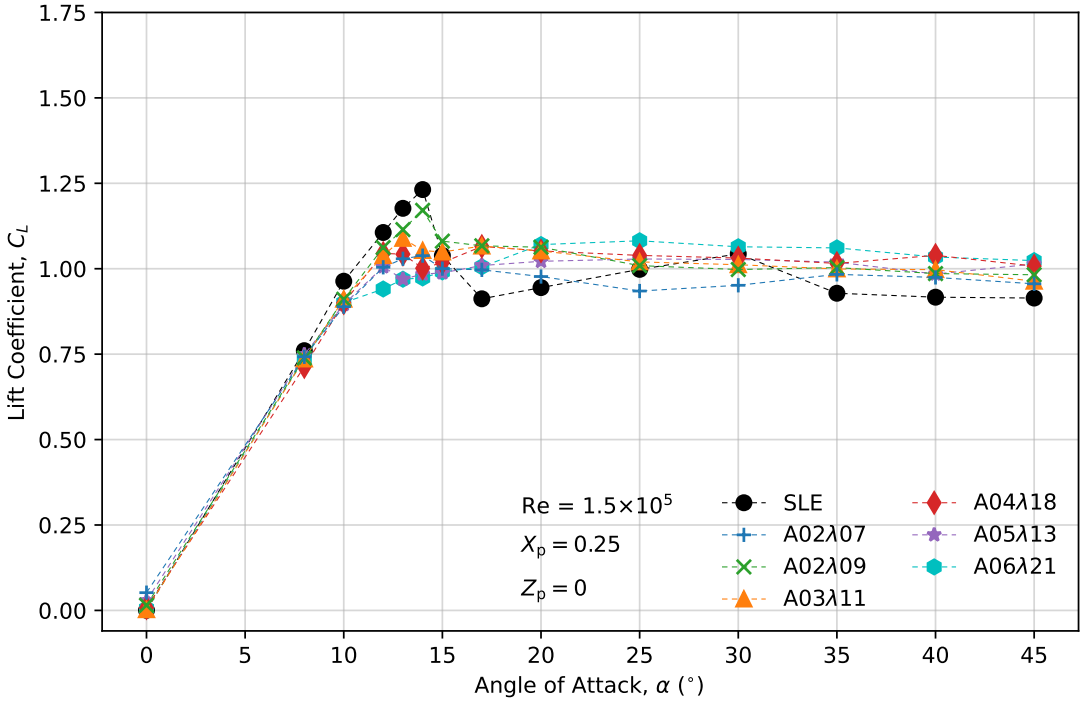

Figure 4.12: Power-on lift coefficients for six tubercle wings with the optimal propeller position at $\mathrm{Re} = 1.5 \times 10^5$.

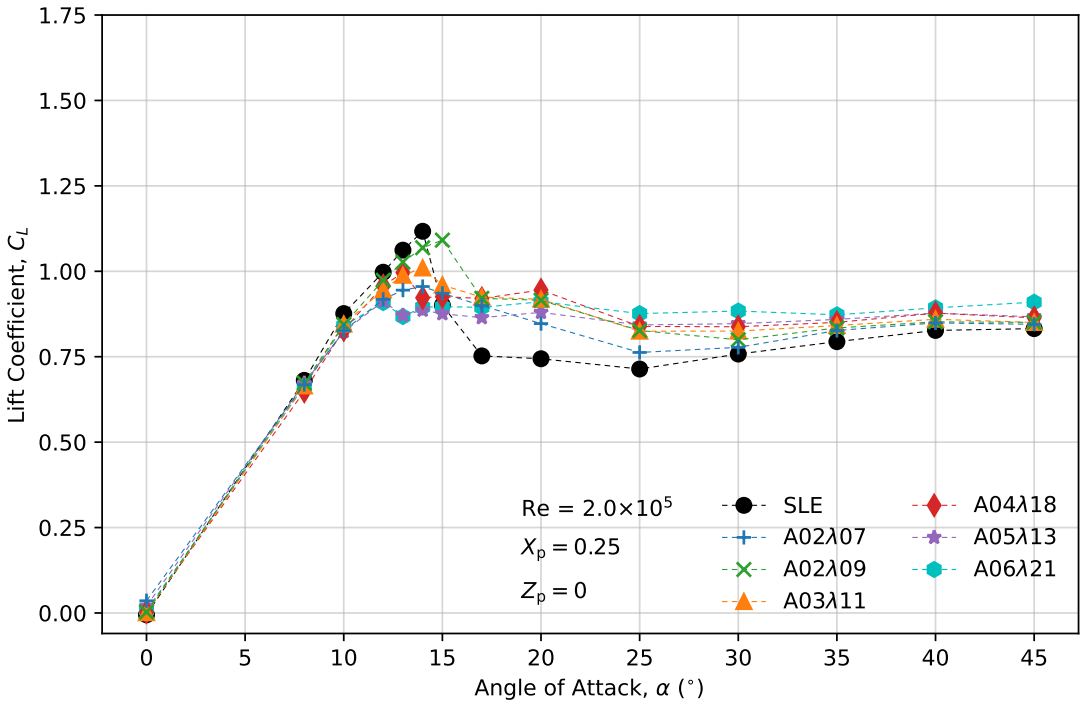

Figure 4.13: Power-on lift coefficients for six tubercle wings with the optimal propeller position at $\mathrm{Re} = 2.0 \times 10^5$.

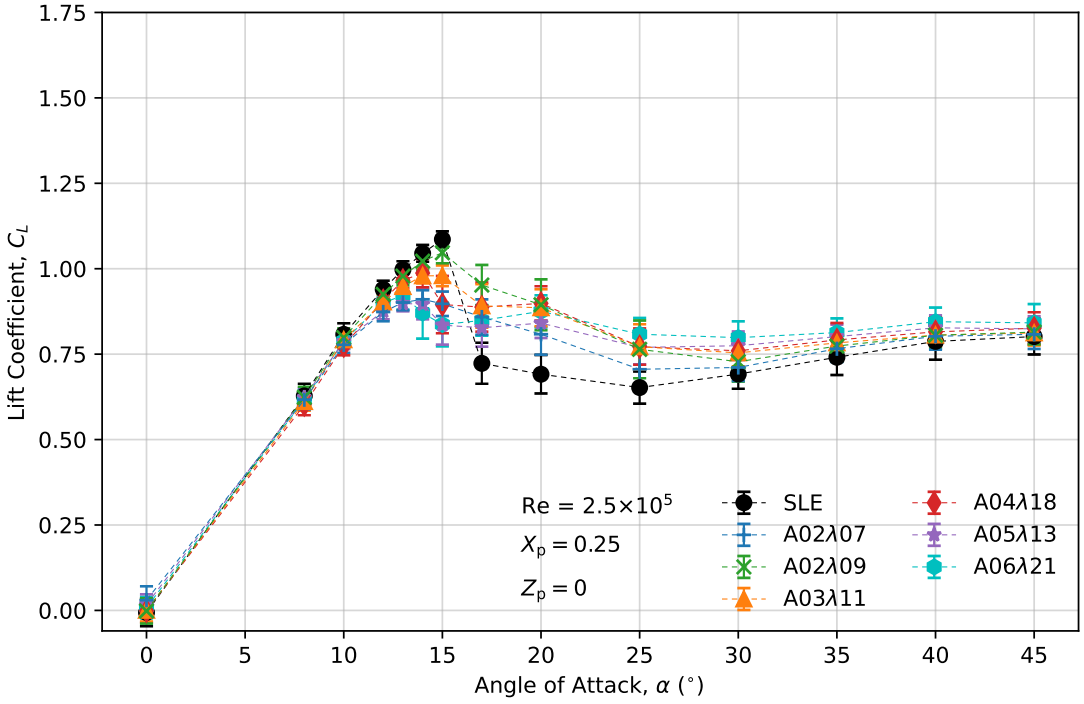

Figure 4.14: Power-on lift coefficients for six tubercle wings with the optimal propeller position at $\mathrm{Re} = 2.5 \times 10^5$.

the tubercle geometry. However, for the power-on condition, small variations in lift performance were still present. These slight differences in the lift performance of each tubercle wing relative to one another remained consistent with the power-off condition. For example, at $\alpha \leq 17^{\circ}$ the A02λ09 wing still produced the greatest lift coefficients, followed by the A03λ11, A04λ18, A02λ07, A06λ21, and finally the A05λ13 wing. This order is identical to the tubercle wings' order of decreasing maximum lift coefficient in Figure 4.6.

Since the propeller rotational rate was maintained at 8000 RPM for all Reynolds numbers, the thrust coefficient of the propeller at the lowest Reynolds number of 1.0×10^5 was the largest, which correlates to faster overall velocities within the propeller slipstream. One of the main mechanisms behind the lift performance of tubercles is the generation of SCRV. The vortex strength and number of vortices per unit span have been shown to depend on tubercle amplitude and wavelength, respectively [39]. This created the differences in lift performance between the tubercle wings for the power-off condition observed in Figure 4.6. The development of the SCRV were likely disrupted by the propeller slipstream at higher thrust coefficients, preventing them from providing any significant benefits. This resulted in the very similar lift performance of all of the tubercle wings. The sections of the wing that existed outside of the propeller slipstream still retained their unique lift performance characteristics that were discussed for the power-off condition, causing the small variations between the tubercle wings seen in Figure 4.11.

For Reynolds numbers of 1.5×10^5, 2.0×10^5, and 2.5×10^5, the lift performance of the tubercle wings were more consistent with the power-off condition. The tubercle wings with the smallest amplitudes showed more abrupt stall characteristics with larger maximum lift coefficients and stall angles, while the tubercle wings with larger amplitudes showed smoother stall characteristics with smaller maximum lift coefficients and stall angles. Figures 4.12 through 4.14 show that the lift performance of the tubercle wings relative to one another were insensitive to the Reynolds numbers for $\mathrm{Re} \geq 1.5 \times 10^5$. For example, the tubercle wings in order of decreasing maximum lift coefficient are the same for $\mathrm{Re} = 1.5 \times 10^5$, 2.0×10^5, and 2.5×10^5. This allows the observations made for one Reynolds number to be representative of the other Reynolds numbers. The results at $\mathrm{Re} = 2.0 \times 10^5$ will be used as this representative Reynolds number and examined in further detail. The relative change in lift coefficient for each tubercle wing with the propeller at the optimal propeller position ($X_\mathrm{p} = 0.25$, $Z_\mathrm{p} = 0$), at a Reynolds number of 2.0×10^5 is presented in Figure 4.15. The SLE wing was used as a baseline for the comparison. The relative change in lift coefficient at $\alpha = 0^{\circ}$ is omitted due to its negligible magnitudes.

The addition of tubercles resulted in up to a 27.0% increase in post-stall lift coefficient at the cost of up to a 19.9% decrease in lift coefficient at pre-stall angles of attack. This was the same general effect that the tubercles had on the power-off condition. When comparing Figure 4.10 and Figure 4.15, apart from the smaller magnitudes in the relative change in lift coefficient for the power-on condition, the tubercle wings with smaller amplitudes appeared to generate less lift in the power-on condition than they did in the power-off condition, while the tubercle wings with larger amplitudes appeared to generate more. This is apparent when examining the two extremes: the A02λ09 wing

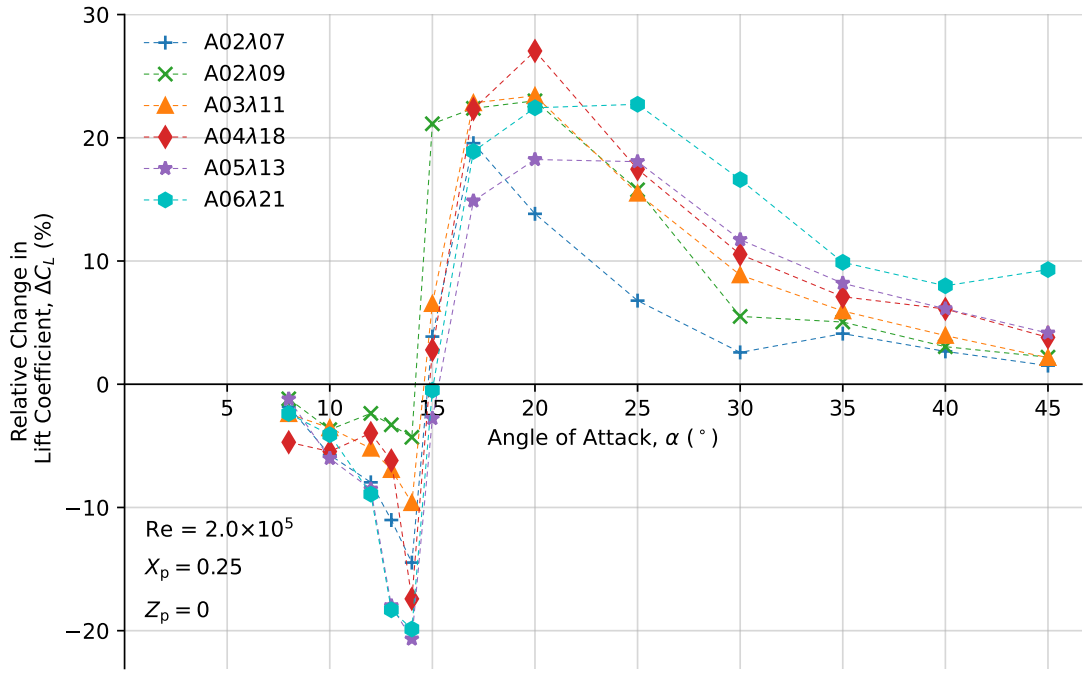

Figure 4.15: Relative change in lift coefficient for each tubercle wing with the optimal propeller position at $\mathrm{Re} = 2.0 \times 10^5$.

and the A06λ21 wing. For the power-off condition the A02λ09 produced the greatest increase in post-stall lift coefficient, while for the power-on condition it is outperformed by both the A04λ18 wing and A03λ11 wing. On the other hand, the A06λ21 wing, which produced the least increase in post-stall lift coefficient for the power-off condition until $\alpha \approx 20°$, was on par with the A03λ11 wing at $\alpha = 20°$ and was the best performing wing for $\alpha \geq 25°$.

As was mentioned for the results at $\mathrm{Re} = 1.0 \times 10^5$ and in Chapter 2, the main mechanism behind the lift modification of tubercles is the generation of SCRV, with the tubercle amplitude dictating the vortex strength, and the wavelength controlling the number of vortices per unit span [39]. The high-swirl environment within the propeller slipstream interferes with the development of these SCRV. For tubercle wings with smaller amplitudes, in other words weaker SCRV, the propeller slipstream may be disrupting the development of the vortices and reducing their effectiveness. The tubercle wings with larger amplitudes apparently generate stronger SCRV that are able to exist despite the propeller swirl, leading to the results in Figure 4.15 favouring the larger amplitude tubercles. This hypothesis is a speculation that requires further investigation. Various flow visualization techniques, such as PIV, pressure sensitive paint, or oil flow visualization could provide the necessary insight into the development of the SCRV in the presence of the propeller slipstream to either confirm or disprove this hypothesis.

Lift Augmentation

The lift augmentation from the propeller slipstream for each tubercle wing was determined using the Equation 3.10, reiterated here:

$$\Delta C_{L_\mathrm{p}} = C_{L_\mathrm{tot}} - C_{L_\mathrm{off}}$$

where ΔC_{L_p} is the calculated lift augmentation, C_{L_tot} is the total lift generated by the wing in the propeller slipstream, and C_{L_off} is the power-off lift coefficient for each respective wing. When comparing the lift augmentation between different tubercle wings, the lift augmentation can be converted to a relative lift augmentation, expressed as a percentage of the power-off lift coefficient:

$$\Delta C_{L_{\mathrm{p},\%}} = \frac{\Delta C_{L_\mathrm{p}}}{C_{L_\mathrm{off}}} \times 100\% \tag{4.3}$$

Figure 4.16 shows the relative lift augmentation for each tubercle wing with the propeller at the optimal position ($X_\mathrm{p} = 0.25$, $Z_\mathrm{p} = 0$), at $\mathrm{Re} = 2.0 \times 10^5$. The relative lift augmentation at $\alpha = 0°$ was omitted due to the negligible magnitudes of the power-off lift coefficient. Results for the SLE wing are also provided for comparison.

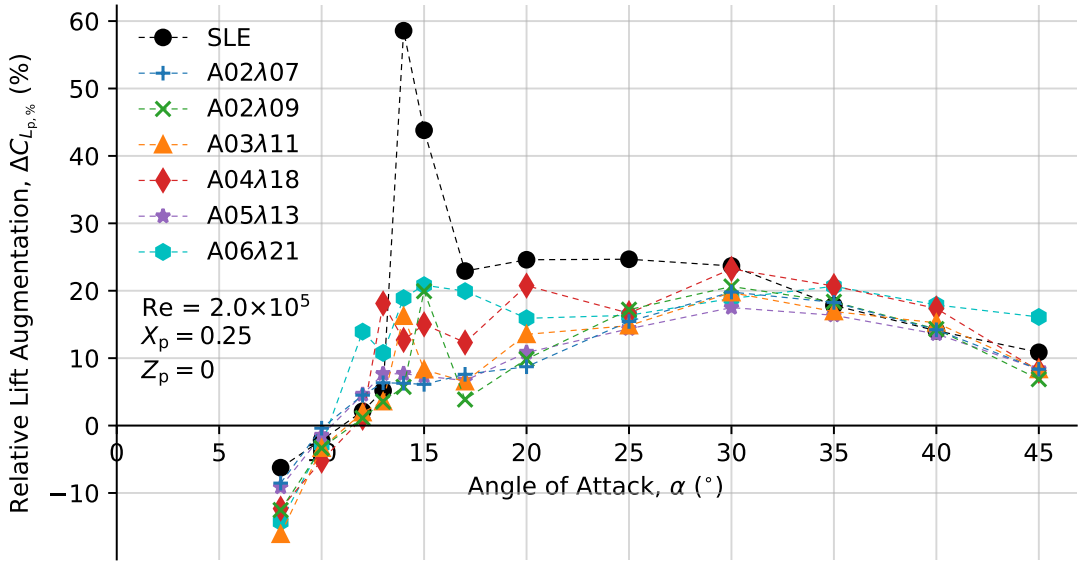

Figure 4.16: Relative lift augmentation of each wing with the propeller at the optimal position at $\mathrm{Re} = 2.0 \times 10^5$.

A Reynolds number of 2.0×10^5 was selected as a representative Reynolds number since the lift augmentation is calculated using the total lift coefficient and power-off lift coefficient, both of which were discussed using the results at $\mathrm{Re} = 2.0 \times 10^5$. The equivalent Figures for $\mathrm{Re} = 1.0 \times 10^5$, 1.5×10^5, and 2.5×10^5 can be found in Appendix C. The large peak in the lift augmentation for the SLE wing at 14° was a result of SLE wing stalling in the power-off condition. Figure 4.16 shows that the majority of the tubercle wings generated less lift augmentation than the SLE wing over the majority of the angles of attack investigated. This does not necessarily equate to less total lift generated. The power-off lift coefficients for the tubercle wings were shown to be much greater

than the SLE wing at post-stall angles of attack in Figures 4.6 through 4.9. This means that even with a smaller relative lift augmentation, the absolute lift augmentation and resulting total lift coefficients of the tubercle wing could be greater than that of the SLE wing, which is the case for post-stall angles of attack as shown in Figures 4.11 through 4.14. However, Figure 4.16 does demonstrate that tubercles do not experience further aerodynamic enhancement by the propeller slipstream (such as the lift enhancement of trailing edge flaps when placed in a propeller slipstream).

This is supported by the lift augmentation scores (LAS) for each tubercle wing. Equation 4.2 was used to calculate the LAS of each wing using the same weightings as presented in Table 4.3. In this case, the LAS is equivalent to taking the weighted area underneath the curves in Figure 4.16. It is important to realize that this score does not describe the total lift performance of the wing, but only represents the total lift augmentation for a given wing and propeller configuration. In other words, the LAS indicates how much the lift performance of a wing benefits from the propeller slipstream. Table 4.5 shows the calculated LAS for each wing at $\mathrm{Re} = 2.0 \times 10^5$.

Table 4.5: Lift augmentation score for each tubercle wing with the propeller at the optimal location at $\mathrm{Re} = 2.0 \times 10^5$.

Wing	LAS
SLE	1.49
A02λ07	0.66
A02λ09	0.54
A03λ11	0.37
A04λ18	0.83
A05λ13	0.60
A06λ21	0.96

The SLE wing had the largest LAS of 1.49, meaning that it gained the most lift augmentation from the propeller slipstream. In general, tubercle wings with larger amplitudes resulted in greater LAS. It is clear that the addition of tubercles, and therefore the generation of SCRV, reduced the effectiveness of the propeller slipstream in providing lift augmentation. The decreasing LAS with decreasing tubercle amplitude suggests that the strength of the SCRV affects the propeller slipstream. Smaller tubercle amplitudes equates to weaker counter-rotating streamwise vortex strengths that are more prone to vortex bursting. There are two criteria for vortex bursting to occur according to Chang [77]: an adverse pressure gradient along the rotational axis of the vortex and a low total pressure within the vortex core. The adverse pressure gradient in the aft segment of the wing coupled with the weaker vortex strengths from smaller amplitudes satisfy these two criteria. When the vortex bursts the flow structure changes drastically, expanding into a bubble-like structure with a deceleration of flow [77, 78]. This could act as a blockage to the propeller slipstream, reducing the effectiveness of the lift augmentation. The larger tubercle amplitudes generate stronger SCRV that would be more resilient to vortex bursting, explaining their improved lift augmentation compared to the smaller amplitudes. Definitive conclusions on the exact interactions between the SCRV and the propeller slipstream cannot be drawn from these results, and require further investigation.

Based on the results presented in this chapter, for the power-off condition, tubercle wings with smaller amplitudes generate the largest increase in lift coefficient at post-stall angles of attack for the smallest decrease in lift coefficient at pre-stall angles of attack. This was demonstrated by the lift performance of the A02λ09 wing shown in Figure 4.8. Increasing the tubercle amplitude resulted in a smoother stall characteristic at the cost of reduced maximum lift coefficient and stall angle. This was demonstrated by the lift performance of the A06λ21 wing in Figure 4.8. When tubercle wings were placed within a propeller slipstream, the slipstream itself was suspected to interfere with the development of the SCRV. For this reason, the tubercle wings with slightly larger amplitudes, such as the A03λ11 wing and the A04λ18 wing, with apparently stronger SCRV performed better, as shown in Figure 4.15. This interaction between the SCRV and the propeller slipstream was also suspected to reduce the effectiveness of the lift augmentation provided by the slipstream. In the context of tilt-wing transition, when only concerned with the lift performance of the wing, tubercles with amplitudes large enough to generate SCRV of adequate strength to develop despite interference from the propeller slipstream are most desirable, such as the A03λ11 wing or the A04λ18 wing. While never the best performing wings, both of these geometries provided consistent benefits at post-stall angles of attack with minimal penalties in lift performance at pre-stall angles of attack. The results presented here were only concerned with the lift performance of each tubercle wing, since lift was identified as the most important aerodynamic parameter for tilt-wing transition. Drag, moment and aerodynamic efficiency were also measured and are presented in Appendix C.

These results can be extended by exploring the design of a wing with tubercles. Incorporating tubercles into the design process of the wing could allow for more effective use of the tubercles by accounting for geometric twist, segments of the wing that exist outside of the propeller slipstream, and the drag performance of the tubercles as well. This future work could involve the optimization of the distribution and geometry of tubercles along the span of the wing.

5 Effect of Tubercles on Transition

This chapter presents the development of a numerical simulation of VTOL transition with sinusoidal leading edge tubercles and application to a representative VTOL unmanned aerial vehicle (UAV), followed by a discussion of the simulation results. The high angles of attack experienced by a VTOL aircraft as it transitions between forward and vertical flight are well-suited for tubercles, which were shown to significantly enhance the post-stall lift of a propeller blown lifting surface in Chapter 4. This chapter will demonstrate the effect of sinusoidal leading edge tubercles on VTOL aircraft by numerically investigating how the enhanced post-stall lift modifies the transition corridor. The investigation involves the design of a UAV capable of VTOL, the simulation of its transition corridor with an analytical model, and an empirical correction factor based on the experimental data obtained in Chapter 4 to simulate the effect of tubercles on the transition corridor.

5.1 Design of the RMC TRV

To investigate the effect of tubercles on VTOL transition a small scale UAV, henceforth referred to as the RMC Transition Research Vehicle (RMC TRV), was developed. This section describes the design of the RMC TRV, a computer aided design (CAD) model of which is shown in Figure 5.1.

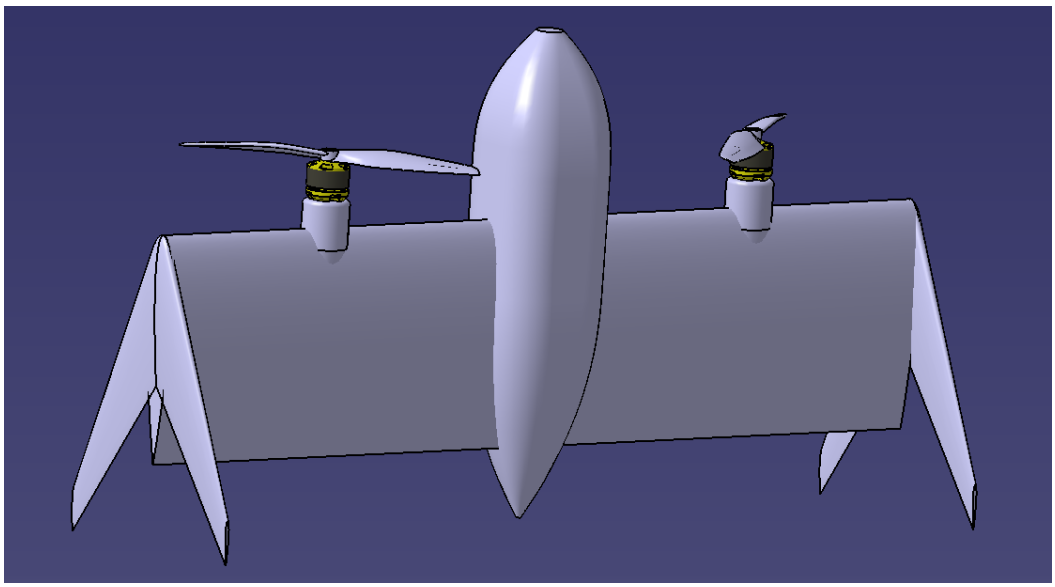

Figure 5.1: CAD model of the RMC TRV.

5.1.1 Design Overview

Figure 5.2 is a three view drawing of the RMC TRV that was designed as a practical analogue to the experimental setup used in the experimental wind tunnel campaign presented in Chapter 4. It uses a tail sitter configuration in place of a tilt-wing configuration. The aerodynamic environment of the wing of a tail sitter and tilt-wing are similar, since both must tilt from an angle of attack of 0° to 90° as the aircraft transitions from forward flight to vertical flight, and both wings exist in the presence of a propeller slipstream. A tail sitter configuration distinguishes itself from a tilt-wing configuration in its simplicity. A complex wing tilt mechanism is not needed since the entire aircraft is rotated through transition rather than just the wing. In addition, while the wing tilt angle and the fuselage angle of attack can be different for a tilt-wing aircraft, the wing is fixed relative to the fuselage at the wing installation angle for a tail sitter. This means that wing tilt angle and aircraft angle of attack do not change relative to one another, eliminating a degree of freedom making it an ideal configuration for this application.

Figure 5.2: Three view drawing of the RMC TRV. All dimensions given in mm.

The dimensions of the RMC TRV were selected to remain consistent with the experimental setup used in Chapter 4. The same NACA 0018 airfoil was used for the wing with the same chord length of 0.1524 m. A larger span of 0.6 m (as opposed to 0.4572 m in the experimental setup) was required to accommodate a fuselage section to house electronic components required for flight. Swept lifting surfaces consisting of a NACA 0009 profile were placed at the wing tips to provide lateral stability and act to as the landing gear. Their placement at the wing tips also served to reduce 3D effects, similar to the function of the elliptical end plates used in the experimental setup. The large

sweep allowed for adequate ground clearance. Other design features and key dimensions of the RMC TRV are summarized in Table 5.1. With these selected dimensions, the wing of the RMC TRV was expected to experience a very similar aerodynamic environment to the experimental setup used in Chapter 4.

Table 5.1: Summary of the design of the RMC TRV.

	Parameter	Symbol	Value	Units
Wing	Airfoil	-	NACA 0018	-
	Chord	c_{w}	0.1524	m
	Span	b_{w}	0.6000	m
	Area	S_{w}	0.0914	m^2
	Installation angle	$\theta_{0,\mathrm{w}}$	2	$^\circ$
Vertical Tails	Airfoil	-	NACA 0009	-
	Root chord	c_{v}	0.1000	m
	Taper ratio	-	0.3	-
	Span	b_{v}	0.1750	m
	Leading edge sweep	Λ_{v}	65	$^\circ$
	Total tail area	S_{v}	0.0240	m^2
Fuselage	Length	l_{f}	0.3210	m
	Maximum height	h_{f}	0.0800	m
	Maximum width	b_{f}	0.0800	m

5.1.2 Weight and Balance

For this work, the transition of the RMC TRV was only simulated using an analytical model, but was designed with the intent of real world flight testing in the future. This entailed the selection and integration of electronic components required for the telemetry system and a flight controller. Table 5.2 shows the selected electronic components and their mass, measured using a *Mettler Toledo AE160* digital analytical balance.

The RMC TRV structure had three components: the fuselage, the wing, and the vertical tail. The fuselage was assumed to be 60 g with its centre of gravity (CG) located at 14% of the wing chord, the wing was assumed to be 100 g with its CG located at 40% of the wing chord, and the vertical tail was assumed to be 80 g with its CG located at 66% of the wing chord. These masses were estimated based on rapid prototypes manufactured using 3D printing, and the locations of each respective CG was estimated using an analysis tool built into the CAD program used to model the RMC TRV. The total mass of the RMC TRV is estimated to be approximately 750 g. The values in Table 5.2 were referenced when positioning each component to control the location of the overall CG for the completed UAV. The component that influenced the location of the CG the most was the lithium polymer (LiPo) battery, which was placed in the nose of the fuselage. To facilitate easy adjustment and fine tuning of the longitudinal location of the CG, extra space was included in the nose segment, which allowed for the battery to be moved forward or aft, or the installation of a larger or smaller battery.

Table 5.2: Mass of electronic components for the RMC TRV required for flight.

Qty	Component	Mass (g)
1×	*Holybro Pixhawk 4* flight controller	48.72
1×	*Holybro SiK* telemetry radio	25.51
1×	*Pixhawk 4 Neo M8N* GPS module	32.73
1×	1500 mAh LiPo battery	148.14
1×	*Holybro PM06 V2* power module	47.61
1×	*EXT-8P-V1.0* power management board	7.39
2×	*Hobbypower Simonk* 30A ESC	26.92
2×	*Sunnysky X2208-15* electric motor	49.95
2×	*APC* 8×4.5MR propeller	8.94
2×	*Longrunner LKY61* micro servo	11.58
1×	*Spektrum AR410* radio receiver	8.21
	Total mass	513.09

Figure 5.3 presents a schematic diagram showing the longitudinal and vertical location of the overall CG. The components were placed symmetrically to set the lateral location of the overall CG (not shown in Figure 5.3) at the aircraft's centreline. The relative positions of the wing and vertical tail aerodynamic centres are also provided. The wing aerodynamic centre (AC) was assumed to be at 25% of the wing chord, and the vertical tail AC was assumed to be at 25% of its mean aerodynamic chord.

Figure 5.3: Longitudinal and vertical location and relative locations of the wing and vertical tail AC (all dimensions given in mm).

5.1.3 Longitudinal and Lateral Static Stability

Based on the estimated longitudinal CG location and as shown in Figure 5.3, the CG of the RMC TRV is expected to be 0.2955 m forward of the wing AC. If the aerodynamic forces generated by the fuselage and the contribution of the rotating propellers are ne-

glected, the stick-fixed neutral point is identical to the aerodynamic centre of the wing and the static margin for the RMC TRV is predicted to be 19%, which is well above the recommended minimum for good handling qualities of 5% [79]. While a static margin of 19% appears to be very large, contributions from the rotating propellers and small vertical offset of the line of thrust to the CG are expected to reduce the static margin.

The largest contributor in dictating the lateral static stability of the RMC TRV is the vertical tail. Equation 5.1 provides an expression for the contribution of the vertical tail to the yaw stability derivative, $C_{n,\beta}$ [79]:

$$C_{n,\beta} = \kappa_{\mathrm{v}} \frac{S_{\mathrm{v}} l_{\mathrm{v}}}{S_{\mathrm{w}} b_{\mathrm{w}}} C_{L_{\mathrm{v}},\alpha} \left(1 - \epsilon_{s,\beta}\right) \tag{5.1}$$

where κ_{v} is the ratio of the dynamic pressure at the vertical tail to the dynamic pressure at the wing, S_{v} is the planform area of the vertical tail, l_{v} is the distance from the AC of the vertical tail to the overall CG, S_{w} is the planform area of the wing, b_{w} is the wing span, $C_{L_{\mathrm{v}},\alpha}$ is the lift curve slope of the vertical tail, and $\epsilon_{s,\beta}$ is the sidewash gradient. For simplicity of calculation, the dynamic pressure ratio, κ_v, was assumed to be 1.0, the lift curve slope of the vertical tail, $C_{L_{\mathrm{v}},\alpha}$, was assumed to be 2π, and the sidewash gradient, $\epsilon_{s,\beta}$ was assumed to be 0. With these assumptions, Equation 5.1 simplifies to:

$$C_{n,\beta} = 2\pi \frac{S_{\mathrm{v}} l_{\mathrm{v}}}{S_{\mathrm{w}} b_{\mathrm{w}}} \tag{5.2}$$

Using the geometric properties of the vertical tail provided in Table 5.1 and the distance from the CG to the AC of the vertical tail provided in Figure 5.3, the RMC TRV has an estimated yaw stability derivative of 0.27, which is an acceptable value according to Phillips [79].

With the presented design, the RMC TRV has been shown to be statically stable in both longitudinal and lateral axes. However, since the RMC TRV does not possess a horizontal tail, it suffers from the same problem as flying wing configurations. While it possess longitudinal static stability, stable trim cannot be maintained, necessitating the need for a stability augmentation system. The proposed *Holybro Pixhawk 4* flight controller satisfies this need since it is capable of active stabilization in flight [80].

5.2 Modelling the Transition Corridor

As first introduced in Chapter 1, the transition of a VTOL aircraft is characterized by a transition corridor. A transition corridor provides the forward flight speeds achievable by the VTOL aircraft for a given wing tilt (or in the case of tail sitter configurations, aircraft tilt) angle. An example of a transition corridor was presented in Figure 1.1. Defining features of a transition corridor are the left and right bounds created by the minimum and maximum allowable flight speeds. Figure 5.4 shows a free-body diagram of the RMC TRV used to model the transition corridor. T is the thrust generated by the propeller, C_{N} is the propeller normal force, L_{w} and D_{w} are the lift and drag generated by the propeller blown wing, α is the tilt angle of the RMC TRV, and W_{tot} is the total weight.

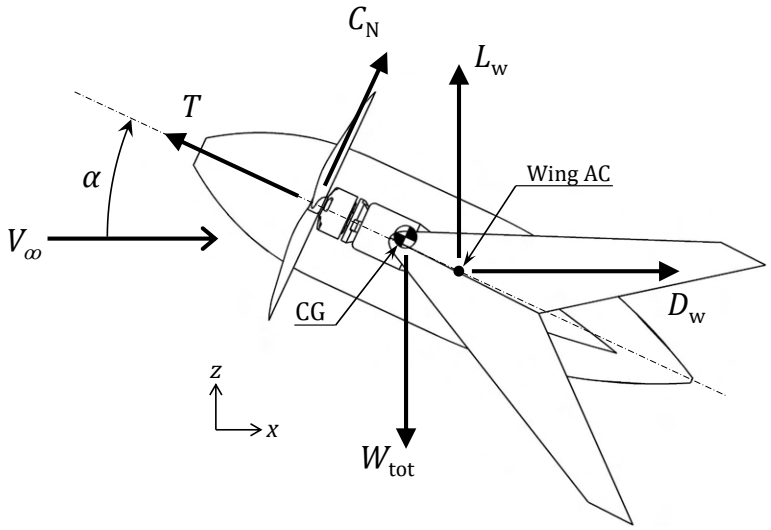

Figure 5.4: Free-body diagram of the RMC TRV used to determine the transition corridor.

The minimum and maximum flight speeds can be calculated using a simple force balance in the vertical and longitudinal directions, as described by the following equations:

$$\begin{aligned} \sum F_x &= -T\cos\alpha + C_N \sin\alpha + D_w = 0 \\ \sum F_z &= T\sin\alpha + C_N \cos\alpha + L_w - W_{tot} = 0 \end{aligned} \tag{5.3}$$

The maximum flight speed is more dependant on an accurate thrust model, which was not developed as part of this method. The results presented in this chapter are focused on the effect of tubercles on the minimum required flight speed. The weight of the RMC TRV is known based on the provided mass of the electronic components (Table 5.2) and the assumed mass of the structure. The thrust was assumed to be constant and equal to the weight of the RMC TRV during the entirety of transition. This leaves only the aerodynamic forces as unknowns. The following subsection presents the aerodynamic model used to obtain these aerodynamic forces.

5.2.1 Aerodynamic Model

An analytical model for estimating the aerodynamic forces of a propeller blown wing developed by Jameson was used [56]. According to Jameson, the total lift and drag generated by a propeller blown wing is given by the following equations [56]:

$$\begin{aligned} C_L &= C_{L_w} + C_{L_T} + C_{L_N} \\ C_D &= C_{D_w} + C_{D_T} + C_{D_N} \end{aligned} \tag{5.4}$$

where C_L and C_D are the total lift and drag coefficients, C_{L_w} and C_{D_w} are the contributions of the wing, C_{L_T} and C_{D_T} are the contributions from the propeller thrust, and C_{L_N} and C_{D_N} are the contributions of the propeller normal forces.

The contributions of the wing are obtained by first dividing the wing planform into segments that exist inside the propeller slipstream, which will be referred to as the

blown segments, and segments that exist outside the propeller slipstream, which will be referred to as unblown segments. The aerodynamic coefficients for the blown segments, C_{L_j} and C_{D_j}, and the unblown segments, C_{L_u} and C_{D_u}, are estimated separately. The estimated coefficients are then combined using the Equation 5.5 to obtain the overall contribution of the propeller-wing combination:

$$\begin{aligned} V^2 S C_{L_\mathrm{w}} &= \left(S - \sum_{\text{props}} S_\mathrm{j}\right) V^2 C_{L_\mathrm{u}} + \sum_{\text{props}} S_\mathrm{j} V_\mathrm{j}^2 \left(C_{L_\mathrm{u}} \cos\epsilon - C_{D_\mathrm{j}} \sin\epsilon\right) \\ V^2 S C_{D_\mathrm{w}} &= \left(S - \sum_{\text{props}} S_\mathrm{j}\right) V^2 C_{D_\mathrm{u}} + \sum_{\text{props}} S_\mathrm{j} V_\mathrm{j}^2 \left(C_{L_\mathrm{u}} \sin\epsilon - C_{D_\mathrm{j}} \cos\epsilon\right) \end{aligned} \tag{5.5}$$

where S is the total planform area of the wing, $\sum_{\text{props}} S_\mathrm{j}$ is the planform area of all the blown segments combined, V is the freestream velocity, V_j is the velocity within the propeller slipstream, and ϵ is the effective angle of attack of the blown segments. Further details on this method with full equations for C_{L_u}, C_{D_u}, C_{L_j}, C_{D_j}, C_{L_p}, C_{D_p}, C_{L_N} and C_{D_N} can be found in reference [56], where the complete method is well explained and documented. An example of the implementation of this method by a third party is also demonstrated by Bronz and Drouin [81].

Figure 5.5 shows the lift and drag coefficients with respect to angle of attack of the propeller and wing of the RMC TRV as predicted using Jameson's method for $\mathrm{Re} = 1.6 \times 10^5$. As described by Equation 5.4, these coefficients included the thrust generated by the propeller as well as the propeller normal forces, explaining the large negative drag coefficients and allowing Equation 5.3 to be reduced to:

$$\begin{aligned} \sum F_x = D_\mathrm{tot} = \frac{1}{2}\rho V^2 S_\mathrm{w} C_D = 0 \\ \sum F_y = L_\mathrm{tot} - W = \frac{1}{2}\rho V^2 S_\mathrm{w} C_L - W = 0 \end{aligned} \tag{5.6}$$

where C_L and C_D are the coefficients obtained from Figure 5.5.

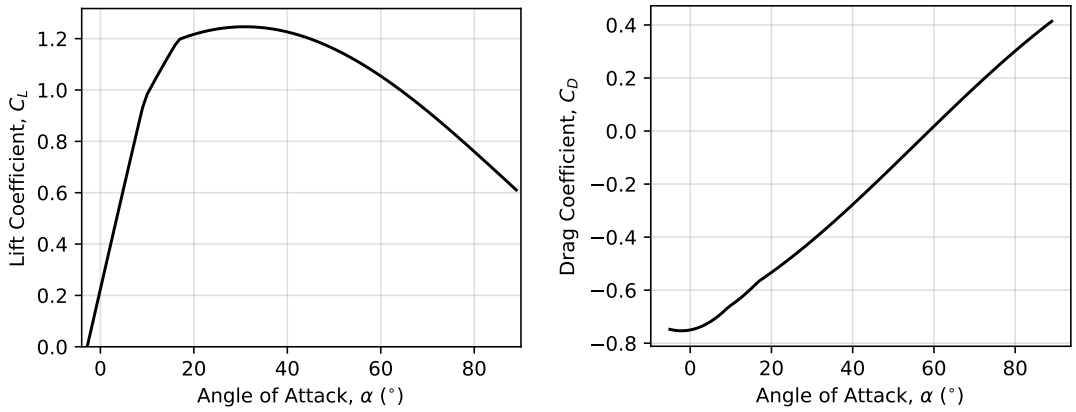

(a) Lift coefficient.

(b) Drag coefficient.

Figure 5.5: Total aerodynamic coefficients of the RMC TRV predicted by Jameson's analytical model.

5.3 Empirical Tubercle Model

The flow physics and mechanisms behind the lift enhancing effect of tubercles are highly unsteady and 3D, making obtaining accurate results with numerical simulations difficult. The presence of a propeller slipstream as well as the fact that most of the lift enhancing effect offered by tubercles occurs post-stall adds further complexity to simulating tubercles. For this reason, to investigate the effect of tubercles on the transition corridor of the RMC TRV, an empirical correction factor to the forces obtained using the presented aerodynamic model was applied. The geometry and aerodynamic design of the RMC TRV was conceptualized to closely resemble the experimental setup used in Chapter 4, allowing for empirical relationships obtained using the experimental data of Chapter 4 to better represent the application of tubercles on the RMC TRV.

As shown in Chapter 4, tubercles have a much more significant impact on the lift performance of the wing than on the drag coefficient. Furthermore, while any changes in the drag performance of the wing would effect the right bound of the transition corridor (maximum speed), changes in the lift performance of the wing are directly linked to the left bound (minimum speed), which is of more interest to the objective of this thesis. For these reasons, an empirical model was only developed for the lift coefficient of the tubercle wings.

The total lift generated by a propeller blown wing with tubercles can be expressed as a lift component of an equivalent SLE wing, plus a change in lift caused by the addition of tubercles. This is described by the following equation:

$$C_{L_{\text{tot}}} = C_{L_{\text{SLE}}} + C_{L_{\text{tbr}}} \tag{5.7}$$

where $C_{L_{\text{tot}}}$ is the total lift coefficient, $C_{L_{\text{SLE}}}$ is the lift coefficient of the equivalent SLE wing, obtained using the aerodynamic model presented in Section 5.2.1, and $C_{L_{\text{tbr}}}$ is the lift enhancement due to the addition of tubercles. If $C_{L_{\text{tbr}}}$ is expressed as a relative change in lift coefficient with respect to the SLE wing, the experimental results of Chapter 4 for each tubercle geometry can be used:

$$C_{L_{\text{tbr}}} = C_{L_{\text{SLE}}} \Delta C_{L_{\text{tbr}}} \tag{5.8}$$

where $\Delta C_{L_{\text{tbr}}}$ is expressed as a percentage of $C_{L_{\text{SLE}}}$, and is equivalent to the relative change in lift coefficient for each tubercle geometry for the power on condition shown in Figure 4.15. An empirical equation can be obtained to describe $\Delta C_{L_{\text{tbr}}}$ depending on the tubercle geometry by fitting an equation to the experimental data from Chapter 4.

The behaviour of the relative change in lift coefficient has a distinct discontinuity at the stall angle, after which the tubercle wings were shown to provide significant lift enhancement. To accommodate this discontinuity, two different models were developed: a pre-stall model and a post-stall model.

5.3.1 Pre-Stall Model

The relative change in lift coefficient for pre-stall angles of attack were observed to follow a linear trend, with the relative change in lift coefficient decreasing with increasing angle

of attack from approximately 8° until the stall angle. Equation 5.9 describes this linear trend:

$$\Delta C_{L_{\text{tbr}}} = K_A \alpha + K_B \quad \text{for: } \alpha \in \left[-\frac{K_B}{K_A}, \alpha_s \right] \tag{5.9}$$

The coefficients K_A and K_B varied depending on the tubercle geometry, and were selected to minimize the root mean square error (RMSE) of the empirical fit to the experimental data. It is important to note that Equation 5.9 is only valid between the angle of attack at which ΔC_L is predicted to be 0, $-\frac{K_B}{K_A}$, and the stall angle, α_s. The values used for K_A and K_B for all tubercle wings tested can be found in Table 5.3.

Table 5.3: Summary of empirical fit coefficients for the pre-stall model for each tubercle wing at $\text{Re} = 2.0 \times 10^5$.

Wing	K_A	K_B	R^2
A02λ07	-113.16	14.31	0.9613
A02λ09	-21.50	1.31	0.5480
A03λ11	-64.50	7.29	0.9029
A04λ18	-83.77	9.12	0.3984
A05λ13	-185.54	26.04	0.9033
A06λ21	-178.98	24.90	0.8778

5.3.2 Post-Stall Model

A general form of the equation describing the relative change in lift coefficient for the tubercle wings is:

$$\Delta C_{L_{\text{tbr}}} = K_1 + K_2 \sin\left(K_3 \sqrt{\alpha - \alpha_s} + \frac{K_2 \sin\left(K_4 \sqrt{\alpha - \alpha_s}\right)}{K_5} \right) + \frac{K_6}{1 + 20 e^{-K_7(\alpha - 2\alpha_s)}}$$
$$\text{for: } \alpha \in (\alpha_s, 45] \tag{5.10}$$

The coefficients K_n, where $n = \{1, 2, 3, 4, 5, 6\}$ and 7, varied depending on the tubercle geometry, and were selected to minimize the RMSE of the empirical fit to the experimental data. Equation 5.10 is only valid between the stall angle and 45°. Figure 5.6 shows an example of both the post-stall and pre-stall models applied to the A03λ11 tubercle geometry at $\text{Re} = 2.0 \times 10^5$. The values used for K_n (for $n = \{1, 2, 3, 4, 5, 6, 7\}$) for all tubercle wings tested can be found in Table 5.4.

5.3.3 Selection of Coefficients

The following minimization problem was solved to obtain the optimal coefficients for the pre-stall empirical model:

$$\begin{aligned} \text{minimize:} \quad & f(x) = \sqrt{\frac{\sum_{i=1}^{5} \left(\Delta C_{L_{\text{tbr}}} - \Delta C_{L_{\text{exp}}} \right)_i^2}{5}} \\ \text{w.r.t:} \quad & x = (K_A, K_B)^T \end{aligned} \tag{5.11}$$

Table 5.4: Summary of empirical fit coefficients for the post-stall model for each tubercle wing at $\mathrm{Re} = 2.0 \times 10^5$.

Wing	K_1	K_2	K_3	K_4	K_5	K_6	K_7	R^2
A02λ07	-15.79	31.58	1.01	2.62	15.78	9.54	8.02	0.9280
A02λ09	-3.47	28.51	-1.61	1.95	6.76	9.18	6.67	0.9710
A03λ11	-11.08	32.88	0.62	2.07	13.68	9.98	9.00	0.9589
A04λ18	-19.39	42.87	-0.48	1.86	13.80	10.24	9.60	0.9584
A05λ13	-20.65	37.66	-1.99	2.90	16.55	9.86	9.68	0.9754
A06λ21	-19.00	42.10	4.76	-0.30	15.00	13.66	16.77	0.9042

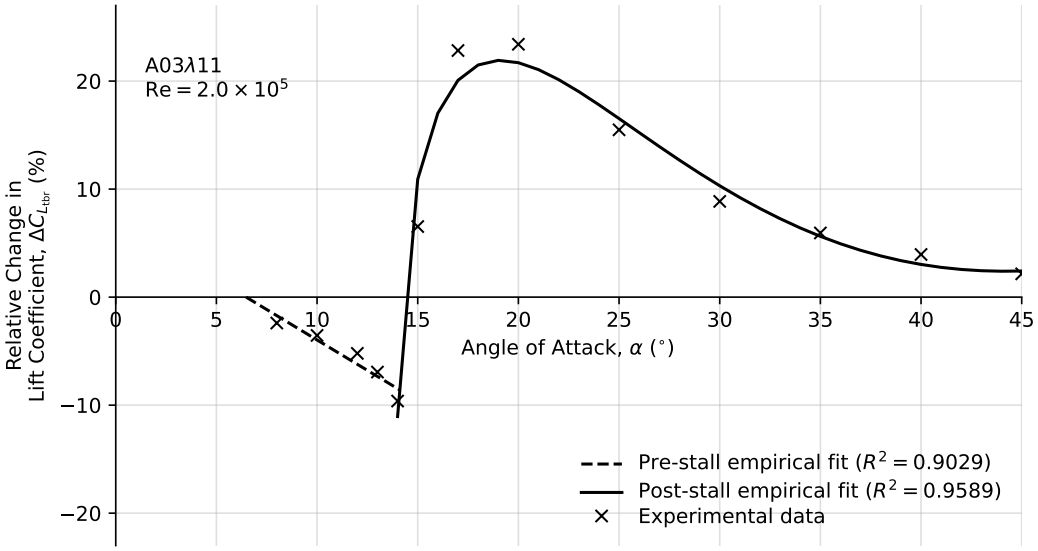

Figure 5.6: Empirical pre-stall and post-stall model for the A03λ11 geometry.

The index i denotes an angle of attack between 8° ($i = 1$) and 14° ($i = 5$), following the angles of attack tested during the experimental campaign as presented in Table 4.2. $\Delta C_{L_{\mathrm{tbr}}}$ is the relative change in lift coefficient calculated using Equation 5.9, and $\Delta C_{L_{\mathrm{exp}}}$ is the experimental relative change in lift coefficient. The fitness function, $f(x)$, is simply the RMSE between the empirical fit and experimental data.

Similarly, the following minimization problem was solved to obtain the optimal coefficients for the post-stall model:

$$\begin{aligned} \text{minimize:} \quad & f(x) = \sqrt{\frac{\sum_{i=1}^{9} \left(\Delta C_{L_{\mathrm{tbr}}} - \Delta C_{L_{\mathrm{exp}}}\right)_i^2}{9}} \\ \text{w.r.t:} \quad & x = (K_1, K_2, K_3, K_4, K_5, K_6, K_7)^T \end{aligned} \tag{5.12}$$

The index i for the post-stall minimization problem denotes an angle of attack of 14° ($i = 1$) through 45° ($i = 9$), following the angles of attack tested during the experimental campaign as presented in Table 4.2. The fitness function, $f(x)$, is the same as presented in Equation 5.11, but with $\Delta C_{L_{\mathrm{tbr}}}$ calculated using Equation 5.10 in place of Equation 5.9.

In both cases a Broyden-Fletcher-Goldfarb-Shanno minimization algorithm (BFGS) was used with a convergence tolerance of 1.0×10^{-4} [82]. This process was completed for each tubercle geometry at a Reynolds number of 100 000, 150 000, 200 000, and 250 000, resulting in an equation to describe the effect of each tubercle geometry on the lift coefficient of the RMC TRV at different points in its transition corridor. As an example, Tables 5.3 and 5.4 summarize the resulting coefficients for the pre-stall and post-stall models, respectively, at $\mathrm{Re} = 2.0 \times 10^5$. The pre-stall model for the A02λ09 and A04λ18 tubercles showed poor coefficients of determination, indicating a poor fit. This was considered when analyzing the resulting effects on the transition corridor, but was not critical to this analysis as the effect of tubercles is more significant at post-stall angles. This empirical model was only applied to the lift coefficient of the wing.

5.4 Results and Discussion

This section presents the results of the simulated transition corridor of the RMC TRV with and without sinusoidal leading edge tubercles. First the predicted transition corridor of the RMC TRV with the SLE will be presented, followed by the results with the empirical tubercle model. All of the transition corridors presented in this section are described by the vehicle tilt angle, θ_f, on the vertical axis, and the forward flight speed, V, on the horizontal axis. The vehicle tilt angle is given by the addition of the angle of attack, α, and the wing installation angle, $\theta_{0,\mathrm{w}}$:

$$\theta_\mathrm{v} = \alpha + \theta_{0,\mathrm{w}} \tag{5.13}$$

When describing the changes in the transition corridor between the RMC TRV with a straight leading edge and tubercles, the transition corridor will be described to contract when the minimum required forward flight speed increases, and expand when the minimum required forward flight speed decreases. The desirable result is the expansion of the transition corridor.

5.4.1 Transition Corridor with Straight Leading Edge

Figure 5.7 presents the transition corridor of the RMC TRV with the SLE. The grey region indicates the transition corridor itself. The left bound indicates the minimum required forward flight speed, with the region to the bottom left of this bound indicating forward flight speeds for which the RMC TRV cannot generate sufficient lift to support its weight. The right bound indicates the maximum forward flight speed, with the region to the top right of this bound indicating forward flight speeds for which the RMC TRV has insufficient thrust.

It is important to emphasize that the minimum and maximum forward flight speed bounds are purely theoretical bounds that are based on assumptions and simplifications presented earlier. The most significant assumption was assuming that the thrust was constant and equal to the total weight of the UAV. In reality, the thrust required is substantially smaller in magnitude during forward flight than during hover. This simplification has a significant influence on the predicted maximum forward flight speed, resulting in its over-prediction, especially at lower vehicle tilt angles when the RMC TRV behaves as a fixed wing aircraft. In addition, the maximum forward flight speed bound

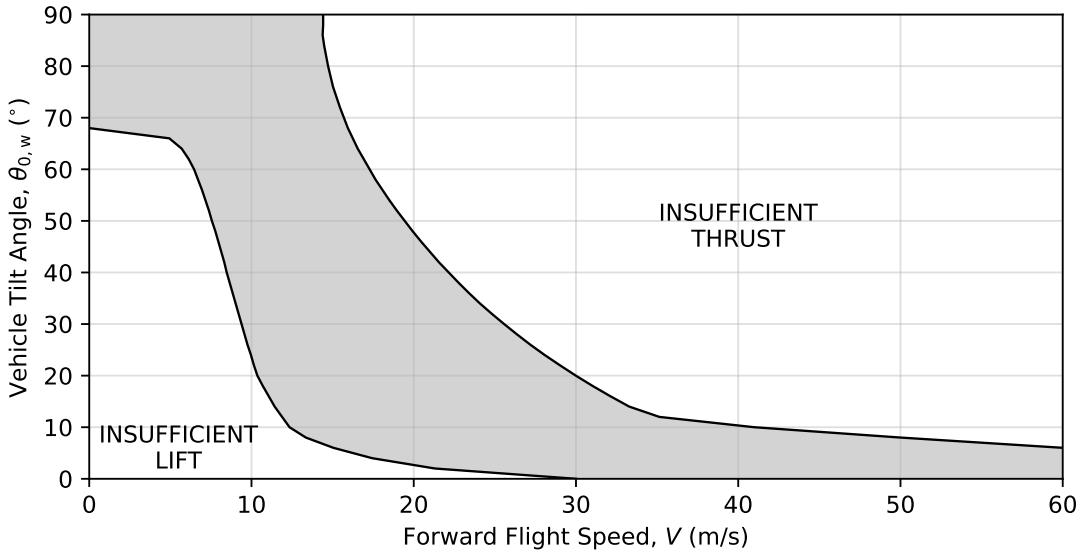

Figure 5.7: Transition corridor of the RMC TRV with a straight leading edge.

does not consider structural limits that would likely restrict the corridor further. The minimum required forward flight speed, of more interest in the context of this thesis, is less dependant on the thrust model, attenuating any negative effects that arise from the simplification. However, this left bound should still be treated as a preliminary estimate since it is based on an analytical model developed for preliminary design of VTOL aircraft. The minimum required forward flight speed was determined through a force balance in the vertical direction, as described by Equation 5.3. It is purely based on the lift performance of the UAV and decouples the predicted forward flight speed from thrust. In other words, it does not consider if indicated speeds are possible given the assumed thrust. An example of this shortcoming of the presented model is apparent at a vehicle tilt angle of approximately 70°, where Figure 5.7 shows that the RMC TRV is capable of hovering ($V = 0$ m/s) at a tilt angle of 70°. As such, the presented minimum required forward flight speed should be interpreted as a theoretical value. The minimum required forward flight speed shown in Figure 5.7 serves as a baseline for comparison against the minimum required forward flight speeds for the RMC TRV with tubercles.

5.4.2 Transition Corridor with Empirical Tubercle Model

Figure 5.8 presents the transition corridor of the RMC TRV with the smallest amplitude tubercles, the A02λ09. The dotted line shows the predicted minimum required forward flight speeds of the RMC TRV with a straight leading edge for reference. A small contraction of the transition corridor (increased minimum required forward flight speed) can be seen for smaller vehicle tilt angles. However, this penalty is counteracted by an expansion of the transition corridor (decreased minimum required forward flight speed) at larger vehicle tilt angles. This effect on the minimum required forward flight speed corresponds to the increased post-stall lift at the cost of decreased lift before stall, observed for tubercle wings in Chapter 4.

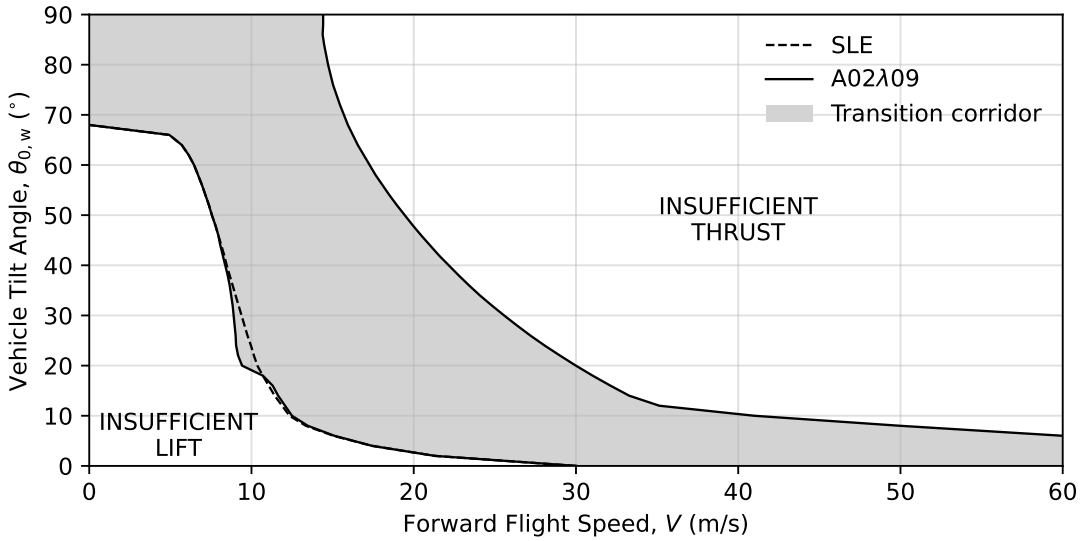

Figure 5.8: Transition corridor of the RMC TRV with the A02λ09 tubercles.

Figure 5.9 shows the transition corridor of the RMC TRV with the largest amplitude tubercles, the A06λ21. Once again, the dotted line shows the predicted minimum required forward flight speeds of the RMC TRV with a straight leading edge for reference. The overall effect of the A06λ21 tubercles on the minimum required forward flight speed is similar to the effect obtained with the smaller A02λ09 tubercles, but to a different degree. Since the larger amplitude tubercles were shown to induce a larger penalty in lift at angles of attack less than stall, a greater increase in minimum required forward flight speed at smaller vehicle tilt angles is to be expected, and is observed in Figure 5.9. Differences in the reduction in minimum required forward flight speed at larger vehicle tilt angles are also present between the A06λ21 and the A02λ09. The larger amplitude A06λ21 reduces the minimum required forward flight speed to a lesser degree over a wider range of vehicle tilt angles, while the smaller amplitude A02λ09 provided a more significant reduction in minimum forward flight speed that is localized to vehicle tilt angles near 20°.

In general, Figures 5.8 and 5.9 show that the extent of the contraction of the transition corridor at lower vehicle tilt angles, and expansion of the transition corridor at larger vehicle tilt angles is proportional to the extent of decreased lift at angles of attack before stall, and increased lift at post stall angles observed for each tubercle wing in Chapter 4. This can be confirmed by examining the relative change in minimum required forward flight speed for each vehicle tilt angle presented in Figure 5.10. Since the empirical tubercle model developed only applies for angles of attack less than 45°, results for vehicle tilt angles greater than 45° are omitted. The annotated arrows on the right hand side of the figure indicates that positive values means a contraction of the transition corridor while negative values means an expansion of the transition corridor.

The remaining four tubercle geometries (A02λ07, A03λ11, A04λ18, and A05λ13) are shown to follow this trend, the respective transition corridors for which can be found in Appendix D. Key parameters from Figure 5.10 are summarized in Table 5.5. The

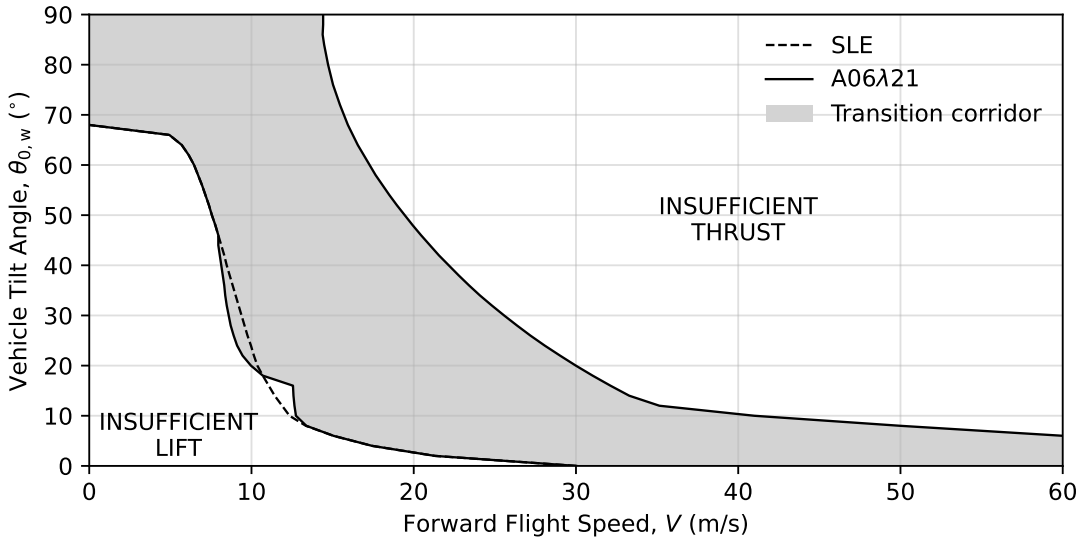

Figure 5.9: Transition corridor of the RMC TRV with the A06λ21 tubercles.

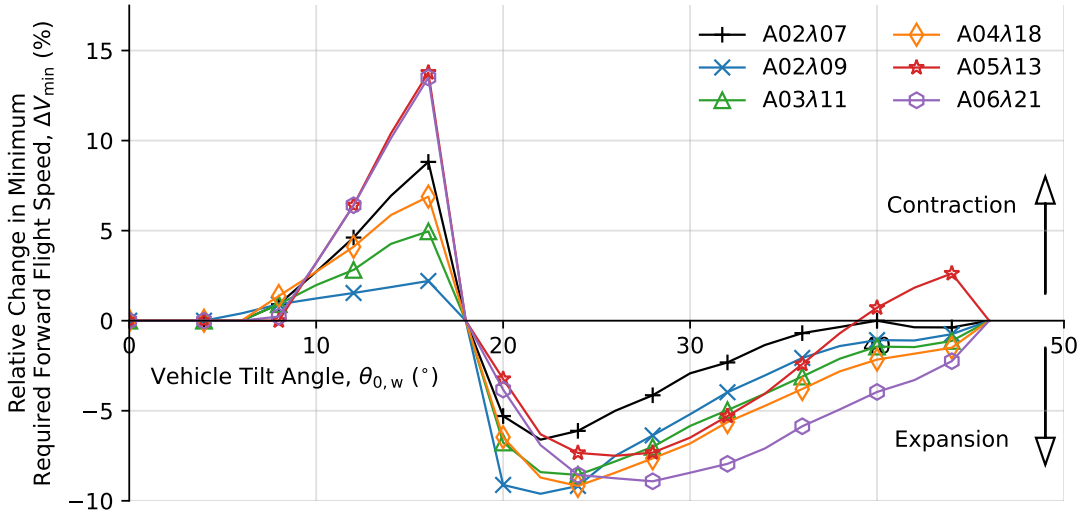

Figure 5.10: Relative change in minimum required forward flight speed for the RMC TRV with tubercles.

contraction area (CA) is defined as the area between the curve and the horizontal axis in Figure 5.10 (units of °%), which describes the overall effect of each respective tubercle on the transition corridor. A negative value signifies that the addition of the tubercles caused a net expansion of the transition corridor (a desirable outcome), while a positive value signifies the opposite (an undesirable outcome). The maximum increase in minimum forward flight speed, $(\Delta V_{\text{min}})_{\text{max}}$, represents the greatest increase in the minimum required forward flight speed (highest point in Figure 5.10). Similarly, the maximum decrease in minimum required forward flight speed, $(\Delta V_{\text{min}})_{\text{min}}$, represents the greatest decrease (lowest point in Figure 5.10).

Table 5.5: Summary of the effect of different tubercle geometries on the minimum required forward flight speed of the RMC TRV.

Wing	Contraction Area (°%)	$(\Delta V_{\min})_{\max}$ (%)	$(\Delta V_{\min})_{\min}$ (%)
A02λ07	-0.40	+8.8	-6.6
A02λ09	-1.82	+2.2	-9.6
A03λ11	-1.67	+4.9	-8.6
A04λ18	-1.70	+6.8	-9.2
A05λ13	-0.41	+13.8	-7.5
A06λ21	-1.65	+13.5	-8.9

The A02λ09 tubercle expanded the transition corridor the most, with a CA of -1.82 °%, followed by the A04λ18, A03λ11, A06λ21, A05λ13, and the A02λ07. While all of the tubercles had a net positive effect on the transition corridor, the A02λ07 and A05λ13 tubercles had very low CA of -0.40 °% and -0.41 °% respectively. Despite the low CA for these two tubercles, it is apparent from Figure 5.10 and the summarized values in Table 5.5 that while their net effect is insignificant, they still alter the minimum required forward flight speeds, and thus the shape of the lower bound of the transition corridor.

This analysis of the effect of tubercles on the transition corridor of the RMC TRV should be treated as a preliminary estimate. A flight test campaign to experimentally map the transition corridor of the RMC TRV would provide definitive results concerning the effectiveness of tubercles during transition. Such an investigation was deemed to exceed the scope of this thesis, but would allow for the effects of the complex flow structures generated by tubercles at post-stall angles of attack to be recreated and measured accurately. It would also provide insight into effects not captured by the present model, such as the effects of tubercles on power requirements during transition.

The numerical simulation shows that tubercles can reduce the minimum required forward flight speed for a tail sitter UAV during transition by up to 9.6%, with the largest changes observed with the A02λ09 tubercle at vehicle tilt angles just after stall. The extent of the modification of the left bound of the transition corridor was shown to correspond to the modification of the lift performance observed for tubercles in Chapter 4. These results can be expected when tubercles are applied to tilt-wing configurations as well, due to the similarities in the aerodynamic environment of the wing. The reduction in the minimum required forward flight speed expands the transition corridor, providing a greater margin of safety when performing a vertical takeoff or landing.

6 Practical Application of Blown Tubercles on a Monocopter

This chapter presents the methodology, results and discussion of the flight test campaign of a monocopter. This flight test campaign serves as a demonstration of an application of sinusoidal leading edge tubercles to a blown system in a practical setting as opposed to the controlled environment of Chapter 4. It consists of an investigation on improving the hover performance of a monocopter with sinusoidal leading edge tubercles.

The flight testing of a tilt-wing aircraft would provide the most credible demonstration of the effects of sinusoidal leading edge tubercles on transition performance. Such a project involves the design of the aircraft, the control system, and the flight test campaign, each with their own unique problems. One of the most critical elements would be the instrumentation of the tilt-wing aircraft, and selecting the parameters to measure that would provide a quantitative insight into the transition performance of the aircraft. This goes hand in hand with designing a flight test campaign that is reliable and repeatable in order to obtain valid results. When all of these elements were considered it was deemed to exceeded the scope of this thesis and time constraints. The idea of flight testing a tilt-wing vehicle is not a novel idea and has been completed by other institutions, most notably the flight testing of the *NASA GL-10 Greased Lightning*, which demonstrates the scale of such a project [8, 83, 84]. In place of a tilt-wing aircraft, a simpler test vehicle with similar aerodynamic effects (propeller blown wing at high angles of attack) called a monocopter was selected as a surrogate test vehicle to demonstrate the effect of sinusoidal leading edge tubercles in a practical setting.

6.1 Background on Monocopters

A monocopter is a rotary wing UAV that uses a single blade which rotates about the vehicle's centre of gravity to generate the lift necessary for flight. The unique single bladed design of the monocopter is bio-inspired by a maple tree samara. A samara is a type of fruit that possesses a winged structure that acts to slow the decent of the fruit, allowing for the seeds to be carried and dispersed by the wind to new locations [85]. The maple tree samara in particular resembles a single wing, or blade, with a concentrated mass at one end that autorotates as it falls to the ground [86]. Figure 6.1 shows a sketch describing the autorotating motion and a dried maple tree samara. The autorotating behaviour of the maple tree samara and the single bladed construction inspired the design of the monocopter.

(a) (b)

Figure 6.1: A dried maple tree samara (6.1a) and its autorotating trajectory (6.1b) [86].

Different configurations for the design of the monocopter have been explored, with the main difference between configurations being the location of the propulsion system that generates the torque to rotate the single blade. Figure 6.2 shows three examples of different configurations by the Massachusetts Institute of Technology (MIT), Shahid Rajee Teacher Training Unversity (SRU), and the University of Glasgow Singapore (UGS), that have flown successfully in the past. All three of these examples use a propeller to generate the thrust required. The MIT monocopter positions the propeller opposite to the blade, the SRU monocopter offsets the propeller by 90° such that the propeller is perpendicular to the blade, while the UGS monocopter places the propeller along the length of the blade.

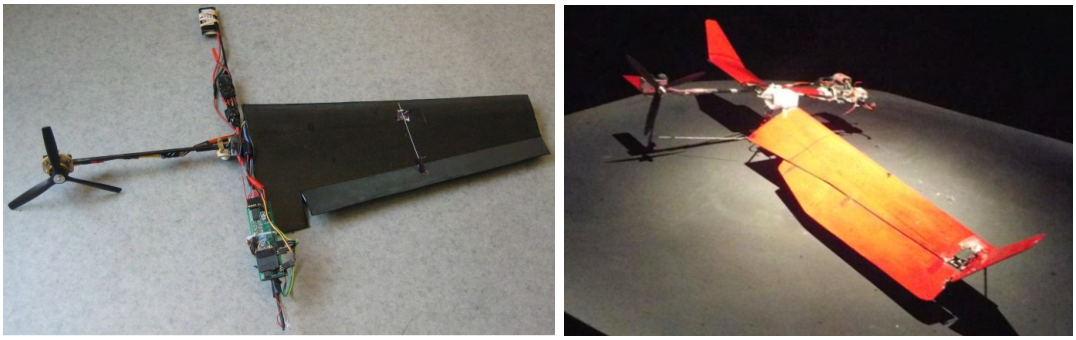

(a) MIT [87]. (b) SRU [88].

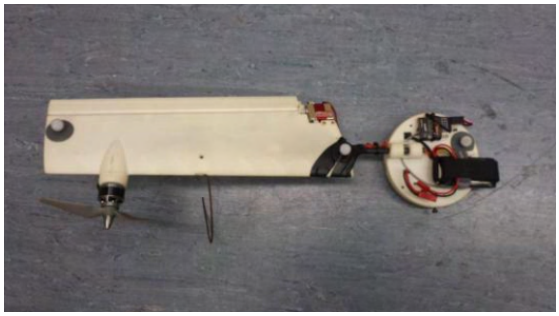

(c) UGS [89].

Figure 6.2: Monocopter designs from three different universities.

A configuration similar to the UGS monocopter is of particular interest, since the location of the propeller places the blade of the monocopter within the propeller slipstream. Furthermore, the angles of attack along a monocopter blade are large due to its rotary nature. This combination creates an aerodynamic environment that is very similar to a blown wing on a tilt-wing aircraft, and the setup used in the experimental wind tunnel campaign. In addition, compared to a tilt-wing aircraft a monocopter is a much simpler vehicle to design, control, and flight test. The control of the monocopter can be further simplified by limiting the investigation to a tethered hover, reducing the scope of the flight test campaign.

6.2 Design and Fabrication of the RMC Monocopter

A total of three different blades were fabricated. The baseline blade had an unmodified, straight leading edge (SLE). The other two blades had the addition of leading edge tubercles. The results of Chapter 4 identified the A02λ09 tubercle as the best performing tubercle for angles of attack just before stall. Since the monocopter blade was expected to operate at these angles of attack, two blades with A02λ09 tubercles were constructed. One of the tubercle blades, which will be referred to as the *A02λ09 blade*, had tubercles along the entire leading edge of the blade. The other tubercle blade, which will be referred to as the *A02λ09p blade*, only included tubercles along the leading edge of the segment directly behind the propeller. Figure 6.3 shows the three blade designs. The tubercles were added as a retrofit, meaning that besides the change in the leading edge geometry, all other aspects of blade design were retained.

(a) SLE blade.

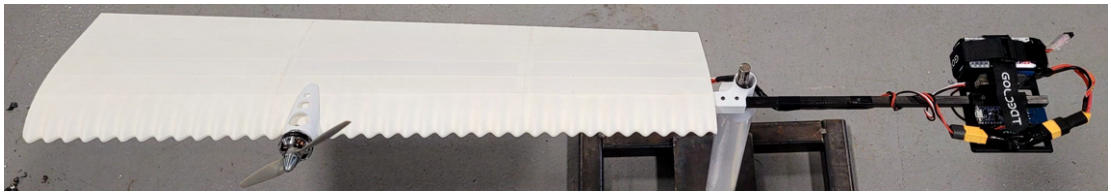

(b) A02λ09 blade.

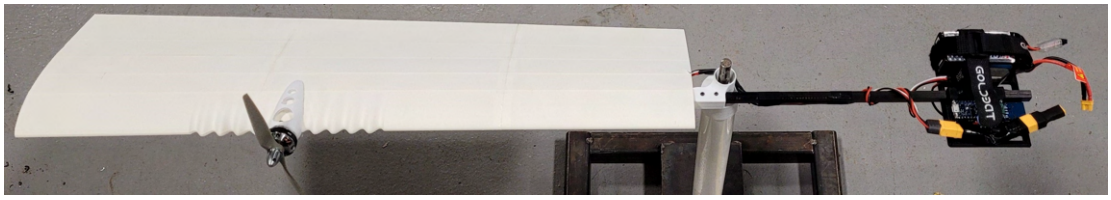

(c) A02λ09p blade.

Figure 6.3: Three monocopter test articles.

The remainder of this section presents the design and fabrication of the monocopter tested, referred to henceforth as the *RMC monocopter*. First, a design code that uses blade element momentum theory will be presented. Next, the design requirements and constraints are defined, followed by a description of the final design of the RMC monocopter. Finally, the methods used to manufacture the monocopter will be presented.

6.2.1 Blade Element Momentum Theory

Blade element momentum theory (BEMT) is a commonly used numerical analysis method to estimate the aerodynamic properties of a rotor. It was used as a design tool to estimate the local angles of attack along the blade, required rotational speed of the monocopter, and figure of merit. BEMT was implemented as described in [75], with correction factors to account for tip losses, drag of non-lifting components, propeller slipstream effects, and a coning angle. A detailed overview of the complete BEMT method, as well as the Python script that was developed can be found in Appendix E. Table 6.1 summarizes the key input parameters for the Python script.

Table 6.1: Key input parameters for the BEMT analysis Python script.

	Parameter	Symbol	Units
Blade geometry	Radius	R	m
	Chord length	c	m
	Blade installation angle	θ_0	°
	Blade twist	θ_{tw}	°
Other	Electronics weight	W_{e}	g
	Radial propeller location	y_{p}	$\%R$
	Propeller diameter	d_{p}	m

6.2.2 Monocopter Design

A configuration with a propeller placed along the length of the blade, like the configuration shown by the UGS monocopter (Figure 6.2c), was selected since the main objective of this flight test campaign was to demonstrate the application of tubercles to a blown surface at high angles of attack. The optimal propeller position determined in Chapter 4 was adopted. The blade geometry was limited to a rectangular planform with linear twist for ease of manufacturing. Initial prototypes were constructed with *DOW*® Styrofoam™ insulation, using a CNC hot wire foam cutter. The blade geometry was further constrained by the capabilities of the CNC hot wire foam cutter itself, as summarized in Table 6.2. Since the CNC hot wire foam cutter was incapable of accurately creating tubercles, the final design was fabricated using fused deposition modelling 3D printing. More details on the fabrication of the monocopter can be found in Section 6.2.3. In addition to the geometric constraints defined in Table 6.2, requirements concerning other aspects of design were imposed. These requirements are listed in Table 6.3.

Table 6.2: Monocopter blade design geometry constraints.

Parameter	Symbol	Constraints	Units
Radius	R	$R \leq 0.6$	m
Chord length	c	$c \leq 0.254$	m
Blade twist	θ_{tw}	$-15 \leq \theta_{\text{tw}} \leq 15$	°

Table 6.3: Monocopter design requirements.

Number	Description
1	The design must include a method of tethering the monocopter to a line for the safety of personnel.
2	The blade must generate enough lift to support the weight of the telemetry system, electronics, and the blade itself in hover out of ground effect (OGE).
3	The blade should be designed to have a low rotational speed for hover.
4	The blade should be designed to incorporate an adequate coning angle such that the monocopter is inherently stable in hover.

To satisfy Requirement 1, a tether system was developed. A diagram describing the tether system is shown in Figure 6.4. The tether system consisted of a ring located at the root of the blade that was concentric with the centre of gravity of the monocopter. This ring will be referred to as the safety ring and can be seen at the root of the blades in Figure 6.3. A tether line was passed through the safety ring before being secured to the takeoff stand. The other end of the tether was looped around a structural beam at the ceiling of the test facility, creating a vertical line that approximately traced the flight path for the monocopter during the flight test mission profile, which is presented in Section 6.3.5. Tension on the tether line was controlled by physically pulling on the free end of the tether. For the majority of the flight, the tether line was slack, allowing the monocopter to hover with minimal influence from the tether. During landing, tension was applied to the line to guide the monocopter back to the takeoff stand. Tension was also applied as a safety measure in the case of the monocopter wandering from a stationary hover.

The remaining requirements were satisfied through careful selection of the parameters presented in Table 6.1. Table 6.4 summarizes the selected parameters. These values were then used in a BEMT analysis to estimate the local angles of attack along the blade, required rotational speed for hover, and figure of merit. The 2D lift, drag, and moment coefficients for the Vertol VR-7 airfoil that were required for the BEMT analysis were obtained from the experimental data of Tung and McAlister, which is shown in Figure 6.5 [90].

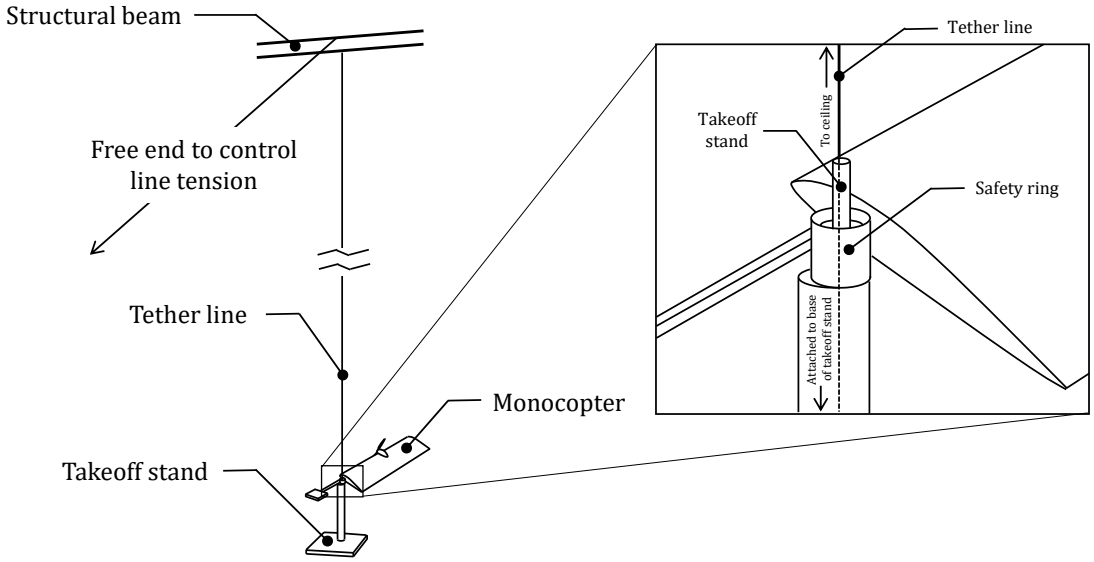

Figure 6.4: Tether system for monocopter flight testing.

Table 6.4: Design parameters of the RMC monocopter.

	Parameter	Symbol	Value	Units
Blade geometry	Airfoil	-	Vertol VR-7	-
	Radius	R	0.60	m
	Chord length	c	0.18	m
	Blade installation angle	θ_0	30	°
	Blade twist	θ_{tw}	-10	°
Other	Electronics weight	W_{e}	271.4	g
	Blade weight	W_{b}	92.6	g
	Radial propeller location	y_{p}	0.6	$\%R$
	Propeller diameter	d_{p}	0.127	m

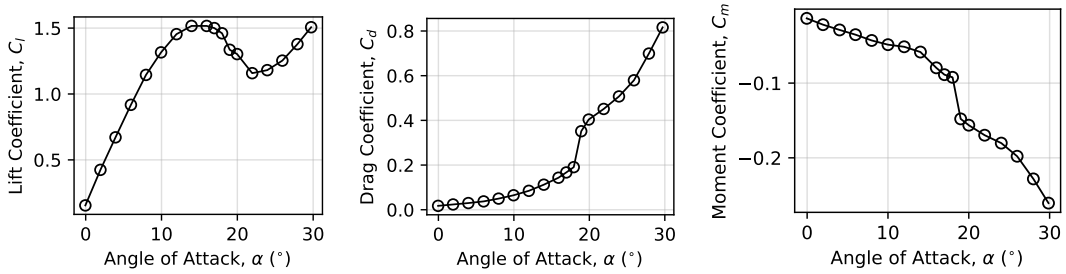

(a) Lift coefficient. (b) Drag coefficient. (c) Moment coefficient.

Figure 6.5: 2D aerodynamic coefficients for the Vertol VR-7 airfoil measured by Tung and McAlister [90].

Figure 6.6 shows the local angles of attack along the blade as predicted by BEMT, where the horizontal axis shows the non-dimensional radial position along the blade

measured from the blade root, r. The abrupt decrease in local angles of attack centred around $r = 0.6$ (60% of the blade radius from the blade root) is a result of the propeller slipstream effects. Since the blade was designed to have a low rotational speed required for hover (Requirement 3), the majority of the blade operates at angles of attack just below stall, where the 2D lift coefficient of the airfoil segment approaches its maximum value. The monocopter was predicted to rotate at 156 RPM in hover OGE, with a coning angle of 12.9°. The coning angle, β, is the angle between the plane of rotation and the monocopter blade, which provides stability to the monocopter in hover similar to how dihedral provides roll stability to fixed wing aircraft. If the axis of rotation of the monocopter begins to tilt in any direction, the coning angle allows the blade to generate a restoring force that brings the monocopter back to a stationary hover. This effect is illustrated in Figure 6.7.

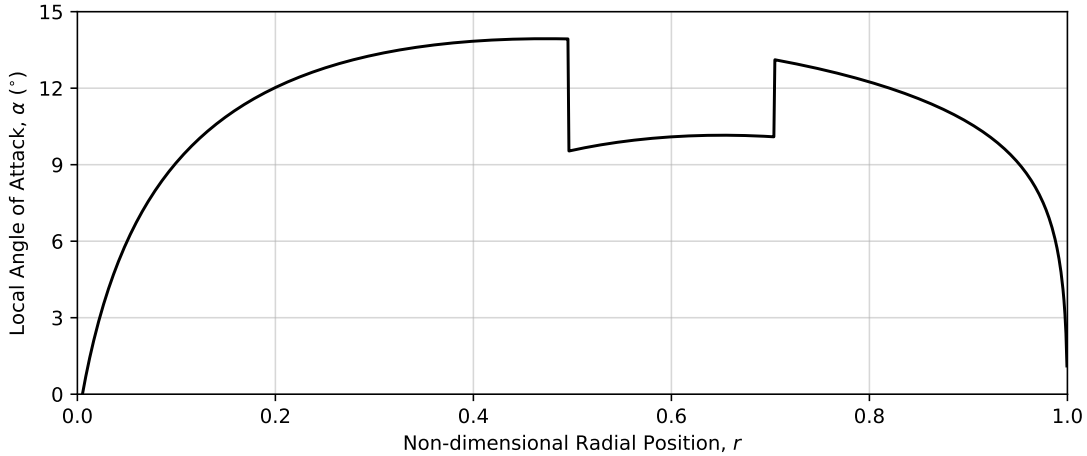

Figure 6.6: Local angles of attack along the blade as predicted by BEMT.

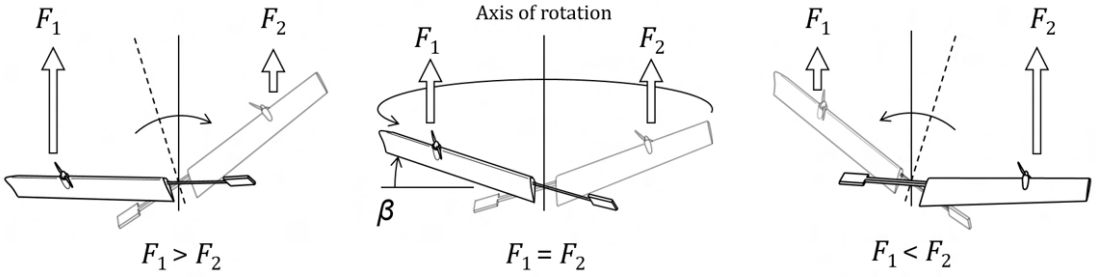

Figure 6.7: Stability in hover provided by the coning angle of the monocopter blade.

6.2.3 Monocopter Fabrication

The RMC monocopter can be divided into five main components: the blade spar, the blade, the telemetry pad, the electric motor mount, and the safety ring. With the exception of the blade spar, all of these components were manufactured using fused deposition modelling (FDM) 3D printing, as it allowed for rapid iteration of designs as well as a simple yet effective method of manufacturing the complex 3D geometry of tubercles. The blade spar was a 0.5 m long carbon fibre rod with an 8 mm by 8

mm square cross section. The remaining components were printed using one of three filaments: *Stratasys* acrylic styrene acrylonitrile (ASA), *eSUN* polylactic acid (PLA), or *eSUN* lightweight polylactic acid (LW-PLA). Table 6.5 summarizes the material used for each component, as well as the machine used to print the component.

Table 6.5: Summary of materials used to manufacture each component of the RMC monocopter.

Component	Material	Machine
Blade spar	Carbon fibre	-
Blade	*eSUN* LW-PLA	*BIQU B1*
Telemetry pad	*Stratasys* ASA	*Stratasys Fortus 450mc*
Electric motor mount	*eSUN* PLA	*BIQU B1*
Safety ring	*eSUN* PLA	*BIQU B1*

While ASA and PLA are widely used materials for FDM 3D printing, the *eSUN* LW-PLA is a less common material, which was selected for manufacturing the blades. As the name suggests, the LW-PLA allows for components to be significantly lighter than they would be if manufactured with regular PLA. It accomplishes this by foaming and expanding when exposed to high temperatures. The expansion of the material allows for a proportionally smaller amount of material to be used to manufacture a component. The amount of expansion of the LW-PLA is determined by the nozzle temperature of the FDM 3D printer. Figure 6.8 shows the expansion of the material as a function of the nozzle temperature. At a nozzle temperature of 240°C the LW-PLA expands to 207% of the volume of regular PLA, which means that the LW-PLA can produce the same component with just 48% of the material that would be required if regular PLA were to be used. This is equivalent to an approximately 52% decrease in weight. However, the LW-PLA does not produce parts with equivalent strength as regular PLA.

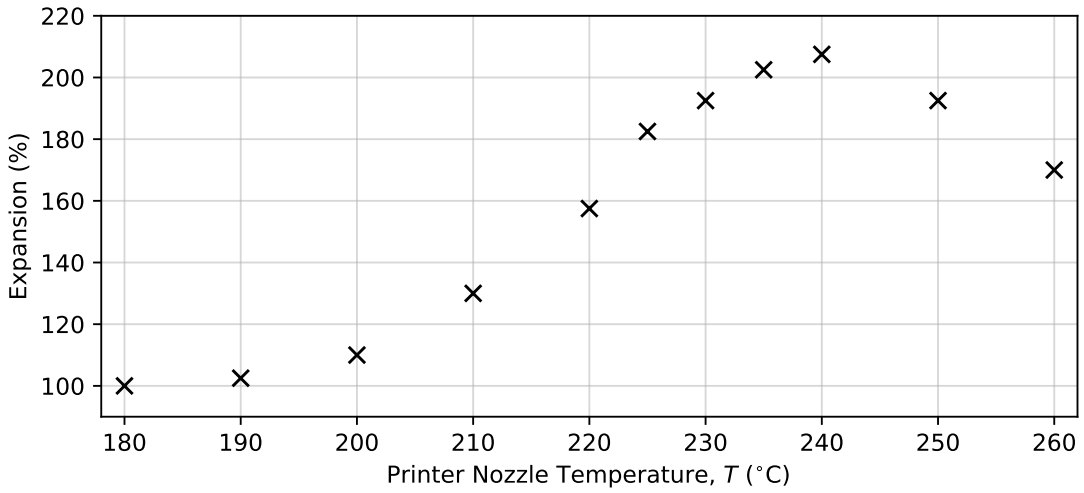

Figure 6.8: Expansion of the *eSUN* LW-PLA as a function of the nozzle temperature.

Three blades were manufactured: the SLE blade, A02λ09 blade, and the A02λ09p blade, which were shown in Figure 6.3. The cross section of the blades included four spars located at 0.24c, 0.38c, 0.54c and 0.72c. The front-most spar included a square sleeve

that terminated 0.25 m from the blade root that transition fit with the carbon fibre blade spar. The blades were manufactured in three segments due to the limitations of the build size of the *BIQU B1* 3D printer. Rectangular tabs were attached to the skin of the segments that were used to assemble segments with cyanoacrylate. Figure 6.9 shows the cross section of the SLE blade, as well as the three segments with the rectangular tabs ready for assembly.

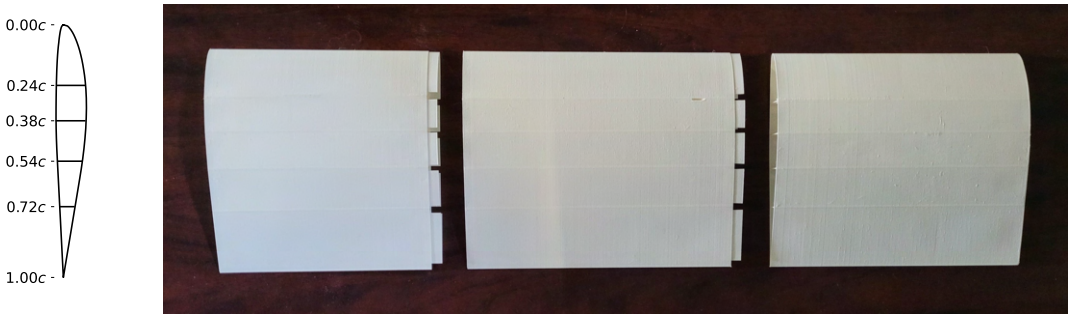

Figure 6.9: 3D printed monocopter blade cross section, and blade segments with rectangular tabs ready for final assembly.

Figure 6.10 shows an isometric drawing of the telemetry pad and a photograph of the telemetry pad with all components mounted. A square sleeve divided the pad into two sections, which will be referred to as the leading edge section and the trailing edge section. The leading edge section corresponds to the side of the telemetry pad that is on the same side as the leading edge of the wing. The carbon fibre spar was fit into the square sleeve and secured using two M4 set screws. The leading edge section contained a raised segment to mount an *Arduino Nano 33 BLE Sense* using M1.7 machine screws, with a cutout below to access the pins. An *ACS711EX* current sensor, and an SD card reader were mounted next to the *Arduino Nano 33 BLE Sense* using M2 machine screws. The trailing edge section contained slots to allow for a LiPo battery and *AR410* radio receiver to be secured using Velcro® straps. A detailed description of the telemetry system is provided in Section 6.3.3.

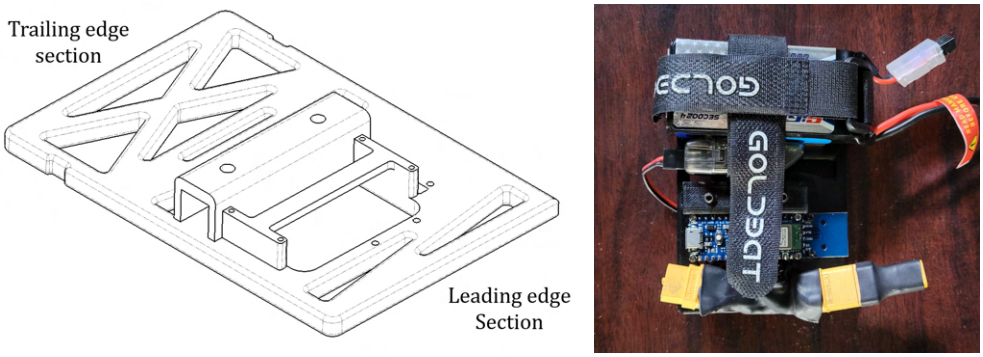

(a) Isometric view. (b) Mounted telemetry system.

Figure 6.10: The RMC monocopter telemetry pad, printed with *Stratasys* ASA.

An isometric drawing of the electric motor mount is shown in Figure 6.11a. The electric motor mount included trapezoidal tabs that clipped into slots integrated behind

the front spar of the blade at the desired radial position for the propeller, as seen in Figure 6.11b.

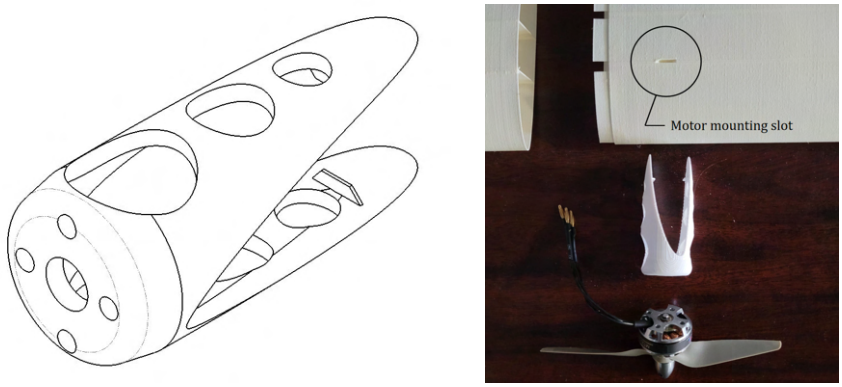

(a) Isometric view. (b) Integrated mounting slot.

Figure 6.11: The RMC monocopter motor mount.

An isometric drawing of the safety ring is shown in Figure 6.12. It included two long tabs that were used to attach it to the front spar of the blade at the blade root. The square hole interfaced with the carbon fibre blade spar with four holes for M4 set screws that were used to lock the blade spar in place after being fit into the blade. Once manufactured with the *eSUN* PLA, the electric motor mount and safety ring were secured to the blade using cyanoacrylate.

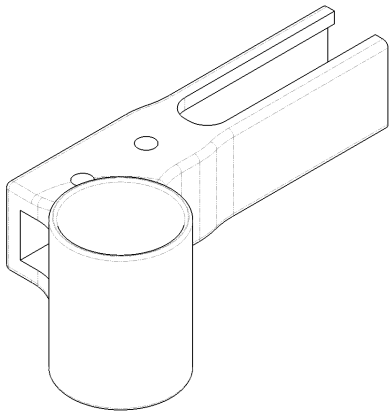

Figure 6.12: Isometric view of the safety ring.

Since the blade and the telemetry pad were both secured to the carbon fibre blade spar using set screws, removal of the blade or adjustment of the position of the telemetry pad was a simple process. Removing the blade was necessary when switching between the blades with different leading edge geometries. The adjustment of the position of the telemetry pad was necessary in order to control the radial location of the centre of gravity.

The mass of each component, measured using a *Mettler Toledo AE160* digital analytical balance, is provided in Table 6.6. The mass of the blades was measured after the three

segments, the electric motor mount, and safety ring were assembled using cyanoacrylate. As shown in Table 6.6, the mass of the blades was relatively consistent despite the addition of tubercles, resulting in little variation in the total mass of the RMC monocopter. This provided more confidence when analyzing the results that the changes in performance were primarily from the differences in the aerodynamic performance of the blades.

Table 6.6: Mass of each component of the RMC monocopter.

Component	Mass (g)
1350 mAh LiPo battery	113.30
Arduino Nano 33 BLE Sense	5.95
Carbon fibre blade spar	19.90
Current sensor	14.16
Electric motor and propeller	30.37
Electronic speed controller	30.65
Telemetry pad	27.56
Radio receiver	7.17
SD card reader	2.33
SLE blade	92.55
A02λ09 blade	90.57
A02λ09p blade	89.52

6.3 Methodology

This section presents the flight test objectives, test facilities, instrumentation and data acquisition system, data post processing methods, and flight test procedures. This flight test campaign was only concerned with measurements during a tethered, out of ground effect (OGE) hover. Limiting the investigation to OGE hover eliminated the need for an active control system and a stability augmentation system, since the monocopter was designed to be inherently stable in hover. This reduced the scope of the flight test campaign to fit within the scope of this thesis. However, since no active control system was included, if the monocopter were to gain a forward velocity there would be no means of correcting the flight back to hover. As such, a tether system as described in Section 6.2.2 was employed as a precaution to ensure the safety of personnel.

6.3.1 Flight Test Objective

The monocopter is a unique rotary wing UAV that (for the configuration investigated in this thesis) possesses a propeller blown segment of blade. As such, the aerodynamics of the monocopter blade are dominated by the rotary motion of the blade, and the interaction between the propeller slipstream and the blade. The results presented in Chapter 4 showed that the addition of tubercles to a propeller blown wing significantly improved the post-stall lift coefficients, with the extent of the improvement depending on the geometry of the tubercles. This flight test campaign aims to apply the experimental results of Chapter 4 and demonstrate how the addition of tubercles can impact

the performance of a blown system. More specifically, the main flight test objective is to determine how leading edge tubercles effect the figure of merit of a monocopter in hover. The results of this flight test campaign serves to demonstrate the potential benefits that a more complex blown system, such as a tilt-wing aircraft, could experience from the addition of tubercles.

6.3.2 Test Facilities

The flight tests were conducted inside a large indoor facility located at the RMC. Access to the building was strictly controlled preventing unaccounted observers from entering during flight tests, eliminating the need for a large safety net when performing flights. A tether system as described in Section 6.2.2 was employed to further ensure safety of personnel. The ceiling was approximately 10 m high, however, structural members were located lower at a height of approximately 5 m. The building provided enough horizontal space for test flights without interference effects from walls, and enough vertical space to hover out of ground effect. Obstructions on the ground were low enough such that they had minimal effect on the out of ground effect hover of the monocopter. Figure 6.13 shows the flight testing location with the point of takeoff marked.

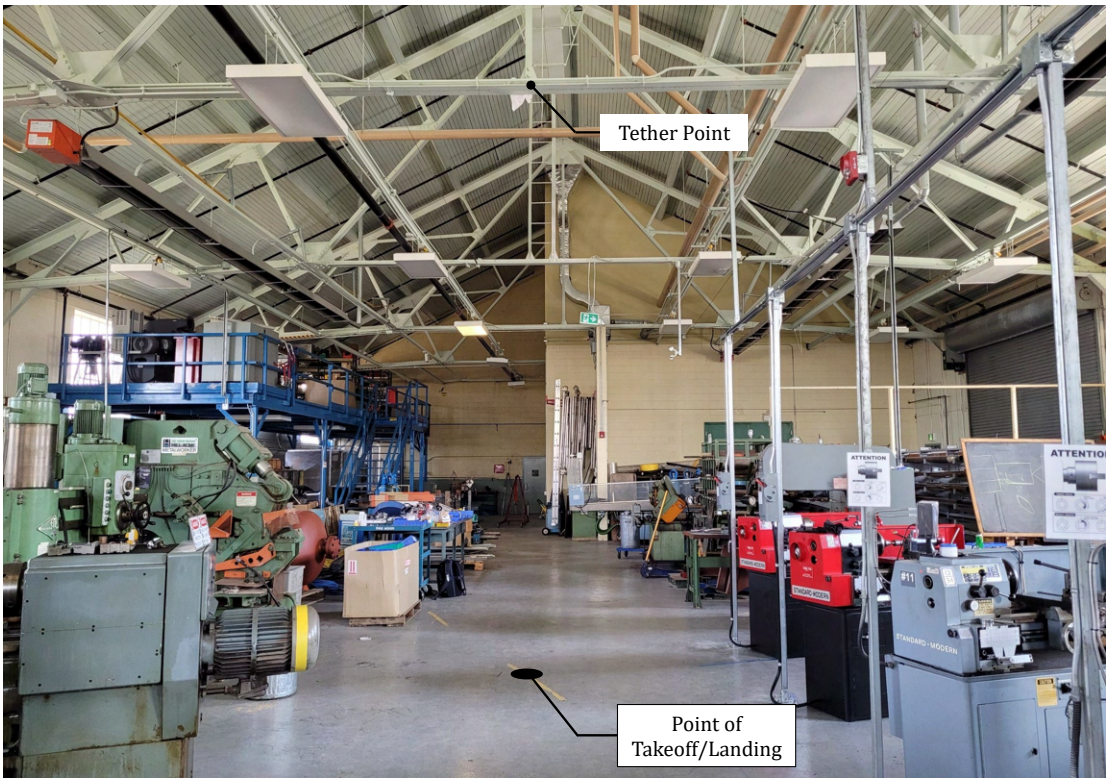

Figure 6.13: Flight testing location with point of takeoff indicated.

6.3.3 Instrumentation and Data Acquisition

Figure 6.14 shows a sketch, along with a schematic diagram of the instrumentation and telemetry system for the monocopter. The *APC* 5×5E propeller was powered by

an *LHI MT2204II*, 2300KV electric motor through a *ZTW Beatles 20A* ESC. Throttle control was transmitted through a *Spektrum DX6e* radio transmitter and received by an *AR410* radio receiver. The telemetry system consisted of an *Arduino Nano 33 BLE Sense* micro controller with an onboard 9-axis *LSM9DS1* inertial measurement unit (IMU), *LPS22HB* barometric pressure sensor, and *NINA-B306* Bluetooth® module. The *LSM9DS1* IMU consists of a 3-axis gyroscope, accelerometer, and magnetometer that was used to record the positional data of the monocopter in flight. This IMU used the axes convention as defined in Figure 6.14. The *LPS22HB* barometric pressure sensor was used to estimate the altitude of the monocopter. The telemetry data could be transmitted through the *NINA-B306* Bluetooth® module in real time to a workstation, or saved to an SD card. The entire system was powered through a 11.1V, 1350 mAh LiPo battery rated for 25C discharge rate. An *ACS711EX* current sensor was used to measure the current draw of the entire monocopter, with the battery voltage measured at the start and end of the flight using an *ElectriFly Triton EQ* LiPo battery charger.

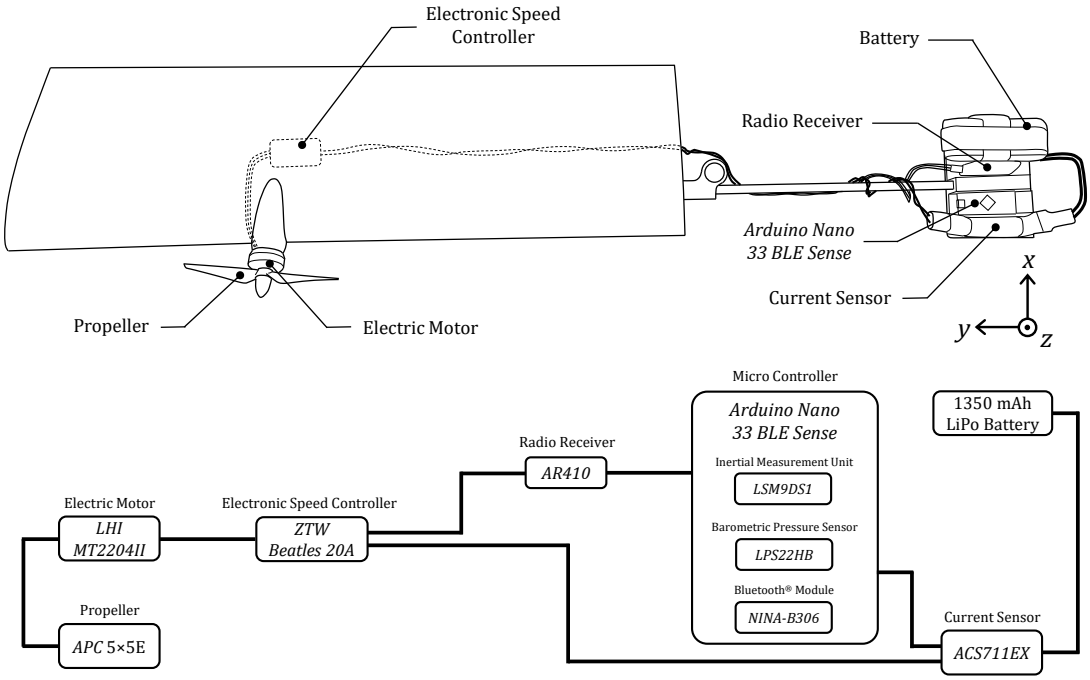

Figure 6.14: Sketch and schematic diagram of the monocopter instrumentation and telemetry system.

As shown in Figure 6.14, the *ZTW Beatles 20A* ESC was located inside the blade to connect to the *LHI MT2204II* electric motor mounted on the blade. The remaining electronic components and telemetry system were located on the telemetry pad. The mass of the components on the telemetry pad were measured using a *Mettler Toledo AE160* digital analytical balance and acted as a counterweight to the blade.

The measurement uncertainty for each value recorded from the telemetry system are summarized in Table 6.7. These values, obtained from their respective manufacturers, were used to determine the uncertainty in the calculated values presented in the following section using the Kline and McClintock uncertainty propagation method in order

to ensure the validity of the results [74]. Details on the uncertainty calculations can be found in Appendix A.

Table 6.7: Measurement uncertainty for the monocopter telemetry system.

Component	Parameter	Symbol	Uncertainty	Units
IMU	Acceleration	a	0.000244	g's
	Magnetic field	B	0.00014	G
	Angular rate	ω	0.07	°/s
Power	Current	I	5	%
	Voltage	V	0.005	V

6.3.4 Data Post Processing

A lowpass filter was applied to the raw data to filter out high frequency noise from the vibration of the electric motor, and any abrupt fluctuations caused by human input during the flight. To select an appropriate filter frequency, the power spectral density (PSD) of the raw data was created. The angular rate measurements from the *LSM9DS1* IMU will be used as an example. Figure 6.15 shows the PSD of the angular rate measurements in all three axes for a sample data set. The increased PSD observed between frequencies of 0.02 Hz and 0.06 Hz was a result of long period oscillations induced by the pilot during hover.

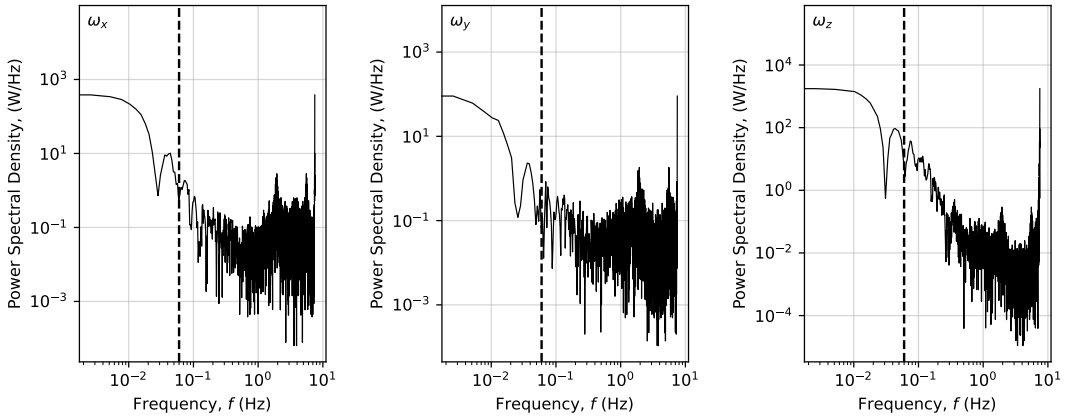

(a) x-axis. (b) y-axis. (c) z-axis.

Figure 6.15: Power spectral density plots for the angular rate in all three axes.

All signals with frequencies greater than 0.06 Hz were considered to be noise, and were filtered from the data. Figure 6.16 shows the filtered angular rate measurements about the z-axis overlaid onto the raw data. The filtering successfully removed abrupt fluctuations in the measurements, while retaining adequate detail in the results.

The other measured outputs from the telemetry system were processed in the same manner to obtain clean data that were used to assess the hover performance of the monocopter. To determine when the monocopter was in hover OGE, the rate of change

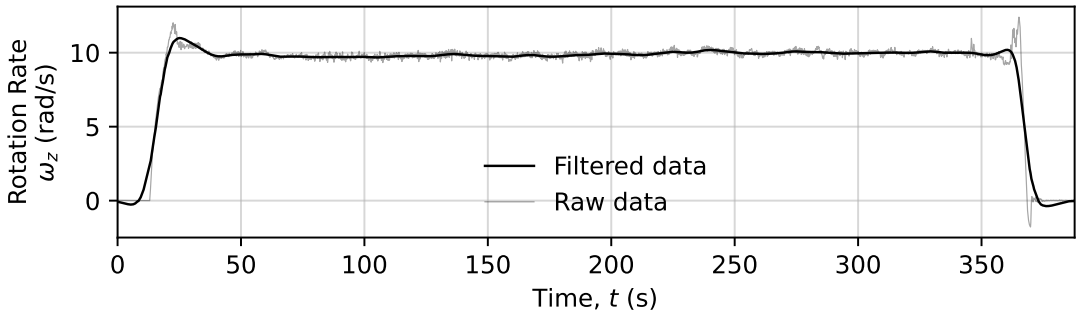

Figure 6.16: Filtered angular rate about the z-axis overlaid onto the raw angular rate measurements.

in altitude was examined. The barometric pressure measurements from the *LPS22HB* pressure sensor were used to estimate the altitude of the monocopter according to the following relationship [91]:

$$h = 44330 \left(1 - (P/101.325)^{1/5.255}\right) \tag{6.1}$$

where h is the altitude in m, and P is the measured barometric pressure. These measurements were numerically differentiated using a finite difference method to obtain the rate of change in altitude. The hover segment of the flight was considered to begin when the magnitude of the rate of change in altitude first decreased below 0.02 m/s, and the magnitude of the rate of change in altitude remained less than 0.1 m/s for the following 40 s. The hover segment was considered to end when the rate of change in altitude decreased below -0.15 m/s. This removed any segments of the flight in which the monocopter had any significant climb or descent speeds due to pilot error. Figure 6.17 shows the rate of change in altitude for a sample data set, with the start and end points of the hover segment indicated.

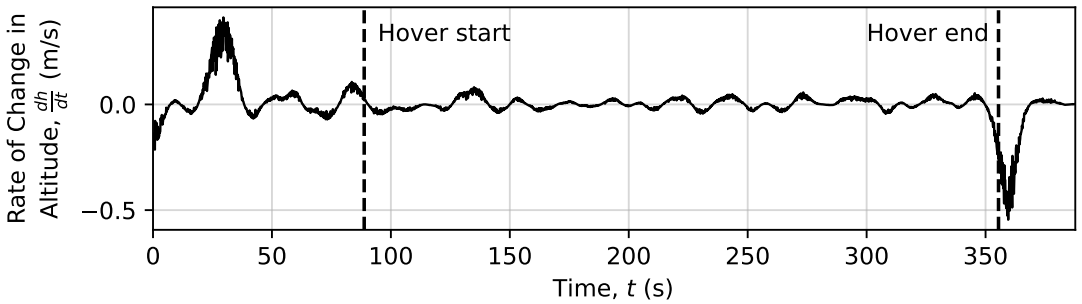

Figure 6.17: Rate of change in altitude for a sample data set, used to determine the start and end points of hover OGE.

The distribution of data points collected during the hover segment of the flight was assumed to follow a normal distribution, allowing the average to be used as an acceptable representative value for the entire data set. Once again using the angular rate measurements from the *LSM9DS1* IMU as an example, histograms of a sample data set were created for the filtered data to validate this assumption, which are shown in Figure

6.18. The distribution of data points for the angular rate about the y-axis is the least similar to a normal distribution. However, this was still deemed acceptable, since the angular rate of interest was the angular rate about the z-axis to provide the rotational speed of the monocopter, which is shown to better approximate a normal distribution. Figure 6.18 shows that this was a reasonable assumption.

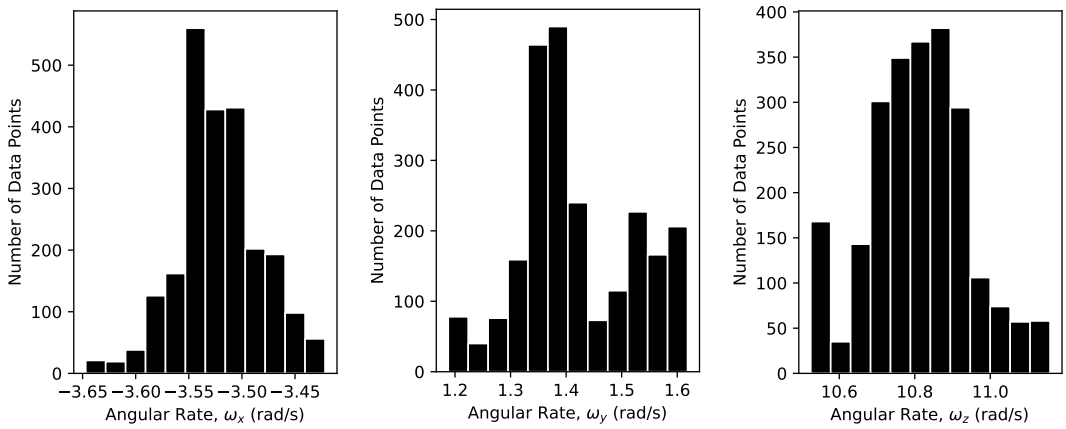

(a) x-axis. (b) y-axis. (c) z-axis.

Figure 6.18: Histograms of a sample data set for the angular rate measurements about all three axes.

The main parameter of interest was the figure of merit (FOM) defined by Leishman as the ratio of the ideal power required to hover to the actual power required [75]:

$$\text{FOM} = \frac{\text{Ideal power}}{\text{Actual power}} = \frac{C_T^{3/2}/\sqrt{2}}{C_P} \tag{6.2}$$

where C_T and C_P are the measured thrust and power coefficients of the monocopter, which Leishman defines as [75]:

$$C_T = \frac{T}{\rho\pi\Omega^2 R^4} \qquad\qquad C_P = \frac{P}{\rho\pi\Omega^3 R^5} \tag{6.3}$$

where T is the thrust required to hover (or the total weight of the vehicle), P is the power required to hover, and R is the radius of the monocopter blade. The rotational speed of the monocopter was measured directly using the *LSM9DS1* IMU. The thrust required for hover was assumed to be equal to the total weight of the monocopter, which was used in Equation 6.3 to calculate the thrust coefficient. To obtain the power coefficient, the power required for hover was calculated using the following equation:

$$P = IV \tag{6.4}$$

where I is the current, and V is the voltage. The current was measured by the *ACS711EX* current sensor. Since the telemetry system did not have a voltage sensor, the battery voltage was assumed to decrease linearly between a measured voltage at the beginning and end of the flight. The resulting power, P, was then used in Equation 6.3 to calculate the power coefficient.

6.3.5 Flight Test Procedure

The flights were manually flown, therefore an extremely simple mission profile was followed to improve repeatability between flights. The flight test mission profile consisted of takeoff, climb OGE, hover OGE, descent, and landing. The mission profile is shown in Figure 6.19, and summarized in Table 6.8. Takeoff started from a takeoff stand that suspended the monocopter off the ground by its centre of gravity. This allowed for free rotation of the blade as it accelerated for takeoff. The structure shown of Figure 6.19 represents the takeoff stand. Figure 6.20 shows a photograph of the takeoff stand with the monocopter resting as it would before takeoff.

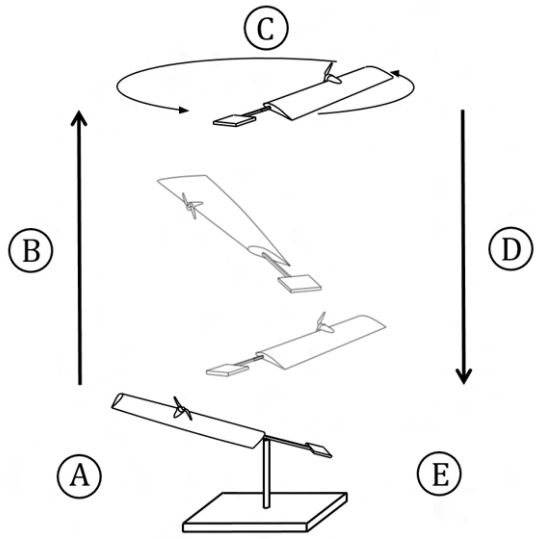

Figure 6.19: Monocopter flight test mission profile.

Table 6.8: Monocopter flight test mission profile.

	Segment	Duration (s)
A	Takeoff	-
B	Climb OGE	15
C	Hover OGE	330
D	Descent	15
E	Landing	-

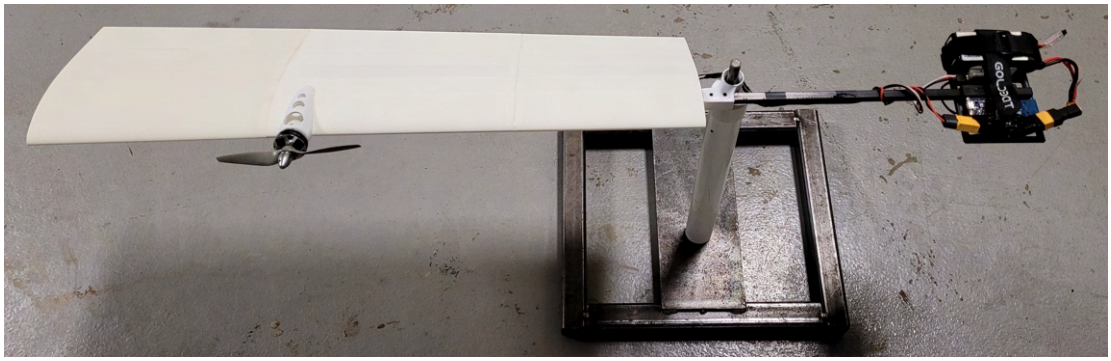

Figure 6.20: Takeoff stand with the monocopter ready for takeoff.

For each flight a checklist was followed to ensure consistency between flights. Each step of the checklist was performed at a specific time to account for the lack of a voltage sensor in the telemetry system. A timer was started once the battery was connected, with subsequent steps following a set schedule. This allowed for the amount of time spent with the battery connected to the monocopter, and the amount of time where throttle was applied to be consistent for all flights, ensuring that any differences in the

measured battery voltage at the end of the flight would only be a result of the blade's performance. The checklist, with the time (written as minutes:seconds) indicating when each step was performed, is provided below. A time stamp of -:-- indicates that the step was performed before the timer was started (before connecting the battery).

-:-- Replace battery with a battery at full charge (12.60 V).
0:00 Connect the battery to the monocopter.
0:10 Connect the telemetry system to the workstation via Bluetooth®.
0:30 Apply throttle, takeoff, and climb OGE.
0:45 Begin hover segment OGE.
6:15 Start descent.
6:30 Land, and decelerate monocopter.
6:45 Disconnect battery.

6.4 Results and Discussion

This section presents the flight test results. Each test flight was flown manually resulting in imperfect hover and introducing small inconsistencies between flights. In order to counteract these inconsistencies, a total of six flights were conducted for each blade, for a total of approximately 30 min of data collected in hover OGE for each blade.

The flight condition of the monocopter blade is constant in hover, hence the local angles of attack of the blade are not expected to vary in flight. This means that the results of this flight test are representative of a tilt-wing at a localized region of its transition corridor. The BEMT analysis predicted local angles of attack between 0° and 14°, which corresponds to the same vehicle tilt angles during transition. Figure 6.21 highlights the region of the transition corridor for which the results of this flight test are applicable.

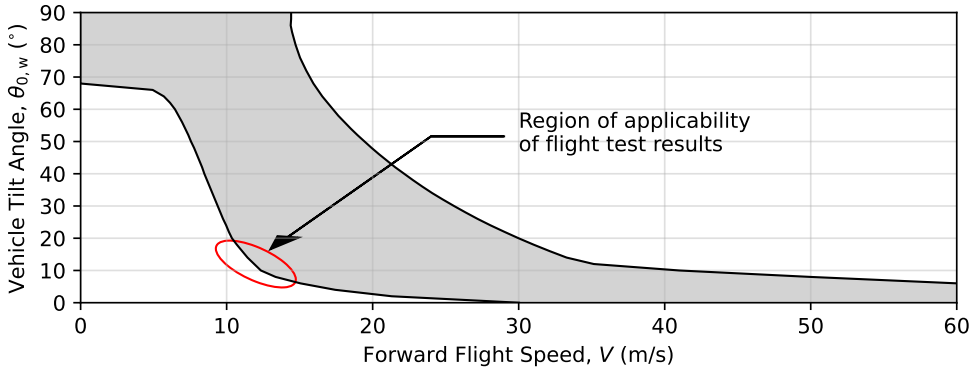

Figure 6.21: Applicability of the monocopter flight test results to transition performance.

The horizontal axis is the forward flight speed and the vertical axis shows the vehicle tilt angle, where an angle of 0° corresponds to forward flight mode and 90° corresponds to vertical flight mode. Further details on the transition corridor can be found in Chapter 5. The remainder of this section is organized as follows. First the hover performance of the straight leading edge blade will be presented, followed by the results for the A02λ09 (full tubercle) blade and A02λ09p (partial tubercle) blade.

6.4.1 Straight Leading Edge Blade

For each flight test, the thrust coefficient, power coefficient, and figure of merit can be shown as a function of time spent in hover. This provides perspective into the extent of the fluctuations caused by human input during the manually flown test flights. Figures 6.22 and 6.23 show the thrust and power coefficients, respectively, for Test Flight 1. The uncertainty of the calculated values are shown by the shaded region. The uncertainty for the thrust coefficient was relatively small compared to the power coefficient, and so the shaded region is difficult to see in Figure 6.22. The figure of merit, which was calculated using Equation 6.2 using the thrust and power coefficients, follows a similar trend with time, which is shown in Figure 6.24. Once again, the shaded region shows the uncertainty in the calculated value. The average value for this test flight is also shown by the dotted line.

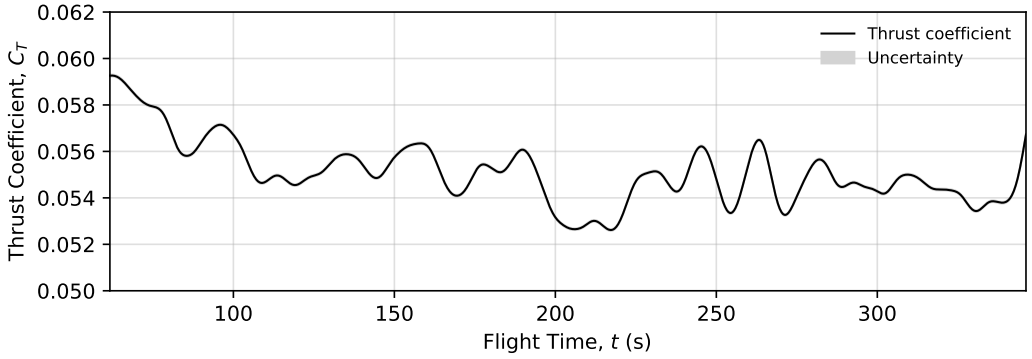

Figure 6.22: Thrust coefficient of the SLE blade in hover OGE for Test Flight 1. The magnitude of the uncertainty is small and cannot be observed.

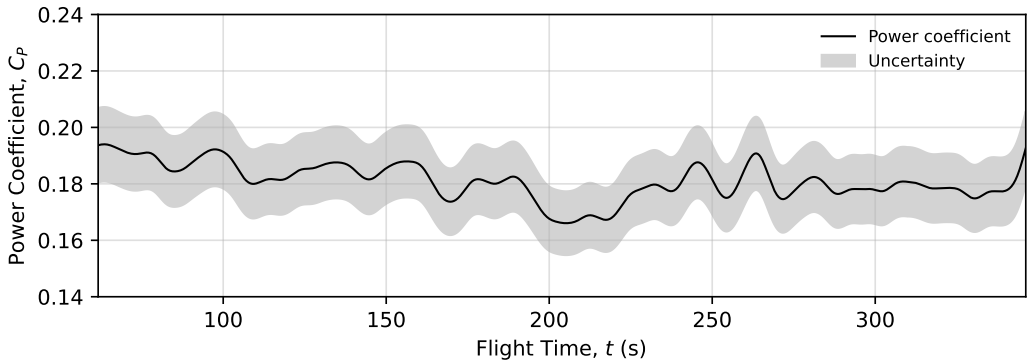

Figure 6.23: Power coefficient of the SLE blade in hover OGE for Test Flight 1.

Figure 6.25 shows histograms of the calculated thrust coefficient, power coefficient, and figure of merit values shown in Figures 6.22, 6.23, and 6.24. All three parameters are shown to approximately follow a normal distribution, allowing the average value to be used to represent the hover performance of the entire test flight. This same procedure was followed to obtain the average thrust coefficient, power coefficient, and figure of merit for each of the six test flights. These results are summarized in Table 6.9, along with the predicted values using BEMT. The average rotational rate of the monocopter

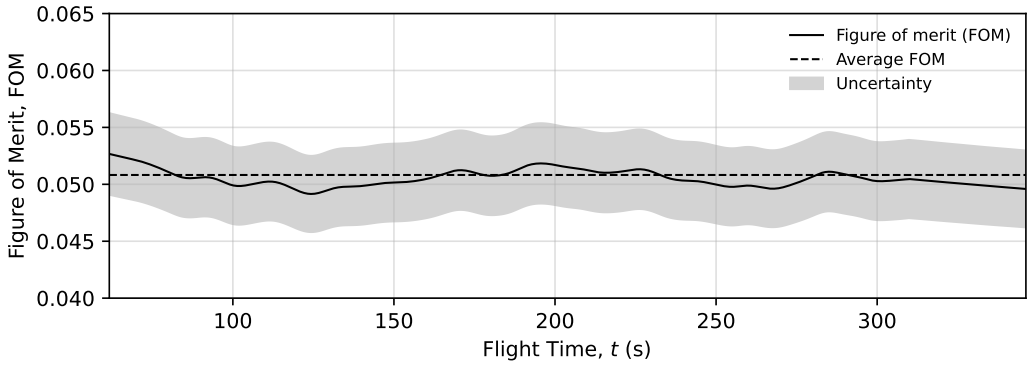

Figure 6.24: Figure of merit of the RMC monocopter in hover OGE for Test Flight 1.

is also provided. The variations in the average figure of merit for each flight are a result of varying ambient conditions for each test.

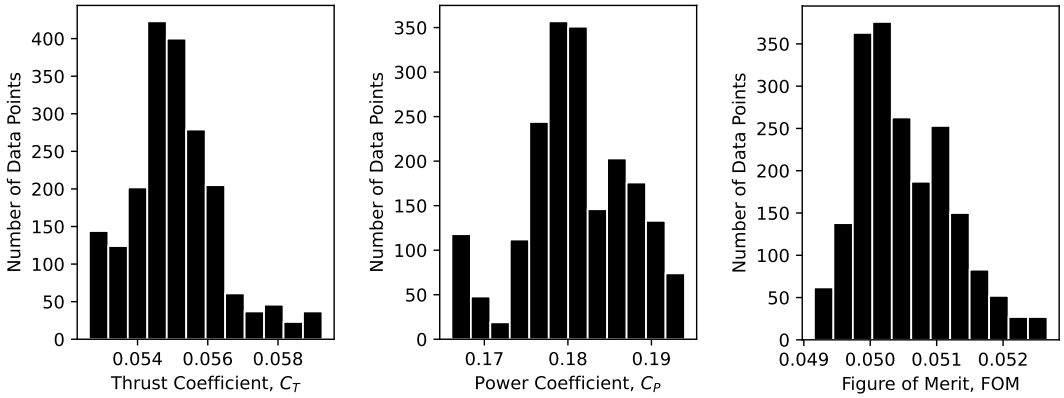

(a) Thrust coefficient. (b) Power coefficient. (c) Figure of merit.

Figure 6.25: Histogram of the calculated values for flight test 1.

Table 6.9: Summary of the flight test results for the RMC monocopter with a straight leading edge blade.

Flight	C_T	C_P	FOM	RPM
1	0.055	0.182	0.051	105
2	0.058	0.202	0.048	103
3	0.069	0.296	0.043	95
4	0.069	0.300	0.043	95
5	0.066	0.284	0.042	97
6	0.069	0.305	0.042	94
BEMT	0.021	0.040	0.054	156

When compared to the flight test results, the BEMT analysis over predicts the rotational speed of the monocopter. This results in a significantly reduced estimate of the thrust coefficient and required power coefficient. However, the thrust and power coefficients were under-predicted by proportional amounts such that the predicted figure of merit

was on the same order of magnitude as the experimental results. The over prediction of the rotational speed of the monocopter is likely due to simplifications and assumptions made when incorporating the propeller slipstream effects, and drag of non-lifting surfaces into the BEMT analysis. More specifically, the telemetry pad was assumed to be a non-lifting surface producing zero lift (or thrust). In reality, the telemetry pad could be generating enough lift to deviate from the BEMT prediction. More details on these assumptions can be found in Appendix E. These results were deemed acceptable and used as a baseline for comparison for the A02λ09 blade and A02λ09p blade.

6.4.2 Effect of Tubercles on Hover Performance

The same procedure described to obtain the results for the SLE blade were followed to obtain the hover performance of the A02λ09 and A02λ09p blades, quantified by the thrust coefficient, power coefficient, figure of merit, and rotational rate. As an example, the thrust coefficient, power coefficient and figure of merit as a function of time spent in hover for the A02λ09 and A02λ09p blades for flight test 1 will be compared to the results for the SLE blade which were presented earlier. Figure 6.26 shows a direct comparison of the calculated thrust coefficients as a function of time spent in hover between the three blades. The magnitude of the uncertainty was similar to the SLE blade, and is not shown to improve the readability of the figure.

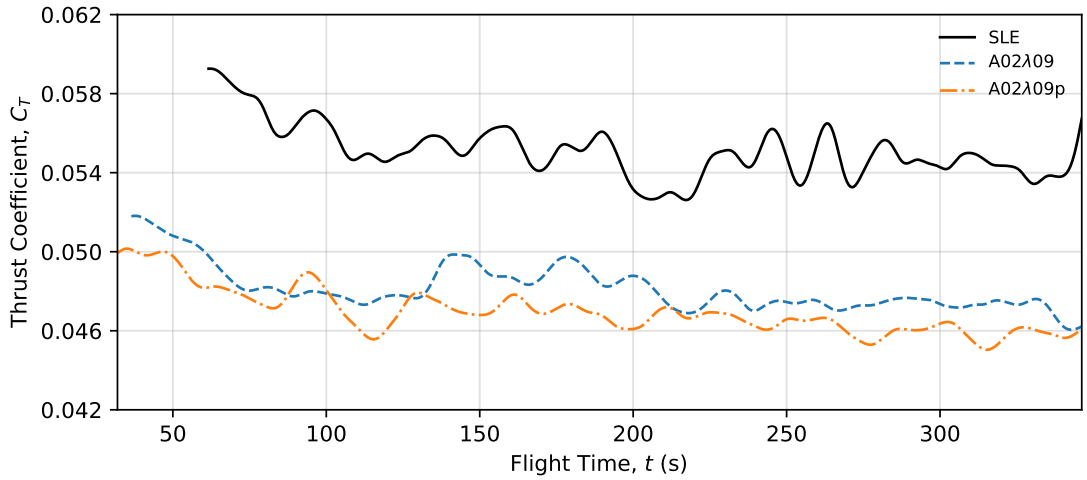

Figure 6.26: Thrust coefficient of the A02λ09 and A02λ09p blades compared to the SLE blade in hover OGE for Test Flight 1.

The thrust required to hover is produced by the lift generated by the blade as the monocopter rotates. Changes in the thrust coefficient can reveal information regarding changes in the lift coefficient of the blade. Since the mass of the monocopter with the different blades did not vary greatly (see Table 6.6), it can be assumed that the thrust required to hover was constant. The addition of tubercles resulted in a 13.2% decrease in average thrust coefficient over the entire time spent in hover for the A02λ09 blade, and a 15.4% decrease for the A02λ09p blade. This is explained by examining an expression for the thrust required to hover, which can be obtained by rearranging Equation 6.3:

$$T = \rho\pi\Omega^2 R^4 C_T \tag{6.5}$$

Further assuming that the ambient conditions are constant, a decrease in the thrust coefficient, C_T, necessitates a proportional increase in the rotational rate, Ω. This was confirmed by examining the measured rotational rate of the monocopter. An average rotational rate of 105 RPM for the SLE blade was measured, while an average rotational rate of 113 RPM (+7.6%) and 114 RPM (+8.6%) was measured for the A02λ09 blade and A02λ09p blade respectively. In addition, since the thrust coefficient is related to the lift generated by the blade, a decrease in the thrust coefficient can only occur alongside a decrease in the local lift coefficients along the blade. Focusing on the A02λ09 blade and returning to Equation 6.5, a 7.6% increase in rotational rate equates to a 13.6% decrease in the thrust coefficient, which is very close to the measured decrease of 13.2%. The subscripts denote the measured values for the respective blades:

$$
\begin{aligned}
T_{\mathrm{SLE}} &= T_{\mathrm{A02\lambda09}} \\
\rho\pi\Omega_{\mathrm{SLE}}^2 R^4 C_{T,\mathrm{SLE}} &= \rho\pi\Omega_{\mathrm{A02\lambda09}}^2 R^4 C_{T,\mathrm{A02\lambda09}} \\
\Omega_{\mathrm{SLE}}^2 C_{T,\mathrm{SLE}} &= \Omega_{\mathrm{A02\lambda09}}^2 C_{T,\mathrm{A02\lambda09}} \\
\Omega_{\mathrm{SLE}}^2 C_{T,\mathrm{SLE}} &= \left(1.076\Omega_{\mathrm{SLE}}\right)^2 C_{T,\mathrm{A02\lambda09}} \\
C_{T,\mathrm{SLE}} &= 1.076^2 C_{T,\mathrm{A02\lambda09}} \\
\frac{1}{1.076^2} &= \frac{C_{T,\mathrm{A02\lambda09}}}{C_{T,\mathrm{SLE}}} \\
\frac{C_{T,\mathrm{A02\lambda09}}}{C_{T,\mathrm{SLE}}} - 1 &= \frac{1}{1.076^2} - 1 \\
\frac{C_{T,\mathrm{A02\lambda09}} - C_{T,\mathrm{SLE}}}{C_{T,\mathrm{SLE}}} \times 100\% &= -13.6\%
\end{aligned}
$$

The results of the experimental wind tunnel campaign presented in Chapter 4 concluded that tubercles provide up to a 45.2% increase in post-stall lift coefficients at the cost of up to a 22.4% reduced lift coefficient just before stall. The local angles of attack estimated using BEMT shown in Figure 6.6 show that the majority of the blade is operating approximately 4° before the stall angle of 18°, according to Tung and McAlister [90]. The measured 13.2% and derived 13.6% decrease in thrust coefficient for the A02λ09 blade are in agreement with the conclusions from Chapter 4. The same conclusions can be drawn for the A02λ09p blade, which had a very similar increase in rotational speed.

The power required to hover is dictated by the drag generated by the blade that must be overcome by the propulsive force of the blade-mounted propeller. Therefore, changes in the power coefficient can be associated with changes in the drag coefficient of the blade. Figure 6.27 shows a direct comparison of the calculated power coefficients as a function of time spent in hover between the three blades for Test Flight 1. The magnitude of the uncertainty was similar to the SLE blade, and is not shown to improve the readability of the figure.
The addition of tubercles had a much more significant impact on the power coefficient than was observed for the thrust coefficient, resulting in a 22.0% and 30.0% decrease in average power coefficient over the entire time spent in hover for the A02λ09 and A02λ09p blades, respectively. Similar to the reduction in thrust coefficient, a portion of this decrease in power coefficient stems from the increased rotational rate. The expected decrease in power coefficient can be determined starting with an expression for the power required for hover, obtained by rearranging Equation 6.3:

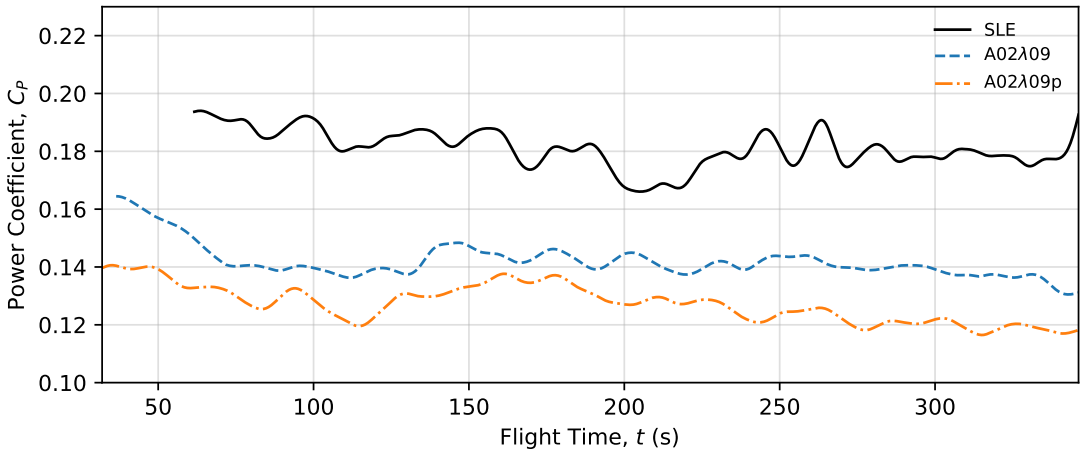

Figure 6.27: Power coefficient of the A02λ09 and A02λ09p blades compared to the SLE blade in hover OGE for Test Flight 1.

$$P = \rho\pi\Omega^3 R^5 C_P \tag{6.6}$$

Using the A02λ09 blade as an example, if the A02λ09 blade required the same power to hover as the SLE blade, but with a higher rotational rate of 113 RPM (+7.6% from SLE rotational rate of 105 RPM) only a 19.7% decrease in power coefficient would be expected, as shown by the following development:

$$\begin{aligned}
P_{\text{SLE}} &= P_{\text{A02}\lambda09} \\
\rho\pi\Omega_{\text{SLE}}^3 R^5 C_{P,\text{SLE}} &= \rho\pi\Omega_{\text{A02}\lambda09}^3 R^5 C_{P,\text{A02}\lambda09} \\
\Omega_{\text{SLE}}^3 C_{P,\text{SLE}} &= \Omega_{\text{A02}\lambda09}^3 C_{P,\text{A02}\lambda09} \\
\Omega_{\text{SLE}}^3 C_{P,\text{SLE}} &= (1.076\Omega_{\text{SLE}})^3 C_{P,\text{A02}\lambda09} \\
C_{P,\text{SLE}} &= 1.076^3 C_{P,\text{A02}\lambda09} \\
\frac{1}{1.076^3} &= \frac{C_{P,\text{A02}\lambda09}}{C_{P,\text{SLE}}} \\
\frac{C_{P,\text{A02}\lambda09}}{C_{P,\text{SLE}}} - 1 &= \frac{1}{1.076^3} - 1 \\
\frac{C_{P,\text{A02}\lambda09} - C_{P,\text{SLE}}}{C_{P,\text{SLE}}} \times 100\% &= -19.7\%
\end{aligned}$$

A decrease in power coefficient of a similar magnitude would be expected for the A02λ09p blade. Since much larger decreases in power coefficient were observed in actuality, another mechanism for reducing the power coefficient must exist. Since the power coefficient is closely linked to the drag generated by the blade, the remaining decrease in power coefficient is likely a result of a decreased drag coefficient generated by the blades with tubercles.

While the drag performance of tubercles were not discussed in Chapter 4, the drag results are presented in Appendix C in Figures C.10 through C.17 for power-off and on cases. Results at $\text{Re} = 1.0 \times 10^5$ are the most representative of the flow conditions

experienced by the blade during the flight tests. The tubercles were shown to alter the drag coefficients at angles of attack around stall by modifying the angle of attack at which stall occurred, thus changing the angle of attack at which the steep drag rise accompanying stall was experienced. This suggests that the SLE blade was actually operating at larger angles of attack closer to, or exceeding, the stall angle of the Vertol VR-7 airfoil, contrary to the predicted local angles of attack presented in Figure 6.6. This would allow the A02λ09 and A02λ09p blades to provide a large decrease in drag by delaying stall, explaining the significant decrease in power coefficient observed in Figure 6.27.

The figure of merit for the A02λ09 and A02λ09p blades as a function of the time spent in hover compared to the SLE blade for Test Flight 1 is shown in Figure 6.28. The average figure of merit for each blade is indicated by the labelled, horizontal dashed lines. The magnitude of the uncertainty was similar to the SLE blade, and is not shown to improve the clarity of the figure.

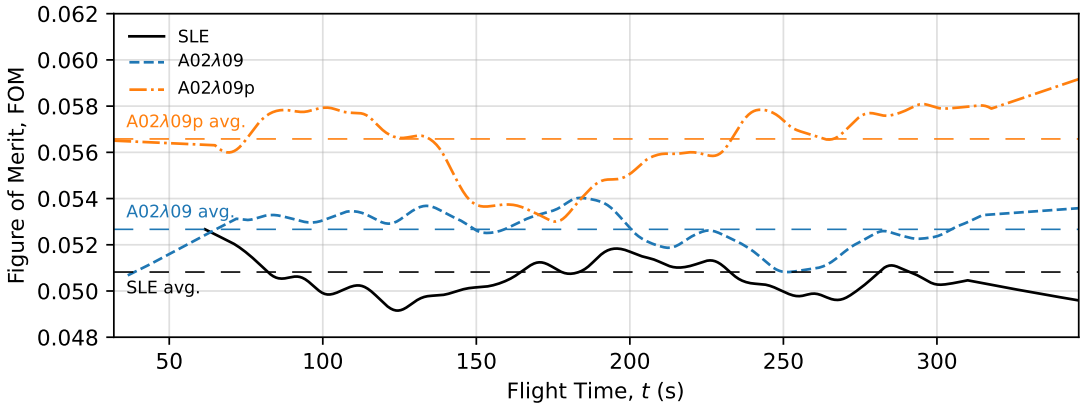

Figure 6.28: Figure of merit of the A02λ09 and A02λ09p blades compared to the SLE blade in hover OGE for Test Flight 1.

The A02λ09 blade increased the average figure of merit by 3.3% and the A02λ09p blade increased the average figure of merit by 10.4%, establishing the A02λ09p as the best performing blade in hover by a significant margin. The figure of merit for a rotor is analogous to the aerodynamic efficiency of a wing. Since the thrust and power coefficients are closely linked to the lift and drag coefficient of the blade sections, insight into the increased figure of merit for the tubercle blades can be provided by examining the aerodynamic efficiency of tubercles compared to an SLE. Figure 6.29 shows the relative change in aerodynamic efficiency for the six tubercle geometries tested in Chapter 3, compared to an SLE wing at Re $= 1.0 \times 10^5$ for angles of attack between 0° and 45°. Figure 6.30 shows the same information for the power-on condition with the propeller positioned at the optimal propeller position determined in Chapter 4.
It is to be noted that these results are for a NACA0018 profile and are not directly applicable to the RMC monocopter blades. However, the general trends still apply to the Vertol VR-7 airfoil. For angles of attack less than approximately 12° all tubercle wings reduced the aerodynamic efficiency by up to 50% for the power-off condition, and 40% for the power-on condition. The A02λ09 tubercle geometry in particular, which was the tubercle geometry that was flight tested on the RMC monocopter is shown to

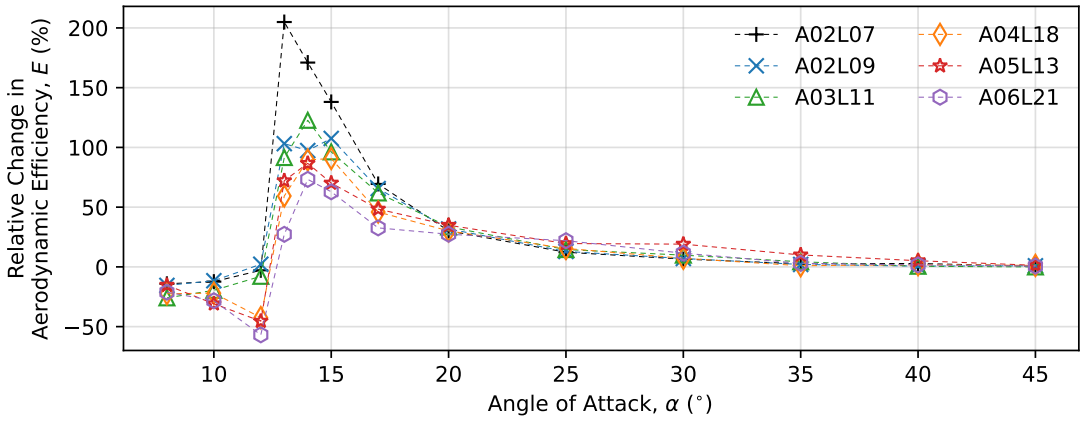

Figure 6.29: Relative change in aerodynamic efficiency for six tubercle wings at $\mathrm{Re} = 1.0 \times 10^5$ with no propeller.

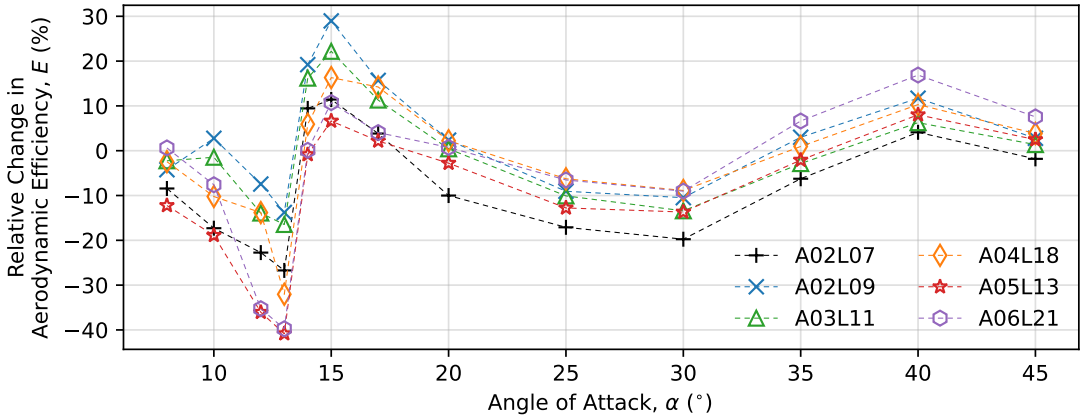

Figure 6.30: Relative change in aerodynamic efficiency for six tubercle wings at $\mathrm{Re} = 1.0 \times 10^5$ with the propeller at the optimal location ($X_\mathrm{p} = 0.25$, $Z_\mathrm{p} = 0$).

provide a 100% increase in aerodynamic efficiency just after stall at the cost of up to a 13% decrease before stall for the power-off condition. When a propeller slipstream is present, the A02λ09 tubercle geometry shows up to a 30% increase in aerodynamic efficiency at the cost of up to a 10% decrease before stall. If the monocopter blades were operating at angles of attack exceeding stall, as suggested by the significantly decreased power coefficients, they would also experience an increase in aerodynamic efficiency, explaining the increased figure of merit.

The effect of the tubercles on the hover performance of the RMC monocopter were consistent across all six test flights. The trends that were identified above for Test Flight 1 apply to Test Flights 2 to 6 as well. Table 6.10 summarizes the hover performance of the RMC monocopter with the A02λ09 and A02λ09p blades, quantified by the thrust coefficient, power coefficient, figure of merit, and rotational rate, for all six test flights. The relative change in these values were calculated using the respective SLE blade results for each test flight. Since the test flights were conducted on separate days, the results were not directly compared between different test flights.

Table 6.10: Summary of flight test results for the RMC monocopter with the A02λ09 and A02λ09p blades.

Flight	Blade	C_T	ΔC_T (%)	C_P	ΔC_P (%)	FOM	ΔFOM (%)	RPM
1	SLE	0.055	-	0.182	-	0.051	-	105
	A02λ09	0.048	-13.2	0.142	-22.0	0.053	+3.6	113
	A02λ09p	0.047	-15.4	0.127	-30.0	0.056	+11.3	114
2	SLE	0.058	-	0.202	-	0.049	-	103
	A02λ09	0.047	-18.5	0.135	-33.2	0.053	+10.2	114
	A02λ09p	0.047	-18.8	0.128	-36.8	0.056	+15.8	114
3	SLE	0.069	-	0.296	-	0.043	-	95
	A02λ09	0.047	-30.9	0.137	-53.6	0.053	+23.7	113
	A02λ09p	0.047	-31.2	0.129	-56.5	0.056	+31.2	109
4	SLE	0.069	-	0.300	-	0.043	-	95
	A02λ09	0.050	-26.7	0.155	-48.1	0.051	+20.7	110
	A02λ09p	0.051	-25.8	0.146	-51.2	0.056	+30.8	109
5	SLE	0.066	-	0.284	-	0.042	-	97
	A02λ09	0.048	-26.2	0.151	-46.9	0.050	+19.5	112
	A02λ09p	0.054	-18.1	0.163	-42.7	0.054	+29.2	106
6	SLE	0.069	-	0.305	-	0.042	-	94
	A02λ09	0.051	-25.5	0.165	-45.7	0.050	+18.3	109
	A02λ09p	0.051	-26.2	0.150	-50.6	0.054	+28.2	109

When comparing the A02λ09 blade to the A02λ09p blade, the A02λ09p blade consistently showed superior hover performance across all six test flights in the form of a larger figure of merit. As shown in Figure 6.3, the A02λ09 blade has tubercles across the entire leading edge of the blade, while the A02λ09p only has tubercles directly behind the propeller, which was located at 60% of the blade radius measured from the blade root. The lower figure of merit of the A02λ09 blade suggests that including tubercles at certain positions along the blade radius penalizes the hover performance of the monocopter. More specifically, placing tubercles at the root and the tip of the blade reduces the figure of merit. This is explained by examining the predicted local angles of attack shown in Figure 6.6. The blade root and blade tip experience angles of attack that are a fraction of the angle of attack in the centre of the blade as a result of low inflow velocities at the root, and tip losses towards the tip. The aerodynamic performance of tubercles is reduced at angles of attack before stall, therefore including tubercles at the radial locations where the local angles of attack are less than the stall angle results in a reduction in hover performance. This occurred with the A02λ09 blade. When the tubercles are only placed at radial locations that operate at angles of attack that ex-

ceed the stall angle, the aerodynamic performance is improved without the aerodynamic penalties at the lower angles of attack. This occurred with the A02λ09p blade.

6.4.3 Implications for Tilt-Wing Aircraft

The results of the flight testing of the RMC monocopter with the SLE, A02λ09, and A02λ09p blades demonstrated the potential gains in aerodynamic performance possible with the addition of tubercles. While not directly comparable to a tilt-wing aircraft, the similarities in the aerodynamic environment of the monocopter blade and the blown wing of a tilt-wing aircraft allows for the results of this flight test campaign to be extrapolated and applied to tilt-wing transition. The flight test results showed that the benefits of tubercles lies in the increased aerodynamic efficiencies at post-stall angles of attack. For the monocopter, this resulted in a larger figure of merit in hover OGE. For a tilt-wing aircraft, this would result in a more power efficient transition that would require less fuel. Less fuel burned during transition would leave more fuel to be used for other segments of the mission, such as extending range or endurance. While tubercles have been shown to penalize aerodynamic performance at lower angles of attack, the analysis conducted in Chapter 5 concluded that the net effect of tubercles was beneficial to transition. The increase in figure of merit for the RMC monocopter with tubercles was significant, with the largest observed increase in figure of merit at 19.6%. The reduction in power required to transition for a tilt-wing aircraft would be less significant since the tilting wing would only operate at post-stall angles of attack for brief periods of time. Finally, early conceptual studies by McKinney *et al.* showed that the largest power requirement for any VTOL aircraft is for hover [19]. The power requirement for transition is not a critical design parameter, and therefore do not have as large of an impact on the overall design of a tilt-wing aircraft as the power requirement for hover (the critical case). For these reasons, while these flight test results successfully demonstrated a practical application of tubercles, the proposed impact on the transition of tilt-wing aircraft is merely a secondary effect to the expansion of the left bound of the transition corridor demonstrated in Chapter 5.

7 Conclusions and Recommendations

The aim of this research was to investigate how sinusoidal leading edge tubercles would affect the transition performance of a tilt-wing aircraft. This final chapter will summarize the research findings, provide concluding remarks, suggestions for improvements, and recommendations for future research on this topic.

7.1 Conclusions

A preliminary experimental wind tunnel campaign with the aim of determining the optimal propeller position for tilt-wing transition was conducted. The investigation consisted of testing a variety of different propeller positions relative to the leading edge of the wing at Reynolds numbers between $\mathrm{Re} = 1.0 \times 10^5$ and $\mathrm{Re} = 2.5 \times 10^5$, at angles of attack between 0° and 45°. The results of this investigation were in good agreement with the current body of knowledge. The main parameter investigated was the lift augmentation, defined as the increase in lift coefficient as a result of the propeller slipstream. It was concluded that the amount of lift augmentation provided by the propeller was a function of the position of the slipstream relative to the wing, which itself was determined to be a function of, in order of significance, the propeller position, and angle of attack. Changing the position of the propeller slipstream relative to the wing modified the local velocities over the pressure and suction surfaces to varying degrees, resulting in the modification of the lift generated by the wing. If the slipstream was positioned such that the suction surface experienced a greater increase in local velocity than the pressure surface, an increase in the lift was observed. The propeller vertical position modified the vertical position of the propeller slipstream relative to the wing, resulting in variations in lift augmentation. Angle of attack resulted in the slipstream skewing in the direction of the freestream, changing how it interacted with the wing, thus modifying the extent of lift augmentation observed at different angles of attack. Lift augmentation was less sensitive to the chordwise position of the propeller slipstream relative to the wing, and so the propeller chordwise position had little effect on the lift augmentation. The propeller position that provided the most lift augmentation was shown to vary with angle of attack. A trade-off in lift augmentation at pre-stall and post-stall angles of attack was identified. Propeller positions above the wing chord provided the most lift augmentation at $\alpha \lesssim 14°$, while positions below the wing provided the most lift augmentation at $\alpha \gtrsim 14°$. It was recommended that for conventional, fixed-wing aircraft that seldom operate at post-stall angles of attack, a propeller installation above the wing provides the most lift augmentation. This is currently typical on

short takeoff and landing aircraft.

To address the interplay between propeller vertical position and angle of attack, and their influence on lift augmentation, a method for evaluating the effectiveness of each propeller position for tilt-wing transition was developed. The method assigned a lift augmentation score to each propeller position that quantified total lift augmentation provided between an angle of attack of 0° and 45°. Using this method, for the Reynolds numbers tested, an optimal propeller position was determined to be 0.25 propeller diameters upstream of the leading edge, with the propeller centred on the wing chord. Six sinusoidal tubercle geometries with varying amplitudes and wavelengths were investigated with the propeller placed at the optimal propeller position. The tubercles provided up to 27% increased post-stall lift at the cost of up to 19.9% decreased lift just before stall. They were also shown to improve the stall behaviour of the wing, by attenuating the abrupt decrease in lift associated with stall of the wing profile tested (NACA 0018). The overall effect of the tubercles on the aerodynamic performance of a blown wing were the same as their effect on an unblown wing, but to a lesser degree. The magnitudes of the increased post-stall lift and decreased pre-stall lift were smaller when blown. This was attributed to the propeller slipstream interfering with the development of the counter-rotating streamwise vortices that are attributed with the lift enhancements. Smaller amplitude tubercles were shown to provide less lift augmentation when blown compared to when unblown, while larger amplitude tubercles were less affected by the propeller slipstream. It was hypothesized that the weaker counter-rotating streamwise vortices generated by smaller amplitude tubercles were undergoing vortex bursting when placed in a propeller slipstream, resulting in their decreased effectiveness in blown conditions. The $0.04c$ amplitude and $0.18c$ wavelength wing was identified as the best overall tubercle configuration in terms of lift augmentation when the entire range of angles of attack were considered, making it the most suitable geometry for improving tilt-wing transition. The $0.02c$ amplitude and $0.09c$ wavelength wing provided the most lift augmentation at moderate angles of attack (just after stall) with the smallest penalty in pre-stall lift.

In order to apply the results of the experimental wind tunnel campaign to the analysis of a tilt-wing aircraft, a detailed concept for a small scale, tail sitter UAV called the RMC Transition Research Vehicle (TRV) was developed. A tail-sitter configuration was selected for its relative simplicity compared to a tilt-wing design, while retaining the same aerodynamic environment that a tilt-wing encounters. An empirical model was developed using the results of the experimental wind tunnel campaign, and paired with a numerical simulation of transition to generate the transition corridor of the RMC TRV, and to simulate the effect of tubercles on transition. Results showed that tubercles are an effective method for improving the safety of tilt-wing transition, allowing for the minimum required forward flight speed during transition to be reduced by nearly 10%. This expanded the transition corridor, increasing the margin of safety during transition. These results show that tubercles are an effective method for improving the safety of tilt-wing transition.

Finally, a surrogate vehicle called a monocopter, which possesses a blown lifting surface that operates at high angles of attack much like the blown wing of a tilt-wing aircraft, was designed and flight tested. This flight test campaign allowed for a practical inves-

tigation of the effect of tubercles on a localized region of the transition corridor that corresponded to the flight condition of the monocopter in hover. Three blades were tested: a straight leading edge blade, called the SLE blade, a blade with $0.02c$ amplitude and $0.09c$ wavelength tubercles along the entire length of the blade, called the A02λ09 blade, and a blade with $0.02c$ amplitude and $0.09c$ wavelength tubercles only along the section of blade directly behind the propeller, called the A02λ09p. The thrust coefficient, power coefficient, and figure of merit of each blade in hover was calculated. The blade with tubercles only behind the propeller increased the figure of merit relative to the SLE blade by up to 31.2%, while the blade with full span tubercles increased the figure of merit by up to 23.7%. This result suggests that in addition to the expansion of the transition corridor, tubercles allow for a more power efficient transition, translating to increased range, endurance, or payload capacity.

7.2 Recommendations for Future Work

A number of potential areas for future investigation have been identified that would contribute to demonstrating the effectiveness of tubercles on a blown system that experiences high angles of attack. This section presents these recommendations.

The behaviour of tubercles when placed in a propeller slipstream was shown to differ from their behaviour with no propeller. These differences were hypothesized to be a result of the interactions between the propeller slipstream and the counter-rotating streamwise vortices generated by the tubercles. More specifically, vortex bursting was suspected to cause smaller amplitude tubercles to provide less lift augmentation when blown. Further experimental testing is recommended to test this hypothesis. Flow visualization techniques that can capture 3D flow structures that exist off the surface of the wing, such as particle image velocimetry, hydrogen-bubble flow visualization, or a wake survey, would provide insight into the validity of this hypothesis.

The numerical simulation of transition along with the empirical model developed to analyze the effect of tubercles on the transition corridor of the RMC TRV served as a preliminary design estimate. The assumed thrust could be replaced with a detailed thrust model to reflect real-world conditions better. Validation of the developed method with higher fidelity aerodynamic modelling techniques, such as 3D panel methods or CFD simulations, is recommended. While these techniques can be employed to validate results at small vehicle tilt angles, accurate prediction of aerodynamic forces at high angles of attack would still be a problem. For this reason, the fabrication and flight testing of the RMC TRV is recommended. While the flight testing of the surrogate monocopter provided insight into the benefits of tubercles on a blown system at high angles of attack, results were only applicable to a small subset of vehicle tilt angles and were not representative of the entire transition corridor of a VTOL aircraft. A flight test campaign of the RMC TRV would accurately capture the complex flow physics of tubercles at high angles of attack, propeller-wing interactions, and other neglected, assumed or simplified factors in the numerical simulations, providing definitive results regarding the effect of tubercles on transition.

Bibliography

[1] Yaoming Zhou, Haoran Zhao, and Yaolong Liu. An evaluative review of the VTOL technologies for unmanned and manned aerial vehicles. *Computer Communications*, 149:356–369, 2020.

[2] Xufei Yan, Bin Lou, Anhuan Xie, Lingkai Chen, and Dan Zhang. A review of advanced high-speed rotorcraft. *IOP Conference Series: Materials Science and Engineering*, 1102(1):012006, March 2021.

[3] Adnan S. Saeed, Ahmad Bani Younes, Chenxiao Cai, and Guowei Cai. A survey of hybrid unmanned aerial vehicles. *Progress in Aerospace Sciences*, 98:91–105, 2018.

[4] D. Finger, Carsten Braun, and Cees Bil. A review of configuration design for distributed propulsion transitioning VTOL aircraft. In *Asia Pacific International Symposium on Aerospace Technology*, Seoul, Korea, October 2017.

[5] Janes Information Group. Bell Boeing V-22 Osprey. https://customer-janes-com.journal.rmc.ca/display/JAWA1176-JAWA, Nov 2022. [Online; accessed 22-February-2023].

[6] Janes Information Group. Bell Eagle Eye. https://customer-janes-com.journal.rmc.ca/display/juav1310-juav, May 2011. [Online; accessed 22-February-2023].

[7] Henry L. Kelley, John P. Reeder, and Robert A. Champine. Summary of a flight-test evaluation of the CL-84 Tilt-Wing V/STOL aircraft. Technical Memorandum TM-X-1914, NASA, March 1970.

[8] William J. Fredericks, Robert G. McSwain, Brian F. Beaton, and David W. Klassman. Greased Lightning (GL-10) flight testing campaign. Technical Memorandum TM-2017-219643, NASA, July 2017.

[9] Airbus. Vahana. https://www.airbus.com/en/urbanairmobility/cityairbus-nextgen/vahana, July 2021. [Online; accessed 22-February-2023].

[10] Janes Information Group. Mcdonnel douglas AV-8B/TAV-8B harrier II plus. https://customer-janes-com.journal.rmc.ca/display/JFS_1606-JFS_, Jan 2023. [Online; accessed 22-February-2023].

[11] William F. Chana and J.F. Coleman. World's first VTOL airplane convair/navy XFY-1 pogo. *SAE Transactions*, 105:1261–1266, 1996.

[12] Janes Information Group. AV SkyTote. https://customer-janes-com.journal.rmc.ca/display/juava025-juav, May 2010. [Online; accessed 22-February-2023].

[13] Dassault Aviation. Mirage III V. https://www.dassault-aviation.com/en/passion/aircraft/military-dassault-aircraft/mirage-iii-v/, April 2013. [Online; accessed 22-February-2023].

[14] Janes Information Group. AeroVironment JUMP series. https://customer-janes-com.journal.rmc.ca/display/JUAVA853-JUAV, Oct 2022. [Online; accessed 22-February-2023].

[15] Adam Cohen, Susan Shaheen, and Emily Farrar. Urban air mobility: History, ecosystem, market potential, and challenges. *IEEE Transactions on Intelligent Transportation Systems*, pages 1–14, June 2021.

[16] Federal Aviation Administration. Urban air mobility and advanced air mobility. https://www.faa.gov/uas/advanced_operations/urban_air_mobility, June 2022. [Online; accessed 17-January-2023].

[17] W. Johnson, C. Silva, and E. Solis. Concept vehicles for VTOL air taxi operations. In *AHS Specialists Conference on Aeromechanics Design for Transformative Vertical Flight*, San Francisco, CA, January 2018.

[18] Richard E. Kuhn. Review of basic principles of V/STOL aerodynamics. In *Conference on V/STOL Aircraft*, Hampton, VA, November 1960.

[19] M. O. McKinney, R. H. Kirby, and W. A. Newsom. Aerodynamic factors to be considered in the design of tilt-wing V/STOL airplanes. *Annals of the New York Academy of Sciences*, 107(1):221–248, 1963.

[20] William F. Chana and T. M. Sullivan. The tilt wing advantage for high speed VSTOL aircraft. *SAE Transactions*, 101:1535–1543, 1992.

[21] Tilt Rotor Project Office Staff. NASA/Army XV-15 tilt rotor research aircraft familiarization document. Technical Memorandum TM-X-62, 407, NASA, January 1975.

[22] John P. Reeder. Handling qualities experience with several VTOL research aircraft. In *NASA Conference on V/STOL Aircraft*, Langley Field, VA, January 1960.

[23] S. Sudhakar, N. Karthikeyan, and L. Venkatakrishnan. Influence of leading edge tubercles on aerodynamic characteristics of a high aspect-ratio uav. *Aerospace Science and Technology*, 69:281–289, 2017.

[24] Stewart J. Reid, Ruben E. Perez, and Asad Asghar. Characterization of tubercle effects on finite span wings. In *AIAA AVIATION Forum*, Dallas, TX, June 2019.

[25] Ryley Colpitts and Ruben E. Perez. Application of leading-edge tubercles on rotor blades. *AIAA Journal*, 61(1):255–270, 2023.

[26] Asad Asghar, Ruben Perez, and William Allan. Application of leading edge tubercles to enhance propeller performance. In *AIAA AVIATION Forum*, Atlanta, GA, June 2018.

[27] A. Asghar, W.D.E. Allan, M. LaViolette, and R. Woodason. Influence of a novel 3D leading edge geometry on the aerodynamic performance of low pressure turbine blade cascade vanes. In *Proceedings of ASME Turbo Expo 2014: Turbine Technical Conference and Exposition*, Düsseldorf, Germany, June 16–20 2014.

[28] D. M. Bushnell and K. J. Moore. Drag reduction in nature. *Annual Review of Fluid Mechanics*, 23(1):65–79, 1991.

[29] Frank E. Fish and Juliann M. Battle. Hydrodynamic design of the humpback flipper. *Journal of morphology*, 225:51–60, July 1995.

[30] P. Watts and F.E. Fish. The influence of passive, leading edge tubercles on wing performance. In *Proceedings of the Twelfth International Symposium on Unmanned Untethered Submersible Technology (UUST01), Autonomous Undersea Systems Inst.*, Lee, NH, August 2001.

[31] Lois King Winn and Howard Elliott Winn. *Wings in the sea: the Humpback Whale*. University Press of New England, 1985.

[32] Frank E. Fish. Biomimetics: Determining engineering opportunities from nature. *Proceedings of SPIE - The International Society for Optical Engineering*, 7401, 08 2009.

[33] Asad Asghar, Ruben E. Perez, and Mohsen Ferchichi. Effect of leading edge tubercles on transonic performance of airfoils. In *35th AIAA Applied Aerodynamics Conference*, Denver, CO, June 2017.

[34] Alexi Levert-Beaulieu, Ruben E. Perez, and Peter W. Jansen. Euler-based aerodynamic shape optimization of leading edge tubercles in transonic flow. In *AIAA SciTech Forum*, San Diego, CA, January 2019.

[35] Hugo T.C. Pedro and M.H. Kobayashi. Numerical study of stall delay on humpback whale flippers. In *46th AIAA Aerospace Sciences Meeting and Exhibit*, Reno, NV, January 2008.

[36] A. Skillen, A. Revell, A. Pinelli, U. Piomelli, and J. Favier. Flow over a wing with leading-edge undulations. *AIAA Journal*, 53(2):464–472, 2015.

[37] Kristy L. Hansen, Nikan Rostamzadeh, Richard M. Kelso, and Bassam B. Dally. Evolution of the streamwise vortices generated between leading edge tubercles. *Journal of Fluid Mechanics*, 788:730–766, January 2016.

[38] Michael Jordan Stanway. Hydrodynamic effects of leading-edge tubercles on control surfaces and in flapping foil propulsion. Master's thesis, Massachusetts Institute of Technology, February 2008.

[39] Derrick Custodio. *The Effect of Humpback Whale-Like Leading Edge Protuberances on Hydrofoil Performance*. PhD thesis, Worcester Polytechnic Institute, May 2012.

[40] Kristy Hansen, Richard Kelso, and Bassam Dally. Performance variations of leading-edge tubercles for distinct airfoil profiles. *AIAA Journal*, 49:185–194, January 2011.

[41] Kristy Lee Hansen. *Effect of Leading Edge Tubercles on Airfoil Performance*. PhD thesis, The University of Adelaide, July 2012.

[42] D. S. Miklosovic, M. M. Murray, L. E. Howle, and F. E. Fish. Leading-edge tubercles delay stall on humpback whale (megaptera novaeangliae) flippers. *Physics of Fluids*, 16, March 2004.

[43] G. B. Schubauer and W. G. Spangenberg. Forced mixing in boundary layers. *Journal of Fluid Mechanics*, 8(1):10–32, 1960.

[44] Mohamed Gad-el Hak and Dennis M Bushnell. Separation control. *Journal of Fluids Engineering*, 113:5–30, March 1991.

[45] Ernst A. van Nierop, Silas Alben, and Michael P. Brenner. How bumps on whale flippers delay stall: An aerodynamic model. *Physical review letters*, 100:054502, March 2008.

[46] Luke H. Peristy, Ruben E. Perez, Asad Asghar, and William D. Allan. Reynolds number effect of leading edge tubercles on airfoil aerodynamics. In *34th AIAA Applied Aerodynamics Conference*, Washington, DC, June 2016.

[47] John D. Anderson. *Fundamentals of Aerodynamics*. McGraw-Hill Education, 5th edition, 2011.

[48] Michael. D. Bolzon, Richard M. Kelso, and Maziar Arjomandi. Tubercles and their applications. *Journal of Aerospace Engineering*, 29(1):04015013, 2016.

[49] Hamid Johari, Charles Henoch, Derrick Custodio, and Alexandra Levshin. Effects of leading-edge protuberances on airfoil performance. *AIAA Journal*, 45:2634–2642, November 2007.

[50] David S. Miklosovic, Mark M. Murray, and Laurens E. Howle. Experimental evaluation of sinusoidal leading edges. *Journal of Aircraft*, 44(4):1404–1408, 2007.

[51] Paul W. Weber, Laurens E. Howle, Mark M. Murray, and David S. Miklosovic. Computational evaluation of the performance of lifting surfaces with leading-edge protuberances. *Journal of Aircraft*, 48(2):591–600, 2011.

[52] Paul W. Weber, Laurens E. Howle, and Mark M. Murray. Lift, Drag, and Cavitation Onset On Rudders With Leading-edge Tubercles. *Marine Technology and SNAME News*, 47(01):27–36, January 2010.

[53] Dillon A. Hesketh, Ruben E. Perez, Peter W. Jansen, and Lucas Diatchencko. Analysis of leading edge tubercles applied to vertical axis wind turbines. In *AIAA AVIATION Forum*, Chicago, IL, June 2022.

[54] S. Roy, Bhumika Das, and Ashis Biswas. A comprehensive review of the application of bio-inspired tubercles on the horizontal axis wind turbine blade. *International Journal of Environmental Science and Technology*, pages 1–28, January 2022.

[55] Devansh Agrawal, Faisal As'ad, Blake Berk, Trevor Long, Jackson Lubin, Christopher Courtin, Mark Drela, R. Hansman, and Jacqueline Huynh. Wind tunnel testing of a blown flap wing. In *AIAA AVIATION Forum*, Dallas, TX, June 2019.

[56] Antony Jameson. Analysis of wing slipstream flow interaction. NASA Contractor Reports CR-1632, NASA, August 1970.

[57] Richard E. Kuhn. Semiempirical procedure for estimating lift and drag characteristics of propeller-wing-flap configurations for vertical-and-short-take-off-and-landing airplanes. NASA Memorandum 1-16-59L, NASA, February 1959.

[58] Dave P. Witkowski, Alex K. H. Lee, and John P. Sullivan. Aerodynamic interaction between propellers and wings. In *26th Aerospace Sciences Meeting*, 1988.

[59] Leonardus Louis Maria Veldhuis. *Propeller Wing Aerodynamic Interference*. PhD thesis, Delft University of Technology, June 2005.

[60] Kwanchai Chinwicharnam, David Gomez, Jean-Marc Moschetta, and Chinnapat Thipyopas. Aerodynamic characteristics of a low aspect ratio wing and propeller interaction for a tilt-body MAV. *International Journal of Micro Air Vehicles*, 5:245–260, December 2013.

[61] Ramon Duivenvoorden, Noah Suard, Tomas Sinnige, and Leo L. Veldhuis. Experimental investigation of aerodynamic interactions of a wing with deployed fowler flap under influence of a propeller slipstream. In *AIAA AVIATION Forum*, Chicago, IL, 2022.

[62] George N. Hawkswell, Rob Miller, and Graham Pullan. Selection of propeller-wing configuration for blown wing aircraft. In *AIAA SciTech Forum*, San Diego, CA, January 2022.

[63] Dave P. Witkowski, Alex K. H. Lee, and John P. Sullivan. Aerodynamic interaction between propellers and wings. *Journal of Aircraft*, 26(9):829–836, 1989.

[64] P. van den Borne and J. van Hengst. Investigation of propeller slipstream effects on the Fokker 50 through in-flight pressure measurements. In *Flight Simulation Technologies Conference and Exhibit*, 1990.

[65] Gavin Ananda, Robert Deters, and Michael Selig. Propeller induced flow effects on wings at low reynolds numbers. *31st AIAA Applied Aerodynamics Conference*, January 2013.

[66] Marvin P. Fink, Robert G. Mitchell, and Lucy C. White. Aerodynamic data on large semispan tilting wing with 0.5-diameter chord, double-slotted flap, and both left- and right-hand rotation of a single propeller. Technical Note TN-D-3375, NASA, April 1966.

[67] Marvin P. Fink. Aerodynamic data on large semispan tilting wing with 0.5-diameter chord, single-slotted flap, and single propeller 0.19 chord below wing. Technical Note TN-D-3884, NASA, April 1967.

[68] Marvin P. Fink. Aerodynamic data on large semispan tilting wing with 0.4-diameter chord, single-slotted flap, and single propeller 0.22 chord below wing. Technical Note TN-D-5016, NASA, January 1969.

[69] James L. Hassell Jr. and Robert H. Kirby. Descent capability of two-propeller tilt-wing configurations. In *Conference on V/STOL and STOL Aircraft*, pages 41–50, Mountain View, CA, April 1966.

[70] L.L.M. Veldhuis. Review of propeller-wing aerodynamic interference. In *24th International Congress of the Aeronautical Sciences*, Yokohama, Japan, 2004.

[71] Robert O. Schade and Robert H. Kirby. Effect of wing stalling in transition on a 1/4-scale model of the VZ-2 aircraft. Technical Note TN-D-2381, NASA, August 1964.

[72] Ion Paraschivoiu. *Wind Turbine Design: With Emphasis on Darrieus Concept*. Presses internationales Polytechniques, 2002.

[73] Dominique Poirel, Yael Harris, and A. Benaissa. Aeroelastic dynamics of a NACA 0012 airfoil in the transitional reynolds number regime. *American Society of Mechanical Engineers, Pressure Vessels and Piping Division (Publication) PVP*, 2006, January 2006.

[74] S.J. Kline and F.A. McClintock. Describing uncertainties in single-sample experiments. *Mechanical Engineering*, 75(1):3–8, 1953.

[75] J. Gordon Leishman. *Chapter 2: Fundamentals of Rotor Aerodynamics*, page 55–114. Cambridge University Press, 2nd edition, 2006.

[76] Michael D. Patterson, Kevin R. Antcliff, and Lee W. Kohlman. A proposed approach to studying urban air mobility missions including an initial exploration of mission requirements. In *Annual Forum and Technology Display*, Phoenix, AZ, May 2018.

[77] Paul K. Chang. Separation of flow. *Journal of the Franklin Institute*, 272(6):433–448, 1961.

[78] Vidyadhar Y. Mudkavi. The phenomenon of vortex breakdown. In *Proceedings of the Fluid Dynamics Symposium*, 1993.

[79] Warren F. Phillips. *Chapter 4: Longitudinal Static Stability and Trim*, pages 339–501. John Wiley and Sons, Inc., 2004.

[80] Holybro. Px4 autopilot user guide. https://docs.px4.io/main/en/. [Online; accessed 10-May-2023].

[81] Murat Bronz and Antoine Drouin. Preliminary design estimation of the V/STOL airplane performance. *International Journal of Micro Air Vehicles*, 7(4):449–462, 2015.

[82] Jorge Nocedal and Stephen J. Wright. *Chapter 6: Quasi-Newton Methods*, page 135–162. Springer, 2nd edition, 2006.

[83] Robert G. McSwain and Louis J. Glaab. Greased lightning (GL-10) performance flight research - flight data report. Technical Report TM-2017-219794, NASA, November 2017.

[84] Paul M. Rothhaar, Patrick C. Murphy, Barton J. Bacon, Irene M. Gregory, Jared A. Grauer, Ronald C. Busan, and Mark A. Croom. NASA Langley distributed propulsion VTOL tilt-wing aircraft testing, modeling, simulation, control and flight test development. In *AIAA Aviation Technology, Integration and Operations (ATIO) Conference*, Atlanta, GA, June 2014.

[85] Douglas S. Green. The terminal velocity and dispersal of spinning samaras. *American Journal of Botany*, 67(8):1218–1224, 1980.

[86] A. Rosen and D. Seter. Vertical autorotation of a single-winged samara. *Journal of Applied Mechanics*, 58:1064–1071, December 1991.

[87] James Houghton and Woody Hoburg. Fly-by-wire control of a monocopter. *Massachusetts Institute of Technology, Project Report*, 2008.

[88] A. Safaee, S. Z. Moussavi, M. S. Mehrabani, M. B. Menhaj, and E. Ghobadi. Construction and control of monocopter using MEMS AHRS. In *11th IEEE International Conference on Control and Automation (ICCA)*, pages 219–224, 2014.

[89] Sutthiphong Srigrarom and Muhammad N. Bin Abdul Malik. Development of UGS monocopter: Platform design and trajectory tracking. In *33rd AIAA Applied Aerodynamics Conference*, Dallas, TX, 2015.

[90] C. Tung and K.W. McAlister. Suppression of dynamic stall with a leading-edge slat on a VR-7 airfoil. Technical Paper 3357, NASA, March 1993.

[91] Nefeli Alushi. Access barometric pressure sensor data on nano 33 BLE sense. https://docs.arduino.cc/tutorials/nano-33-ble-sense/barometric-sensor. [Online; accessed 28-March-2023].

[92] APC Propellers. Performance data. https://www.apcprop.com/files/PER3_5x5E.dat. [Online; accessed 17-April-2023].

[93] Frank M. White. *Fluid Mechanics*. McGraw Hill, 7th edition, 2011.

[94] Daniel P. Raymer. *Aircraft Design: A Conceptual Approach*. AIAA Education Series, 1992.

Appendices

A Measurement Uncertainty Calculations

This appendix provides a details on the uncertainty calculations for the post processing of all the data presented in this thesis. First, the uncertainty calculations for the experimental wind tunnel campaign presented in Chapters 3 and 4 will be presented, followed by uncertainty calculations for the flight testing of the monocopter that was discussed in Chapter 6.

A.1 Uncertainty of Wind Tunnel Results

The measured values during the experimental wind tunnel campaign presented in this thesis consisted of *ATI Industrial Mini85* force/torque sensor measurements for the aerodynamic forces generated by the wing, *ATI Industrial Mini27 Titanium* force/-torque sensor measurements of the propeller thrust, and *Scanivalve MPS4264* pressure transducer measurements of surface pressures on the pressure and suction surfaces of the wing. The data measured by each sensor were recorded for 40 seconds at steady state to obtain a set of data for each angle of attack and freestream velocity.

The distribution of the data points collected was shown to be approximately normal, as shown in Figure 3.8. This allowed the average of each data set to be used as an acceptable representative value for each test condition. These averaged values were then used in the equations presented in Section 3.1.5 to obtain the lift, drag and moment coefficients, aerodynamic efficiency, pressure and propeller thrust coefficients that are presented in Chapters 3 and 4, and in Appendix B. The standard deviation of the data sets for each of the measured values (normal force, tangential force, surface pressure, etc.) were compared to the measurement uncertainty reported by each of the sensor's respective manufacturers, shown in Table 3.1. The greater of the two values was used as the actual measurement uncertainty. The uncertainty of the calculated values were obtained using the Klint and McClintock uncertainty propagation method [74]. The following developments show the derivation of the uncertainty for each of the calculated values.

A.1.1 Air Density

The density of the air was calculated using the measured temperature and pressure, assuming air is an ideal gas.

$$P_\infty = \rho R_{\text{air}} T_\infty \quad \longrightarrow \quad \rho = \frac{P_\infty}{R_{\text{air}} T_\infty} \tag{A.1}$$

where P_∞ and T_∞ are the measured pressure and temperature, and R_{air} is the gas constant for air ($R_{\text{air}} = 287.05 \frac{\text{J}}{\text{kg K}}$). The uncertainty of the calculated air density is:

$$\delta\rho = \pm\sqrt{\left(\frac{\partial\rho}{\partial P_\infty}\delta P_\infty\right)^2 + \left(\frac{\partial\rho}{\partial T_\infty}\delta T_\infty\right)^2} \tag{A.2}$$

$$= \pm\sqrt{\left(\frac{1}{RT_\infty}\delta P_\infty\right)^2 + \left(-\frac{P_\infty}{RT_\infty^2}\delta T_\infty\right)^2} \tag{A.3}$$

where $\frac{\partial}{\partial x}$ indicates the partial derivative with respect to some variable x, and the symbol δx represents the uncertainty of that same variable x. In this case, $x = [P_\infty, T_\infty]$.

A.1.2 Lift and Drag Coefficients

By Equation 3.2 and 3.3, the lift force L and drag force D can be obtained as follows:

$$\begin{aligned} L &= F_{y,w}\cos\alpha + F_{x,w}\sin\alpha \\ D &= -F_{y,w}\sin\alpha - F_{x,w}\cos\alpha \end{aligned} \tag{A.4}$$

where $F_{y,w}$ and $F_{x,w}$ are averaged values measured from the *ATI Industrial Mini85* force/torque transducer. The uncertainty of the lift and drag can be determined as follows:

$$\begin{aligned} \delta L &= \pm\sqrt{\left(\frac{\partial L}{\partial F_{y,w}}\delta F_{y,w}\right)^2 + \left(\frac{\partial L}{\partial F_{x,w}}\delta F_{y,w}\right)^2 + \left(\frac{\partial L}{\partial\alpha}\delta\alpha\right)^2} \\ &= \pm\sqrt{\left(\cos\alpha\delta F_{y,w}\right)^2 + \left(\sin\alpha\delta F_{x,w}\right)^2 + \left(\left(-F_{y,w}\sin\alpha + F_{x,w}\cos\alpha\right)\delta\alpha\right)^2} \\ \delta D &= \pm\sqrt{\left(\frac{\partial D}{\partial F_{y,w}}\delta F_{y,w}\right)^2 + \left(\frac{\partial D}{\partial F_{x,w}}\delta F_{y,w}\right)^2 + \left(\frac{\partial L}{\partial\alpha}\delta\alpha\right)^2} \\ &= \pm\sqrt{\left(-\sin\alpha\delta F_{y,w}\right)^2 + \left(-\cos\alpha\delta F_{x,w}\right)^2 + \left(\left(-F_{y,w}\cos\alpha + F_{x,w}\sin\alpha\right)\delta\alpha\right)^2} \end{aligned} \tag{A.5}$$

In this case, $x = [F_{y,w}, F_{x,w}, \alpha]$. Finally, the lift and drag coefficients were determined by Equation 3.4, with the uncertainty calculated using the following equations:

$$\begin{aligned} \delta C_L &= \pm\sqrt{\left(\frac{\partial C_L}{\partial L}\delta L\right)^2 + \left(\frac{\partial C_L}{\partial\rho}\delta\rho\right)^2 + \left(\frac{\partial C_L}{\partial U}\delta U\right)^2} \\ &= \pm\sqrt{\left(\frac{2}{\rho U^2 S}\delta L\right)^2 + \left(-\frac{2L}{\rho^2 U^2 S}\delta\rho\right)^2 + \left(-\frac{4L}{\rho U^3 S}\delta U\right)^2} \\ \delta C_D &= \pm\sqrt{\left(\frac{\partial C_D}{\partial D}\delta D\right)^2 + \left(\frac{\partial C_D}{\partial\rho}\delta\rho\right)^2 + \left(\frac{\partial C_D}{\partial U}\delta U\right)^2} \\ &= \pm\sqrt{\left(\frac{2}{\rho U^2 S}\delta D\right)^2 + \left(-\frac{2D}{\rho^2 U^2 S}\delta\rho\right)^2 + \left(-\frac{4D}{\rho U^3 S}\delta U\right)^2} \end{aligned} \tag{A.6}$$

A.1.3 Moment Coefficient

The moment measured at the half chord by the force/torque transducer was converted to a moment at the quarter chord using Equation 3.5, with the uncertainty calculated using the following equation:

$$\begin{aligned}\delta M_{c/4} &= \pm\sqrt{\left(\frac{\partial M_{c/4}}{F_{y,w}}\delta F_{y,w}\right)^2 + \left(\frac{\partial M_{c/4}}{\partial M_{c/2}}\delta M_{c/2}\right)^2} \\ &= \pm\sqrt{\left(\frac{c}{4}\delta F_{y,w}\right)^2 + \delta M_{c/2}^2}\end{aligned} \tag{A.7}$$

The uncertainty of the moment coefficient is then given by the following equation:

$$\delta C_{M_{c/4}} = \pm\sqrt{\left(\frac{2}{\rho U^2 Sc}\delta M_{c/4}\right)^2 + \left(-\frac{2M_{c/4}}{\rho^2 U^2 Sc}\delta\rho\right)^2 + \left(-\frac{4M_{c/4}}{\rho U^3 Sc}\delta U\right)^2} \tag{A.8}$$

A.1.4 Aerodynamic Efficiency

The aerodynamic efficiency is the ratio of the lift coefficient to the drag coefficient:

$$E = \frac{C_L}{C_D} \tag{A.9}$$

The uncertainty of the aerodynamic efficiency was calculated using the following equation:

$$\begin{aligned}\delta E &= \pm\sqrt{\left(\frac{\partial E}{\partial C_L}\delta C_L\right)^2 + \left(\frac{\partial E}{\partial C_D}\delta C_D\right)^2} \\ &= \pm\sqrt{\left(\frac{1}{C_D}\delta C_L\right)^2 + \left(-\frac{C_L}{C_D^2}\delta C_D\right)^2}\end{aligned} \tag{A.10}$$

A.1.5 Pressure Coefficient

The pressure coefficients were calculated using Equation 3.7, with the uncertainty calculated using the following:

$$\begin{aligned}\delta C_P &= \pm\sqrt{\left(\frac{\partial C_P}{\partial \Delta P}\delta \Delta P\right)^2 + \left(\frac{\partial C_P}{\partial \rho}\delta\rho\right)^2 + \left(\frac{\partial C_L}{\partial U}\delta U\right)^2} \\ &= \pm\sqrt{\left(\frac{2}{\rho U^2}\delta P\right)^2 + \left(-\frac{2P}{\rho^2 U^2}\delta\rho\right)^2 + \left(-\frac{4P}{\rho U^3}\delta U\right)^2}\end{aligned} \tag{A.11}$$

A.1.6 Propeller Thrust Coefficient

The propeller thrust coefficient was calculated using Equation 3.8, with the uncertainty calculated using the following equation:

$$\begin{aligned}\delta C_T &= \pm\sqrt{\left(\frac{\partial C_T}{\partial T_\mathrm{p}}\delta T_\mathrm{p}\right)^2 + \left(\frac{\partial C_T}{\partial \rho}\delta\rho\right)^2 + \left(\frac{\partial C_T}{\partial \Omega}\delta\Omega\right)^2} \\ &= \pm\sqrt{\left(\frac{1}{\rho\Omega^2 d_\mathrm{p}^4}\delta T_\mathrm{p}\right)^2 + \left(-\frac{T_\mathrm{p}}{\rho^2\Omega^2 d_\mathrm{p}^4}\delta\rho\right)^2 + \left(-\frac{2T_\mathrm{p}}{\rho\Omega^3 d_\mathrm{p}^4}\delta\Omega\right)^2}\end{aligned} \tag{A.12}$$

A.2 Uncertainty of Monocopter Flight Test Results

The measured values from the flight testing of the RMC monocopter consisted of angular rate measurements from the *LSM9DS1* IMU onboard the *Arduino Nano 33 BLE Sense* microcontroller, a current measurement from the *ACS711EX* current sensor, and a voltage reading from the *ElectriFly Triton EQ* LiPO battery charger. These measurements were used in Equation 6.3 and 6.2 to obtain the thrust coefficient, power coefficient, and figure of merit for the RMC monocopter in hover OGE. The following developments show the derivation of the uncertainty for each of these calculated values.

A.2.1 Power Required for Hover

The power required for hover was obtained using the measured current and battery voltage in Equation 6.4, which is provided below for convenience:

$$P = IV$$

The uncertainty for the power required was determined using the following equation:

$$\begin{aligned} \delta P &= \pm\sqrt{\left(\frac{\partial P}{\partial I}\delta I\right)^2 + \left(\frac{\partial P}{\partial V}\delta V\right)^2} \\ &= \pm\sqrt{(V\delta I)^2 + (I\delta V)^2} \end{aligned} \tag{A.13}$$

A.2.2 Thrust and Power Coefficients

The uncertainty of the thrust coefficient was calculated using the following equation:

$$\begin{aligned} \delta C_T &= \pm\sqrt{\left(\frac{\partial C_T}{\partial T}\delta T\right)^2 + \left(\frac{\partial C_T}{\partial \Omega}\delta \Omega\right)^2} \\ &= \pm\sqrt{\left(\frac{1}{\rho\pi\Omega^2 R^2}\delta T\right)^2 + \left(\frac{-T}{\rho\pi\Omega^3 R^2}\delta \Omega\right)^2} \end{aligned} \tag{A.14}$$

Where the thrust required for hover was assumed to be equal to the total weight of the RMC monocopter, and accompanying uncertainty was retrieved from the manufacturer of the XXX electronic scale used to measure the mass of the RMC monocopter.

The uncertainty of the power coefficient was calculated using the following equation, derived in the same manner:

$$\begin{aligned} \delta C_P &= \pm\sqrt{\left(\frac{\partial C_P}{\partial P}\delta P\right)^2 + \left(\frac{\partial C_P}{\partial \Omega}\delta \Omega\right)^2} \\ &= \pm\sqrt{\left(\frac{1}{\rho\pi\Omega^3 R^5}\partial P\right)^2 + \left(\frac{-3P}{\rho\pi\Omega^4 R^5}\partial \Omega\right)^2} \end{aligned} \tag{A.15}$$

A.2.3 Figure of Merit

The figure of merit (FOM) was calculated using Equation 6.2, with the uncertainty determined as follows:

$$\begin{aligned}\delta\text{FOM} &= \pm\sqrt{\left(\frac{\partial\text{FOM}}{\partial C_T}\delta C_T\right)^2 + \left(\frac{\partial\text{FOM}}{\partial C_P}\delta C_P\right)^2} \\ &= \pm\sqrt{\left(\frac{3C_T^{1/2}}{2\sqrt{2}C_P}\delta C_T\right)^2 + \left(\frac{-C_T^{3/2}}{\sqrt{2}C_P^2}\delta C_P\right)^2}\end{aligned} \tag{A.16}$$

B Effect of Propeller Position on Wing Performance: Extended Results

B.1 Extended Contour Plots for Stage 2

This section presents the contour plots that show the lift augmentation at all angles of attack specified for Stage 2 of the experimental wind tunnel campaign discussed in Chapter 3. The value in parentheses indicates the power-off lift coefficient. The angles of attack tested are summarized in Table 3.2. The trends identified for the lift augmentation with varying propeller position remained consistent for the four different Reynolds numbers tested (Re = 1.0×10^5, 1.5×10^5, 2.0×10^5, and 2.5×10^5). More on the effect of varying Reynolds number will be discussed in Section B.2. The propeller position with the most lift augmentation is shown to shift to lower positions with increasing angle of attack.

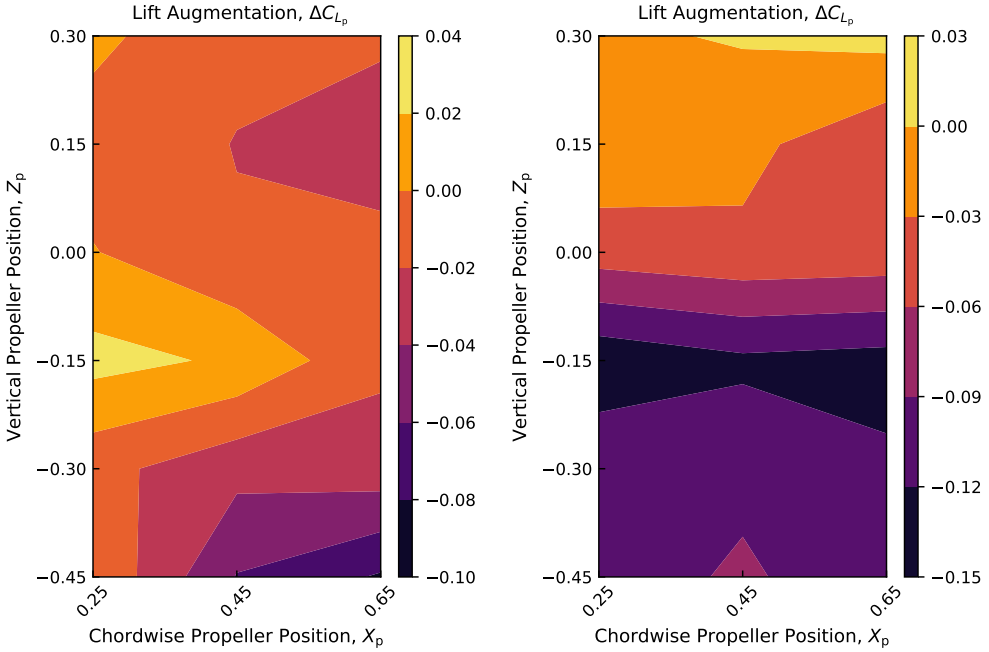

(a) $\alpha = 0°$ ($C_{L_{\text{off}}} = 0.00$) (b) $\alpha = 8°$ ($C_{L_{\text{off}}} = 0.73$)

Figure B.1: Lift augmentation for propeller positions in Grid 2 at Re = 2.0×10^5.

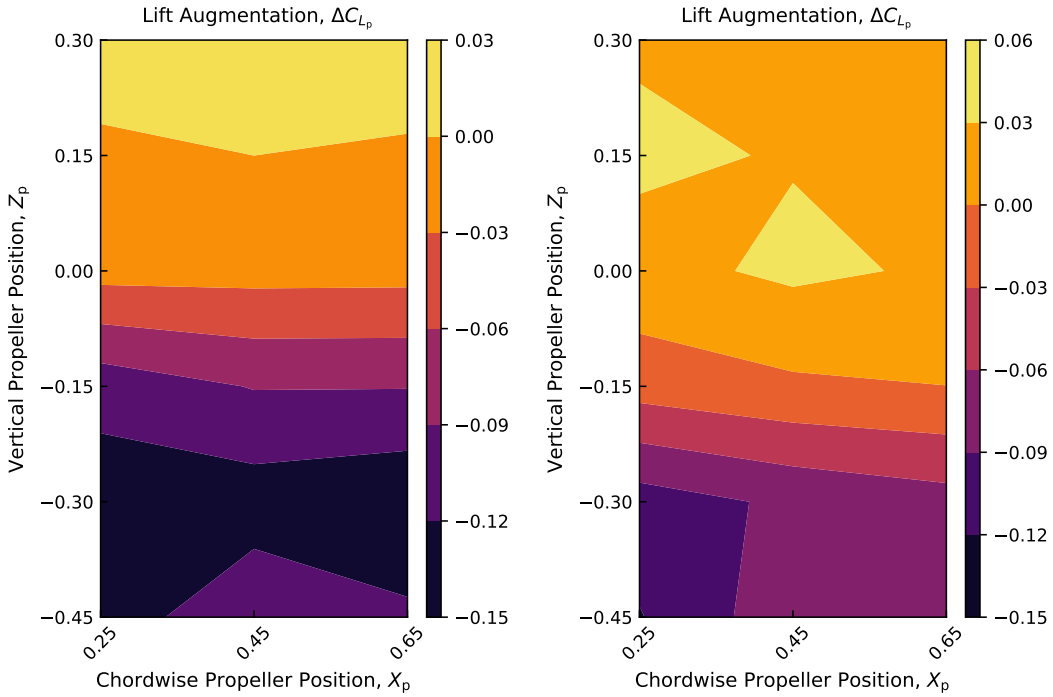

(a) $\alpha = 10°$ ($C_{L_{\text{off}}} = 0.90$) (b) $\alpha = 12°$ ($C_{L_{\text{off}}} = 0.98$)

Figure B.2: Lift augmentation for propeller positions in Grid 2 at $\text{Re} = 2.0 \times 10^5$.

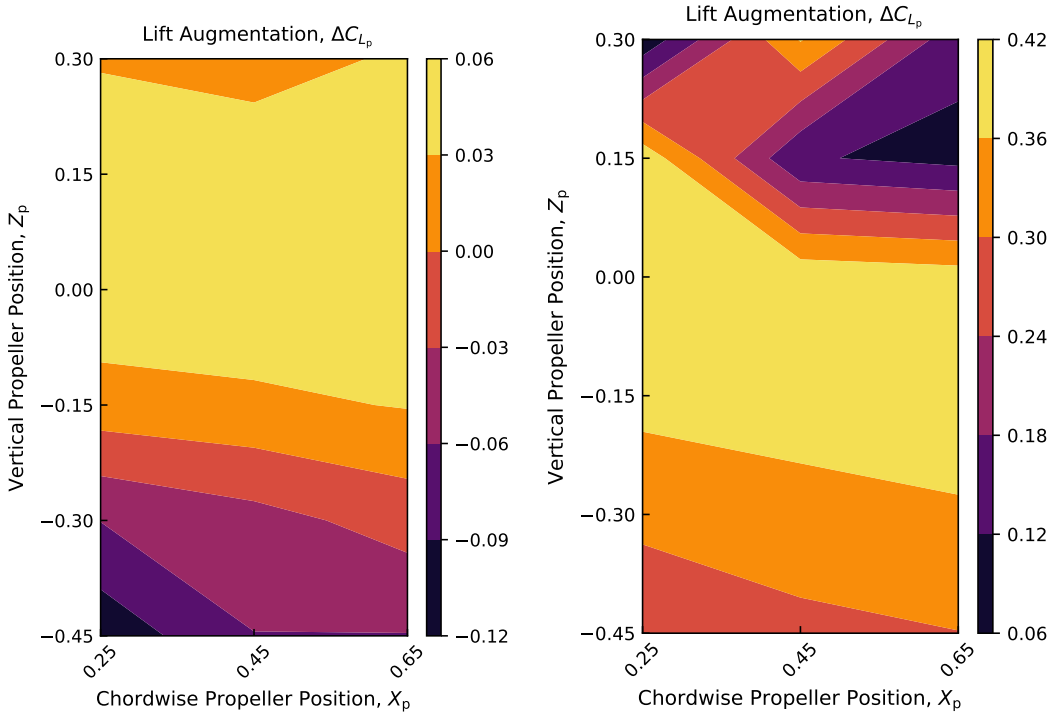

(a) $\alpha = 13°$ ($C_{L_{\text{off}}} = 1.01$) (b) $\alpha = 14°$ ($C_{L_{\text{off}}} = 0.70$)

Figure B.3: Lift augmentation for propeller positions in Grid 2 at $\text{Re} = 2.0 \times 10^5$.

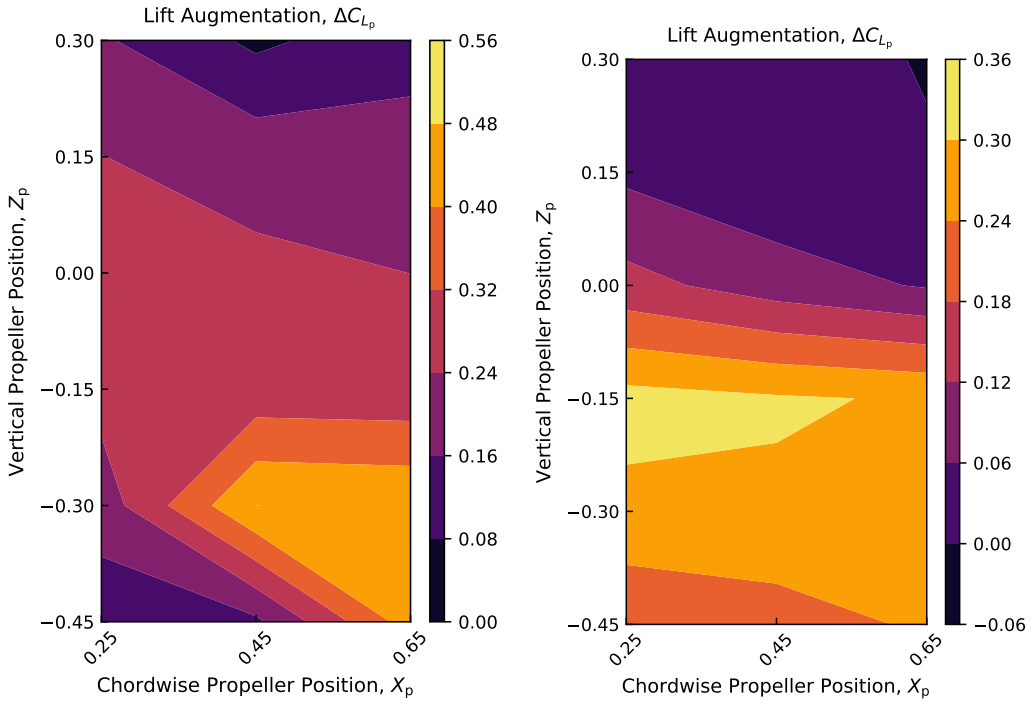

(a) $\alpha = 15°$ ($C_{L_{\text{off}}} = 0.63$) (b) $\alpha = 17°$ ($C_{L_{\text{off}}} = 0.61$)

Figure B.4: Lift augmentation for propeller positions in Grid 2 at $\text{Re} = 2.0 \times 10^5$.

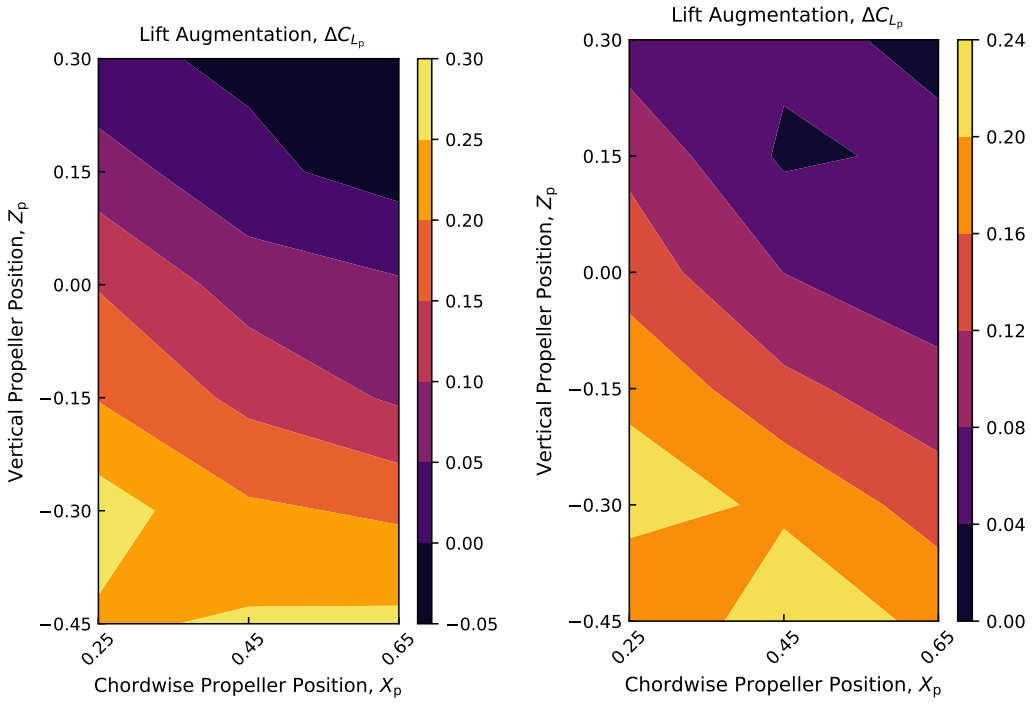

(a) $\alpha = 20°$ ($C_{L_{\text{off}}} = 0.60$) (b) $\alpha = 25°$ ($C_{L_{\text{off}}} = 0.57$)

Figure B.5: Lift augmentation for propeller positions in Grid 2 at $\text{Re} = 2.0 \times 10^5$.

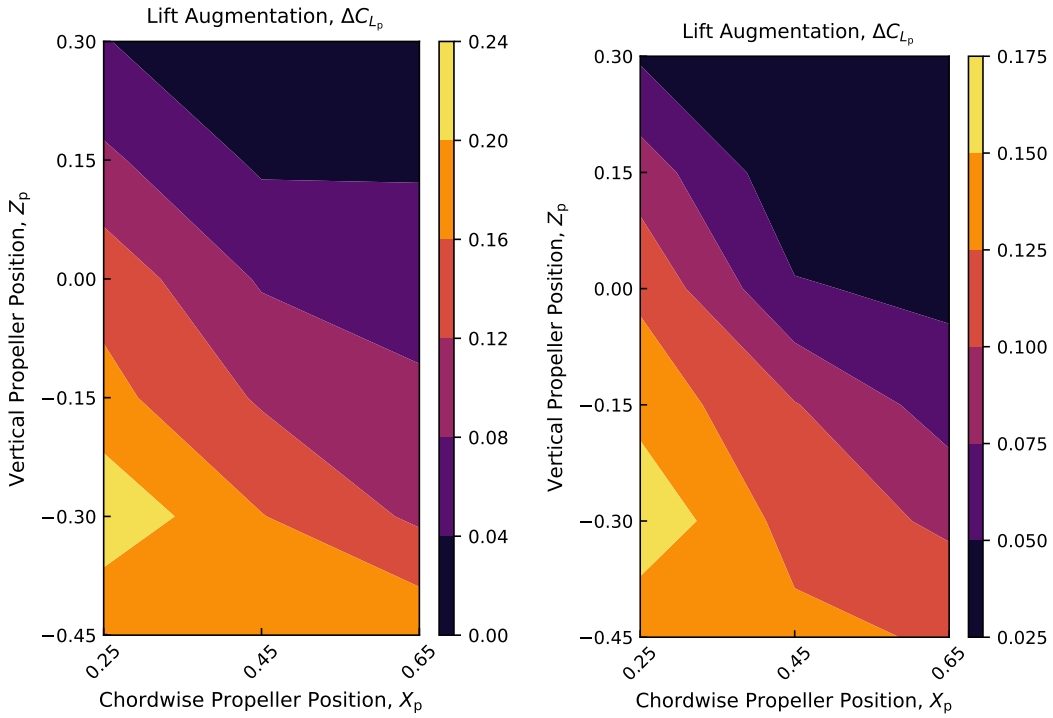

(a) $\alpha = 30°$ ($C_{L_{\text{off}}} = 0.61$) (b) $\alpha = 35°$ ($C_{L_{\text{off}}} = 0.67$)

Figure B.6: Lift augmentation for propeller positions in Grid 2 at $\text{Re} = 2.0 \times 10^5$.

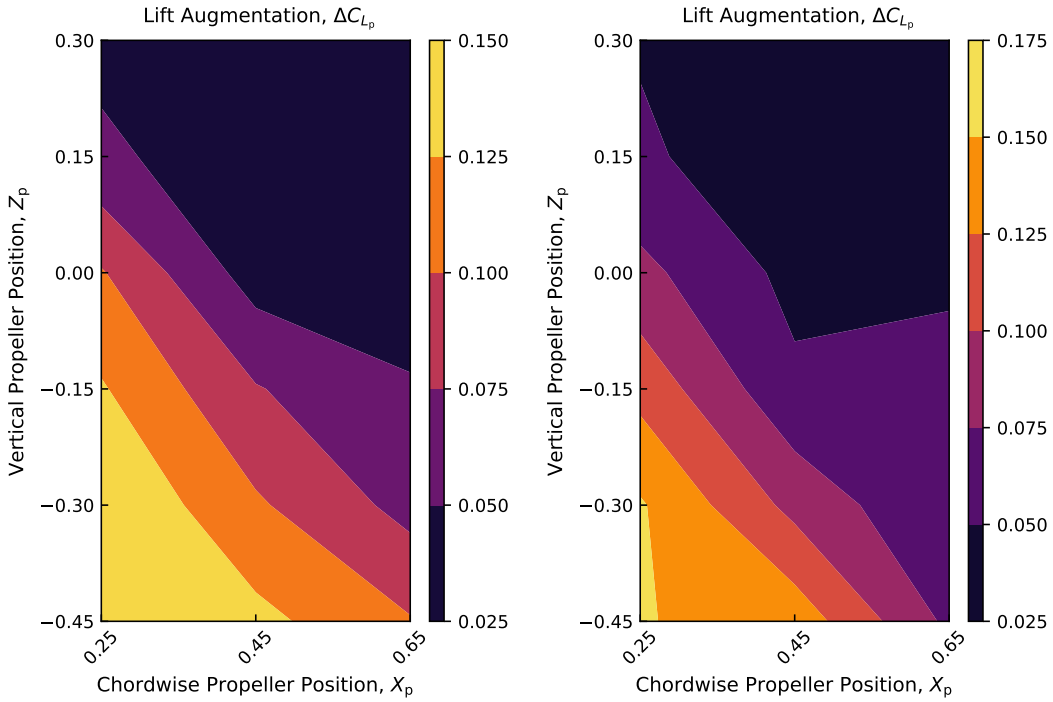

(a) $\alpha = 40°$ ($C_{L_{\text{off}}} = 0.72$) (b) $\alpha = 45°$ ($C_{L_{\text{off}}} = 0.75$)

Figure B.7: Lift augmentation for propeller positions in Grid 2 at $\text{Re} = 2.0 \times 10^5$.

B.2 Effect of Reynolds Number

To demonstrate the effect of Reynolds number on the lift augmentation of the propeller slipstream, the propeller position of $X_p = 0.25$ and $Z_p = 0.00$ will be used as a representative position. Figure B.8 shows the power-off and power-on lift coefficients with increasing angle of attack at Re $= 1.0 \times 10^5$, 1.5×10^5, 2.0×10^5, and 2.5×10^5. The scale of the y-axes are the same to allow for easier comparison.

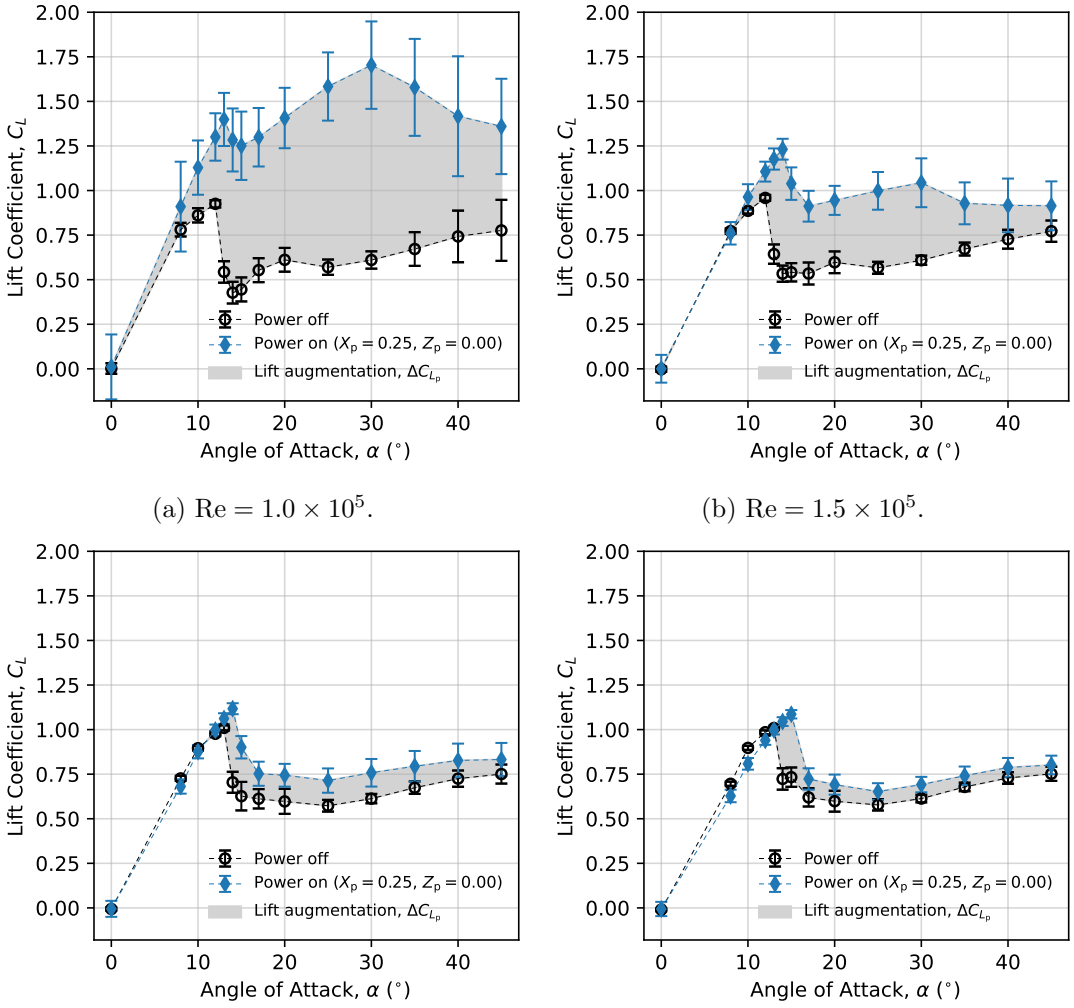

(a) Re $= 1.0 \times 10^5$.

(b) Re $= 1.5 \times 10^5$.

(c) Re $= 2.0 \times 10^5$.

(d) Re $= 2.5 \times 10^5$.

Figure B.8: Lift coefficient with increasing angle of attack for power-off and power-on ($X_p = 0.25$, $Z_p = 0$) at different Reynolds numbers.

As the Reynolds number increases, the lift coefficients for the power-on condition and the lift coefficients for the power-off condition are shifted towards each other, nearly meeting at $C_L \approx 0.75$ by Re $= 2.5 \times 10^5$. The noticeable decrease in lift augmentation observed at higher Reynolds numbers are caused mainly by the changing thrust performance of the propeller with varying Reynolds numbers. The advance ratio, J, is a common non-dimensional parameter used to describe the operating condition of a propeller, calculated as shown in Equation B.1:

$$J = \frac{U}{\frac{\Omega}{60} d_{\mathrm{p}}} \tag{B.1}$$

where J is the advance ratio, U is the freestream velocity, Ω is the rotational speed of the propeller converted from RPM to rotations per second, and d_{p} is the diameter of the propeller. The performance of a propeller is significantly impacted by the advance ratio. The propeller thrust measurements at $\alpha = 0°$ for all the Reynolds numbers can be used to generate a plot of the variation in thrust coefficient with increasing advance ratio. This is shown in Figure B.9. Previous data for the same *APC Thin Electric* 10×5E propeller measured by Asghar *et al.*, Ohio State University (OSU), and the University of Illinois at Urbana-Champaign (UIUC) are also shown for comparison [26].

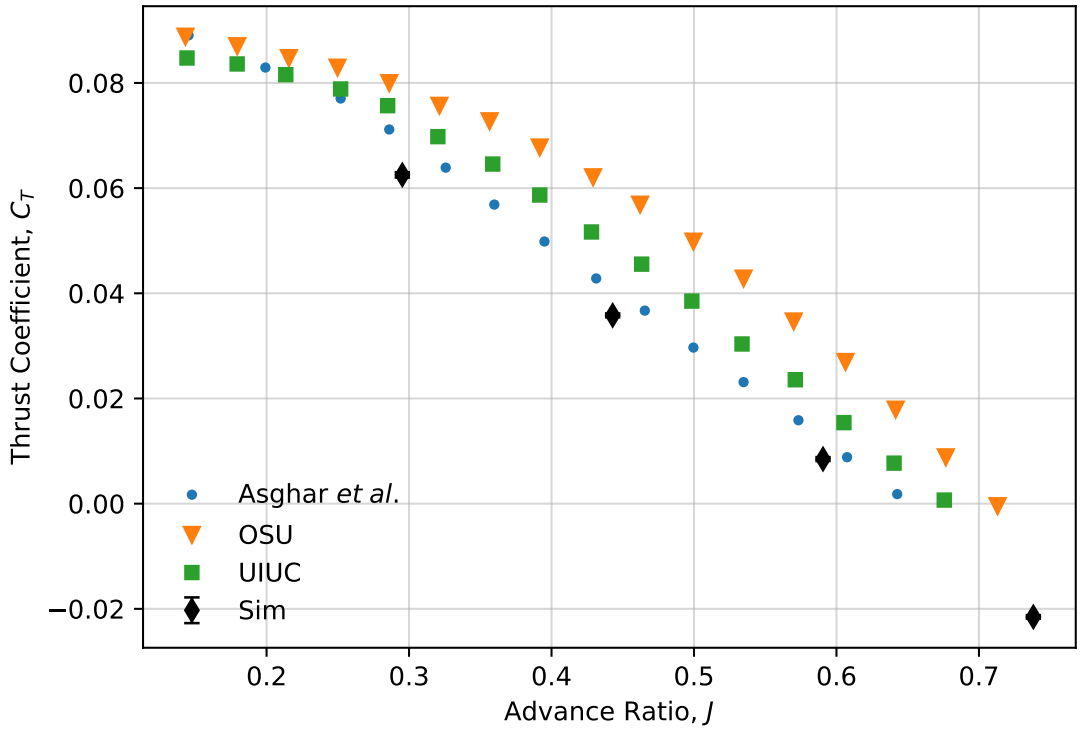

Figure B.9: Variation in thrust coefficient with advance ratio for the *APC Thin Electric* 10×5E propeller.

The results obtained from this experimental campaign (labelled Sim) appear to under predict the thrust coefficient. However, it is important to highlight the presence of the wing within the propeller slipstream for these results. This would act as a partial blockage to the propeller resulting in the slightly reduced thrust coefficients shown. Since the propeller rotational speed was maintained at 8000 RPM, increasing the Reynolds number results in an increase in advance ratio. As the advance ratio increases the thrust coefficient decreases. The negative thrust coefficient at an advance ratio of approximately 0.74 indicates that the propeller is no longer producing thrust, but windmilling and generating drag.

Another method of visualizing the propellers performance that compliments the lift curves shown in Figure B.8 is to show the variation in thrust coefficient with angle of

attack. This is shown in Figure B.10. Both the Reynolds number and corresponding advance ratio for the propeller are indicated.

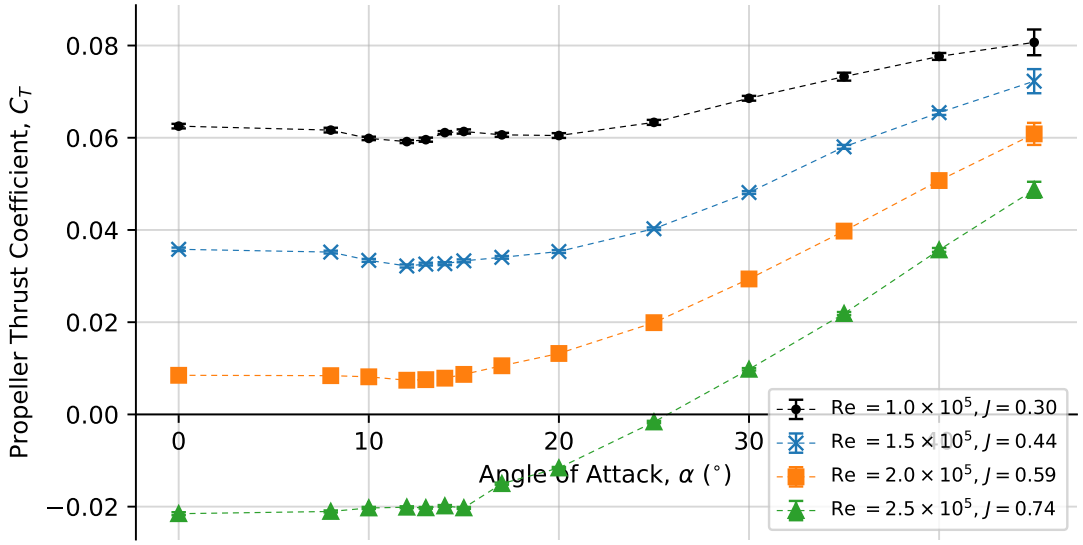

Figure B.10: Propeller thrust coefficient at different angles of attack for all Reynolds numbers tested.

At Re $= 2.5 \times 10^5$ the thrust coefficient is negative for $\alpha < 25°$. Despite this, Figure B.8d still shows a small amount of lift augmentation for $\alpha > 12°$. This could be due to the swirl generated by the windmilling slightly increasing the velocity over the wing creating a small lift augmenting effect. For all Reynolds numbers, the thrust coefficient increases with increasing angle of attack. When an angle of attack is induced, the component of the freestream velocity that is aligned with the rotational axis decreases, effectively reducing the advance ratio of the propeller, which, made apparent in Figure B.9, leads to an increase in thrust coefficient.

The decreasing thrust coefficient with increasing Reynolds number that is responsible for the decreasing lift augmentation with increasing Reynolds number is clearly displayed in Figure B.10. As the thrust coefficient decreases, so does the difference in velocities between the freestream and the propeller slipstream. This causes the lift coefficients for the power-on condition to shift to lower values, while the lift coefficients for the power-off conditions shift to higher values as a result of the increased Reynolds number. The net result is a decrease in lift augmentation. The effect of Reynolds number was consistent across all propeller positions tested, therefore the conclusions made in Chapter 3 still apply at different Reynolds numbers.

B.3 Other Aerodynamic Performance Parameters

This section presents contour plots that show the moment coefficients, drag coefficients, and aerodynamic efficiencies at different angles of attack. The analysis on the effect of chordwise position on the lift performance of the wing presented in Chapter 3 showed that the chordwise propeller position was not as influential as the vertical position. For

this reason, the results presented here are from Stage 2 of testing at a Reynolds number of 2.0×10^5, which included a wider range of vertical propeller positions at a limited set of chordwise positions. The full details of the test conditions for Stage 2 can be found in Table 3.2.

B.3.1 Moment Coefficients

The moment coefficient is closely linked to the lift coefficient of the wing in the sense that the moment at the quarter chord is generated by the net lift force acting at a distance from the quarter chord. As such, the trends in the moment coefficient at each propeller position observed across all angles of attack follow the trends identified for the lift augmentation. The propeller positions that generated the most lift augmentation translated to a larger negative pitching moment (nose down) as a result of the increased lift. This can be observed in Figures B.11 through B.17, which shows the moment coefficient at each propeller position in Grid 2 (Figure 3.10) at the angles of attack specified for Stage 2 of testing (Table 3.2). The power-off moment coefficient is provided in the figure captions. A negative moment coefficient represents a nose down moment, while positive moment coefficients represent a nose up moment. The brightest regions of the contour plots indicate the most positive moment coefficients while the darker regions indicate the most negative moment coefficients. The darker regions that indicate propeller positions that generated larger nose down pitching moments in Figures B.11 through B.17 coincide with the brighter regions in Figures 3.22 through 3.29 that indicate propeller positions that generated more lift augmentation.

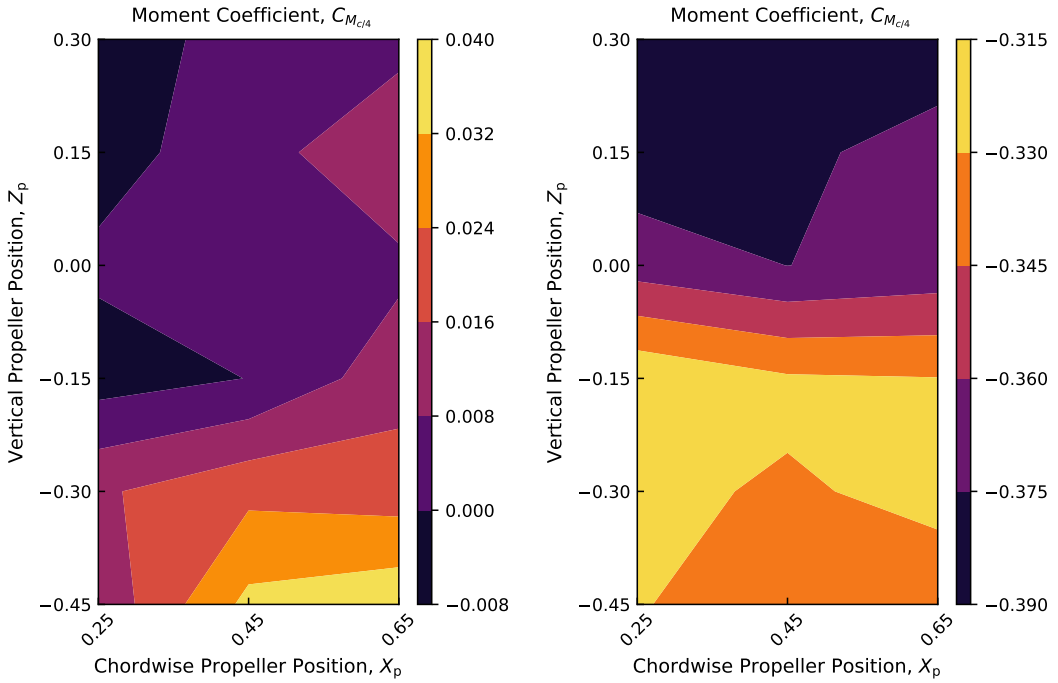

(a) $\alpha = 0°$ ($C_{M_{\text{off}}} = 0.00$)

(b) $\alpha = 8°$ ($C_{M_{\text{off}}} = -0.38$)

Figure B.11: Moment coefficient for propeller positions in Grid 2 at $\text{Re} = 2.0 \times 10^5$.

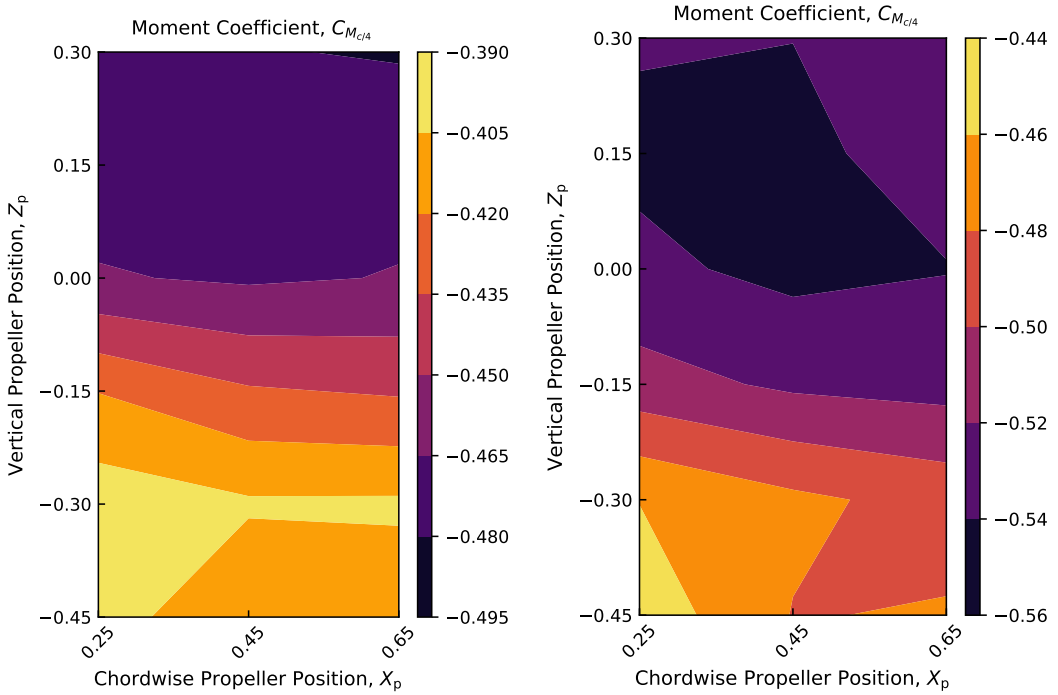

(a) $\alpha = 10°$ ($C_{M_{\text{off}}} = -0.47$) (b) $\alpha = 12°$ ($C_{M_{\text{off}}} = -0.52$)

Figure B.12: Moment coefficient for propeller positions in Grid 2 at $\text{Re} = 2.0 \times 10^5$.

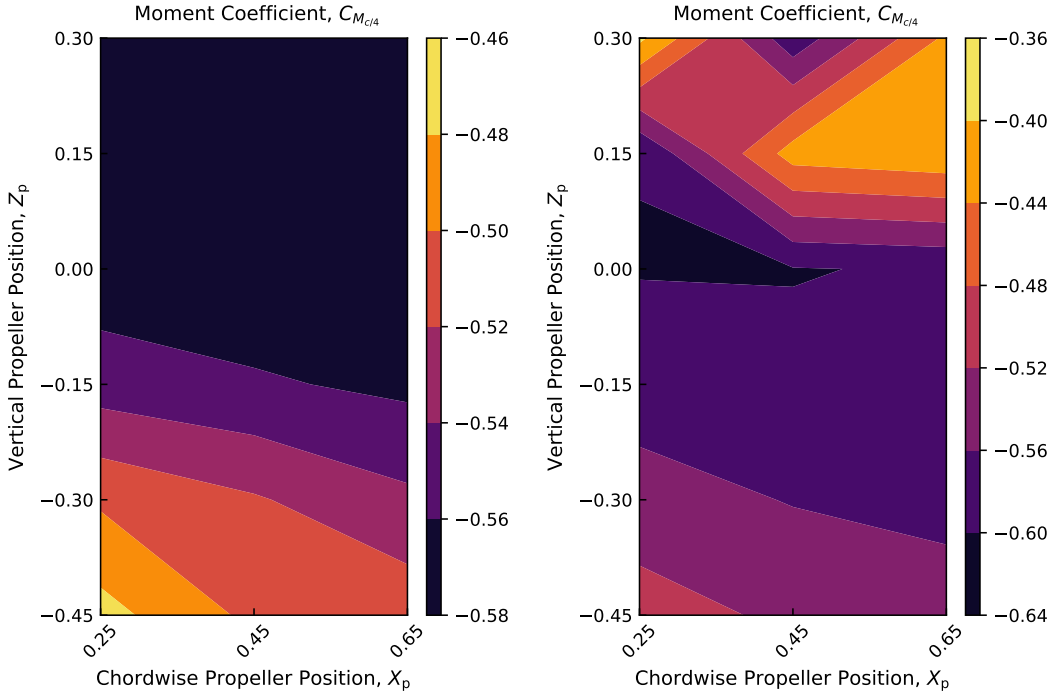

(a) $\alpha = 13°$ ($C_{M_{\text{off}}} = -0.55$) (b) $\alpha = 14°$ ($C_{M_{\text{off}}} = -0.35$)

Figure B.13: Moment coefficient for propeller positions in Grid 2 at $\text{Re} = 2.0 \times 10^5$.

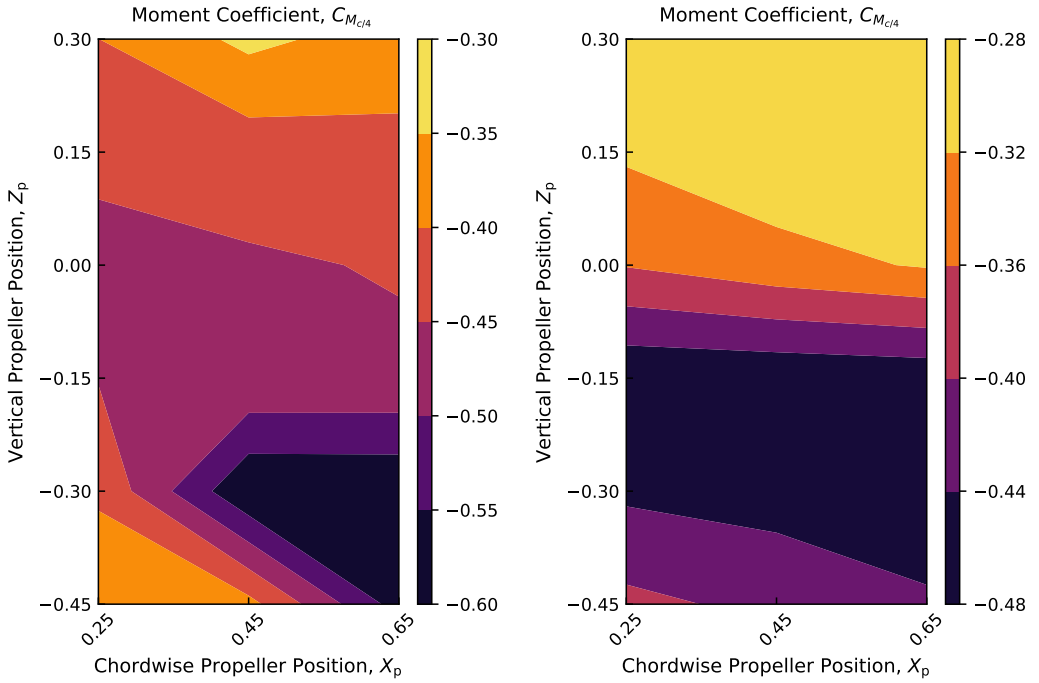

(a) $\alpha = 15°$ ($C_{M_{\text{off}}} = -0.30$) (b) $\alpha = 17°$ ($C_{M_{\text{off}}} = -0.29$)

Figure B.14: Moment coefficient for propeller positions in Grid 2 at $\text{Re} = 2.0 \times 10^5$.

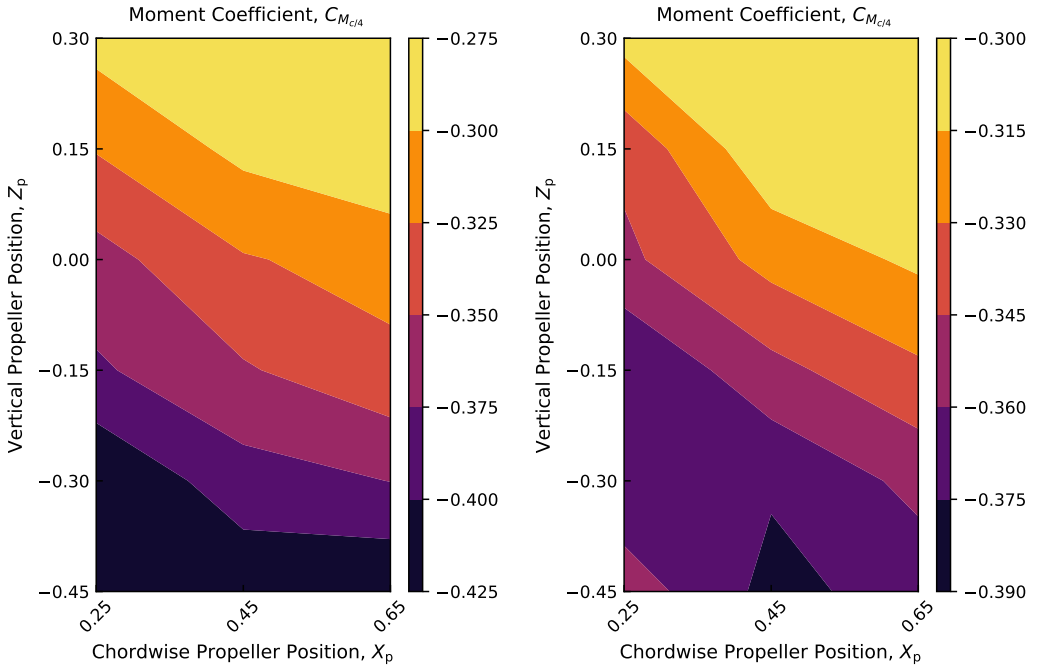

(a) $\alpha = 20°$ ($C_{M_{\text{off}}} = -0.28$) (b) $\alpha = 25°$ ($C_{M_{\text{off}}} = -0.29$)

Figure B.15: Moment coefficient for propeller positions in Grid 2 at $\text{Re} = 2.0 \times 10^5$.

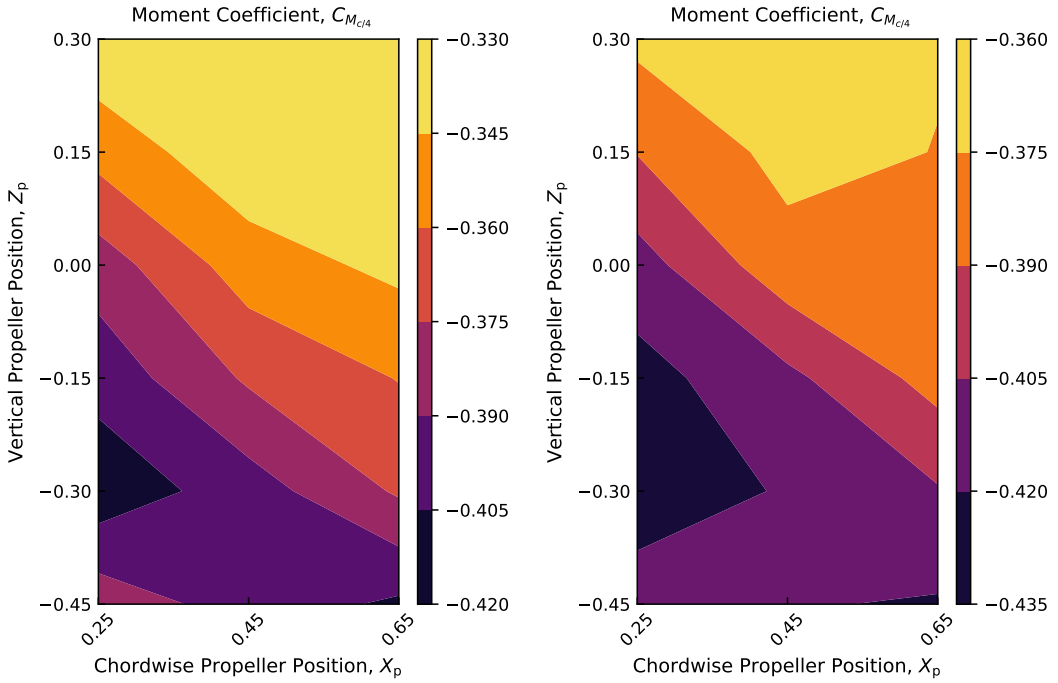

(a) $\alpha = 30°$ ($C_{M_{\text{off}}} = -0.32$) (b) $\alpha = 35°$ ($C_{M_{\text{off}}} = -0.35$)

Figure B.16: Moment coefficient for propeller positions in Grid 2 at $\text{Re} = 2.0 \times 10^5$.

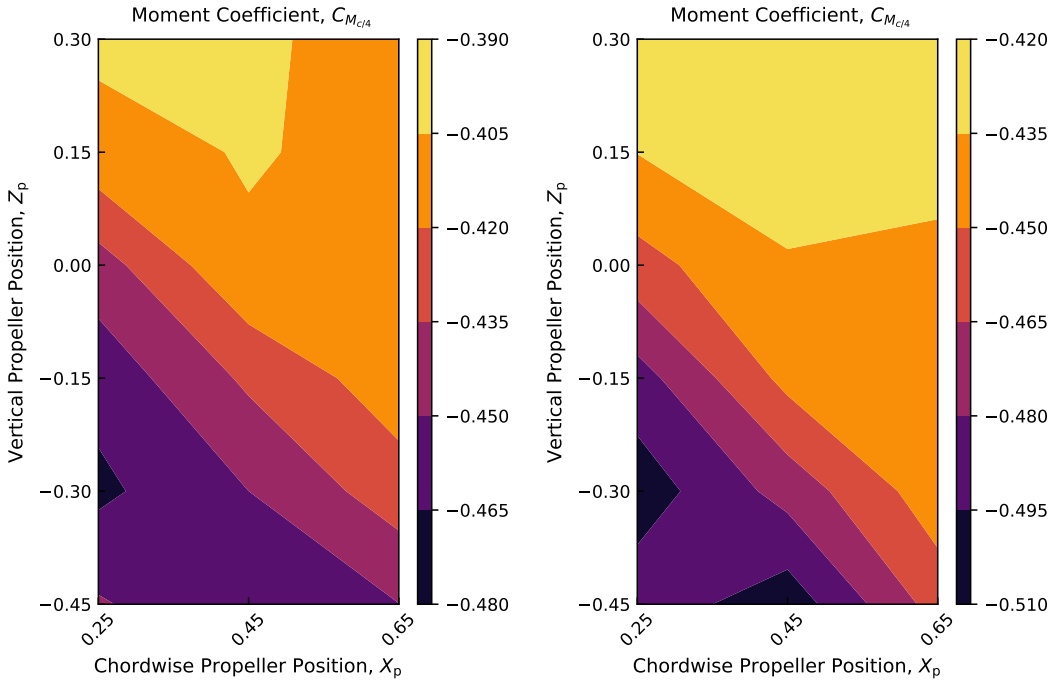

(a) $\alpha = 40°$ ($C_{M_{\text{off}}} = -0.38$) (b) $\alpha = 45°$ ($C_{M_{\text{off}}} = -0.41$)

Figure B.17: Moment coefficient for propeller positions in Grid 2 at $\text{Re} = 2.0 \times 10^5$.

B.3.2 Drag Coefficients

Similar to the decomposition of the lift coefficient into a power-off lift coefficient plus a power-on lift augmentation term, the drag coefficient can also be separated into equivalent components. This is demonstrated by Equation B.2, and shown in Figure B.18 using the propeller position at $X_p = 0.25$ and $Z_p = 0$ as an example. In Equation B.2, $C_{D_{tot}}$ is the total drag coefficient of the wing, $C_{D_{off}}$ is the power-off drag coefficient, and ΔC_{D_p} is the drag reduction due to the propeller slipstream. Note the subtraction of the ΔC_{D_p} term, indicating that positive values of ΔC_{D_p} represents a decrease in drag.

$$C_{D_{tot}} = C_{D_{off}} - \Delta C_{D_p} \tag{B.2}$$

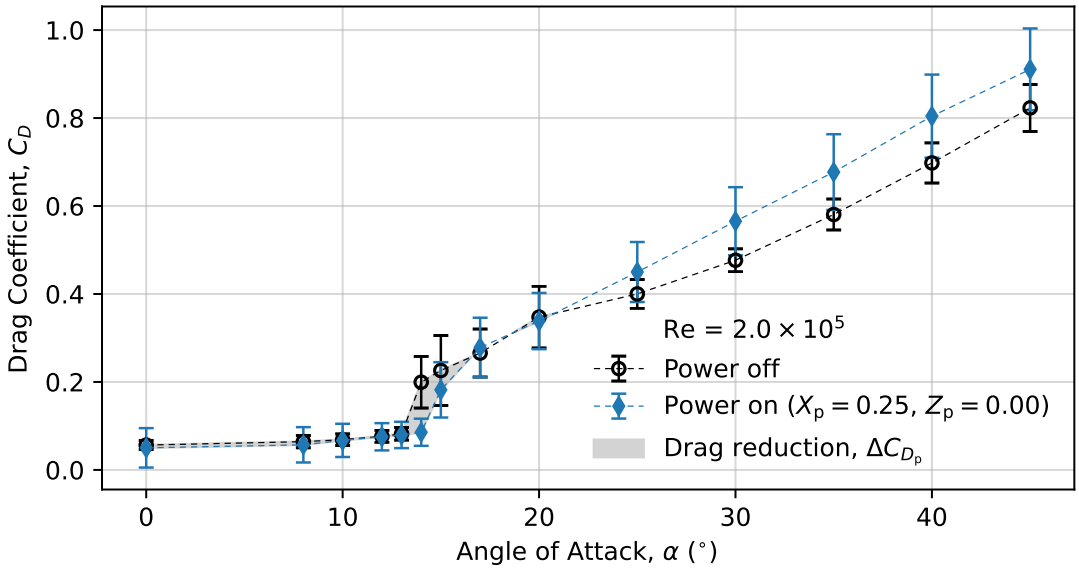

Figure B.18: power-off and power-on drag coefficients showing the drag reduction from the propeller slipstream.

At angles of attack before stall ($0° \leq \alpha \leq 12°$) the magnitude of the drag reduction for different propeller positions were smaller than the experimental error. For this reason, no definitive conclusions regarding the drag reduction at low angles of attack could be made. However, the majority of the drag reduction provided by the propeller slipstream was observed to be at angles of attack near stall. This is clearly shown in Figure B.18 by the grey region that represents the drag reduction having the most area at angles of attack between 13° and 20°. This is mainly a result of the propeller slipstream delaying flow separation, which is accompanied by a large increase in drag. The propeller slipstream accomplishes this through the same two mechanisms that were introduced in Chapter 3: an increase in velocities over the wing, and a change in effective angle of attack by redirection of flow. Figures B.19 through B.25 shows the drag reduction at each propeller position in Grid 2 (Figure 3.10) at the angles of attack specified for Stage 2 of testing (Table 3.2). As a result of the experimental error, the results for angles of attack between 0° and 8° should be interpreted with caution. For these contour plots, the brighter regions indicate propeller positions that provided the most drag reduction, while darker regions indicate propeller positions that provided the least drag reduction.

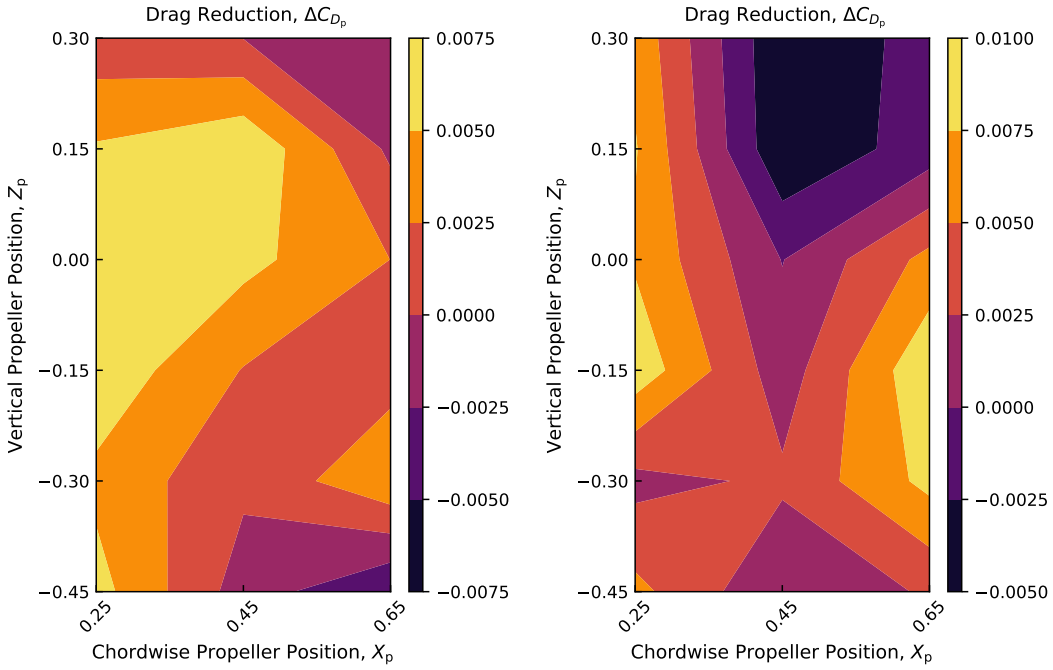

(a) $\alpha = 0°$ ($C_{D_{\text{off}}} = 0.056$) (b) $\alpha = 8°$ ($C_{D_{\text{off}}} = 0.064$)

Figure B.19: Drag reduction for propeller positions in Grid 2 at $\text{Re} = 2.0 \times 10^5$.

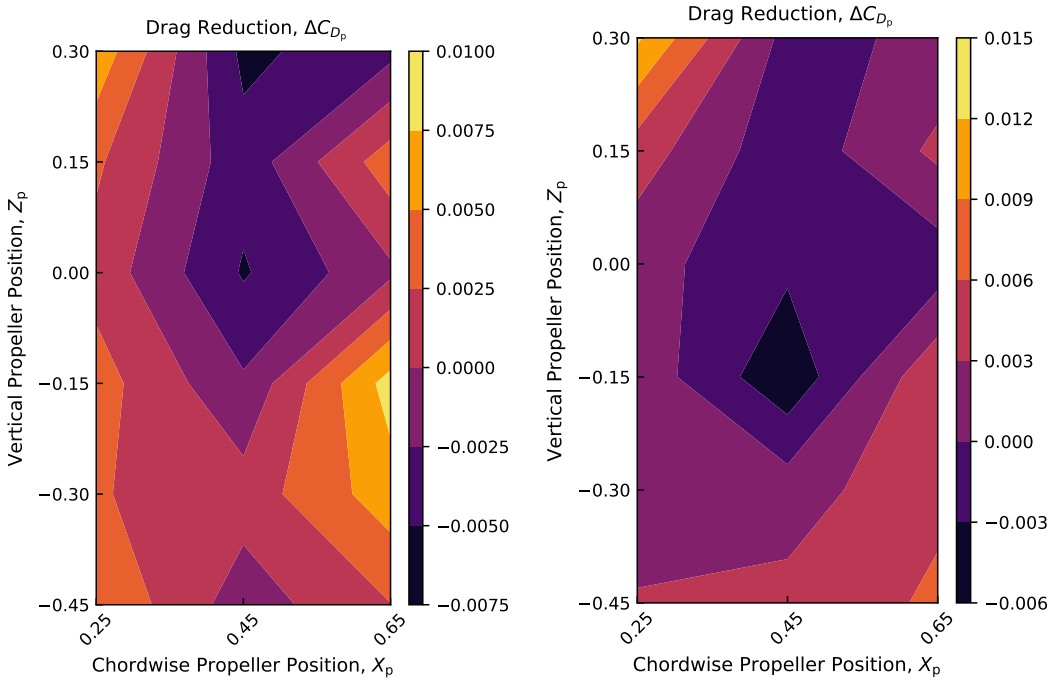

(a) $\alpha = 10°$ ($C_{D_{\text{off}}} = 0.069$) (b) $\alpha = 12°$ ($C_{D_{\text{off}}} = 0.076$)

Figure B.20: Drag reduction for propeller positions in Grid 2 at $\text{Re} = 2.0 \times 10^5$.

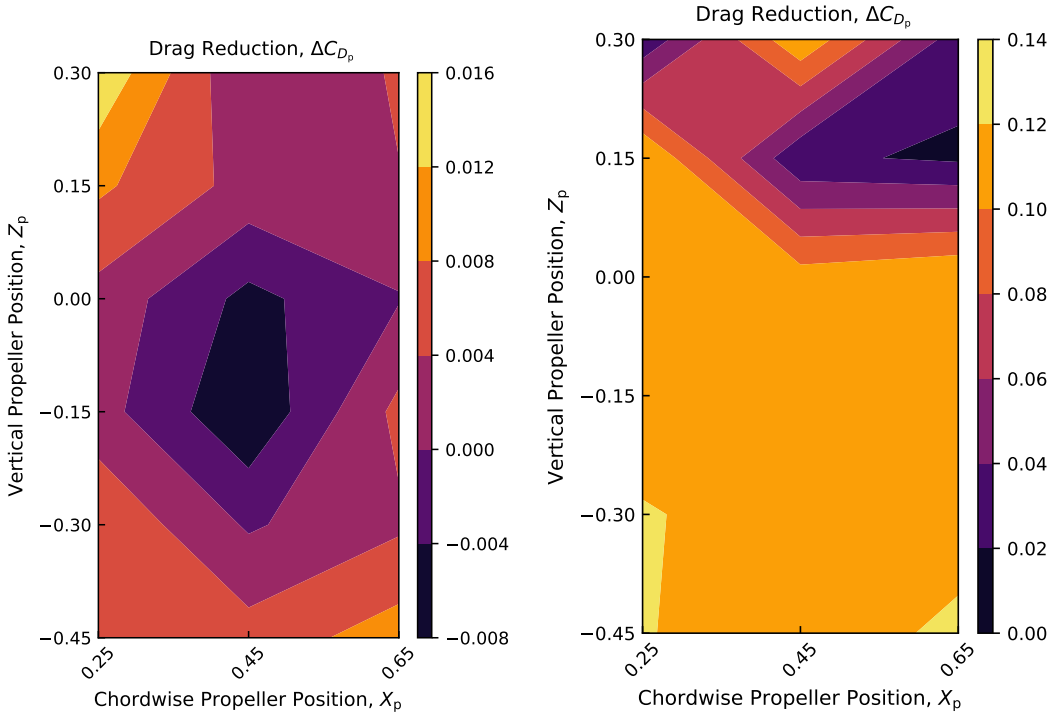

(a) $\alpha = 13°$ ($C_{D_{\text{off}}} = 0.082$) (b) $\alpha = 14°$ ($C_{D_{\text{off}}} = 0.199$)

Figure B.21: Drag reduction for propeller positions in Grid 2 at $\text{Re} = 2.0 \times 10^5$.

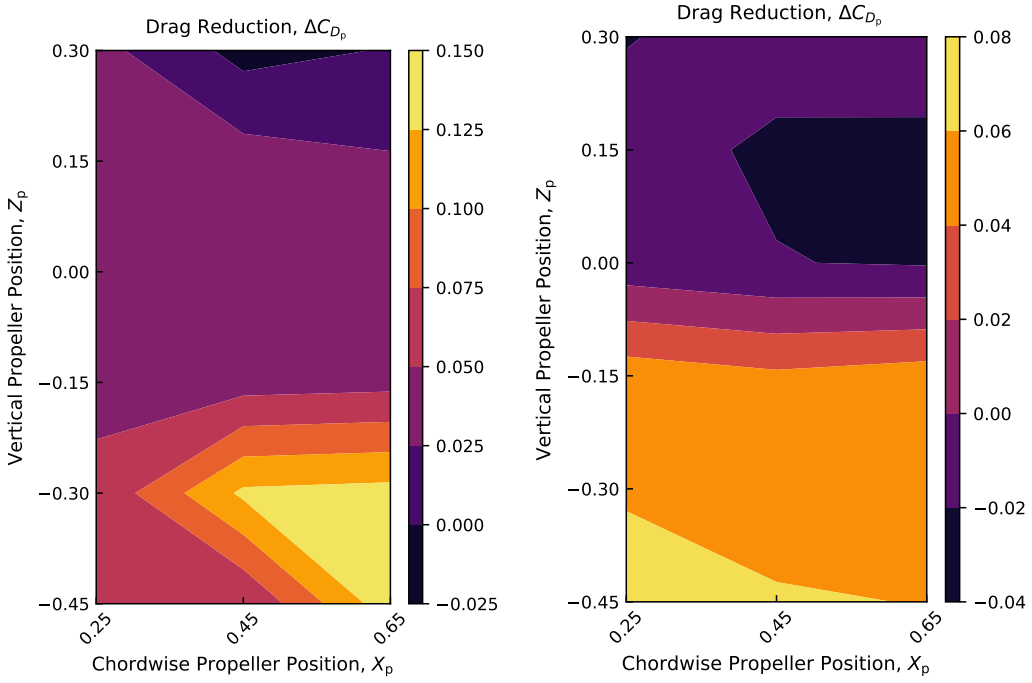

(a) $\alpha = 15°$ ($C_{D_{\text{off}}} = 0.226$) (b) $\alpha = 17°$ ($C_{D_{\text{off}}} = 0.266$)

Figure B.22: Drag reduction for propeller positions in Grid 2 at $\text{Re} = 2.0 \times 10^5$.

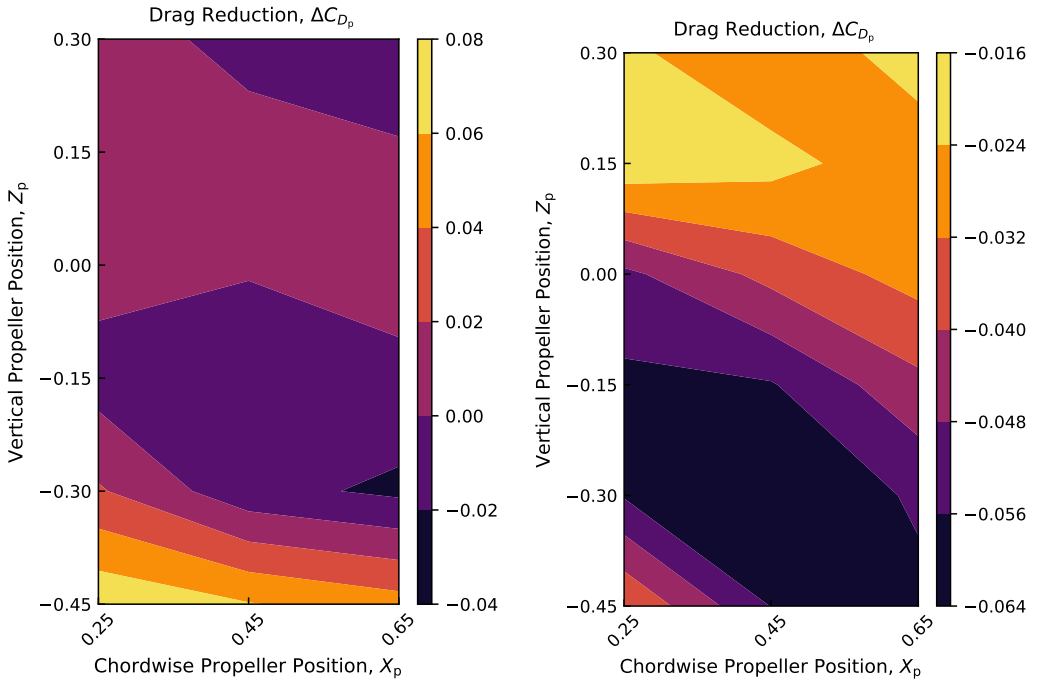

(a) $\alpha = 20°$ ($C_{D_{\text{off}}} = 0.347$) (b) $\alpha = 25°$ ($C_{D_{\text{off}}} = 0.400$)

Figure B.23: Drag reduction for propeller positions in Grid 2 at $\text{Re} = 2.0 \times 10^5$.

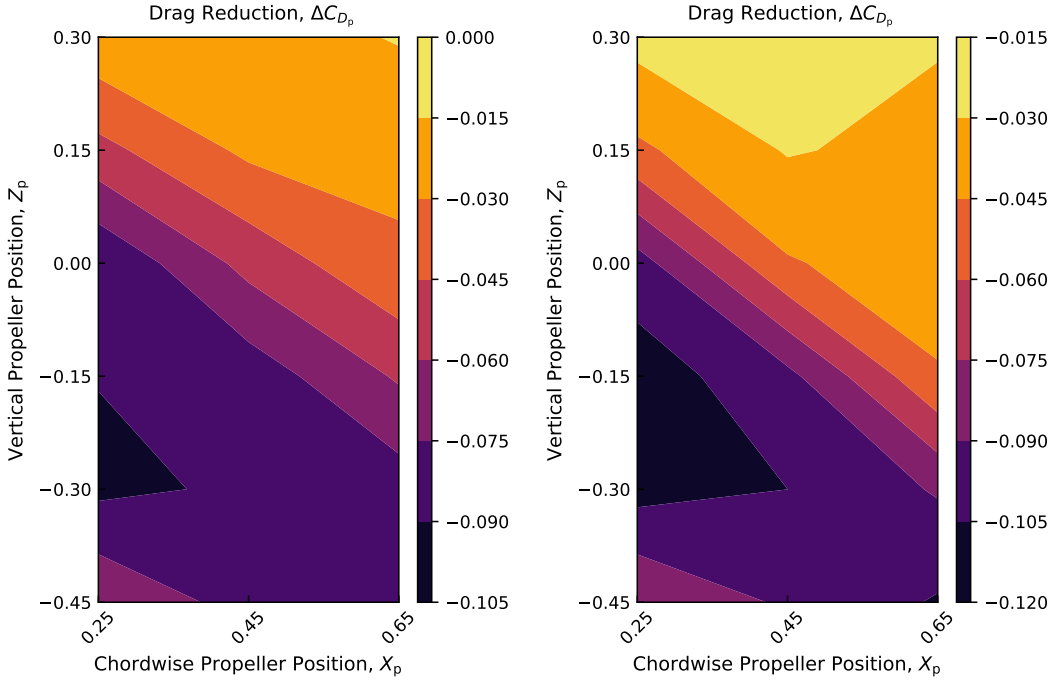

(a) $\alpha = 30°$ ($C_{D_{\text{off}}} = 0.477$) (b) $\alpha = 35°$ ($C_{D_{\text{off}}} = 0.581$)

Figure B.24: Drag reduction for propeller positions in Grid 2 at $\text{Re} = 2.0 \times 10^5$.

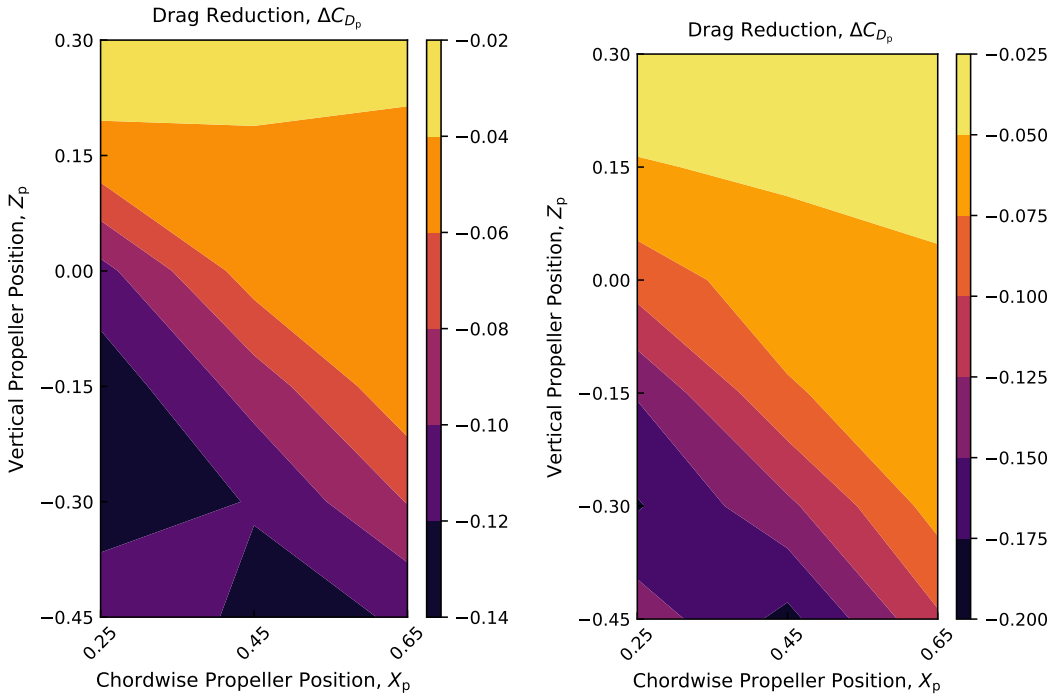

(a) $\alpha = 40°$ ($C_{D_{\text{off}}} = 0.698$) (b) $\alpha = 45°$ ($C_{D_{\text{off}}} = 0.823$)

Figure B.25: Drag reduction for propeller positions in Grid 2 at $\text{Re} = 2.0 \times 10^5$.

B.3.3 Aerodynamic Efficiency

The aerodynamic efficiency is defined as the ratio between the lift coefficient and drag coefficient, as described by Equation A.9. It provides an overview on the overall aerodynamic performance of the wing at each propeller position that takes into account both the amount of lift augmentation and drag reduction. The aerodynamic efficiency of the wing for each propeller position was compared to the aerodynamic efficiency of the power-off condition to calculate the total change in aerodynamic efficiency, which is shown in the following equation:

$$\Delta E_{\text{p}} = E_{\text{tot}} - E_{\text{off}} \tag{B.3}$$

where ΔE_{p} is the change in aerodynamic efficiency as a result of the propeller slipstream, E_{on} is the aerodynamic efficiency of the wing for the power-on condition (at each propeller position), and E_{off} is the power-off aerodynamic efficiency. Figures B.26 through B.32 show contour plots of the change in aerodynamic efficiency at each propeller position in Grid 2 (Figure 3.10) at the angles of attack specified for Stage 2 of testing (3.2). The aerodynamic efficiency for the power-off condition is provided in the figure captions. The brighter regions indicate propeller positions where the change in aerodynamic efficiency is the largest (most positive) while the darker regions indicate propeller positions where the change in aerodynamic efficiency is the smallest (most negative). Since the lift augmentation effect was more significant than the drag reduction, the general trends observed with the change in aerodynamic efficiency with different propeller positions follow those that were identified for the lift augmentation in Chapter 3.

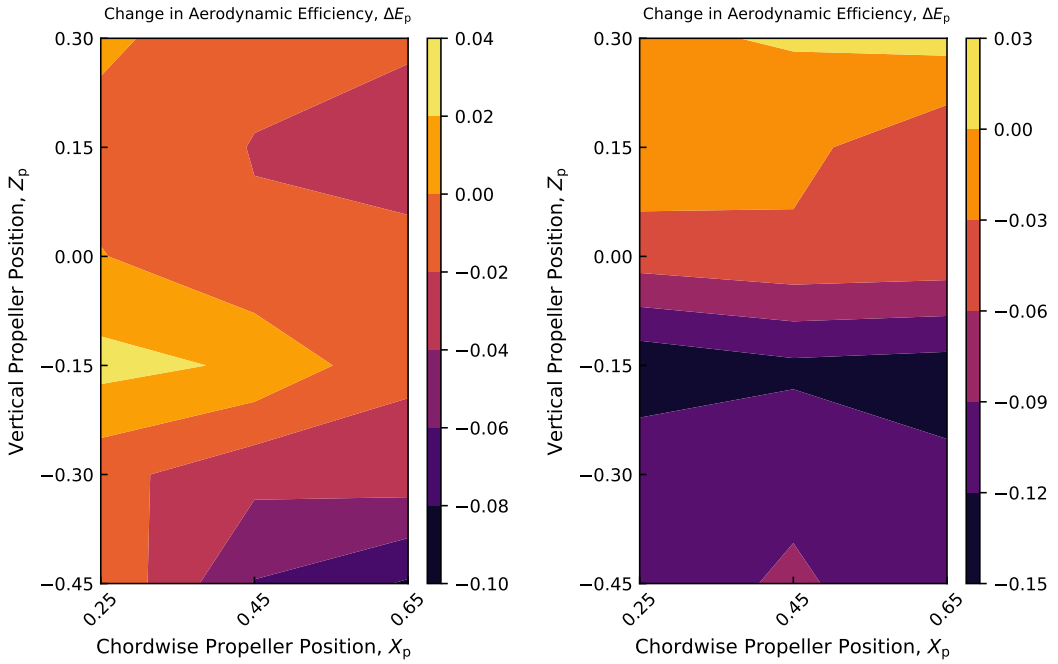

(a) $\alpha = 0°$ ($E_{\text{off}} = -0.11$) (b) $\alpha = 8°$ ($E_{\text{off}} = 11.30$)

Figure B.26: Change in aerodynamic efficiency for propeller positions in Grid 2 at $\text{Re} = 2.0 \times 10^5$.

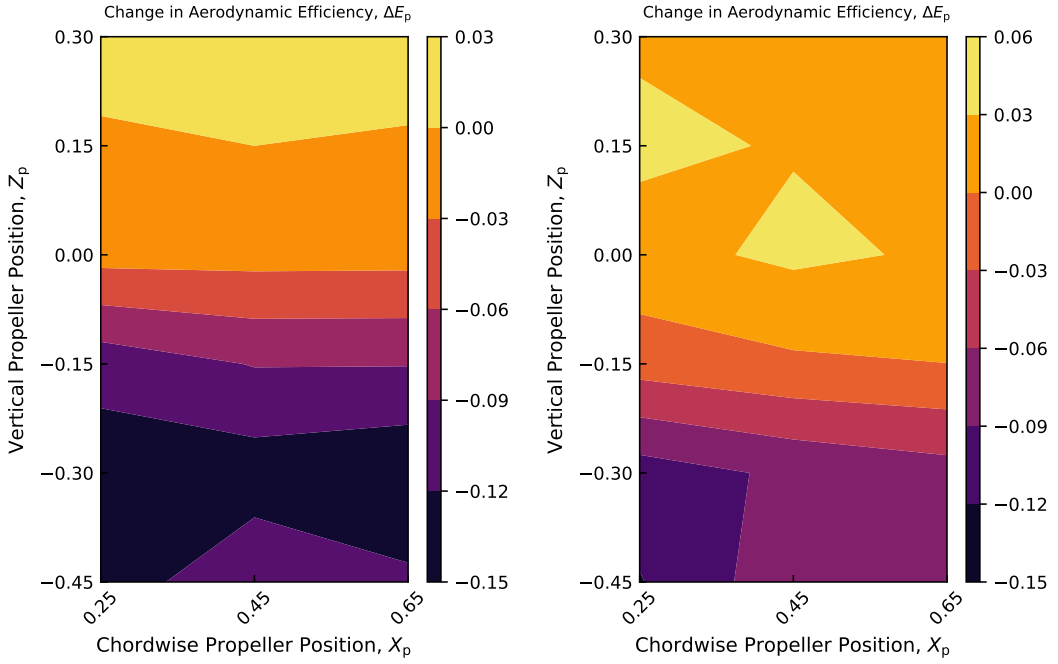

(a) $\alpha = 10°$ ($E_{\text{off}} = 13.04$) (b) $\alpha = 12°$ ($E_{\text{off}} = 12.77$)

Figure B.27: Change in aerodynamic efficiency for propeller positions in Grid 2 at $\text{Re} = 2.0 \times 10^5$.

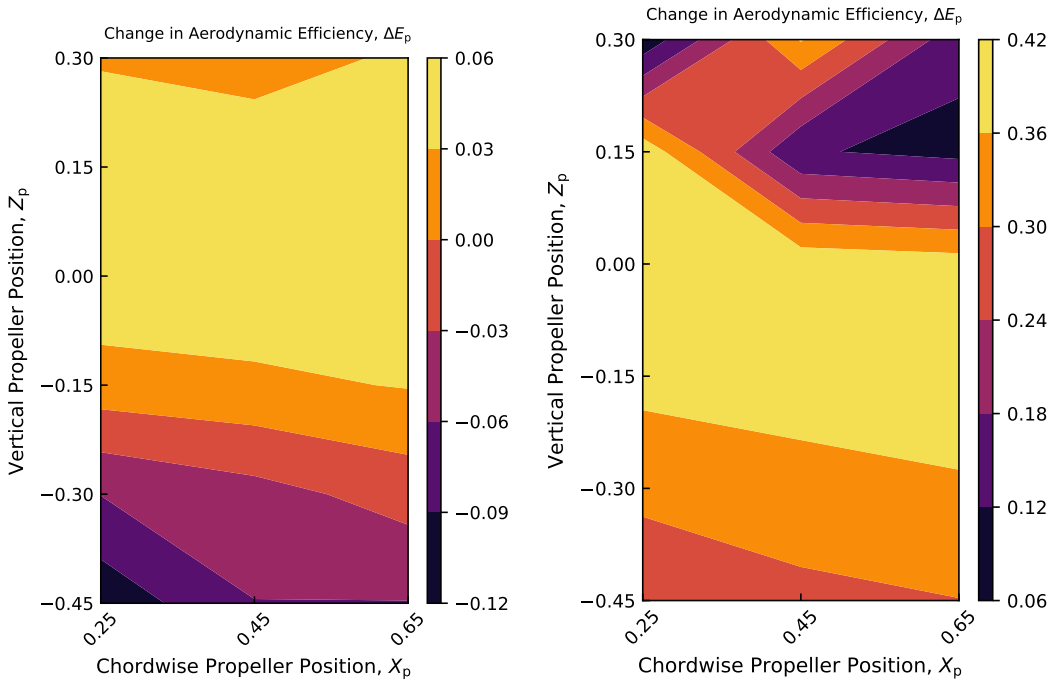

(a) $\alpha = 13°$ ($E_{\text{off}} = 12.31$) (b) $\alpha = 14°$ ($E_{\text{off}} = 3.53$)

Figure B.28: Change in aerodynamic efficiency for propeller positions in Grid 2 at $\text{Re} = 2.0 \times 10^5$.

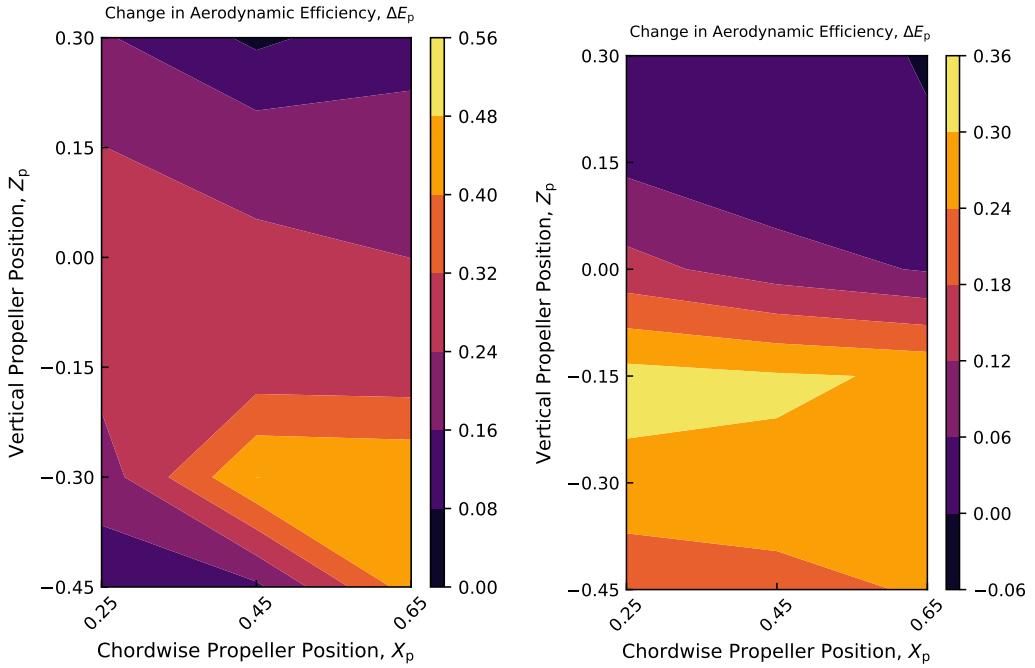

(a) $\alpha = 15°$ ($E_{\text{off}} = 2.77$) (b) $\alpha = 17°$ ($E_{\text{off}} = 2.30$)

Figure B.29: Change in aerodynamic efficiency for propeller positions in Grid 2 at $\text{Re} = 2.0 \times 10^5$.

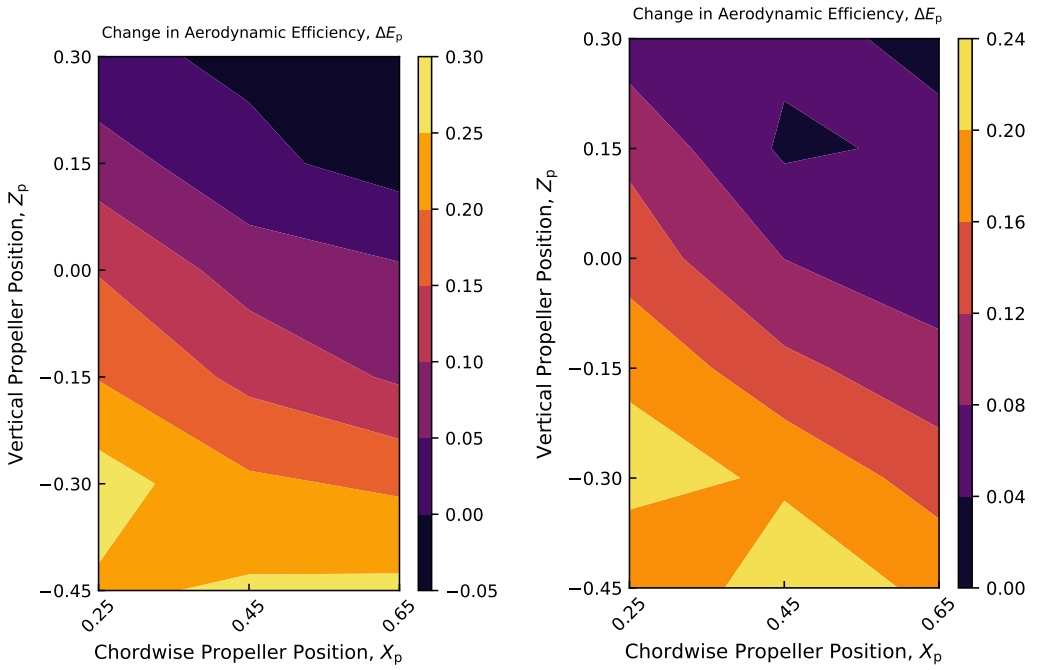

(a) $\alpha = 20°$ ($E_{\text{off}} = 1.72$) (b) $\alpha = 25°$ ($E_{\text{off}} = 1.43$)

Figure B.30: Change in aerodynamic efficiency for propeller positions in Grid 2 at $\text{Re} = 2.0 \times 10^5$.

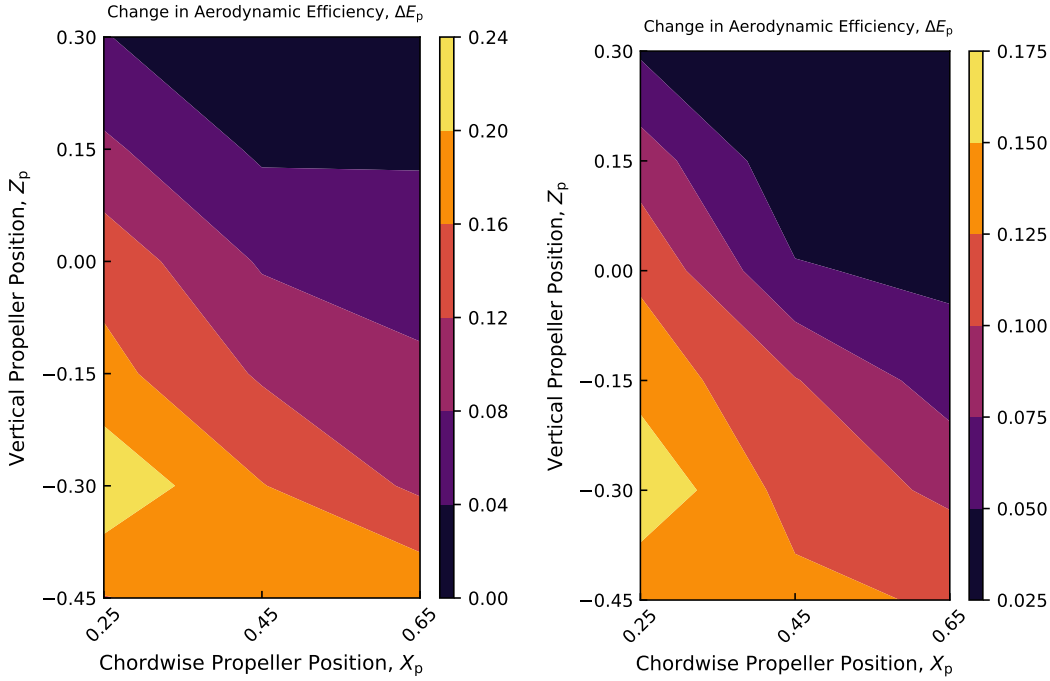

(a) $\alpha = 30°$ ($E_{\text{off}} = 1.28$) (b) $\alpha = 35°$ ($E_{\text{off}} = 1.16$)

Figure B.31: Change in aerodynamic efficiency for propeller positions in Grid 2 at $\text{Re} = 2.0 \times 10^5$.

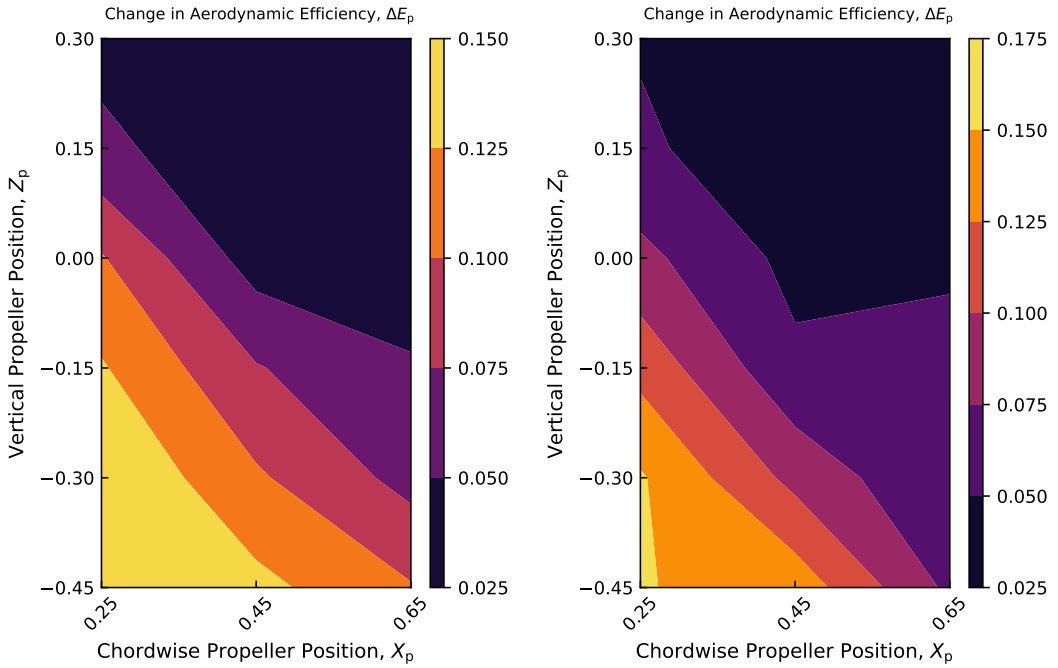

(a) $\alpha = 40°$ ($E_{\text{off}} = 1.04$)

(b) $\alpha = 45°$ ($E_{\text{off}} = 0.91$)

Figure B.32: Change in aerodynamic efficiency for propeller positions in Grid 2 at $\text{Re} = 2.0 \times 10^5$.

C Aerodynamic Performance of Blown Tubercles: Extended Results

C.1 UAM Mission Profile

Figure C.1 presents a general mission profile for a UAM vehicle, defined by Patterson *et al* [76]. This was used to appropriately select weighting factors for each angle of attack when determining the optimal propeller position.

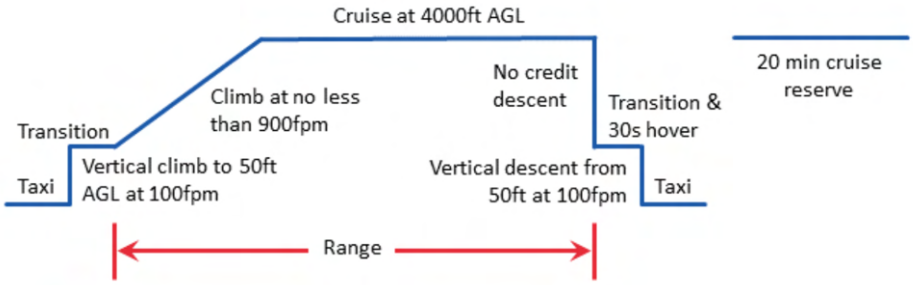

Figure C.1: Typical mission profile for a UAM vehicle [76].

C.2 Extended Aerodynamic Data

The lift performance of the wing was identified as the most important aerodynamic parameter when concerned with tilt-wing transition in Chapter 4. However, the addition of tubercles does have a noticeable impact on the moments and drag generated by the wing as well. The measured moments and drag, as well as the aerodynamic efficiency of each tubercle wing for the power-off and power-on conditions are presented in this section. The figures themselves are found at the end of this section. The propeller was positioned at the optimal position as determined in Chapter 4 ($X_\mathrm{p} = 0.25$, Z_p=0) for the power-on measurements.

C.2.1 Moment Coefficients

The moment coefficients about the quarter chord for each tubercle wing at $\mathrm{Re} = 1.0 \times 10^5$, 1.5×10^5, 2.0×10^5, and 2.5×10^5 are presented in Figures C.2 through C.9. Figures

C.2 through C.5 show the power-off measurements, and Figures C.6 through C.9 show the power-on measurements. Results for the SLE wing are provided for comparison. A negative moment coefficient signifies a nose down pitching moment, while a positive moment coefficient signifies a nose up pitching moment. The measurement uncertainty is only shown for the results at $\mathrm{Re} = 2.5 \times 10^5$ to improve the readability of the figures. The moment coefficient is closely linked to the lift coefficient of the wing. This is due largely in part to the fact that the moment is generated by the lift coefficient acting at a distance from the quarter chord. Any variations in lift coefficient will have a proportional effect on the moment coefficient, resulting in the moment coefficient curves of each tubercle wing resembling inverted versions of their respective lift curves. In this sense, trends identified with the different tubercle geometries are preserved. This dependency on the lift coefficient is also observable in Equation 3.5, which was used to convert the measured moment about the half chord to the quarter chord.

C.2.2 Drag Coefficients

The drag coefficients for each tubercle wing at $\mathrm{Re} = 1.0 \times 10^5$, 1.5×10^5, 2.0×10^5 and 2.5×10^5 are presented in Figures C.10 through C.17. Figures C.10 through C.13 show the power-off measurements, and Figures C.14 through C.17 show the power-on measurements. The measurement uncertainty is only provided for $\mathrm{Re} = 2.5 \times 10^5$ to improve the readability of the figures. The results for the SLE wing are provided for comparison. Much like the modification to the lift coefficient, the effect of the tubercles on the drag coefficient is most apparent at angles of attack near stall, namely $10^\circ \leq \alpha \leq 17^\circ$. One of the conclusions of Chapter 4 was that increasing the tubercle amplitude yields a smoother stall characteristic at the cost of a reduced maximum lift coefficient and reduced stall angle. This is represented in Figures C.10 through C.17 by the drag rise experienced by the wings with larger tubercle amplitudes occurring at lower angles of attack when compared to the SLE wing. The wings with smaller tubercle amplitudes show the opposite, with a delay in the drag rise that accompanies stall as a result of their increased stall angles. These observations remain consistent across all four of the Reynolds numbers tested.

C.2.3 Aerodynamic Efficiencies

The aerodynamic efficiencies for each tubercle wing at $\mathrm{Re} = 1.0 \times 10^5$, 1.5×10^5, 2.0×10^5 and 2.5×10^5 are presented in Figures C.18 through C.25. Figures C.18 through C.21 show the power-off measurements, and Figures C.22 through C.25 show the power-on measurements. The results for the SLE wing are provided for comparison. The aerodynamic efficiency is impacted by any modifications to the lift performance or the drag performance of the wing. The effect of the tubercles is most significant on the lift performance of the wing, and so the resulting trends in aerodynamic efficiency are generally the same as the trends in lift coefficient. The aerodynamic efficiency is reduced for pre-stall angles of attack when compared to the SLE wing, and increased for post-stall angles of attack, with the tubercle wings with smaller amplitudes producing larger post-stall aerodynamic efficiencies, than larger tubercle amplitudes. The trends remain consistent across all four Reynolds numbers.

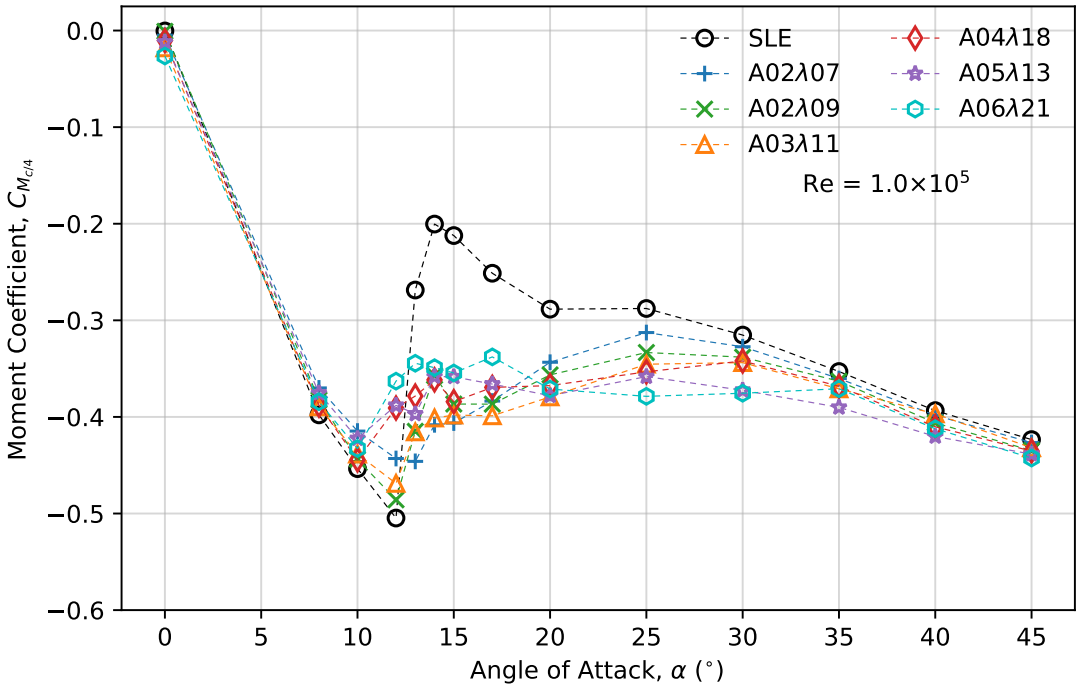

Figure C.2: power-off moment coefficients about the quarter chord for six tubercle wings at $\mathrm{Re} = 1.0 \times 10^5$.

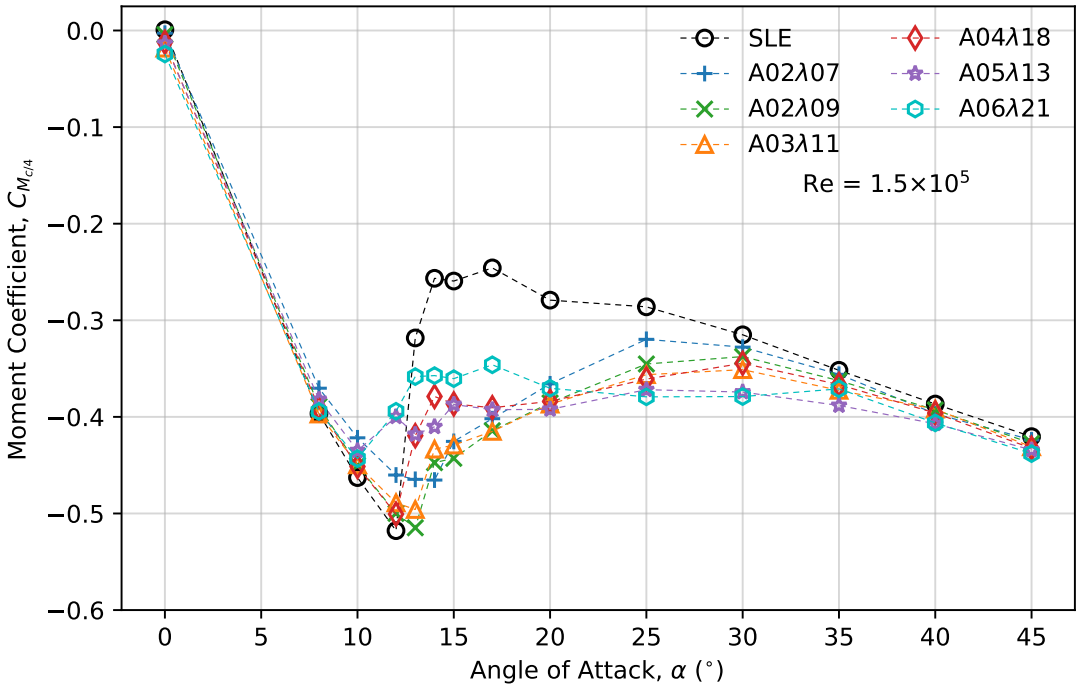

Figure C.3: power-off moment coefficients about the quarter chord for six tubercle wings at $\mathrm{Re} = 1.5 \times 10^5$.

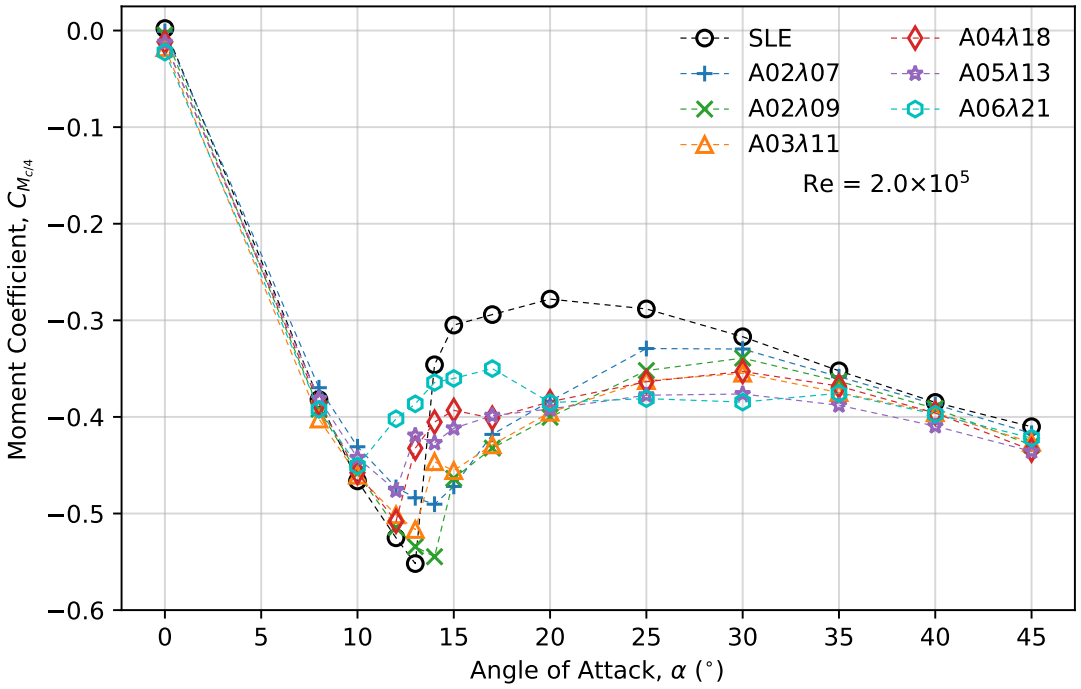

Figure C.4: power-off moment coefficients about the quarter chord for six tubercle wings at $\mathrm{Re} = 2.0 \times 10^5$.

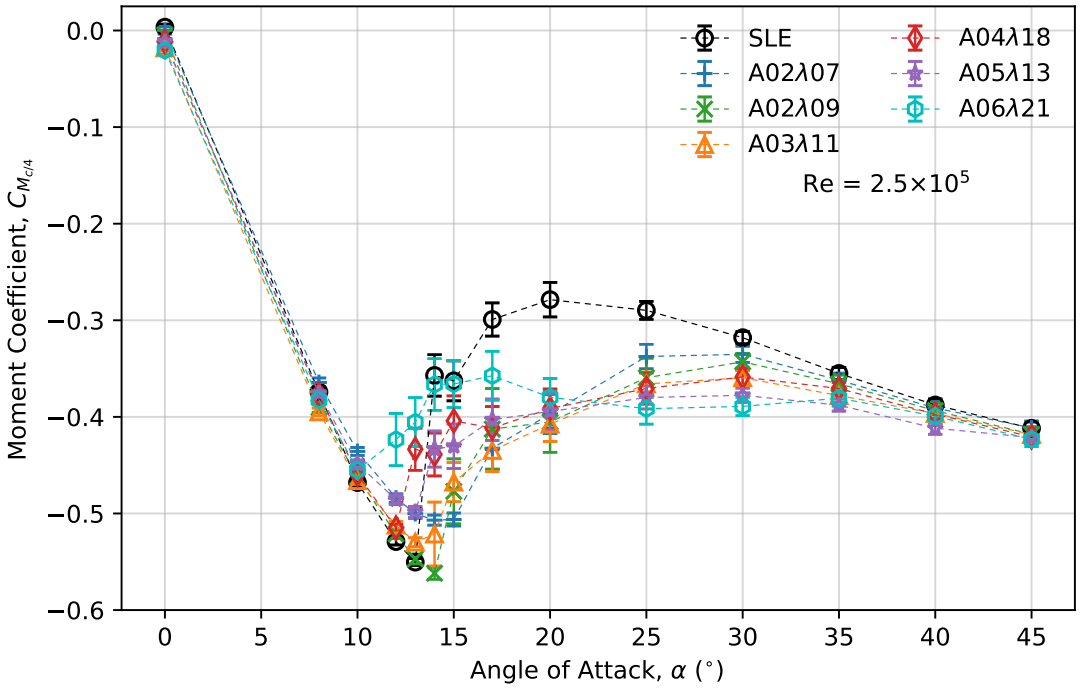

Figure C.5: power-off moment coefficients about the quarter chord for six tubercle wings at $\mathrm{Re} = 2.5 \times 10^5$.

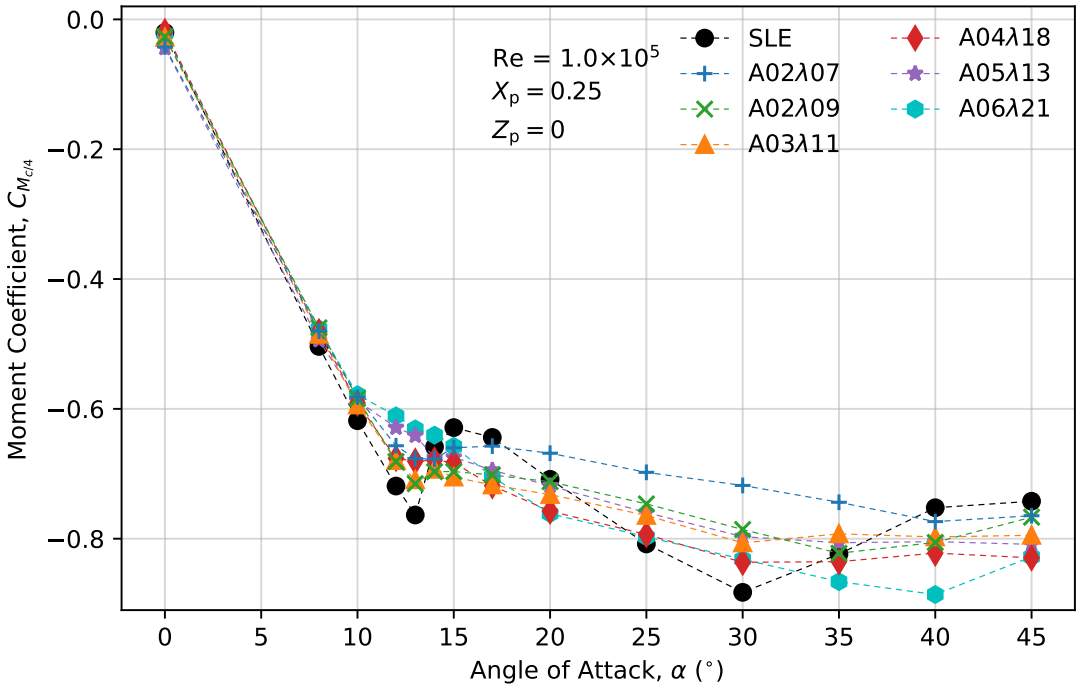

Figure C.6: power-on moment coefficients about the quarter chord for six tubercle wings with the optimal propeller position at $\mathrm{Re} = 1.0 \times 10^5$.

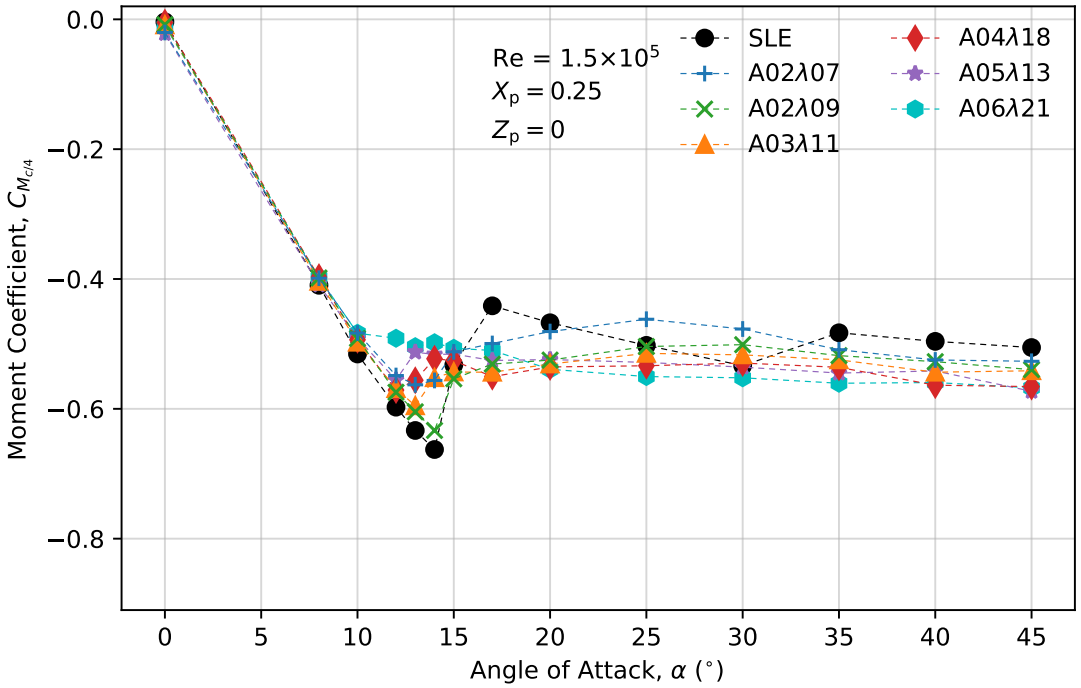

Figure C.7: power-on moment coefficients about the quarter chord for six tubercle wings with the optimal propeller position at $\mathrm{Re} = 1.5 \times 10^5$.

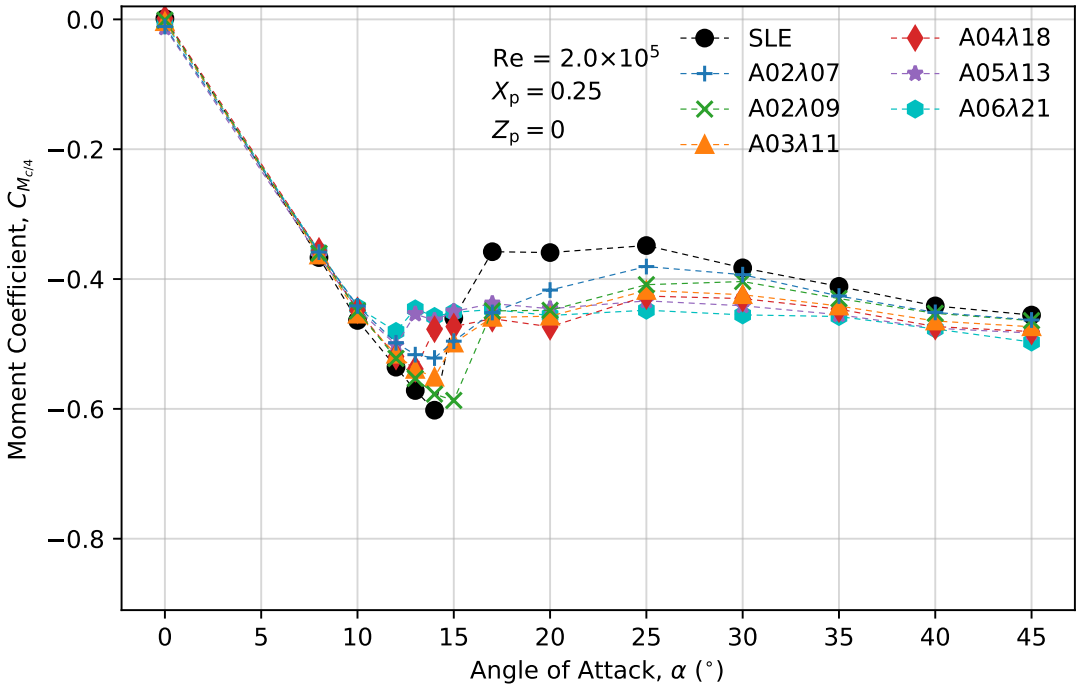

Figure C.8: power-on moment coefficients about the quarter chord for six tubercle wings with the optimal propeller position at $\mathrm{Re} = 2.0 \times 10^5$.

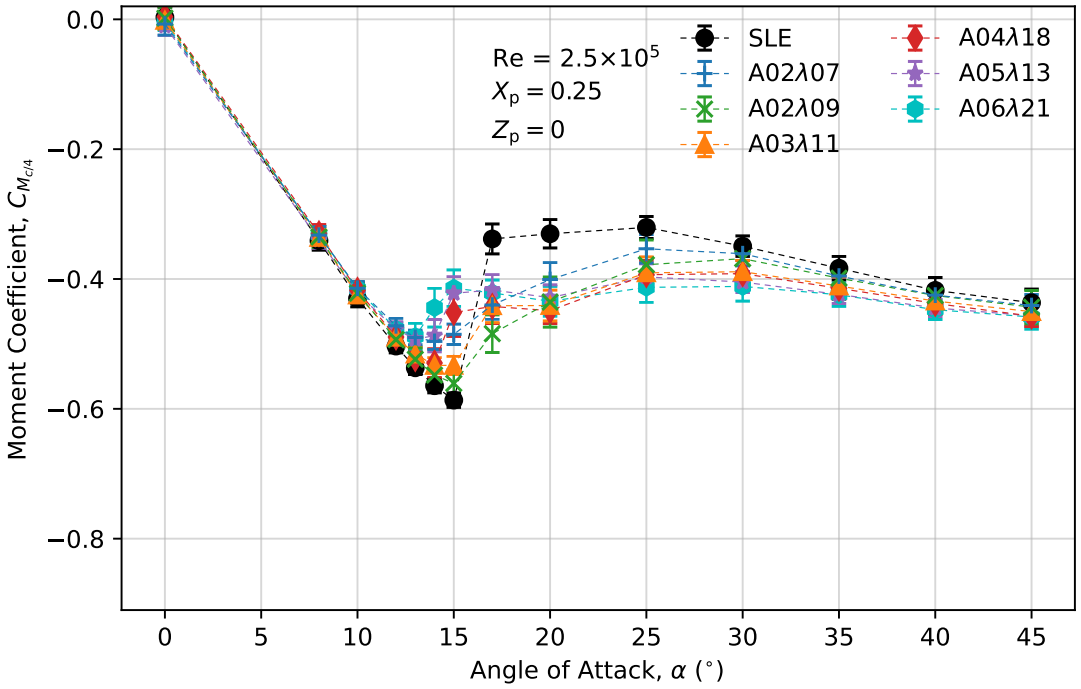

Figure C.9: power-on moment coefficients about the quarter chord for six tubercle wings with the optimal propeller position at $\mathrm{Re} = 2.5 \times 10^5$.

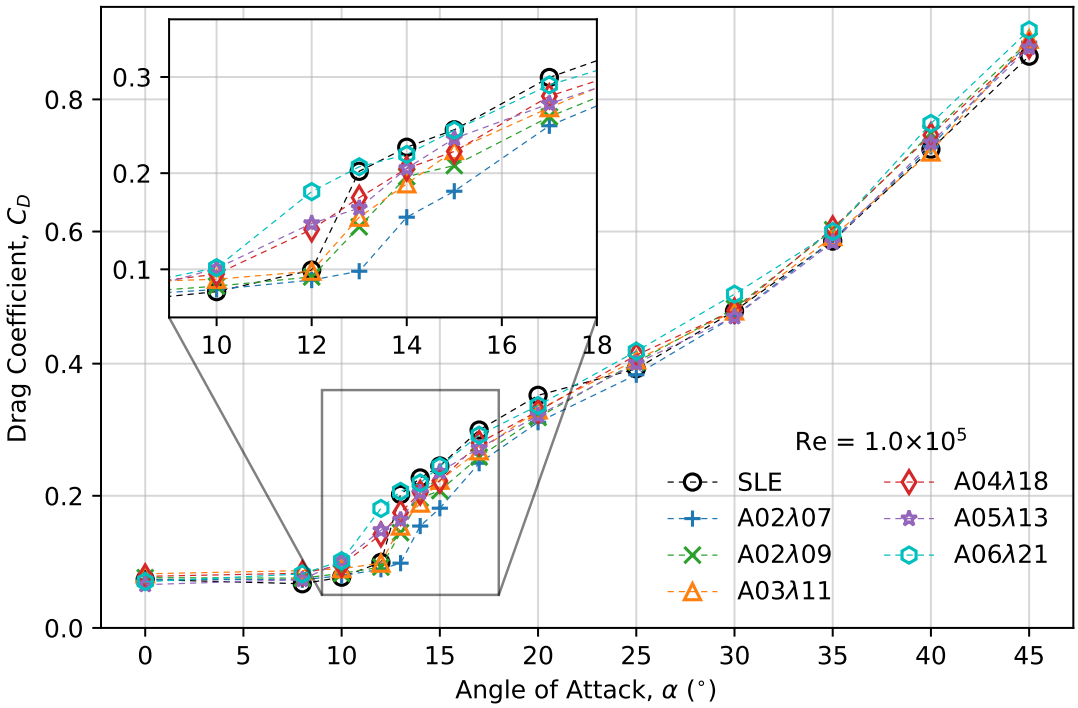

Figure C.10: power-off drag coefficients for six tubercle wings at Re = 1.0×10^5.

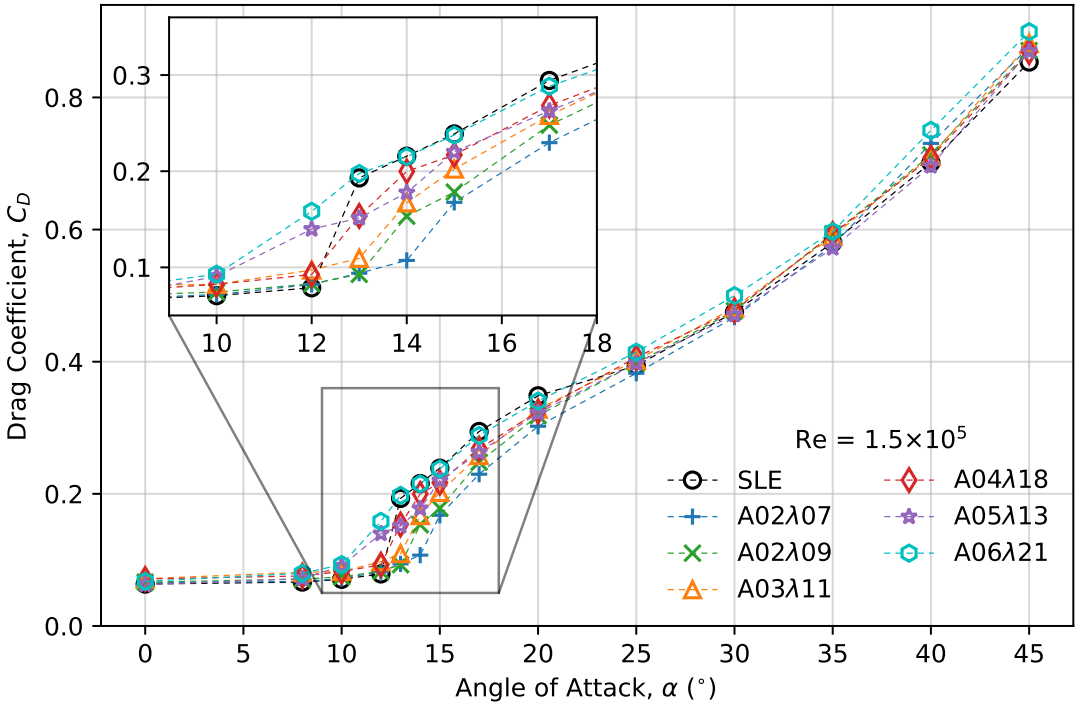

Figure C.11: power-off drag coefficients for six tubercle wings at Re = 1.5×10^5.

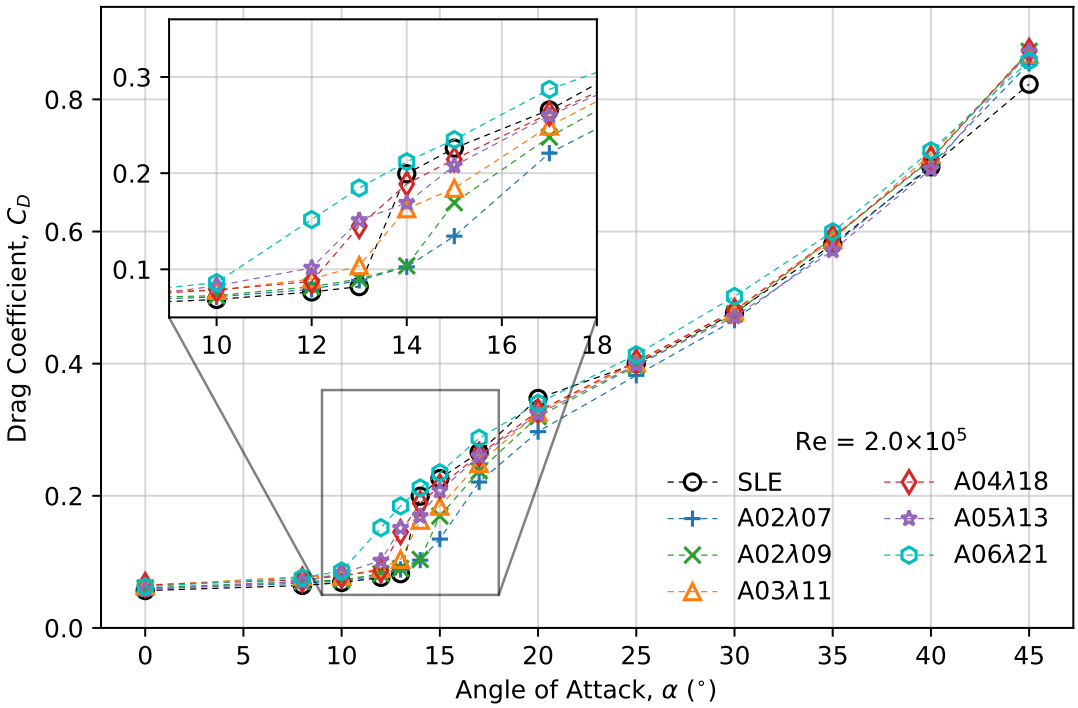

Figure C.12: power-off drag coefficients for six tubercle wings at Re = 2.0×10^5.

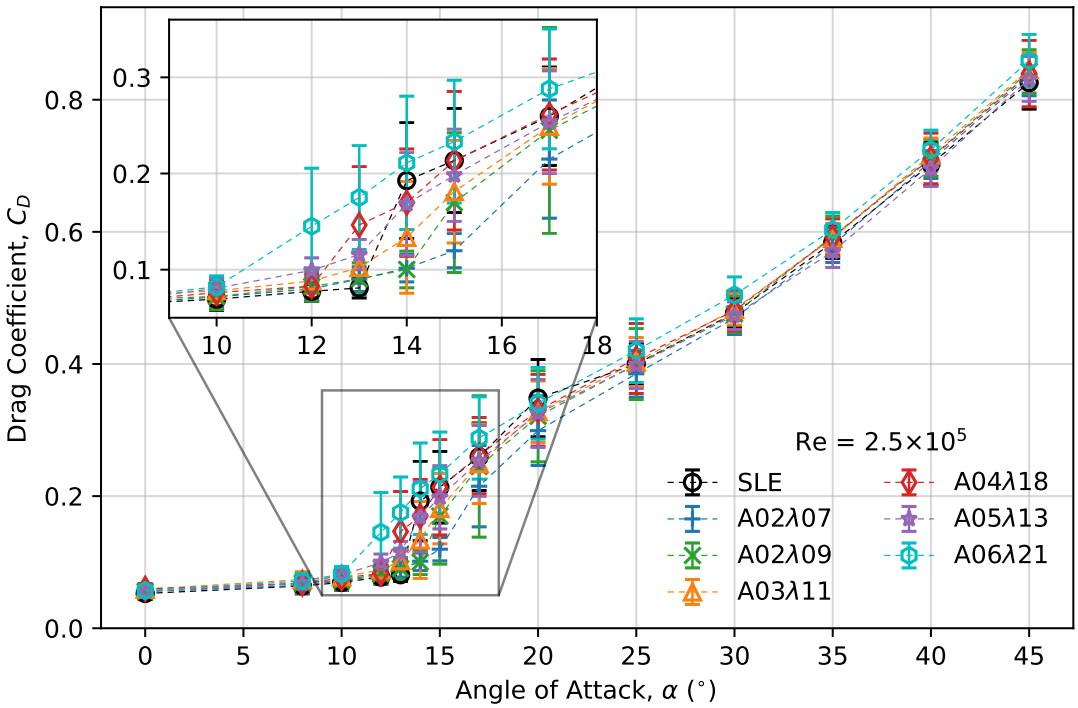

Figure C.13: power-off drag coefficients for six tubercle wings at Re = 2.5×10^5.

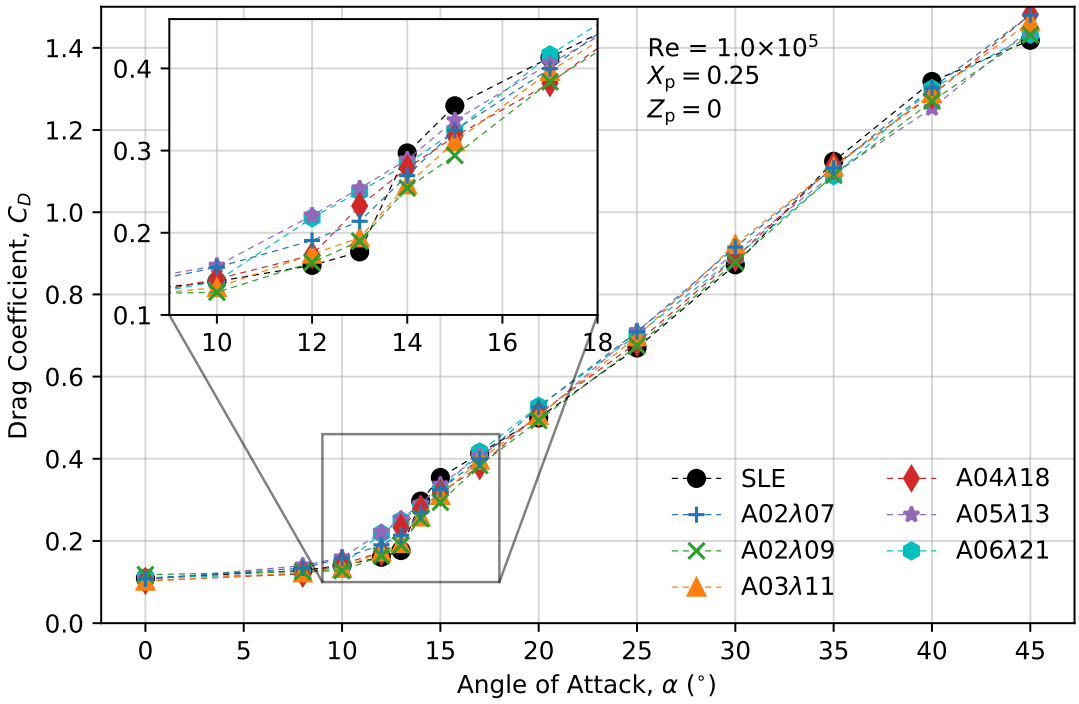

Figure C.14: power-on drag coefficients for six tubercle wings with the optimal propeller position at $\mathrm{Re} = 1.0 \times 10^5$.

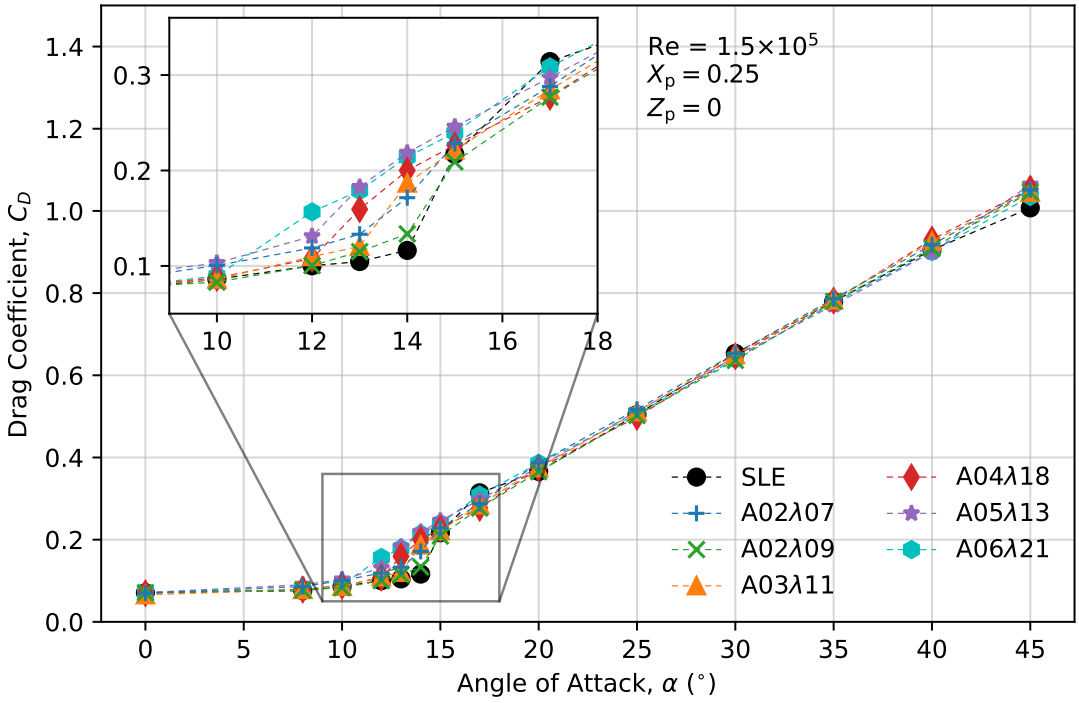

Figure C.15: power-on drag coefficients for six tubercle wings with the optimal propeller position at $\mathrm{Re} = 1.5 \times 10^5$.

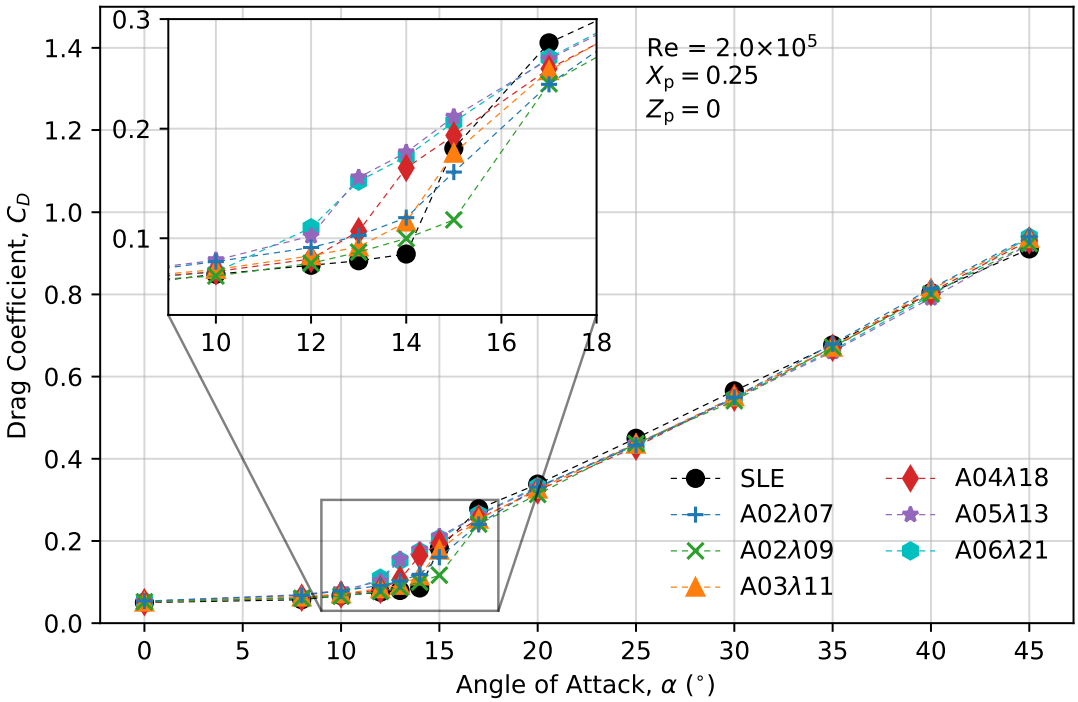

Figure C.16: power-on drag coefficients for six tubercle wings with the optimal propeller position at $\mathrm{Re} = 2.0 \times 10^5$.

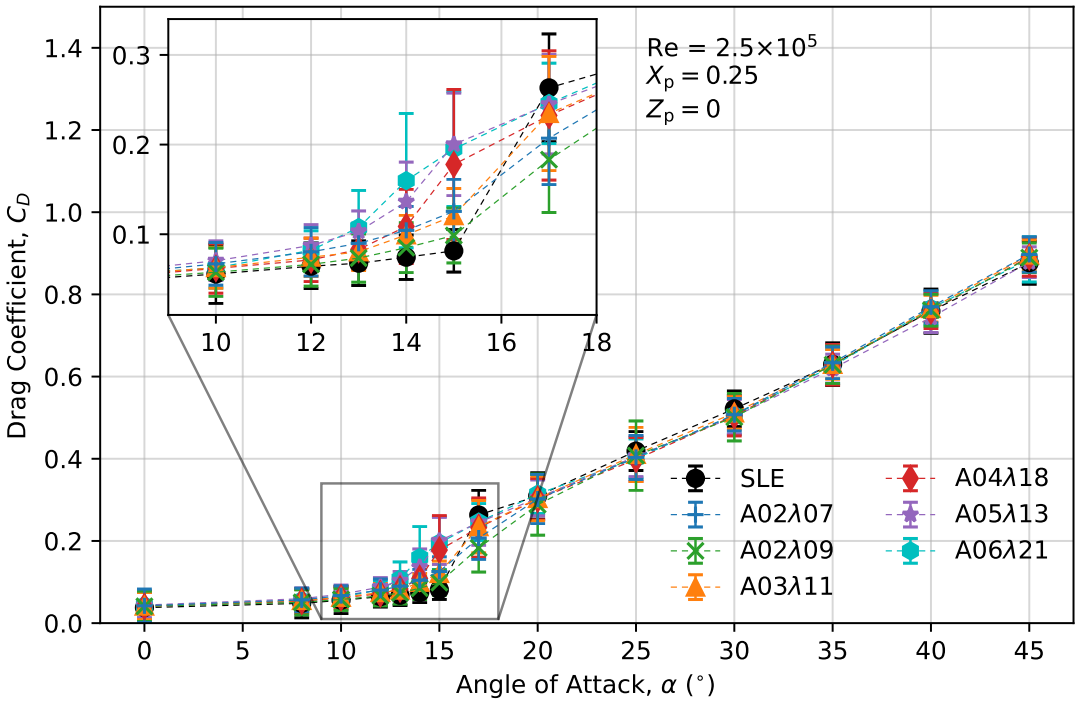

Figure C.17: power-on drag coefficients for six tubercle wings with the optimal propeller position at $\mathrm{Re} = 2.5 \times 10^5$.

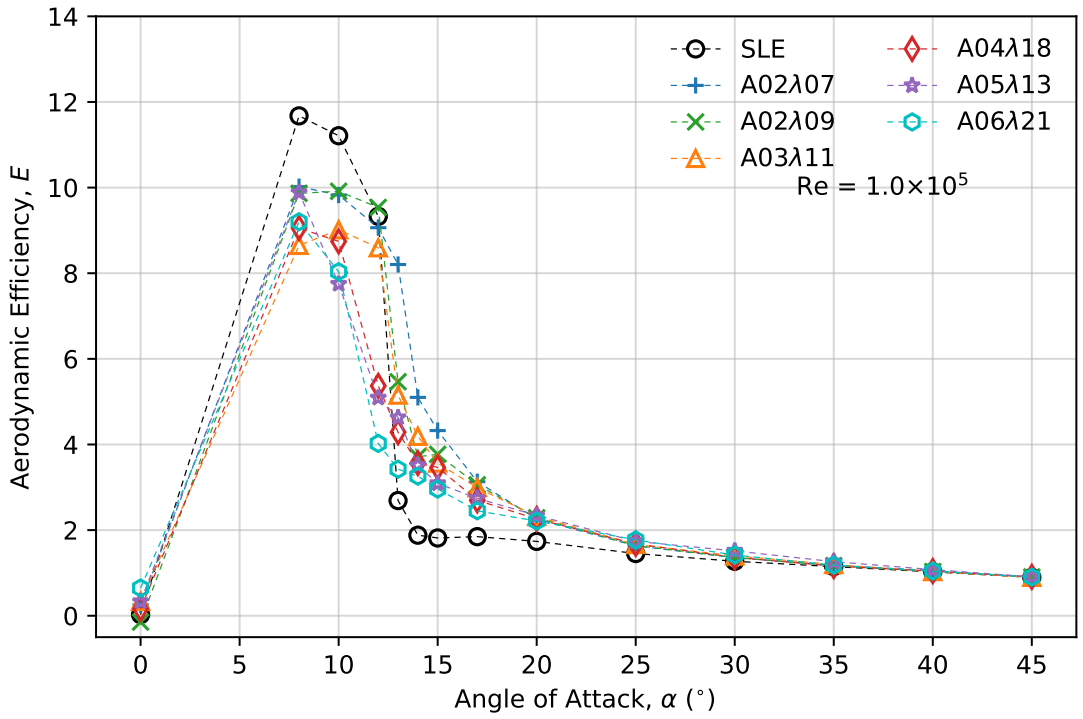

Figure C.18: power-off aerodynamic efficiency for six tubercle wings at $\mathrm{Re} = 1.0 \times 10^5$.

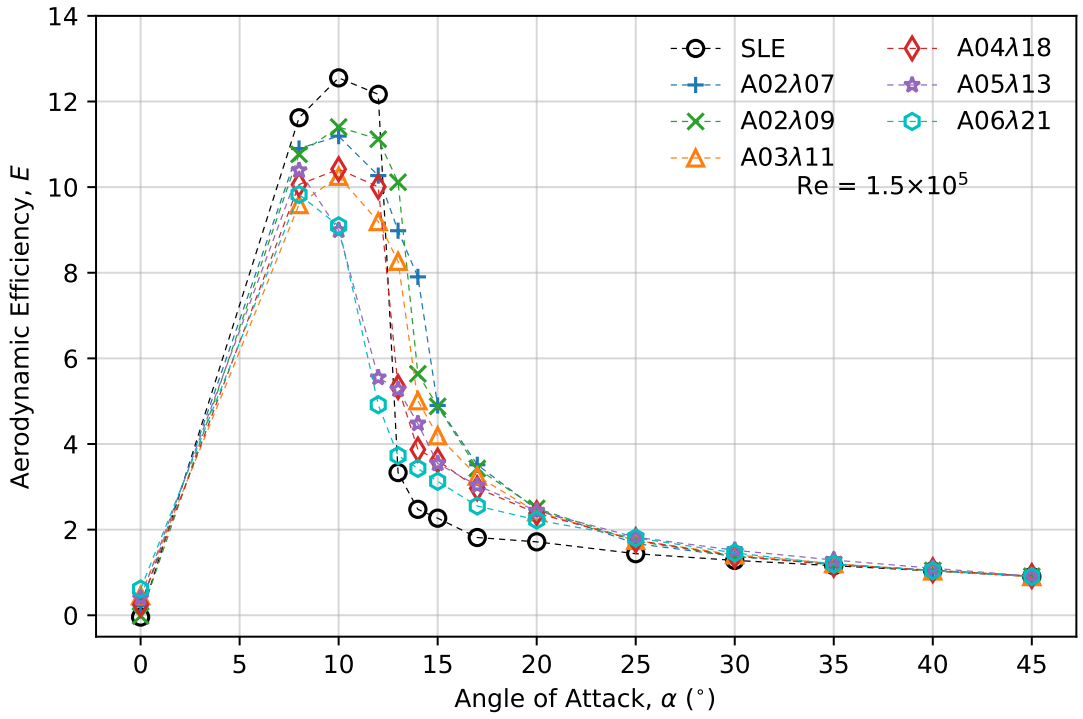

Figure C.19: power-off aerodynamic efficiency for six tubercle wings at $\mathrm{Re} = 1.5 \times 10^5$.

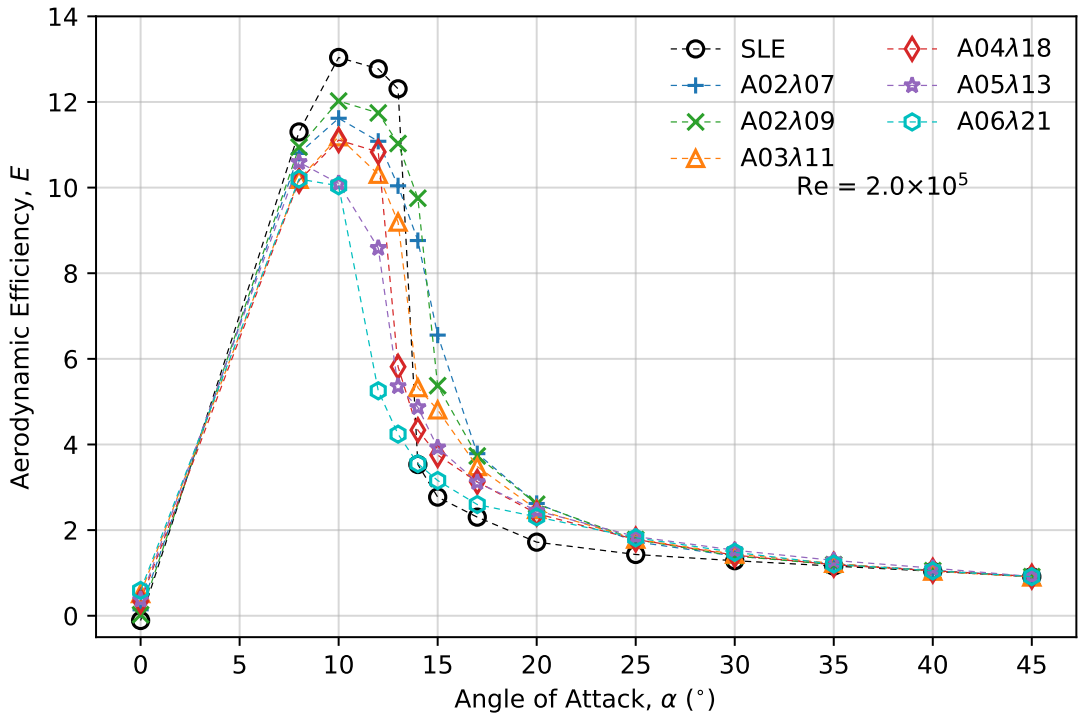

Figure C.20: power-off aerodynamic efficiency for six tubercle wings at $\mathrm{Re} = 2.0 \times 10^5$.

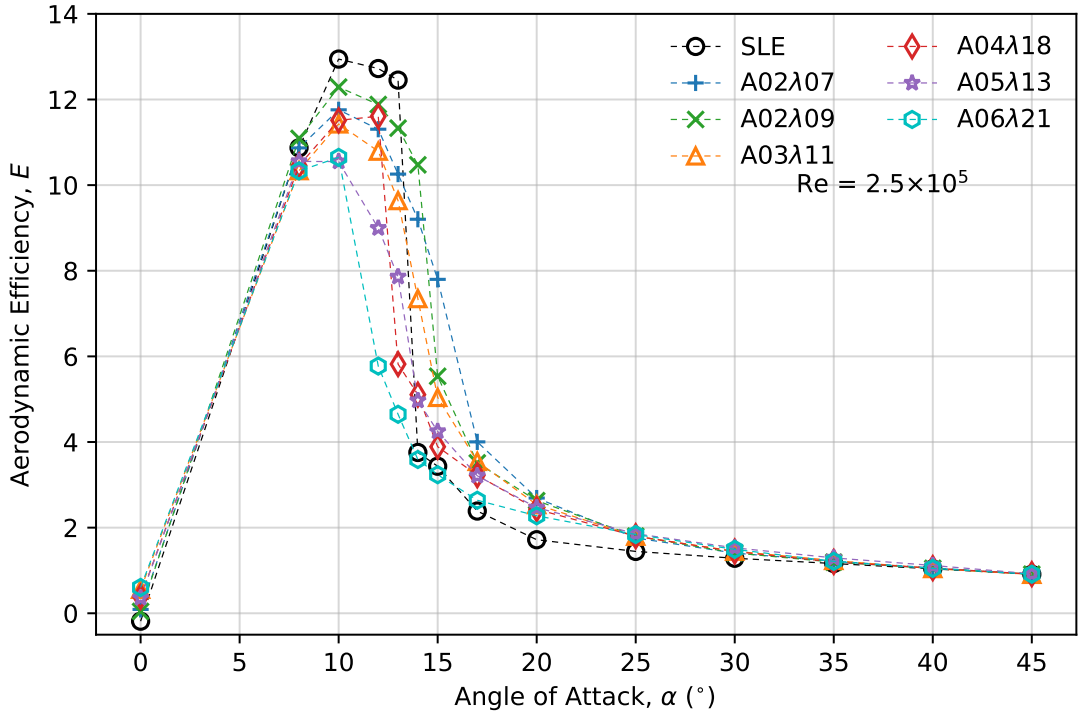

Figure C.21: power-off aerodynamic efficiency for six tubercle wings at $\mathrm{Re} = 2.5 \times 10^5$.

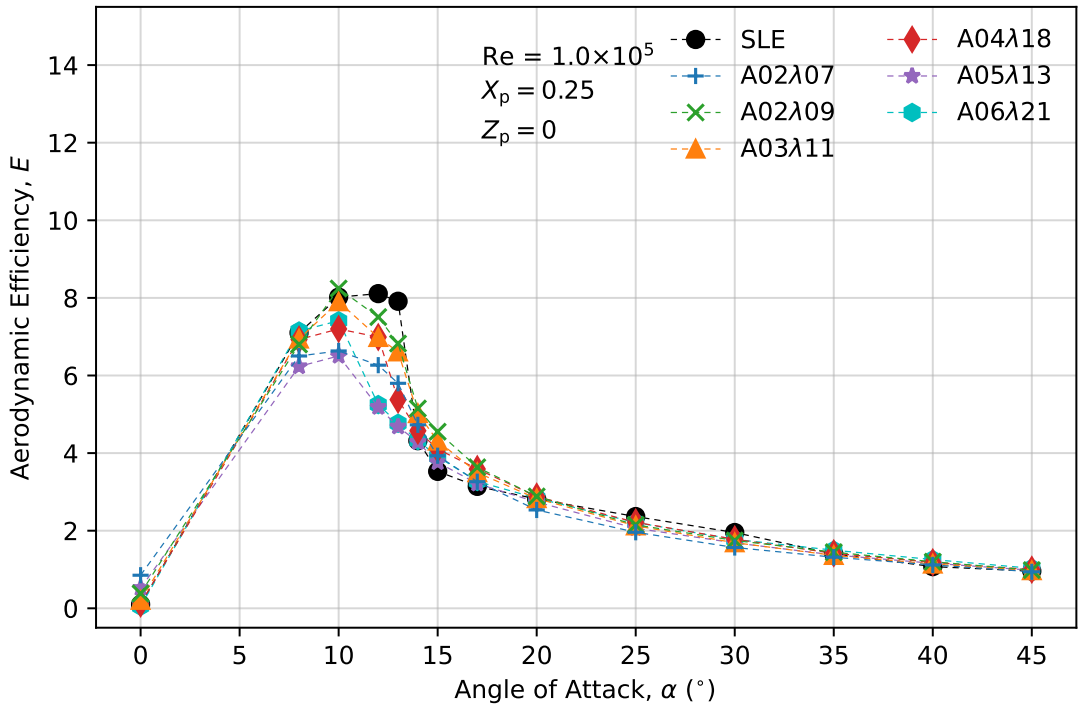

Figure C.22: power-on aerodynamic efficiency for six tubercle wings with the optimal propeller position at $\mathrm{Re} = 1.0 \times 10^5$.

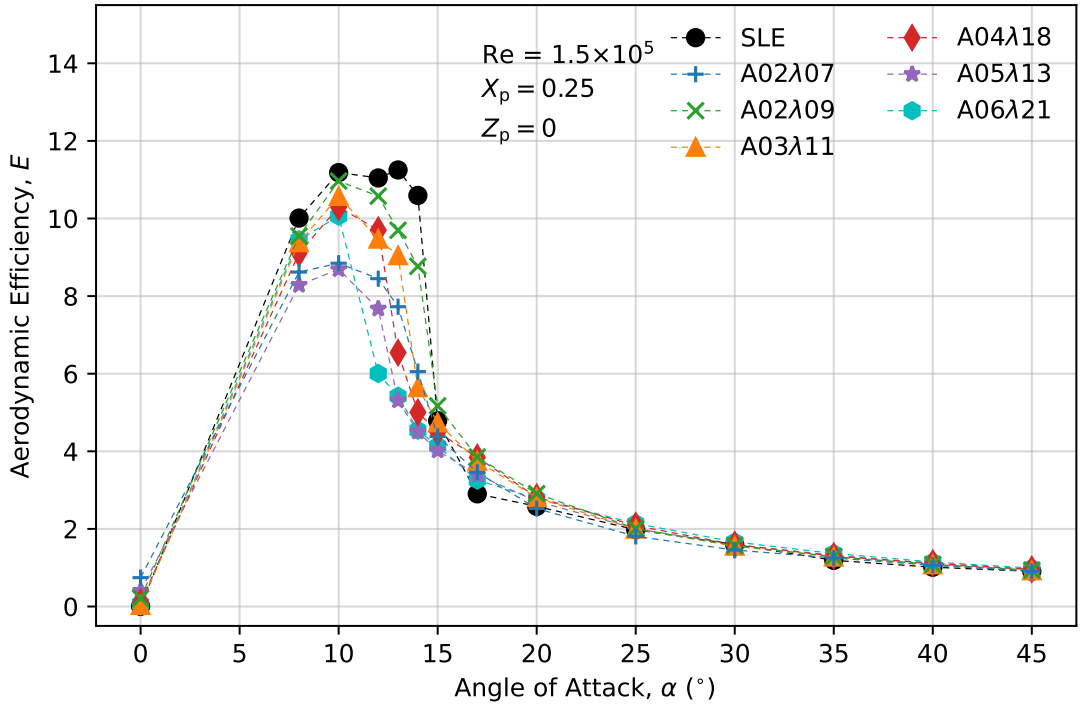

Figure C.23: power-on aerodynamic efficiency for six tubercle wings with the optimal propeller position at $\mathrm{Re} = 1.5 \times 10^5$.

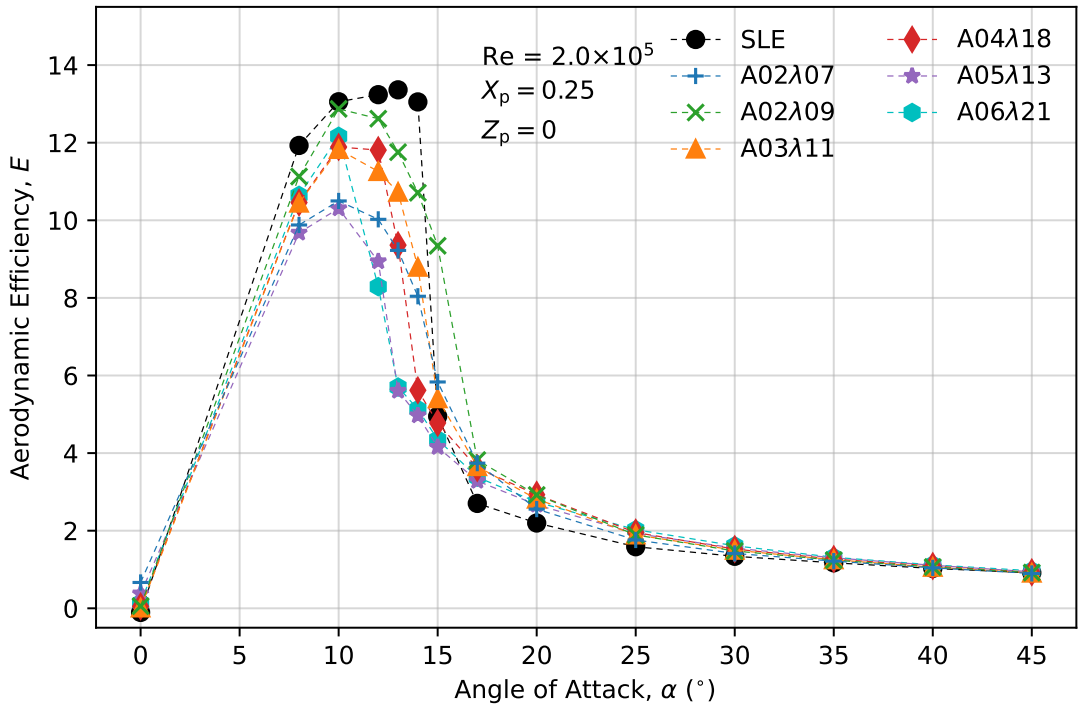

Figure C.24: power-on aerodynamic efficiency for six tubercle wings with the optimal propeller position at Re = 2.0×10^5.

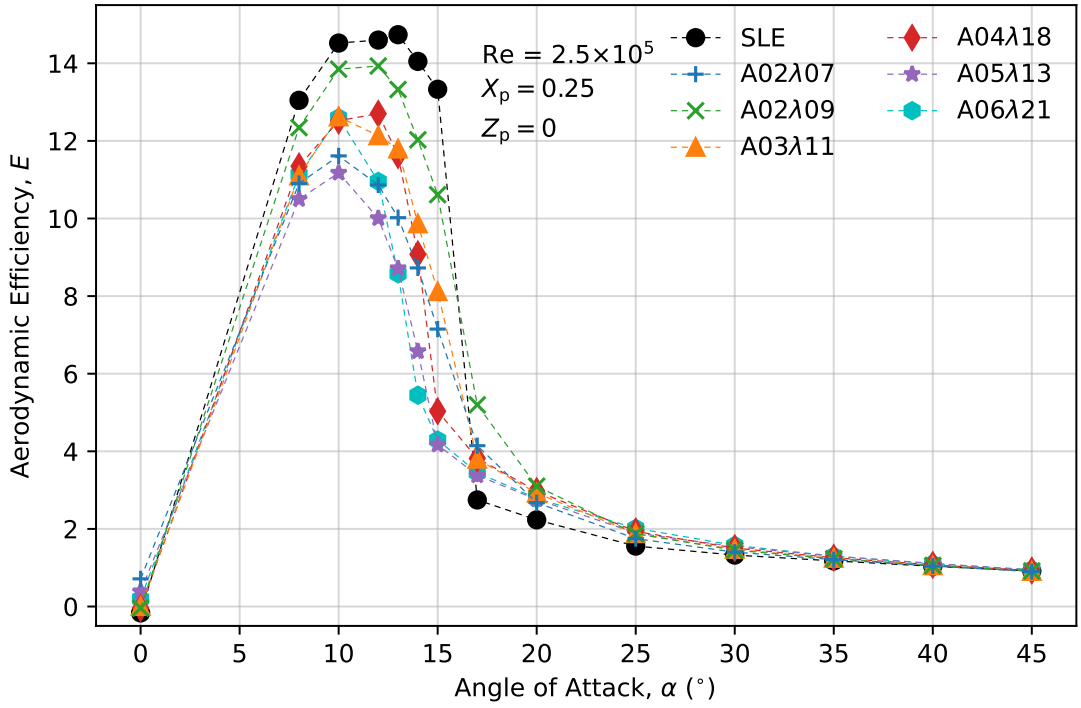

Figure C.25: power-on aerodynamic efficiency for six tubercle wings with the optimal propeller position at Re = 2.5×10^5.

C.3 Lift Augmentation of Different Tubercle Wings

The lift augmentation portion of the total lift coefficient for each tubercle wing with the propeller at the optimal position ($X_p = 0.25$, $Z_p = 0$), at Re $= 1.0 \times 10^5$, 1.5×10^5, and 2.5×10^5 are presented in Figures C.26, C.27 and C.28 respectively. The conclusions made in Chapter 4 still apply.

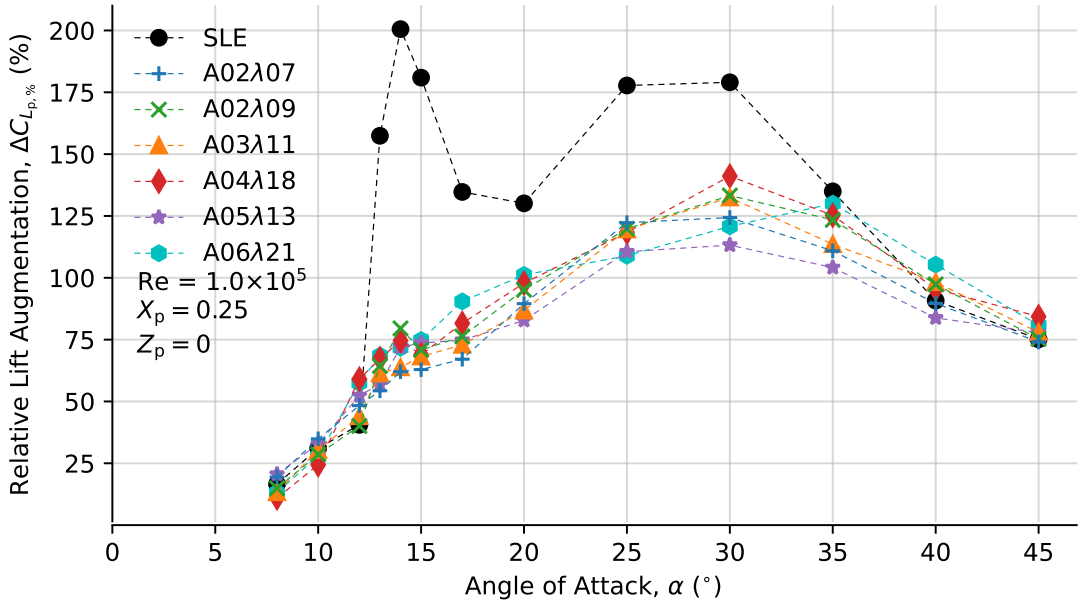

Figure C.26: Lift augmentation of each wing with the propeller at the optimal position at Re $= 1.0 \times 10^5$.

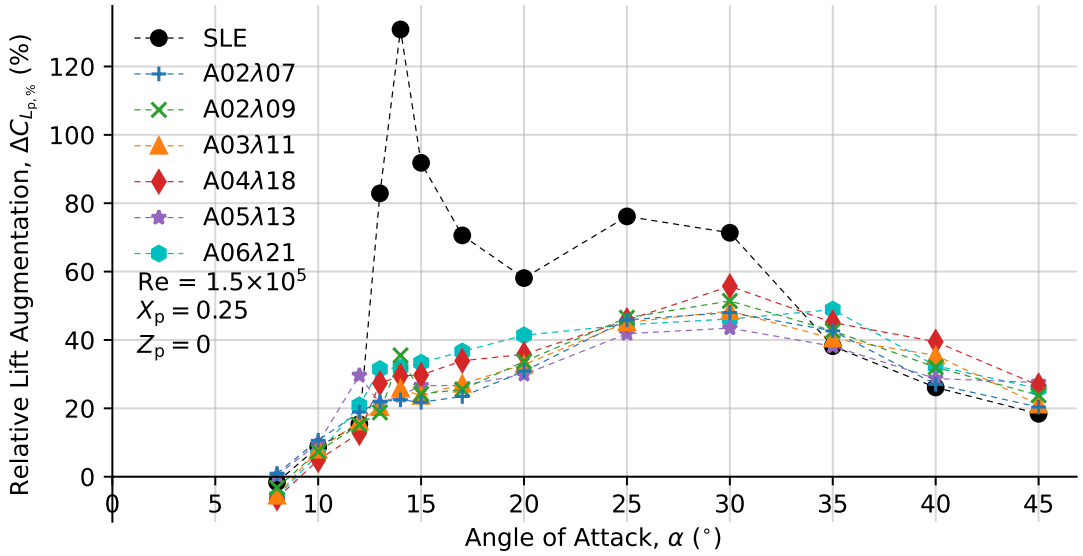

Figure C.27: Lift augmentation of each wing with the propeller at the optimal position at Re $= 1.5 \times 10^5$.

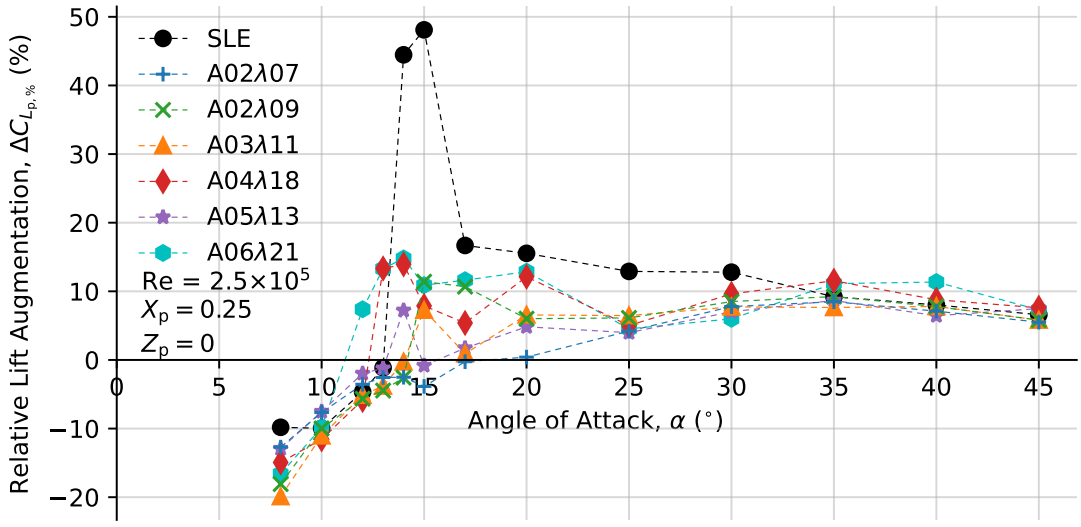

Figure C.28: Lift augmentation of each wing with the propeller at the optimal position at $\mathrm{Re} = 2.5 \times 10^5$.

D Transition Corridors with Tubercles

The transition corridors for the RMC TRV with different tubercle geometries are presented below. All observations and conclusions drawn in Chapter 5 apply.

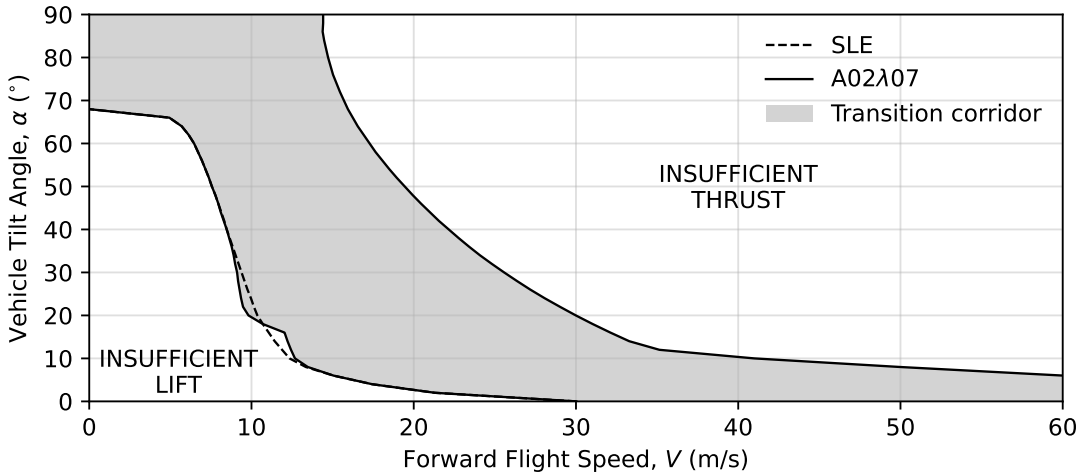

Figure D.1: Transition corridor of the RMC TRV with the A0λ07 tubercles.

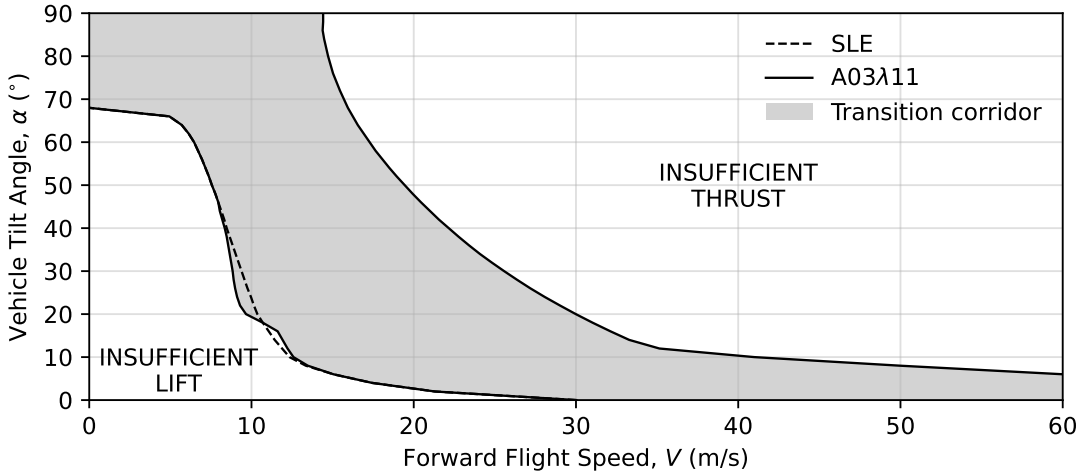

Figure D.2: Transition corridor of the RMC TRV with the A03λ11 tubercles.

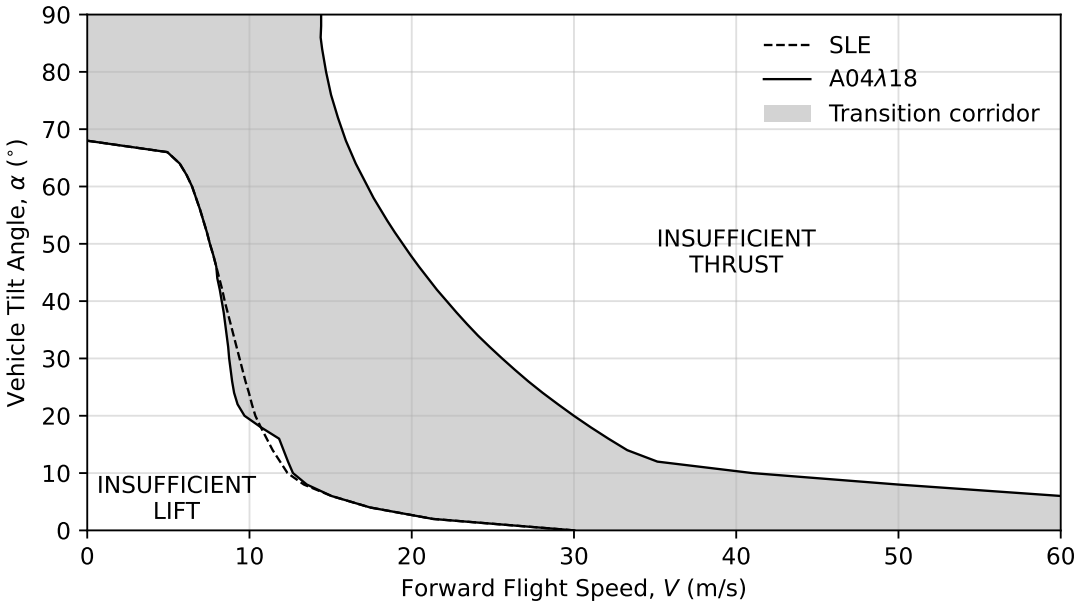

Figure D.3: Transition corridor of the RMC TRV with the A04λ18 tubercles.

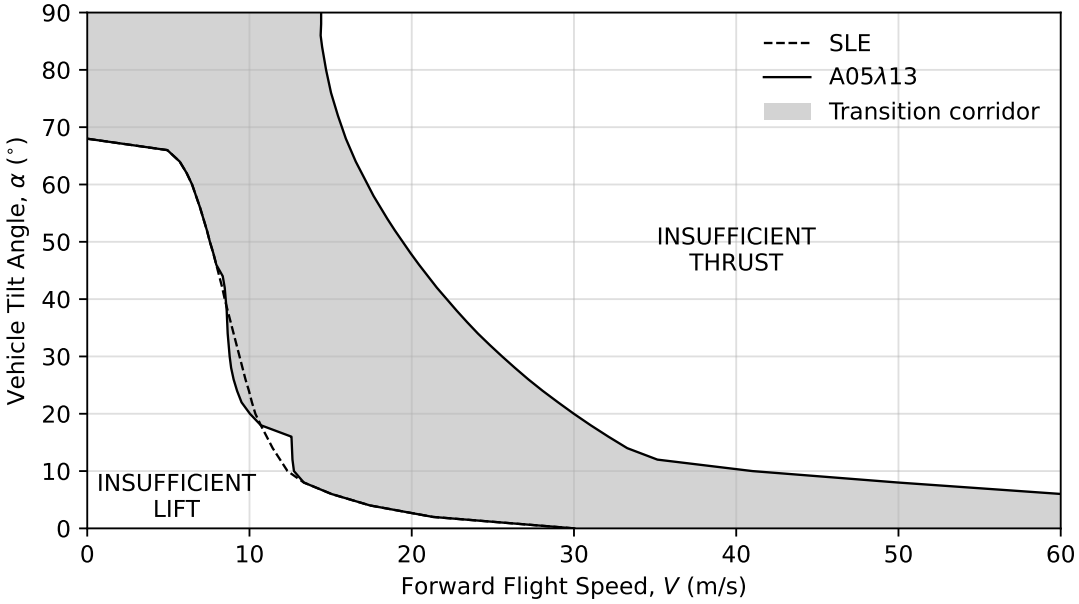

Figure D.4: Transition corridor of the RMC TRV with the A05λ13 tubercles.

E Blade Element Momentum Theory with Correction Factors

Blade element momentum theory is a commonly used numerical analysis method to estimate the aerodynamic properties of a rotor. BEMT was used as a design tool to verify the design of the monocopter blade in Chapter 6. The variable r is a value between 0 and 1 that is used to describe the non-dimensional radial position along the blade, given by Equation E.1, where y is the dimensional radial position and R is the radius of the blade. The basis of BEMT is the discretization of the blade into radial elements dr, which is described in Figure E.1.

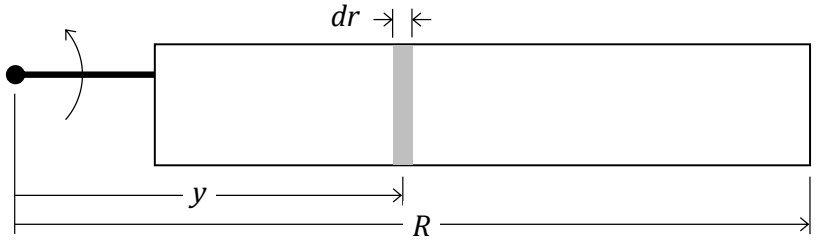

$$r = \frac{y}{R} \tag{E.1}$$

Figure E.1: Blade discretization for BEMT (adapted from [75]).

The lift and drag coefficients were obtained from experimental data for the selected airfoil profile, and used in Equation E.2 to calculate the incremental thrust coefficient and power coefficients for each blade element [75].

$$dC_T = \frac{1}{2}\sigma C_l r^2 dr \qquad\qquad dC_P = 4\lambda^3 r dr + \frac{1}{2}\sigma C_d r^3 dr \tag{E.2}$$

where C_l and C_d are the section lift and drag coefficients, r is the non-dimensional radial position, and dr is the discretized blade segment width. The variable σ is a geometric parameter known as the blade solidity. It is defined as the ratio of the planform area of the blade to the area of the circle traced by the blade tip over one revolution [75]:

$$\sigma = \frac{S_\mathrm{b}}{\pi R^2} \tag{E.3}$$

where S_b is the planform area of the blade, and R is the blade radius. The variable λ is the inflow ratio. The inflow ratio is the ratio between the component of the velocity seen by the blade element that is perpendicular to the plane of rotation, U_P, and the component tangential to the blade, U_T. This is described in Figure E.2, and shown by the following equation, where $C_{l,\alpha}$ is the lift curve slope of the selected airfoil, θ is the

pitch angle of the blade element, and α_0 is the zero lift angle of attack for the selected airfoil. [75]:

$$\lambda = \frac{U_P}{U_T} = \frac{\sigma C_{l,\alpha}}{16}\left(\sqrt{1 + \frac{32}{\sigma C_{l,\alpha}}(\theta - \alpha_0)\, r} - 1\right) \tag{E.4}$$

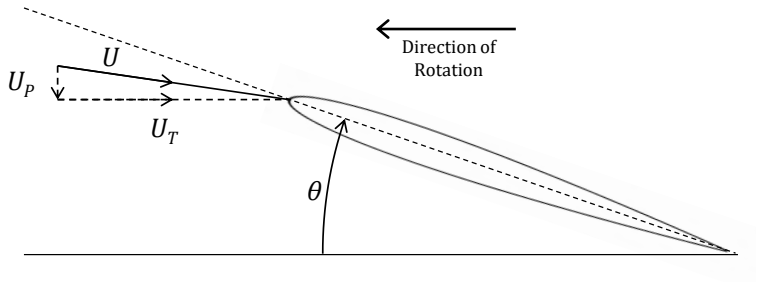

Figure E.2: View of a blade element showing perpendicular and tangential velocity components (adapted from [75]).

The incremental thrust and power coefficients were then numerically integrated using a trapezoidal approximation method to obtain the overall thrust and power coefficients. Additional corrections were made to account for tip losses, propeller effects, the coning angle, and drag of non-lifting components, which are discussed below.

E.1 Tip Losses

Tip losses were incorporated into the BEMT analysis using Prandtl's tip loss function by including a factor, F, in Equation E.4 [75]:

$$\lambda = \frac{\sigma C_{l,\alpha}}{16F}\left(\sqrt{1 + \frac{32F}{\sigma C_{l,\alpha}}(\theta - \alpha_0)\, r} - 1\right) \tag{E.5}$$

where the only difference from Equation E.2 is the inclusion of Prandtl's tip loss factor, F, which is calculated using the following equation [75]:

$$\begin{aligned} F &= \left(\frac{2}{\pi}\right)\cos^{-1}\left(\exp\left(-f\right)\right) \\ f &= \frac{1}{2}\left(\frac{1-r}{\lambda}\right) \end{aligned} \tag{E.6}$$

The variable f is a function of the inflow, λ, and an iterative approach was used to converge to a corrected inflow distribution.

E.2 Propeller Effects

The power coefficient and torque coefficient are numerically the same ($C_P \equiv C_Q$) [75]. This allows the power coefficient obtained using BEMT without any correction factors to be used to estimate the thrust required from the propeller:

$$\begin{aligned} Q &= \rho\pi\Omega^2 R^5 C_Q \\ T_\mathrm{p} &= \frac{Q}{y_\mathrm{p} R} \end{aligned} \tag{E.7}$$

where Q is the torque required, C_Q is the torque coefficient (C_P), y_p is the radial location of the propeller (as a percentage of the radius), and T_p is the required thrust from the propeller to produce the torque, Q. By simplifying the propeller as an actuator disc, momentum theory was used to approximate the velocity of the flow within the propeller slipstream [75]:

$$w = k_w \sqrt{\frac{T_\mathrm{p}/\cos\theta_\mathrm{p}}{2\rho\pi R^2}} \tag{E.8}$$

The estimated thrust required, T_p is divided by the cosine of the blade pitch angle to account for the propeller installation angle. The variable k_w takes on the value 2 if the slipstream is fully developed. For the RMC monocopter the propeller was positioned close to the leading edge and the slipstream was not assumed to be fully developed, so a value of $k_w = 1.5$ was used. The component of the slipstream velocity, w, perpendicular to the plane of rotation was added to U_P in Equation E.4 to calculate the inflow corrected for the propeller slipstream effects:

$$\lambda = \frac{U_P + w_P}{U_T} = \frac{\sigma C_{l,\alpha}}{16F}\left(\sqrt{1 + \frac{32F}{\sigma C_{l,\alpha}}(\theta - \alpha_0)\, r} - 1\right) + \frac{w_P}{U_T} \tag{E.9}$$

A secondary effect of the propeller is the component of thrust that contributes to the lift generated by the blade as a result of the installation angle. This component of thrust was included in the BEMT. The propeller slipstream effects were iterated alongside Prandtl's tip loss factor, using the power coefficient of the previous iteration to obtain a better estimate for the thrust required from the propeller. The performance data for the *APC* 5×5E propeller was obtained from the manufacturer [92]. The propeller efficiency is provided for various flight speeds and rotational rates. The rotational rate of the propeller during flight testing was estimated by determining the blade passing frequency, BPF using a power spectral density plot of a 30 second audio recording from a video of a flight test, shown in Figure E.3.

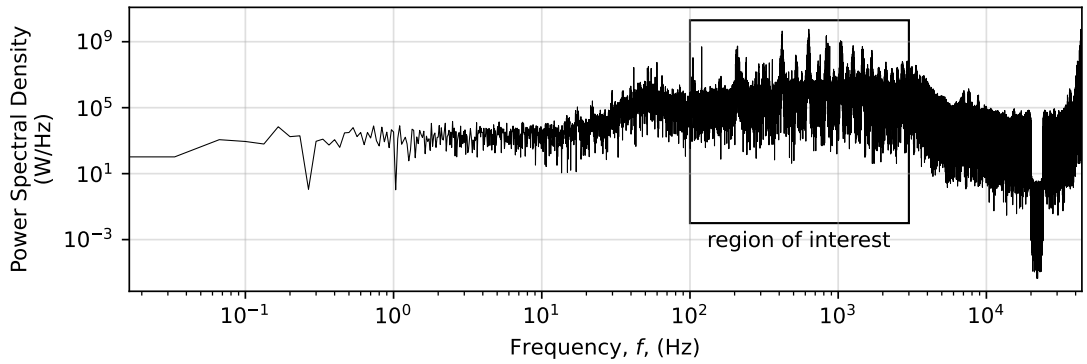

Figure E.3: Power spectral density plot for the audio from a video recording of a flight test.

Figure E.4 shows a zoomed in view of the region of interest indicated in Figure E.3. The BPF and corresponding harmonics are labelled. A BPF of 208 Hz for the two-bladed *APC* 5 × 5E propeller resulted in an estimated rotational rate of 6240 RPM:

$$\Omega = \frac{\text{BPF}}{2} \times \frac{60 \text{ s}}{\text{min}} = \frac{208 \text{ Hz}}{2} \times \frac{60 \text{ s}}{\text{min}} = 6240 \text{ RPM} \approx 6000 \text{ RPM}$$

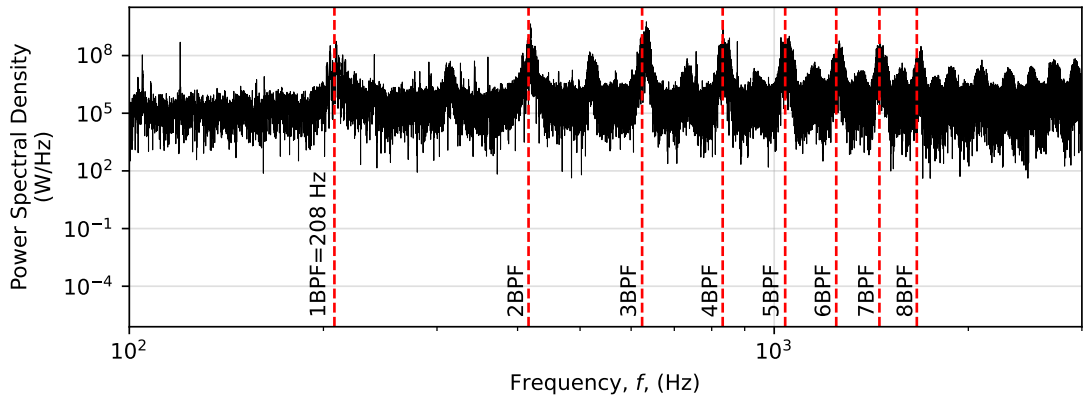

Figure E.4: Power spectral density plot zoomed in to the region of interest labelled in Figure E.3 showing the blade passing frequency.

The measured monocopter rotational rate results in a tangential velocity of 3.6 m/s (approximately 8 mph) at the radial location of the propeller. This corresponds to a propeller efficiency of $\eta_\text{p} = 0.39$ for the estimated propeller rotational rate of approximately 6000 RPM. The efficiency of the *LHI MT2204* electric motor was assumed to be $\eta_\text{m} = 0.75$, and 2% cable losses were assumed ($\eta_\text{c} = 0.98$). The final power coefficient estimated by BEMT was divided by these efficiencies to account for these non-ideal effects.

E.3 Coning Angle Correction

The coning angle of the blade results in the lift vector of the blade (or thrust vector of the monocopter) pointing towards the axis of rotation, rather than directly vertical. This reduces the component of lift that contributes to the thrust generated by the monocopter. The coning angle was estimated by taking the sum of the moments about the centre of gravity, as shown in Figure E.5. In Figure E.5, L_b is the lift generated by the monocopter blade, F is the centrifugal force generated by the component denoted by the subscript, W is the weight of the component denoted by the subscript, and R is the distance between the component centre of gravity, denoted by the subscript, and the centre of gravity of the monocopter. Subscript b denotes the blade, m denotes the motor, esc denotes the electronic speed controller, L denotes the lift, and t denotes the telemetry pad. The moment produced by the electric motor driving the propeller was neglected.

The centrifugal force is dependant on the rotational rate of the component, and its distance from the rotational axis. The centrifugal forces were determined using the following equation:

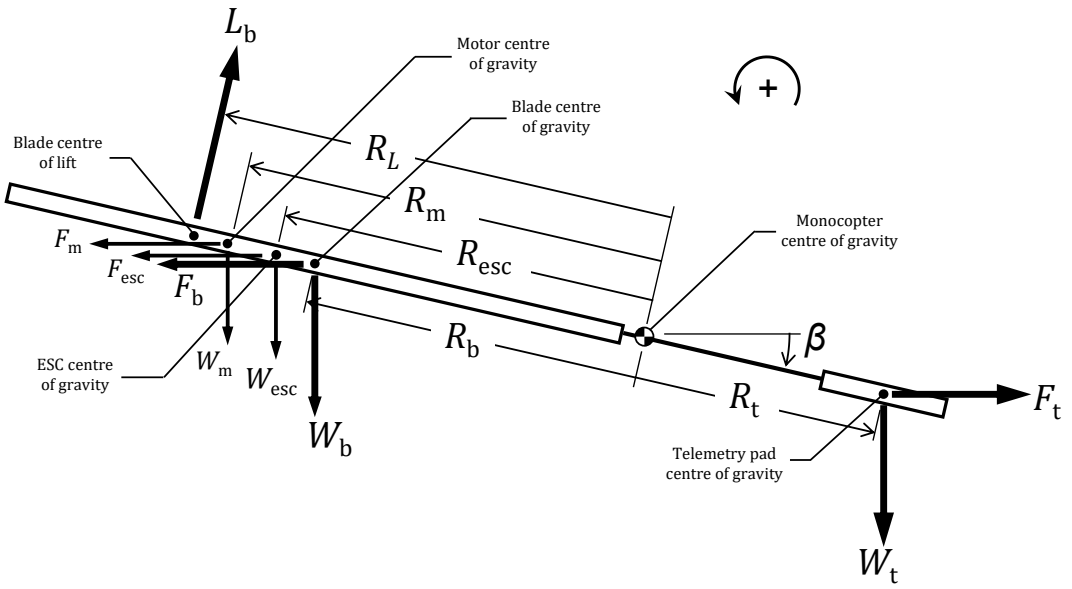

Figure E.5: Forces and moments considered when estimating the coning angle.

$$
\begin{aligned}
F_{\mathrm{b}} &= m_{\mathrm{b}} \frac{(\Omega R_{\mathrm{b}} \cos\beta)^2}{R_{\mathrm{b}} \cos\beta} = m_{\mathrm{b}} \Omega^2 R_{\mathrm{b}} \cos\beta \\
F_{\mathrm{m}} &= m_{\mathrm{m}} \frac{(\Omega R_{\mathrm{m}} \cos\beta)^2}{R_{\mathrm{b}} \cos\beta} = m_{\mathrm{m}} \Omega^2 R_{\mathrm{m}} \cos\beta \\
F_{\mathrm{esc}} &= m_{\mathrm{esc}} \frac{(\Omega R_{\mathrm{esc}} \cos\beta)^2}{R_{\mathrm{esc}} \cos\beta} = m_{\mathrm{esc}} \Omega^2 R_{\mathrm{esc}} \cos\beta \\
F_{\mathrm{t}} &= m_{\mathrm{t}} \frac{(\Omega R_{\mathrm{t}} \cos\beta)^2}{R_{\mathrm{t}} \cos\beta} = m_{\mathrm{t}} \Omega^2 R_{\mathrm{t}} \cos\beta
\end{aligned}
\tag{E.10}
$$

where the mass of each component, m, can be found in Table 6.6. The moment due to the centrifugal force is calculated simply by multiplying Equation E.10 by the distances between their respective centre of gravity and the centre of gravity of the monocopter:

$$
\begin{aligned}
M_{F_{\mathrm{b}}} &= m_{\mathrm{b}} \left(\Omega R_{\mathrm{b}}\right)^2 \cos\beta \sin\beta \\
M_{F_{\mathrm{m}}} &= m_{\mathrm{m}} \left(\Omega R_{\mathrm{m}}\right)^2 \cos\beta \sin\beta \\
M_{F_{\mathrm{esc}}} &= m_{\mathrm{esc}} \left(\Omega R_{\mathrm{esc}}\right)^2 \cos\beta \sin\beta \\
M_{F_{\mathrm{t}}} &= m_{\mathrm{t}} \left(\Omega R_{\mathrm{t}}\right)^2 \cos\beta \sin\beta
\end{aligned}
\tag{E.11}
$$

The moment due to the weight of each component acting at a distance from the centre of gravity of the monocopter was calculated using the following equation:

$$
\begin{aligned}
M_{m_{\mathrm{b}}} &= W_{\mathrm{b}} R_{\mathrm{b}} \cos\beta \\
M_{m_{\mathrm{m}}} &= W_{\mathrm{m}} R_{\mathrm{m}} \cos\beta \\
M_{m_{\mathrm{esc}}} &= W_{\mathrm{esc}} R_{\mathrm{esc}} \cos\beta \\
M_{m_{\mathrm{t}}} &= -W_{\mathrm{t}} R_{\mathrm{t}} \cos\beta
\end{aligned}
\tag{E.12}
$$

Finally, the moment generated by each blade element can be determined and numerically integrated to obtain the total moment generated by the blade, $M_{L_{\mathrm{b}}}$. In Figure

E.5, this total lift force is represented by L_b acting at a distance of R_L from the centre of gravity of the monocopter.

By taking the sum of the moments about the centre of gravity, an expression for the coning angle can be obtained:

$$\sum M = 0$$

$$M_{F_\mathrm{b}} + M_{F_\mathrm{m}} + M_{F_\mathrm{esc}} + M_{F_\mathrm{t}} + M_{m_\mathrm{b}} + M_{m_\mathrm{m}} + M_{m_\mathrm{esc}} = M_{m_\mathrm{t}} + M_{L_\mathrm{b}}$$

$$\begin{aligned} m_\mathrm{b}\left(\Omega R_\mathrm{b}\right)^2 \cos\beta \sin\beta + m_\mathrm{m}\left(\Omega R_\mathrm{m}\right)^2 \cos\beta \sin\beta \\ + m_\mathrm{esc}\left(\Omega R_\mathrm{esc}\right)^2 \cos\beta \sin\beta + m_\mathrm{t}\left(\Omega R_\mathrm{t}\right)^2 \cos\beta \sin\beta + W_\mathrm{b} R_\mathrm{b} \cos\beta \\ + W_\mathrm{m} R_\mathrm{m} \cos\beta + W_\mathrm{esc} R_\mathrm{esc} \cos\beta = W_\mathrm{t} R_\mathrm{t} \cos\beta + L_\mathrm{b} R_L \cos\beta \end{aligned}$$

$$\begin{aligned} \left(m_\mathrm{b}\left(\Omega R_\mathrm{b}\right)^2 + m_\mathrm{m}\left(\Omega R_\mathrm{m}\right)^2 + m_\mathrm{esc}\left(\Omega R_\mathrm{esc}\right)^2 + m_\mathrm{t}\left(\Omega R_\mathrm{t}\right)^2\right) \sin\beta \\ + W_\mathrm{b} R_\mathrm{b} + W_\mathrm{m} R_\mathrm{m} + W_\mathrm{esc} R_\mathrm{esc} = W_\mathrm{t} R_\mathrm{t} + L_\mathrm{b} R_L \end{aligned}$$

$$\sin\beta = \frac{W_\mathrm{t} R_\mathrm{t} + L_\mathrm{b} R_L - W_\mathrm{b} R_\mathrm{b} - W_\mathrm{m} R_\mathrm{m} - W_\mathrm{esc} R_\mathrm{esc}}{\left(m_\mathrm{b}\left(\Omega R_\mathrm{b}\right)^2 + m_\mathrm{m}\left(\Omega R_\mathrm{m}\right)^2 + m_\mathrm{esc}\left(\Omega R_\mathrm{esc}\right)^2 + m_\mathrm{t}\left(\Omega R_\mathrm{t}\right)^2\right)}$$

$$\beta = \sin^{-1}\left(\frac{W_\mathrm{t} R_\mathrm{t} + L_\mathrm{b} R_L - W_\mathrm{b} R_\mathrm{b} - W_\mathrm{m} R_\mathrm{m} - W_\mathrm{esc} R_\mathrm{esc}}{\left(m_\mathrm{b}\left(\Omega R_\mathrm{b}\right)^2 + m_\mathrm{m}\left(\Omega R_\mathrm{m}\right)^2 + m_\mathrm{esc}\left(\Omega R_\mathrm{esc}\right)^2 + m_\mathrm{t}\left(\Omega R_\mathrm{t}\right)^2\right)}\right) \tag{E.13}$$

The final equation, Equation E.13 was used to obtain the coning angle, β. The total weight of the monocopter was increased proportional to the coning angle to account for the component of lift that does not contribute to the lift generated by the blade:

$$W_\mathrm{tot} = \frac{W_\mathrm{tot}}{\cos\beta} \tag{E.14}$$

E.4 Drag of Non-Lifting Components

The components of the RMC monocopter that were assumed to be non-lifting components included the carbon fibre blade spar and the telemetry pad. The added drag of the carbon fibre blade spar was accounted for by treating the rod as second blade with a square cross section. The 2D drag coefficient of the square profile was assumed to be 2.1, obtained from White [93]. This was used in the expression for the power coefficient shown in Equation E.2, and numerically integrated to obtain the contribution of the carbon fibre blade spar. The first term in Equation E.2 for the power coefficient is the induced power coefficient. Since the blade spar was assumed to be a non-lifting component, this term was assumed to be zero:

$$dC_{P,\mathrm{r}} = \cancelto{0}{4\lambda^3 r dr} + \frac{1}{2}\sigma C_d r^3 dr = \frac{2.1}{2}\sigma r^3 dr \tag{E.15}$$

Estimating the drag of the telemetry pad was a more involved process. The drag build up method described by Raymer was used to estimate the total drag coefficient of the telemetry pad [94]. The drag coefficient was used to determine the total drag

force, which was then used to determine the torque based on the moment arm of the telemetry pad. This torque was non-dimensionalized and added to the torque coefficient of the entire monocopter estimated by BEMT. Since the torque coefficient and the power coefficient are numerically identical, the increase in power coefficient due to the estimated drag of the telemetry pad was obtained. The calculated increase in the power coefficient due to the drag of the telemetry pad using this method was $\Delta C_P = +0.0060$.

E.5 BEMT Analysis Python Script

The following Python script implements the BEMT analysis with the correction factors for tip losses, propeller effects, coning angle, and the drag of non-lifting components. This script was used to generate the predicted hover performance for the RMC monocopter presented in Chapter 6.

```
'''
monocopter.py

This code runs BEMT including coning and propeller effects on monocopter blade

History
-------
    v. 1.0   - Initial code development (FS, Feb 2022)
    v. 1.1   - Include coning effects (FS, Oct 2022)
             - Correct coning effect to include pad weight
             - Include propeller blown effect
    v. 1.2   - Rewrite BEMT (FS, Nov 2022)
    v. 1.3   = Include effect of thrust vector due to twist (FS, Dec 2022)
    v. 1.4   - Include drag correction for telemtry pad (FS, Jan 2023)
'''

# ================================================
# Standard Python Modules
# ================================================
import numpy as np
import matplotlib.pyplot as plt
from matplotlib.patches import Rectangle
import pdb


def BEMT(N, R, c_r, c_t, r_t, i_0, twist, We, yp, dp, re, etap, etam, etac):
    '''
    Blade element momentum theory
    Inputs:
        - N -> INT: number of blade elements
        - R -> FLOAT: blade radius [in]
        - c_r -> FLOAT: root chord [in]
        - c_t -> FLOAT: tip chord [in]
        - r_t -> FLOAT: taper start location
        - i_0 -> FLOAT: installation angle [deg]
        - twist -> FLOAT: washout [deg]
        - We -> FLOAT: electronics weight [lbf]
        - yp -> FLOAT: propeller location [fraction of R]
        - dp -> FLOAT: propeller diameter [in]
```

```
40          - re -> FLOAT: electronics moment arm [fraction of R]
41          - etap -> FLOAT: propeller efficiency
42          - etam -> FLOAT: electric motor efficiency
43          - etac -> FLOAT: cable losses
44      Outputs:
45          - CT -> FLOAT: Thrust coefficient
46          - CP -> FLOAT: Power coefficient
47          - Omega -> FLOAT: rotational rate
48          - C -> FLOAT: current required
49          - beta -> FLOAT: Coning angle
50          - FM -> FLOAT: figure of merit
51      '''
52      # Load VR7 polars and obtain a_0
53      VR7_Cl = np.load('VR7_Cl.npy')
54      VR7_Cd = np.load('VR7_Cd.npy')
55      VR7_Cm = np.load('VR7_Cm.npy')
56      a_0 = -np.interp(0, VR7_Cl[:,0], VR7_Cl[:,1])/((VR7_Cl[1,1] - VR7_Cl[0,1])
        /(VR7_Cl[1,0] - VR7_Cl[0,0]))*np.pi/180
57      _, Cla = np.polynomial.polynomial.polyfit(VR7_Cl[0:4,0], VR7_Cl[0:4,1], 1)
        *180/np.pi
58      Cla = Cla*0.8
59      Wesc = 0.082
60
61      # Estimate blade weight
62      Wb = 0.200
63      MTOW = Wb + We
64      print(MTOW)
65
66      # Divide blade into elements
67      dr = 1/N
68      r = np.arange(0, 1, dr)
69      r = r + dr/2
70
71      # Blade geometric properties
72      A_blade = c_r*R*r_t + (c_r+c_t)/2*R*(1-r_t)
73      sldy = A_blade/(np.pi*R**2)
74      theta = (i_0 - r*twist)*np.pi/180
75
76      # Blade performance without prop effects, tip loss, or coning
77      inflow = sldy*Cla/16*((1 + (32/sldy/Cla*(theta-a_0)*r))**(1/2) - 1)
78      Phi = inflow/r
79      AoA = theta - Phi
80      Cl = np.zeros(len(r))
81      for i,cl in enumerate(Cl):
82          Cl[i] = np.interp(AoA[i]*180/np.pi, VR7_Cl[:,0], VR7_Cl[:,1])
83      Cd = np.zeros(len(r))
84      for i,cd in enumerate(Cd):
85          Cd[i] = np.interp(AoA[i]*180/np.pi, VR7_Cd[:,0], VR7_Cd[:,1])
86
87      dCT = 0.5*sldy*Cl*r**2*dr
88      dCP = 4*inflow**3*r*dr + 0.5*sldy*Cd*r**3*dr
89      CT = np.trapz(dCT)
90      CP = np.trapz(dCP)
91      Omega = (MTOW/(0.0023769*((np.pi*R**2)/144)*((R/12)**2)*CT))**(1/2)
```

```
92
93      # Include prop effects, tip losses, and coning
94      e_losses = 1
95      beta = 0
96      while e_losses >= 0.01:
97
98          # Propeller effects
99          Q = CP*0.0023769*(np.pi*R**2)/144*Omega**2*(R/12)**3
100         Tp = Q/(yp*R/12)
101         rp = int(yp/dr)
102         w = 1.5*((Tp/np.cos(theta[rp]))/(2*0.0023769*(np.pi*R**2)/144))**(1/2)
103         yp1 = yp - dp/2/R
104         yp2 = yp + dp/2/R
105         for i in range(len(r)):
106             if r[i] >= yp1 and r[i] <= yp2:
107                 inflow[i] += w*np.sin(theta[i])/(Omega*R/12)
108
109         # Thrust based lift vector
110         Lp = Tp*np.tan(theta[rp])
111
112         # Tip losses
113         Phi = inflow/r
114         f = 0.5*((1-r)/(r*Phi))
115         F = (2/np.pi)*np.arccos(np.exp(-f))
116         inflow_tl = np.copy(inflow)
117         for i in range(len(r)):
118             if r[i] >= yp1 and r[i] <= yp2:
119                 inflow_tl[i] = (sldy*Cla/16/F[i]*((1 + (32*F[i]/sldy/Cla*(theta
    [i]-a_0)*r[i]))**(1/2) - 1)
120                                 + w*np.sin(theta[i])/(Omega*R/12))
121             else:
122                 inflow_tl[i] = sldy*Cla/16/F[i]*((1 + (32*F[i]/sldy/Cla*(theta[
    i]-a_0)*r[i]))**(1/2) - 1)
123             e_tip = abs(inflow[i] - inflow_tl[i])/inflow_tl[i]
124             inflow[i] = inflow_tl[i]
125             while e_tip >= 0.0005:
126                 Phi[i] = inflow[i]/r[i]
127                 f[i] = 0.5*((1-r[i])/(r[i]*Phi[i]))
128                 F[i] = (2/np.pi)*np.arccos(np.exp(-f[i]))
129                 if r[i] >= yp1 and r[i] <= yp2:
130                     inflow_tl[i] = (sldy*Cla/16/F[i]*((1 + (32*F[i]/sldy/Cla*(
    theta[i]-a_0)*r[i]))**(1/2) - 1)
131                                     + w*np.sin(theta[i])/(Omega*R/12))
132                 else:
133                     inflow_tl[i] = sldy*Cla/16/F[i]*((1 + (32*F[i]/sldy/Cla*(
    theta[i]-a_0)*r[i]))**(1/2) - 1)
134                 e_tip = abs(inflow[i] - inflow_tl[i])/inflow_tl[i]
135                 inflow[i] = inflow_tl[i]
136
137         # Coning estimation
138         Phi = inflow/r
139         AoA = theta - Phi
140         Cl = np.zeros(len(r))
141         for i,cl in enumerate(Cl):
```

```
142             Cl[i] = np.interp(AoA[i]*180/np.pi, VR7_Cl[:,0], VR7_Cl[:,1])
143         L = np.zeros(len(r))
144         for i in range(len(r)):
145             if r[i] >= yp1 and r[i] <= yp2:
146                 L[i] = 0.5*0.0023769*(Omega*r[i]*R/12 + w*np.cos(theta[i]))**2*
    c_r/12*Cl[i]*dr*R/12
147             else:
148                 L[i] = 0.5*0.0023769*(Omega*r[i]*R/12)**2*c_r/12*Cl[i]*dr*R/12
149         dMb = L*r*R/12
150         Mb = np.trapz(dMb)
151         dMFb = 0.0099208*dr*R*(Omega*r*R/12)**2
152         MFb = np.trapz(dMFb)/32.174
153         MFe = (We-Wesc)*(Omega*re*R/12)**2/32.174
154         MFesc = Wesc*(Omega*0.53*R/12)**2/32.174
155         Mp = Lp*yp*R/12*np.cos(beta)
156         MQp = 0.06/12       # motor torque from APC props
157         beta = np.arcsin((Mb + Mp + MQp + ((We-Wesc)*re*R/12 - Wb*0.5*R/12 -
    Wesc*0.53*R/12)*np.cos(beta))/(MFb + MFe + MFesc))
158
159         # Recalculate blade performance
160         Cd = np.zeros(len(r))
161         for i,cd in enumerate(Cd):
162             Cd[i] = np.interp(AoA[i]*180/np.pi, VR7_Cd[:,0], VR7_Cd[:,1])
163         dCT = 0.5*sldy*Cl*r**2*dr
164         dCP = 0.5*sldy*(Phi*Cl + Cd)*r**3*dr
165         CT = np.trapz(dCT)
166         CP = np.trapz(dCP)
167         Omega_i = (MTOW/(0.0023769*((np.pi*R**2)/144)*((R/12)**2)*CT))**(1/2)
168         e_losses = abs(Omega - Omega_i)
169         Omega = Omega_i
170
171     # Correct for thrust based lift and coning
172     MTOW = MTOW/np.cos(beta)
173     MTOW -= Lp*np.sin(theta[rp])
174     Omega = (MTOW/(0.0023769*((np.pi*R**2)/144)*((R/12)**2)*CT))**(1/2)
175
176     # Estimate pitching moment from blade
177     Cm = np.zeros(len(r))
178     for i,cm in enumerate(Cm):
179         Cm[i] = np.interp(AoA[i]*180/np.pi, VR7_Cm[:,0], VR7_Cm[:,1])
180     dM = Cm*0.5*0.0023769*(Omega*r*R/12)**2*(c_r/12)**2*dr*R/12
181     M = np.trapz(dM)
182
183     # Add electronics pod drag to CQ = CP
184     CPe = 0.0188/(0.0023769*(np.pi*R**2)/144*Omega**2*0.7087**3)
185     CP += CPe
186     dl = 1/N
187     l = np.arange(0, 1, dl)
188     l = l + dl/2
189
190     # Add square rod drag
191     sldy_rod = 8*290/(np.pi*290**2)
192     dCPr = 0.5*sldy_rod*2.1*l**3*dl
193     CPr = np.trapz(dCPr[0:int(0.57*N)]) + np.trapz(dCPr[int(0.83*N):N])
```

```
194     CP += CPr
195
196     # Account for component efficiencies
197     CP = CP/etap/etam/etac
198     P = CP*0.0023769*(np.pi*R**2)/144*(Omega*R/12)**3*1.36
199     C = P/12
200
201     FM = CT**(3/2)/(2**(1/2)*CP)
202
203     # Plot local angles of attack
204     fig,ax = plt.subplots(figsize=(9,3.5))
205     ax.plot(r, AoA*180/np.pi, 'k')
206     ax.set_xlabel(r'Non-dimensional␣Radial␣Position,␣$r$')
207     ax.set_ylabel(r'Local␣Angle␣of␣Attack,␣$\alpha$␣($^{\circ}$)')
208     ax.set_xlim([0,1])
209     ax.set_ylim([0,15])
210     ax.set_yticks(np.arange(0,18,3))
211     ax.grid('major', alpha=0.5)
212     plt.savefig('local_AoA.pdf', bbox_inches='tight')
213     plt.close()
214     return CT, CP, Omega*60/2/np.pi, C, beta*180/np.pi, FM
215
216 if __name__ == '__main__':
217
218     CT, CP, Omega, C, beta, FM = BEMT(1000, 24, 7, 7, 1, 30, 10, 0.554, 0.6, 5,
          0.35, 0.39, 0.75, 0.98)
219     print(CT, CP, Omega, C, beta, FM)
```